UNIVERSITY OF CALIFORNIA,
IRVINE

Engineered Artificial Fe Proteins

DISSERTATION

submitted in partial satisfaction of the requirements
for the degree of

DOCTOR OF PHILOSOPHY

in Chemistry

by

Kelsey Rose Miller

Dissertation Committee:
Professor A. S. Borovik, Chair
Professor Alan F. Heyduk
Professor Michael T. Green

2020

DEDICATION

For my mother – a promise fulfilled
For my father – the Seta forded

Self-esteem is courage, the courage of one's convictions. It is confidence, the confidence to stand up and own your dreams, every bit of them. It is respect, respecting each and every feeling – both negative and positive – that may come up in the process of fulfilling that dream. It is honoring one's life, honoring the struggle, the challenge, the ability to take one more step on a road that feels unbelievably long and winding, and it is faith, from the time we make up our minds to accomplish something to seeing the result of that determination. It is that in-between time, when the doubt and self-loathing and the fear creep in, all the dreams feel as if they are falling or slipping away – that's when we get to see what we're made of; that's when we reveal our own inner strength and limitless potential. That's when I realized what it means to be a woman of unlimited self-esteem.
Amy Schor Ferris

TABLE OF CONTENTS

LIST OF FIGURES

LIST OF TABLES

LIST OF SCHEMES

LIST OF EQUATIONS

ACKNOWLEDGEMENTS

The word mentor has an extremely important place in my heart. Throughout my graduate career, I have had the honor of being mentored by many truly amazing people. This process would not have been possible without their efforts. To my advisor, Andy: I give my utmost appreciation to you as my mentor. I know I came into your lab by basically stalking you and your lab, making a huge binder, and being "pleasantly aggressive" or your favorite; "a lot, all at once." I have always appreciated how you hold yourself as a scientist, your ethical standard, and your willingness to stand up for your ideas, even if you may be the only voice in the room. Being in your lab has helped me become not only a better scientist, but also a more confident woman. There have been many struggles in our science over the years, and I know that many of them were because I am extremely stubborn. Even when nothing seemed to be working, and I was talking your ear off about a blue crystal for four straight years, you did not give up on me. I will always be appreciative of your mentorship and the relationship that we have built over the last six years.

I would also like to thank my committee members: Professor Alan Heyduk and Michael Green for serving on my committee and their time. Alan, my favorite memory of our interactions was a time in my first year. I was in your Physical Inorganic class and I had a units problem in our last problem set – I called it the "second gauss" because it could not be cancelled in the problem we were doing. After pestering Lindsey for a while, I remember coming to your office and you told me, "I've been told you were coming, and I know why you're here, but I'm not sure what the answer is." Even from the beginning, when you did not know how to answer my question, you sat with me through all of my post-it note questions and truly helped me understand. Thank you for being a wonderful mentor throughout this process. M.T., I asked you to be on my defense committee because in each of my exams, I felt that you pushed me and made me dig deep to understand how a good scientist should think about their science. Especially, after my candidacy exam, we spent a few months together on the roof with your chalkboard. You spent time with me, a student you barely knew, just to help fill a gap in my knowledge. For your time and mentorship, I will always be grateful.

One of the most wonderful parts about being in the Borovik lab is the community and friendships that are cultivated. The lab I came into was a close-knit group of people that welcomed me immediately, even though I was always in an "excited state." My labmates, Jon, Sarah, Ethan, Sam, Jason, Nate, and Victoria showed me what an amazing team can look like. They showed me through their discipline and integrity what it takes to do great science. I will always be appreciative for the standard they set, and that they took the time to help me to reach it. I have to make a special shoutout to Jon and Sam – my AMP mentors. Jon, thank you for starting this project. I know it must have taken a lot of courage to jump into something completely unknown and without you, I would not have been able to have the same graduate career. DR. SAM MANN – it is hard to properly tell you exactly what you have done for me. From the moment I started working on AMP, you were so patient and tolerant. I did not know anything when I joined the group and you stayed with me at every

turn and made sure I would be successful. You put up with so much from me – immediately talking to you right as you came into lab, taking over the peanut table because I needed to talk out science with you, or cleaning up your bench when you specifically told me not to. You are a wonderful mentor and I hope you know how appreciative I am for everything you have done for me. AND HERE WE GO….my cubby mate…Victoria Frances Oswald. There are not many people you meet in life that are both your mentor and your best friend. Most of my happiest memories in graduate school include you: pushing each other to do our best science, making each other laugh all day long, playing pranks on people, planning surprises, dancing in lab to that "mounting" song, Starbucks trips, late nights, early mornings, and of course, giving Andy hell. I could not have foreseen what a blessing it was that Andy put me behind you in the "cubby from hell." I hope you know how much you mean to me. I'll always be in your cubby. A special shoutout to two postdocs – Maisha (a.k.a. M-DISHA) and Lisa. Maisha, I felt like you came into my life at the exact perfect moment. I know that I was a lot all the time but you always made me feel like I could come to you with anything. You are an amazing mentor, especially for a young woman trying to gain some confidence. I treasure your friendship and mentorship immensely. Lisa, you always told me to continue working on what I was passionate about and always believed in my abilities as a scientist. All those nights, you gave me pep talks as I was setting up crystals at 9 p.m., helped me more than you know. I am continually grateful for your support. For those who came after me, j, Dolores, Sunny, Meghen, Ankita, Francisco, Natalie, Ali, Jennifer, and Phan, I have enjoyed getting to know all of you. The Borovik lab is a special place to grow as a person and as a scientist. Take advantage of everything this lab has to offer and push yourselves to honor your dreams and the scientists that have come before.

My graduate work relies heavily on collaboration with other labs and scientists. I have a special gratitude for the mentorship of a few students not in the Borovik lab. First, Alec…oh Alec…you are the reason I got Precious. Need I say more? You have literally stayed up with me until 2 a.m. collecting structures, letting me bother you at both UCI and now at Caltech, and answering every one of my phone calls. I can always count on you to want to talk about science and want to get margaritas at Cabo Cantina! Second, Melissa DENLER, the few months you spent in our lab are some of my favorite memories. You are a rockstar, powerhouse of a female and scientist, and I am so blessed to have you as a friend. You cannot escape me! Third, Andrew, thank you for always being willing to talk with me…even when you somehow manage to bring up dimers in almost every discussion. I have appreciated your efforts to help me in all my crazy science problems more than you realize. Also, I had the wonderful opportunity to spend three months in Tom Ward's lab at the University of Basel in Switzerland. I will cherish that experience for the rest of my life and will always consider my time in Switzerland to be the turning point in my graduate career. While everyone in the Ward lab was wonderful, I want to specially thank two postdocs, Ryan and Joan. Together as the "Three Musketeers," their mentorship helped me progress my science and helped me grow as a scientist in ways for which I will always be grateful. Lastly, the ladies of my cohort, Bianca, Kellen, Megan, and Monica, I felt so fortunate to

come in with a class of such incredible women. You have helped me grow in countless ways and you each will always have a friend in me.

I began my scientific journey at Mount St. Mary's College under the mentorship of Dr. Eric Stemp and my student mentor Dr. Anne Esguerra. I owe a special debt of gratitude to both of you for your outstanding patience and mentorship, giving me an excellent foundation to go after my dreams. You both having my unwavering gratitude and respect. Thank you for seeing something in me, even when I may not have seen it in myself.

Aside from my scientific mentors, my family and friends have been a constant source of inspiration and mentorship throughout my entire life. I have been fortunate to be the older sister to four amazing women, Brigitte, Annie, Becky and Mariah (KBBAM). You ladies were my first mentors. You taught me what unconditional love is and there is not anything I would not do for any of you (and of course my precious, perfect niece Lillian). My cousin Nicole (Nicole's cousins), you brought me to my first chemistry class and ignited the spark which started this whole path. The six of us will always be the OG team. My best friends, Leah, Julia, Denise (Team Tardis), Ziva, and Alyson, you taught me what great friendship is and what unwavering support looks like. You are all powerful women that constantly inspire me. My love and respect for each of you knows no bounds.

I am eternally grateful to my parents. Mom, I made you a promise when I was 6 years old that I would get my Ph.D. I watched you change our lives with education, and I could not be more grateful for everything you have done. You have supported me in every way imaginable and never wavered in your belief that I could accomplish this dream. It is my great fortune to have you as my mother. Dad, when I was struggling in college, you gave me encouragement from *Reply to Yasaburo*. You told me that all I had to do was make a choice. Every choice I have made, I always had your full support. We are the "Ever-Campaigning Millers" and words cannot express my gratitude for all your efforts. Nichiren says it best, "Mount Sumeru is paltry in comparison to the towering debt you owe your father; the great ocean is shallow compared to the profoundness of the debt you owe your mother." The debt of gratitude I owe to you both is profound and I will always be humbled by your love and support.

To my fiancée Chris, we found each other at interesting times in both of our lives and grew in both friendship and love. As most who know me understand, I can be pretty stubborn and you have stood by me through everything in the past five years. You have had a profound impact on my life and I am so excited to spend our lives together. I am always on your team.

I would not have been able to pursue my dream of getting my Ph.D. without the constant mentorship and support of all of these people and many more. I am forever grateful for all of you.

Last but not least, I would like to thank my Starbucks Milk Tea, without which, none of this chemistry would be possible.

CIRRICULUM VITAE

Education

University of California – Irvine April 2020
Ph.D. Chemistry, Specific Field: Inorganic
Research Advisor: A.S. Borovik
Mount St. Mary's College May 2013
B.S. Biochemistry, Minor: French

Publications

1. **K. R. Miller**, J. D. Paretsky, A. H. Follmer, T. Heinisch, K. Mittra, S. Gul, I.-S. Kim, F. D. Fuller, A. Batyuk, K. D. Sutherlin, A. S. Brewster, A. Bhowmick, N. K. Sauter, J. Yano, M. T. Green, T. R. Ward, A. S. Borovik. "Artificial Iron Proteins: Modelling the Active Sites in Non-Heme Dioxygenases." *Inorg. Chem.* **2020**, 59, 6000-6009.

2. A. Mazaheripour, G. Kladnik, J. M. Jocson, A.G. Wardrip, C. B. Markegard, N. Frey, A. Cossaro, L. Floreano, A. Verdini, A. Bartlett, A. M. Burke, N. Hüsken, **K. Miller**, K. V. Wonterghem, R. C. Lopez, M. Lu, A. Masurkar, M. N. Dickson, S. Sharifzadeh, H. D. Nguyen, I. Kymissis, D. Cvetko, A. Morgante, A. A. Gorodetsky. "Unexpected Length Dependence of Excited-state Charge Transfer Dynamics for Surface-confined Perylenediimide Ensembles." *Mater. Horiz.* **2017**, 4, 437-441.

3. **K. R. Miller**, A. H. Follmer, A. Jasniewski, S. Biswas, S. Sabuncu, T. Albert, P. Möenne-Loccoz, M. P. Hendrich, A. S. Borovik. "Artificial Metalloproteins with Dinuclear Iron Centers." *In preparation.*

4. **K. R. Miller**, J. Serrano-Plano, R. L. Peterson, A.H. Follmer, S. Biswas, T. Albert, P. Möenne-Loccoz, M. P. Hendrich, T. R. Ward, A. S. Borovik. "Trapping Dioxygen Species in Artificial Iron Proteins." *In preparation.*

Awards and Fellowships

National Science Foundation Graduate Research Fellowship	2015-2020
UCI Associated Graduate Student Winter Travel Grant Award	2018
Mount St. Mary's College President's Award	2013
Stogryn Award for Excellence in Undergraduate Research	2012, 2013

Presentations

K. R. Miller, A. S. Borovik. Artificial Iron Proteins using Biotin-Streptavidin Technology. Abstracts of Papers, 259th ACS National Meeting & Exposition, Philadelphia, PA, United States March, 22-26, 2020. Talk. (Meeting cancelled)
K. R. Miller, A. S. Borovik. Artificial Iron Proteins using Biotin-Streptavidin Technology. Abstracts of Papers, SoCal Bioinorganic Conference, Los Angeles, CA, United States, December 7, 2019. Talk.

K. R. Miller, A. S. Borovik. Artificial Iron Proteins using Biotin-Streptavidin technology. Abstracts of Papers, 258th ACS National Meeting & Exposition, San Diego, CA, United States, August 25-29, 2019. Talk.
K. R. Miller, A. S. Borovik. Designed Artificial Iron Proteins. Abstracts of Papers, 257th ACS National Meeting & Exposition, Orlando, FL, United States, March 31-April 4, 2019. Talk.
K. R. Miller, A. S. Borovik. Designed artificial Iron Proteins. Bioinorganic Gordon Research Seminar, Ventura, CA, United States, Jan 31-Feb 3, 2019. Talk and Poster.
K. R. Miller, A. S. Borovik. Bioinspired Synthetic Inorganic Chemistry: Artificial Metalloproteins. SoCal Bioinorganic Conference, Los Angeles, CA, United States, December 2, 2018. Poster.
K. R. Miller, A. S. Borovik. Design of Artificial Iron Proteins using Biotin-Streptavidin technology. UCI Student Inorganic Seminar Series, Irvine, CA, United States, May 10, 2018. Talk.
K. R. Miller, A. S. Borovik. Design of Artificial Metalloproteins using Biotin-Streptavidin Technology. Abstracts of Papers, 255th ACS National Meeting & Exposition, New Orleans, LA, United States, March 18-22, 2018. Talk and Poster.
K. R. Miller, Eric Stemp. Use of Osmium (III) Complexes to determine Influence of Base Bismatches on DNA-Protein Crosslinking. Abstracts of Papers, 16th International Conference on Bioinorganic Chemistry, Grenoble, France, July 22-26, 2013. Poster.
K. R. Miller, Zitadel Perez, Eric Stemp. 8-Oxoguanine Oxidation and Production in Duplex DNA. Abstracts of Papers, 245th ACS National Meeting & Exposition, New Orleans, LA, United States, April 7-11, 2013. Talk.
K. R. Miller, Zitadel Perez, Eric Stemp. 8-Oxoguanine Production and Oxidation in Duplex DNA. Abstracts of Papers, Southern California Conferences for Undergraduate Research, CSU Channel Islands, Camarillo, CA, United States, November 17, 2012. Talk.
K. R. Miller, Zitadel Perez, Amanda Madison, Eric Stemp. Selective Oxidation of 8-oxo-guanine by $Os(phen)_2dppzCl_2$ as visualized by DNA-Protein Crosslinking. Abstracts of Papers, 243th ACS National Meeting & Exposition, San Diego, CA, United States, March 25-29, 2012. Poster.
K. R. Miller, Zitadel Perez, Eric Stemp. Selective Oxidation of 8-oxo-guanine by $Os(phen)_2dppzCl_2$ as visualized by DNA-Protein Crosslinking. Southern California Conferences for Undergraduate Research, Mount San Antonio College, Walnut, CA, United States, November 19, 2011. Talk.
Zitadel Perez, **K. R. Miller**, Amanda Madison, Eric Stemp. Effects of DNA Mismatches on DNA-Protein Crosslinking from Guanine Oxidation. Abstracts of Papers, 241th ACS National Meeting & Exposition, Anaheim, CA, United States, March 27-31, 2011. Poster.
Zitadel Perez, **K. R. Miller**, Eric Stemp. Effects of DNA mismatches on DNA-Protein Crosslinking from Guanine Oxidation. Southern California Conferences for Undergraduate Research, Pepperdine University, Malibu, CA, United States, November 20, 2010. Poster.

ABSTRACT OF THE DISSERTATION

Engineered Artificial Fe Proteins

by

Kelsey Rose Miller

Doctor of Philosophy in Chemistry

University of California, Irvine, 2020

Professor A. S. Borovik, Chair

Nature employs metalloproteins to mediate chemical transformations with impressive rates and selectivities. The efficiency of metalloproteins has been attributed in part to the control of the local environments surrounding their functional active metal center(s). This control is often achieved by non-covalent interactions including hydrogen bonds (H-bonds) from amino acid residues and extended H-bonding networks that include water molecules. In synthetic systems, it has been difficult to establish similar noncovalent interactions with control and predictability. In this dissertation, an approach has been used to model the active sites of metalloproteins by immobilizing metal complexes within a protein host. Using biotin-Streptavidin (Sav) technology, artificial metalloproteins (ArMs) have been designed that model several important features in both the primary and secondary coordination sphere that are seen in native metalloproteins.

Chapter 2 describes the development of Fe^{II} and Fe^{III} artificial proteins that model key structural aspects in mononuclear Fe dioxygenases. Structural characterization showed that there was coordination from two nitrogen atom donors from the synthetic ligand and one oxygen atom donor from a nearby glutamate amino acid residue that models the 2-His-

1-carboxylate facial triad found in mononuclear nonheme Fe enzymes. Additionally, the water molecules that complete the coordination sphere of the Fe center participated in H-bonding, which is also seen in native metalloproteins.

Chapter 3 discusses the efforts to bind an α-ketoglutarate analog, phenylpyruvate, and dioxygen to the Fe^{II} ArM from Chapter 2. A combination of spectroscopic and crystallographic techniques supported the docking of phenylpyruvate near the Fe active site through a π-stacking interaction with the synthetic ligand. Further structural characterizations from multiple crystals showed that dioxygen can coordinate to the Fe center in different conformations. Mössbauer studies supported the formation of an Fe^{III}–peroxido species within Sav.

Chapter 4 details the design of di-Fe^{III} ArMs. An optical screen was designed to determine the proper match of synthetic ligand and Sav variant to form a di-Fe active site. The optical screen utilized endogenous phenolate coordination to produce a blue color to determine the correct match. Spectroscopic and crystallographic techniques supported phenolate coordination to the Fe center and the formation of a di-Fe^{III} center with a μ–oxido/hydroxido bridging ligand within Sav. Additionally, studies with exogenous ligands, acetate, azide, isothiocyante, and cyanide, showed the Fe···Fe distance ranged between 3.7-4.1 Å and are comparable with native di-Fe proteins.

CHAPTER 1

Introduction

Bioinorganic chemists have long sought answers to fundamental questions about how metalloproteins perform their numerous functions under ambient conditions. The impressive rate and selectivity by which metalloproteins perform difficult chemical transformations have motivated synthetic chemists to design experiments that address how metalloproteins function in nature. From the fields of synthetic chemistry and biology, pivotal studies on the structure and function relationships of metalloproteins have shown that the coordination environment surrounding the metal center(s) significantly contributes to the properties of the metallocofactor and the overall function of the metalloprotein. The coordination environment around the metal center(s) is made up of a combination of the primary coordination sphere – the ligands directly bound to the metal center(s) – and the secondary coordination sphere – the noncovalent interactions such as hydrogen-bonding (H-bonding) networks, electrostatic interactions, and steric interactions that surround the metallocofactor. Noncovalent interactions aid in regulating substrate access and preventing unproductive chemistry at the metalloprotein active site. It has been shown that removing noncovalent interactions around a metallocofactor often decreases or halts the reactivity of a metalloprotein. The combined influence of the primary and secondary coordination spheres is necessary for efficient metal-mediated processes.[1]

The superfamily of mononuclear non-heme Fe enzymes highlights the contributions of both the primary and secondary coordination spheres to metalloprotein function. Several mononuclear non-heme Fe enzymes are characterized by a common structural motif known as the 2-His-1-carboxylate facial triad.[2–8] The facial triad motif consists of

three endogenous protein ligands, two histidine residues and one glutamate/aspartate residue, arranged to coordinate in a facial geometry to an Fe center.[2–4] Additionally, the facial triad motif is conserved over several Fe proteins, including the catechol dioxgenases, Rieske dioxygenases, α-ketoglutarate (α-KG)-dependent enzymes, pterin-dependent hydroxylases, and other oxidases. These enzymes facilitate dioxygen activation and the oxidation of several substrates, including α-KG, catechol, pterin, and other arenes.[2–4] For example, taurine dioxygenase (TauD) is an α-KG-dependent enzyme that catalyzes the conversion of 2-aminoethanesulfonate (Tau) to sulfite and aminoacetaldehyde while decomposing α-KG to succinate and carbon dioxide.[5]

Work by Bollinger and Krebs elucidated the mechanism of TauD, and highlighted the importance of the coordination environment around the Fe center for function. The resting state of TauD is a ferrous species coordinated by H99, H255, D101, and three additional water molecules to complete the primary coordination sphere (Figure 1.1). Upon cofactor α-KG binding and the substrate Tau docking, one labile water molecule is displaced to reveal an open coordination site for dioxygen to coordinate. Once dioxygen binds, oxidative decarboxylation generates the competent oxidant, an Fe^{IV}–oxido species, which performs substrate oxidation (Figure 1.1).[9] Work by Hausinger and Elkins illustrated the importance of the secondary coordination sphere to the substrate oxidation reactivity of TauD.[10–12] As shown by the molecular structure of TauD determined by X-ray diffraction (XRD) studies, several H-bonding interactions and one salt bridge place α-KG and Tau in the optimal location for reactivity. The α-KG molecule coordinates in a bidentate fashion to the ferrous center and is stabilized by a salt bridge to R266 and a H-bond to T126. In contrast, Tau does not coordinate to the ferrous metal center.[10,11,13] Instead, Tau docks ~5

Å away from the ferrous metal center and is stabilized in a pre-organized pocket by H-bonds to Y73, N95, S158, R270, H70, and V102 (Figure 1.1).[10,11] Additionally, work by McCusker and Klinman showed that a nearby F159 residue plays an important steric role in positioning Tau in the correct orientation to undergo hydrogen atom transfer (HAT) to the Fe^{IV}–oxido intermediate.[14,15] Disruption of these noncovalent interactions has been shown to affect the overall reactivity of TauD.

As shown in TauD, the coordination environment around a metal center in a metalloprotein is important for modulating the reactivity of metalloproteins. The amino acid residues and water molecules that are present in the active site of the metalloprotein can either coordinate to the metal center or act as H-bond acceptors/donors within the local environment of the active site. The cooperation of the primary and secondary coordination spheres can also be seen in native di-Fe proteins, such as in hemerythrin (Hr). Hr is a dioxygen carrier protein found in the phyla of marine invertebrates. Hr contains a di-Fe active site with five histidine and two bidentate bridging carboxylate amino acid residues buried within a 4-helix-bundle structural motif.[16] An additional hydroxido ligand

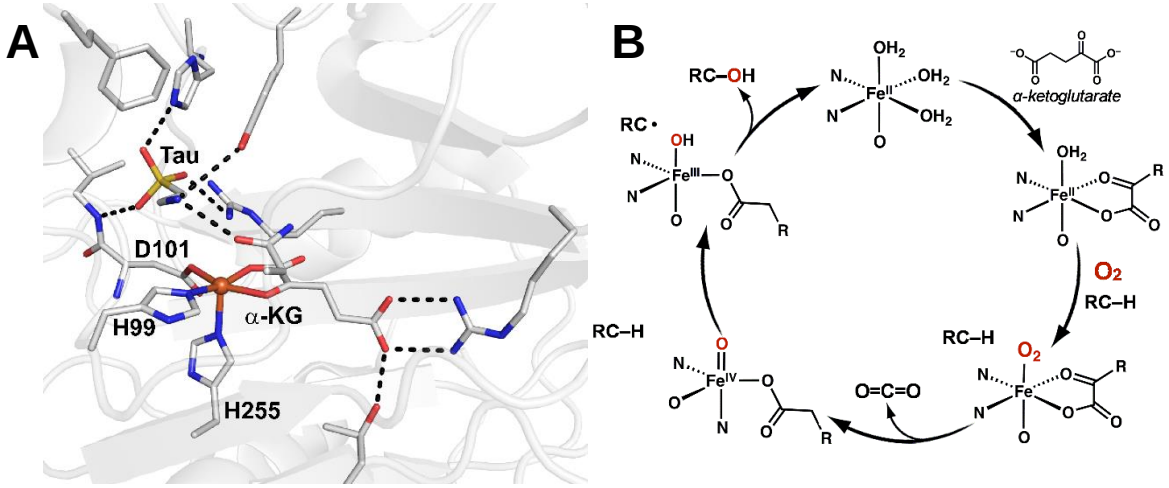

Figure 1.1 Active site (**A**, PDB 1OS7) and proposed mechanism of TauD (**B**). H-bonding network is shown with black dashed lines.

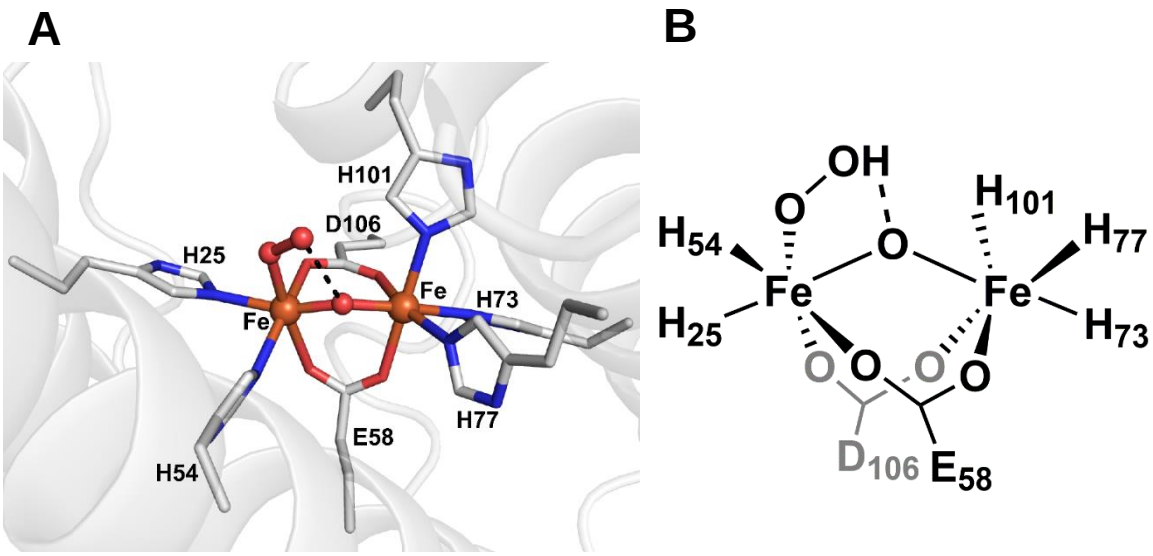

Figure 1.2 Molecular structure (**A**: PDB 1HMO) and ChemDraw representation of OxyHemerythrin active site (**B**: OxyHr). H-bonds are shown as black dashed lines.

bridges the two Fe^{II} metal centers, facilitating antiferromagnetic coupling between the two metal centers. One of the Fe^{II} metal centers has an open coordination site, which has been demonstrated by Stenkemp and coworkers to be the site of dioxygen binding.[16–21] Upon dioxygen coordination, the Fe_2^{II} active site forms an $Fe^{II}Fe^{III}$–superoxido adduct, which is stabilized by a H-bond with the proton on the hydroxido bridging ligand (Figure 1.2).[22] The $Fe^{II}Fe^{III}$–superoxido adduct undergoes proton and electron transfer to form a hydroperoxido species (OxyHr). Solomon and Brunold described OxyHr as a (μ–oxo)di-Fe^{III} species with a terminally bound hydroperoxido ligand that is H-bonded to the oxido bridging ligand.[22] The H-bonding interaction between the hydroxido ligand and bridging oxido ligand provides the pathway by which Hr is able to reversibly bind dioxygen within the active site.

Molecular Design in Synthetic Systems

The importance of both the primary and secondary coordination sphere effects for producing highly functional metalloproteins has been clearly demonstrated for numerous

proteins, and has prompted the synthetic community to prepare metal complexes that can access similar levels of selectivity and reactivity.[23–39,39–61] However, in synthetic systems, it is often difficult to replicate the precise control over the primary and secondary coordination spheres seen in metalloproteins. Some challenges that rational design must overcome are 1) the placement of functional groups which can act as H-bond donors/acceptors or ligands near a metal center and 2) the prevention of multi-metallic complex formation from reactive species which often undergo unproductive chemistry.

One of the first examples of a synthetic system that was able to overcome these challenges is the "picket-fence" porphyrin, developed by Collman, to model the chemistry performed by hemoglobin (Hb) and myoglobin (Mb). Through H-bonding interactions that stabilize the dioxygen adduct, Hb and Mb reversibly bind dioxygen at a heme active site that is buried within the protein. In the absence of a protein host, Fe porphyrin complexes tend to dimerize and form Fe–oxido/hydroxido-bridged species in the presence of

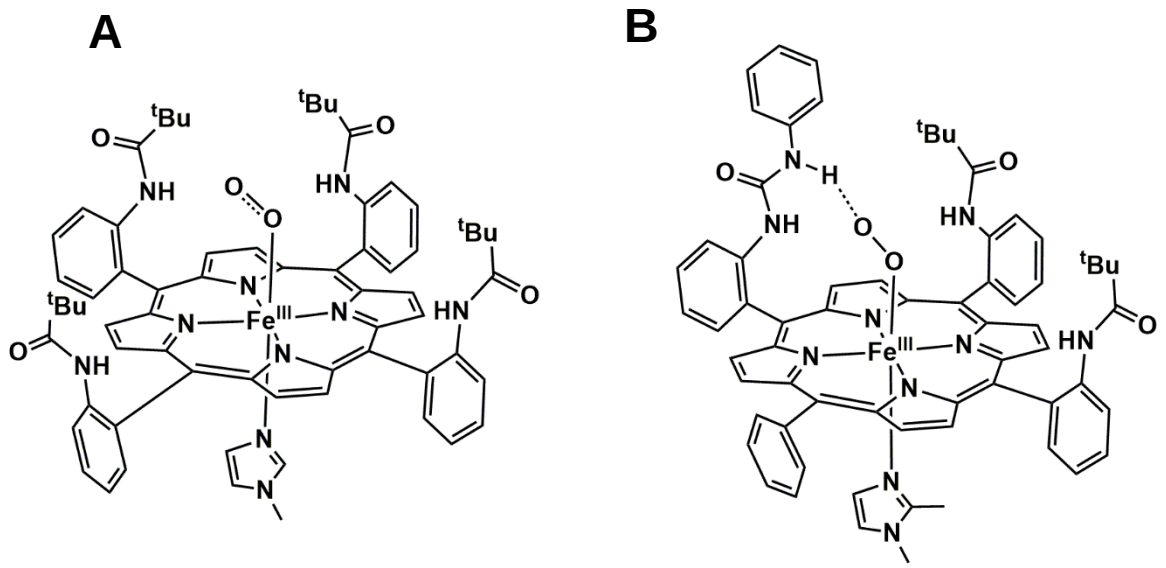

Figure 1.3 Collman's structurally characterized picket-fence porphyrin stabilizing an Fe–O_2 adduct (**A**) and the modified phenyl-urea picket-fence porphyrin capable of H-bonding (**B**, H-bond indicated by a dashed line).

dioxygen. To prevent dimerization and protect the Fe–O_2 adduct, Collman site-isolated his Fe center by designing a picket-fence porphyrin with bulky pivalamido moieties to "fence off" one face of the porphyrin. In addition, he used a sterically encumbered imidazole to bind one of the axial coordination sites at the Fe center, leaving only one coordination site available within the cavity for dioxygen to bind.[62,63] The design of the primary coordination sphere of the picket-fence porphyrin replicated the active site of Hb and Mb and synthetically enabled the reversible binding of dioxygen (Figure 1.3). Although the original design of the "picket-fence" porphyrin was intended to enable H-bonding of the superoxido ligand to the pivalamido groups, the molecular structure revealed that the pivalamido groups were over 5 Å away from the Fe^{III}–superoxido adduct, which made the formation of intramolecular H-bonds impossible. New derivatives of the picket-fence porphyrin were developed to install H-bonding moieties closer to the exogenous O_2 unit. One derivative appended a phenyl urea moiety to the picket-fence framework and was found to enhance the Fe porphyrin's affinity for O_2 binding (Figure 1.3).[64] The increased affinity was attributed to the formation of a H-bonding interaction between the urea N–H group and the superoxido ligand.

Since the development of Collman's picket-fence porphyrin, the use of rigid ligand frameworks has produced a variety of complexes which have been instrumental in improving our understanding of how the coordination environment around a metal center affects function. For over two decades, the Borovik group has been interested in studying biologically relevant metal-mediated processes and how the coordination environment around the metal center(s) can be modulated to access reactive intermediates. Our group has designed a variety of multifunctional, rigid ligand frameworks that incorporate

secondary coordination sphere interactions within proximity of an open coordination site on a transition metal complex. With this approach, the group has demonstrated the power of designing H-bond accepting/donating ligands to trap reactive intermediate species.[44,65–67] For example, the ligand $[H_3buea]^{3-}$ is a *C*$_3$-symmetric tripodal ligand framework that provides H-bond-donating urea groups to stabilize nucleophilic metal-oxido complexes. $[H_3buea]^{3-}$ was used successfully to trap the first examples of crystallographically characterized Mn^{III}–oxido and Fe^{III}–oxido complexes,[68–70] the second example of an Fe^{IV}–oxido complex,[71,72] and a spectroscopically characterized Mn^{V}–oxido species (Figure 1.4).[73,74]

In addition to $[H_3buea]^{3-}$, which demonstrated that H-bonding can stabilize reactive intermediates, a hybrid ligand framework, $[H_2bupa]^{2-}$, was designed containing two urea arms and a pivalamide-functionalized pyridine to act as a H-bond accepting group. $[H_2bupa]^{2-}$ was shown to stabilize a Mn^{III}–peroxido intermediate derived from dioxygen (Figure 1.4).[75] Subsequent studies showed that the $[Mn^{II}H_2(bupa)]^-$ complex catalyzed the reduction of dioxygen to water and that a Mn^{III}–peroxido complex was formed as an on-pathway intermediate. Furthermore, the pivalamide moiety was thought to play an important role in the catalytic activity of $[Mn^{II}H_2(bupa)]^-$. During the cycle, the pivalamide switched between coordinating to the Mn center, acting as a basic site to shuttle protons to

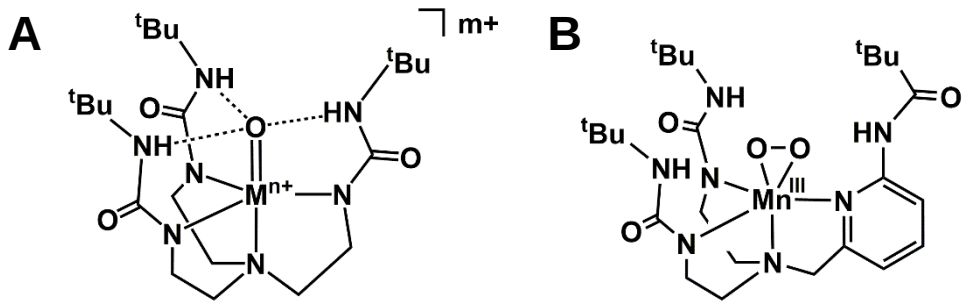

Figure 1.4 Generic metal–oxido complex with $[H_3buea]^{3+}$ (**A**) and $[Mn^{III}H_3bupa(O_2)]^-$ (**B**).

the Mn^{III}–peroxo, and displacing the water molecule formed in the catalytic cycle to regenerate the starting Mn^{II} complex.[76] With the $[H_2bupa]^{2-}$ ligand framework, our group demonstrated the importance of positioning functional moieties in the secondary coordination sphere, as well as how H-bonds can play a key role in the activation of small molecules.

In addition to the $[H_3buea]^{3-}$ and the $[H_2bupa]^{2-}$ ligand frameworks that incorporated H-bond-donating groups to stabilize oxido/hydroxido ligands, another ligand was designed to incorporate intramolecular H-bond-accepting sulfonamido groups to aid in stabilizing ligands with multiple protons, such as water and ammonia. However, this redesign of the ligand cavity to form the ligand $[MST]^{3-}$ had an unexpected benefit; it created an auxiliary binding site for secondary metal ions that allowed for the preparation of discrete hetero- and homobimetallic complexes. Designing discrete bimetallic complexes is an attractive synthetic target because many metalloproteins facilitate cooperative multi-electron processes with more than one transition metal ion in the active site. The development of $[MST]^{3-}$ allowed for the isolation of several hetero- and homobimetallic complexes with a hydroxido bridging ligand to both a redox-inactive metal ion or a first-

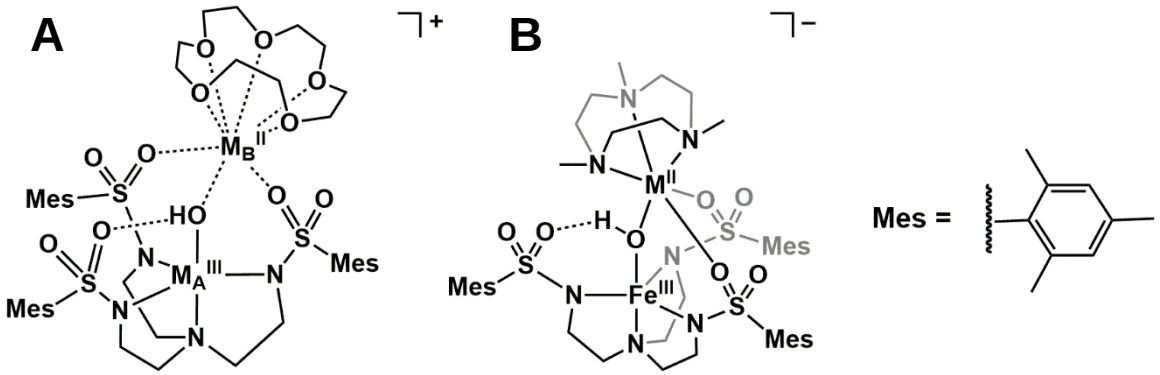

Figure 1.5 Generic bimetallic complex [15c5⊃M_B^{II}–(μ–OH)–M_A^{III}MST]. M_B^{II} = Ca, Sr, or Ba and M_A^{III} = Mn or Fe (**A**) and [TMTACN⊃Fe^{III}–(μ–OH)–M^{II}MST]. M^{II} = Mn, Fe, Co, Ni, Cu, Zn (**B**).

row transition metal ion (Figure 1.5).[77–81] An important result from the studies with $[MST]^{3-}$ showed that Fe and Mn complexes exhibited enhanced O_2 activation rates when a redox-inactive group II metal ion was present, similar to what is observed in the oxygen-evolving complex of Photosystem II.[78]

Although synthetic model complexes have been successfully used to trap several important reactive intermediates and elucidate mechanistic steps within metalloprotein function, it is often difficult for synthetic complexes to establish the extended noncovalent interactions, such as water channels or electron transfer relays, that are essential for function in proteins. For most synthetic complexes, control of the coordination spheres is limited to secondary sphere interactions that are in close proximity to the metal center(s). Furthermore, there are additional limitations in the solubility and stability of metal complexes in aqueous solutions, and it is synthetically challenging to design synthetic complexes that position functional groups within a sufficient range to participate in both coordination spheres of a metal complex as is observed for the amino acid residues and water molecules in metalloprotein active sites.

Molecular Design in Artificial Metalloproteins

A new field of bioinorganic chemistry, which is capable of expanding on the approach of synthetic complexes, emerged through the development of artificial metalloproteins (ArMs). ArMs incorporate non-native metal ions or metal complexes in a naturally occurring or synthetic protein host. These ArMs have been used to study the structure and function of native metalloproteins and to design new metalloproteins with different or enhanced functionalities. From a design perspective, a protein host can provide endogenous ligands from amino acid residues, and when combined with synthetic ligands

can create new and unique primary coordination spheres. Additionally, the protein host provides noncovalent interactions that can extend the secondary coordination sphere interactions to include extensive H-bonding networks that are difficult to achieve in purely synthetic systems.

Beginning in the 1950s,[82] ArMs were conceptualized as a method to combine the advantages of homogeneous catalysis, which has a broad catalytic scope, and enzymatic catalysis, which has high activity and selectivity under mild conditions.[83] In synthetic complexes, the catalytic activity and selectivity are almost completely dominated by the primary coordination sphere of the metal complex. However, in enzymatic catalysis, the secondary coordination sphere is known to play an important role in establishing catalytic activity and selectivity through noncovalent interactions. The use of ArMs provides the ability to control the primary coordination sphere and to develop a variety of long-ranging secondary coordination sphere interactions.

There are two general approaches to the design of ArMs: 1) rational design and 2) directed evolution. Several methods have been utilized to develop new ArMs through the rational design approach, such as the *de novo* design of peptides, the creation of new or enhanced active sites in native proteins, and protein self-assembly.[83–102] Additionally, as an alternative to synthetic catalysts, bioinorganic chemists have employed directed evolution as a systematic method to repeat cycles of mutagenesis to generate artificial metalloenzymes that are genetically optimized for stereoselectivity, regioselectivity, and activity.[103]

De-novo-designed peptides were first developed in the 1980s by Degrado and coworkers.[104–106] *De-novo* design proteins utilize single-chain peptides that fold into three- or four-helix bundles that can model the naturally-occurring structural motifs seen in native metalloproteins and bind metal ions via amino acid residues in the interior of the peptide fold. Degrado has developed many *de novo* peptides that model several important active sites in nature, such as porphyrins and FeS clusters.[104] One important family of *de novo*-designed peptides are the *due ferri* (DF) proteins, which are composed of an antiparallel four-helix bundle with either a di-Zn, di-Mn, or di-Fe active site. The di-Fe DF proteins have a primary coordination sphere consisting of either a 2-His/4-carboxylate (DFT2) or 3-His/4-carboxylate motif and can catalyze a wide variety of O_2-dependent reactions with rates similar to those exhibited by native proteins (Figure 1.6).[104,107] For example, by making subtle mutations to the microenvironment around the di-Fe active site, the DF proteins can catalyze the ferroxidase reaction, the oxidation of 4-aminophenol to the corresponding quinonemonoimine, the oxidation of 3,5-di-tert-butylcatechol to

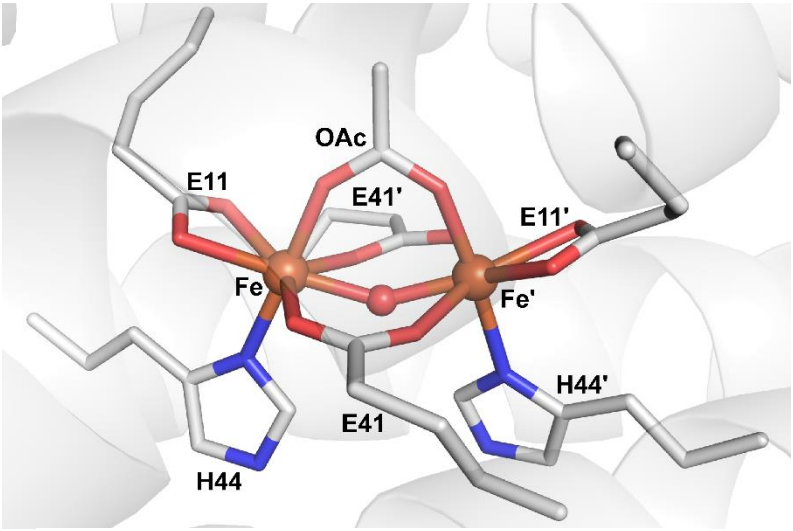

Figure 1.6 Molecular structure of di-Fe^{III} DFT2.

quinone, and the hydroxylation of arylamines, such as the conversion of *p*-anisidine to *p*-hydroxylamino-anisole.[104]

ArMs have also been designed by engineering novel active sites in native proteins to achieve different or enhanced functionality. Three key parameters must be considered when converting native proteins into ArMs: 1) the transition metal complex/catalyst, 2) the protein scaffold, and 3) the mode of attachment of the transition metal complex/catalyst to the scaffold.[83] The first example of a redesigned protein host was reported by Whitesides, who embedded a biotinylated diphosphinerhodium(I) complex within the protein avidin. The resulting ArM catalyzed the asymmetric hydrogenation of α-acetamidoacrylic acid with an enantioselectivity of 41%.[108] Since that seminal paper, the use of biotin-(strept)avidin (Sav) technology to generate ArMs has been pioneered by Ward through the design of several biotinylated organometallic complexes that catalyze a wide variety of reactions, including hydrogenation, alcohol oxidation, sulfoxidation, dihydroxylation, allylic alkylation, transfer hydrogenation, Suzuki cross-coupling, C–H bond activation, and metathesis.[98,109–117] For example, Ward and coworkers designed a biotinylated Rh^{III} pianostool complex that, when immobilized in wild-type (WT) Sav, exhibited moderate selectivity and good activity in the coupling of benzamides and alkenes to form dihydroisoqinolones.[118] No molecular structure was obtained for this Rh ArM; however, the molecular structure was later reported of a crystallized Ir pianostool complex that highlighted the location of complex immobilization in Sav (Figure 1.7).[119] Additionally, in the Rh^{III} ArM, two subsequent mutations to nearby amino acid residues $S_{112}Y$ and $K_{121}E$ imparted a nearly 100-fold rate acceleration over the activity of the isolated rhodium complex. It is postulated that the engineered carboxylate-containing amino acid residue

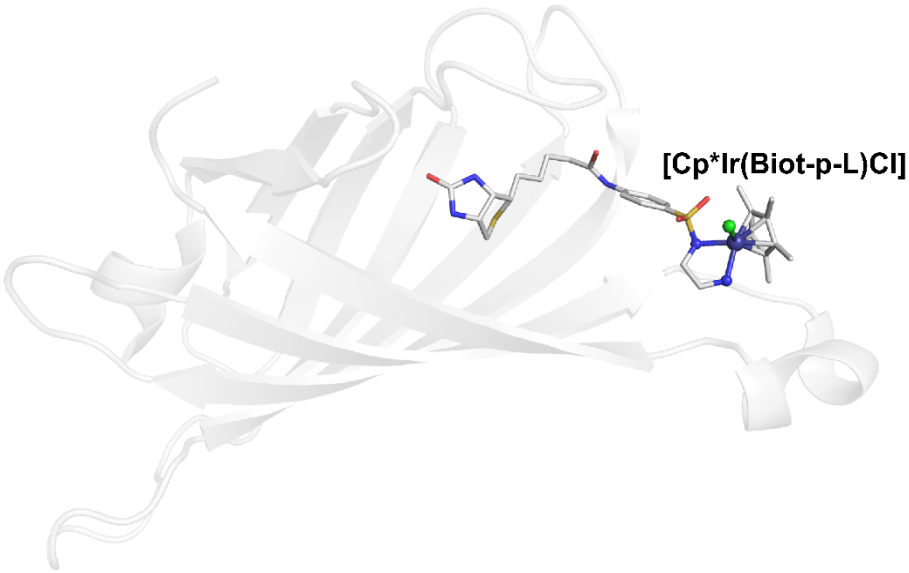

Figure 1.7 Structure of a Sav artificial transfer hydrogenase with an anchored biotinylated Ir complex (PDB 3PK2).

plays a key role in the C–H bond activation step by deprotonating the *ortho*-C_{aryl}–H bond, which is the turnover-limiting step.

In addition to the biotin-Sav technology, several other ArMs have been designed using different protein hosts. For example, the groups of Lu and Watanabe demonstrated the incorporation of unnatural metal porphyrin and salen complexes into Mb;[96,120–124] Fontcave and Arturo installed synthetic models of [FeFe] hydrogenase into HydF;[125] Ménage showed the inclusion of a synthetic mononuclear Fe complex into the Ni-binding protein NikA;[126,127] and Roelfes successfully docked a Cu complex into LmrR.[128] More recently, Jared Lewis synthesized a dirhodium complex based on a tetradentate Esp ligand with a bicyclo[6.1.0]nonyne (BCN) covalent anchor and immobilized it within the *Pfu* prolyl oligopeptidase (POP) enzyme (Figure 1.8). Lewis and coworkers showed that the selectivity of the dirhodium catalyst in styrene cyclopropanation was significantly improved by establishing two-point cofactor binding within POP. Through directed

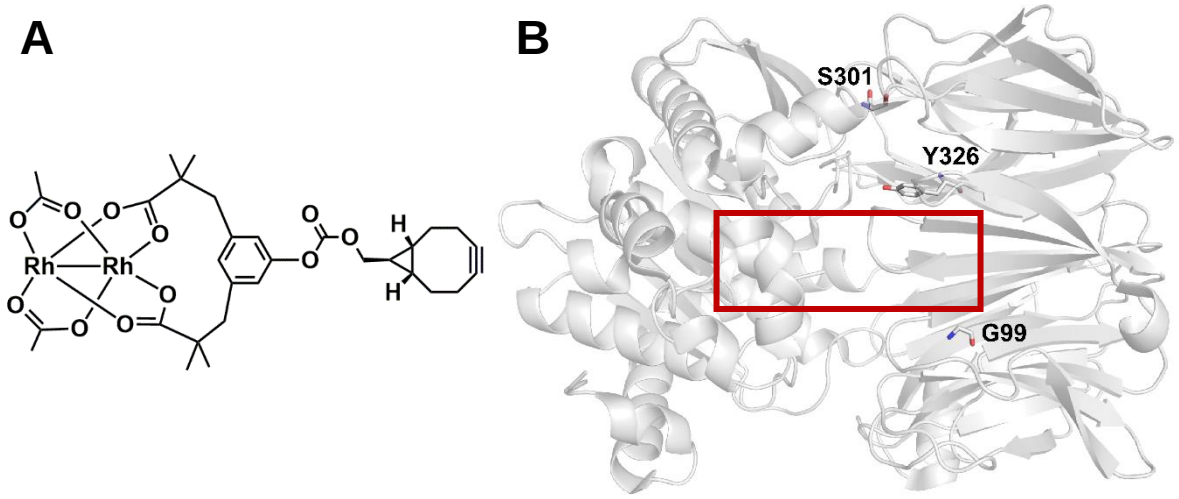

Figure 1.8 ChemDraw representation of Lewis's dirhodium catalyst (**A**) and recently solved *Pfu* POP structure with predicted placement of the dirhodium catalyst (**B**, labeled with red box between Y326 and G99).

evolution of the POP ArMs, Lewis and coworkers achieved improved cyclopropanation and the ability to perform carbene insertion into Si–H, S–H, and N–H bonds. Additionally, the POP ArMs showed increased selectivity in the presence of salt (> 0.5 M NaBr or NaCl), which Lewis attributed to secondary coordination sphere effects based on significant conformational changes that occur in the interdomain protein loops and result in a more ordered hydrophobic active site.[129]

Protein self-assembly is another approach for designing ArMs. In general, this approach utilizes monomeric proteins as ligands for building larger supramolecular constructs through metal-mediated self-assembly. Specifically, this approach uses the surfaces of proteins to design metal binding sites through self-assembly. Tezcan and coworkers have advanced this work with the heme protein cytochrome *cb*$_{562}$ (cyt *cb*$_{562}$). Using metal-mediated self-assembly, Tezcan demonstrated that a tetrameric Zn-mediated cyt *cb*$_{562}$ protein complex could be stabilized and serve several functions: 1) a metal-selective conformational switch, 2) an esterase and *in vivo* evolvable β-lactamase, and 3) an allosteric assembly that links metal binding to bond formation-breakage events.[85,130]

Previous Work on Artificial Metalloproteins in the Borovik Group

For many researchers, the study of ArMs is motivated by the search for efficient catalysts that can achieve increased activity or selectivity as a result of their protein hosts. However, the Borovik lab is interested in developing structure-function relationships of metalloproteins and, specifically, how the primary and secondary coordination spheres around the metal center(s) can affect function. As described above, the Borovik lab has designed several synthetic complexes that have advanced the field of bioinorganic chemistry by improving our understanding of the influence of the coordination environment. In order to expand our approach to include the design of more biologically relevant active sites, we turned to the design of ArMs. The foundation for ArM development that best suited our requirements was the biotin-Sav technology because of its ability to reproducibly embed synthetic inorganic complexes within Sav. Sav is a homotetrameric protein that does not contain natural metal cofactors. One important structural property of

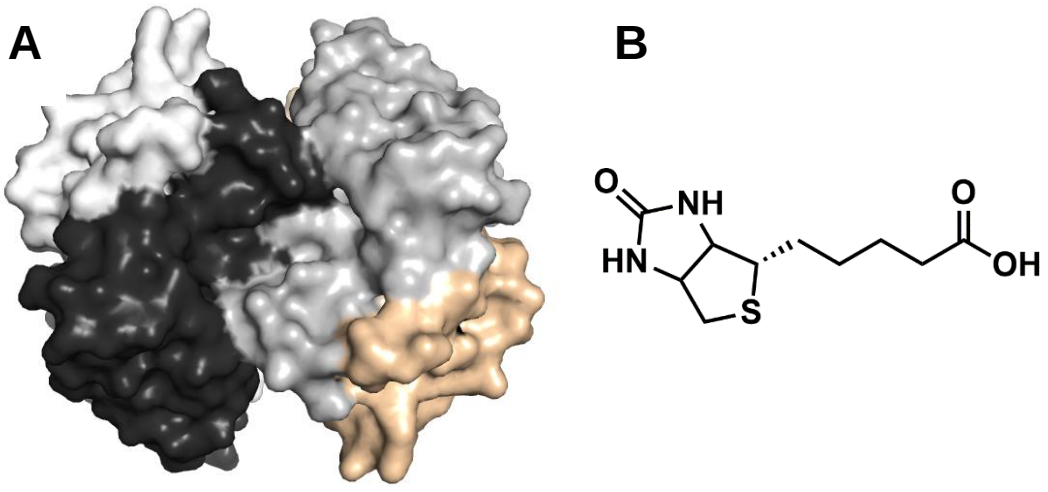

Figure 1.9 Surface representation of tetrameric Sav (**A**) and a ChemDraw representation of biotin (**B**).

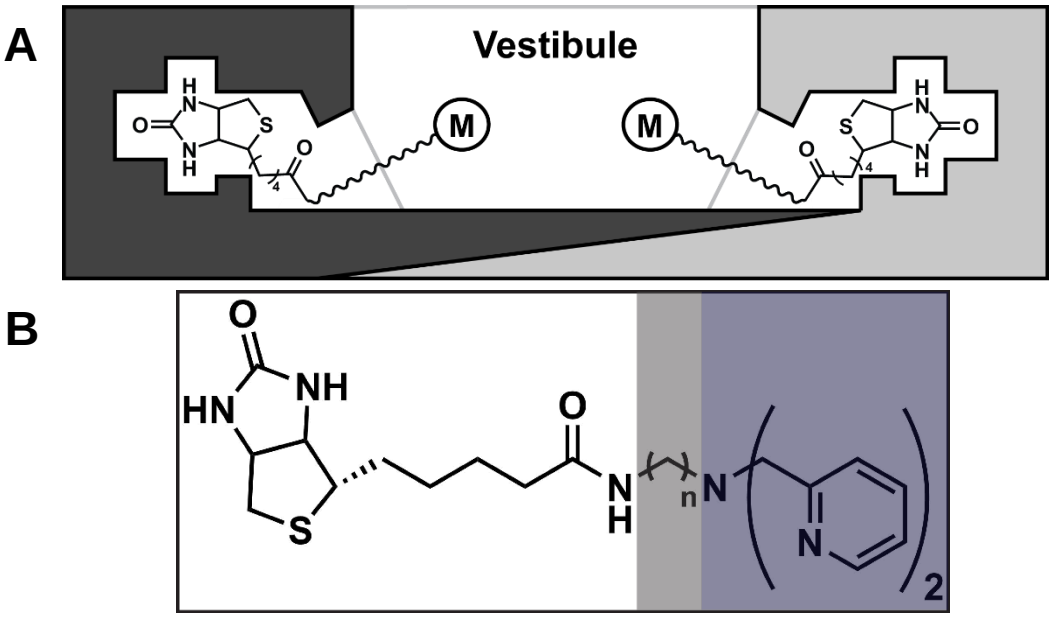

Figure 1.10 Diagram of one Sav dimer showing metal complexes anchored in the vestibule (**A**) and a ChemDraw representation of the biotinylated ligands used in this dissertation (n = et, pr, bu) (**B**).

Sav is that it assembles as a dimer of dimers, where the biotin binding sites face each other (Figure 1.9).[118,131–135] The only known function of Sav is to bind biotin, which occurs with a high binding affinity ($K_a \sim 10^{13}$ M^{-1}).[131,136] Our approach takes advantage of this unusually high binding affinity through the design of biotinylated metal complexes that can be reproducibly anchored within Sav. The dimer assembly positions the biotin-binding domains close to one another across a volume of space denoted as the vestibule (Figure 1.10). The vestibule is solvent accessible and offers space within the protein to house metal complexes. The biotin-Sav technology offers the additional biological advantages of using site-directed mutagenesis to mutate amino acid residues within the vestibule (Figure 1.10). The combined synthetic and biological approach offers the possibility of controlling the

primary coordination sphere by changing the endogenous ligands (Sav amino acid residues) that coordinate to an anchored metal center. Moreover, this approach allows for greater control over the microenvironment around the embedded metal complexes by mutating amino acid residues that can participate in extensive H-bonding networks. An additional benefit of the biotin-Sav technology is the ability to work in aqueous environments, which allows for a more accurate model of metalloprotein environments.

As described above, the biotin-Sav technology has been advanced by the Ward lab at the University of Basel in Switzerland. Previously, in collaboration with the Ward lab, our lab used the biotin-Sav technology to design several artificial copper proteins. Using a series of biotinylated dipyridylethylamine (dpea) ligands with linkers of varying lengths in

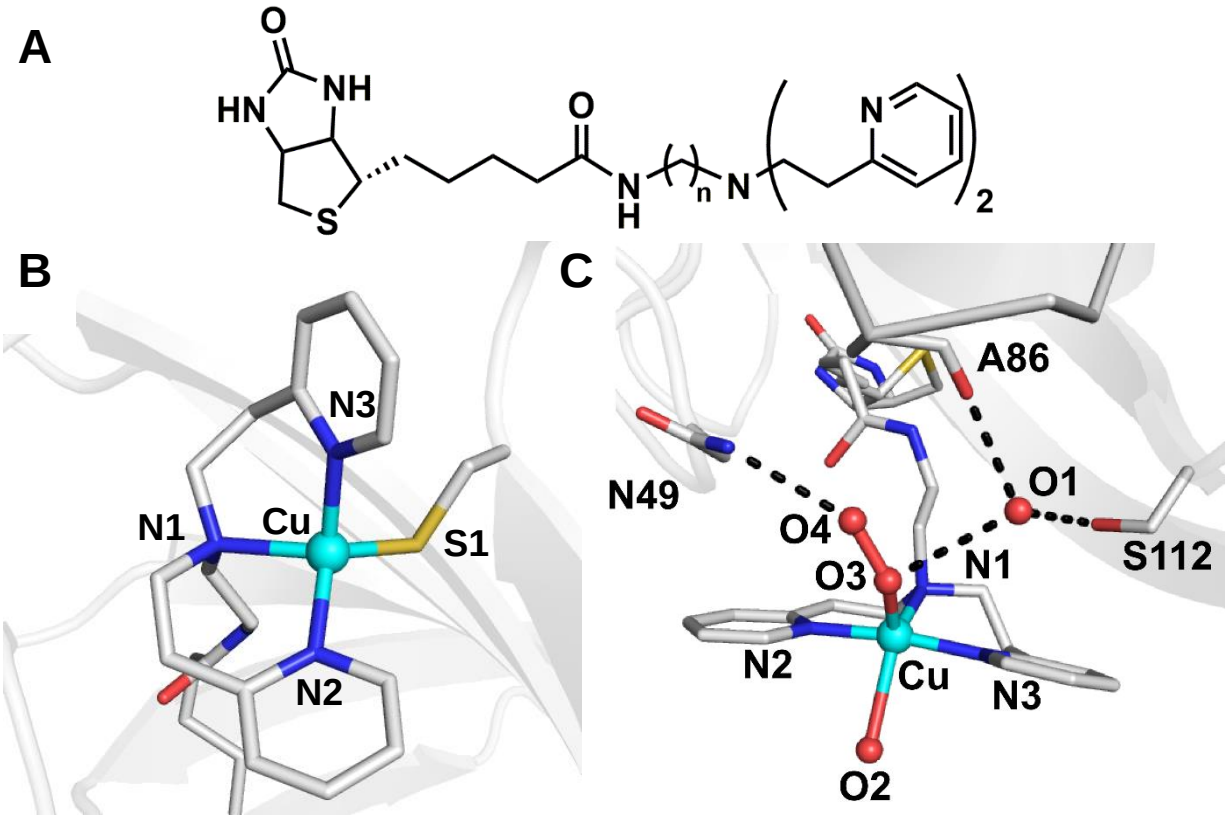

Figure 1.11 ChemDraw representation of the biotinylated ligands used for previous Cu ArM studies (**A**, n = et, pr, bu); the molecular structure of an artificial cupredoxin (**B**); and the molecular structure of a Cu^{II}–hydroperoxido species in WT-Sav (**C**, H-bonds shown as black dashed lines).

combination with the $S_{112}C$ variant of Sav, which places a thiolate-containing cysteine residue close to the Cu center, we modeled the structure and properties of Type 1 Cu sites (Figure 1.11).[137] These results showed the ability to tune the position of the Cu center within Sav, the effect of the placement of the Cu center on the properties of the ArM, and the ability to use an amino acid residue to coordinate a metal ion and serve as a second anchor point for the complex. We also successfully trapped a reactive intermediate: a Cu^{II}–hydroperoxido species. Using the ArM [Cu^{II}-(biot-et-dpea)$(H_2O)_2$]⊂WT-Sav, we spectroscopically and crystallographically characterized a Cu^{II}–hydroperoxido species that was stabilized by H-bonds interactions with the nearby amino acid residues N_{49} and S_{112} (Figure 1.11). Moreover, we showed that we could tune the stability and reactivity of this species by mutating N_{49} and S_{112} to eliminate the H-bonding network.[138] These results laid the foundation for the research in this thesis, which was to utilize the biotin-Sav technology to design new Fe ArMs and probe their structure and function.

Overview of Remaining Chapters

The research described in this dissertation continues to build on the study of biotin-Sav in the design of ArMs with a focus on the development of mononuclear and dinuclear Fe ArMs that model key structural and functional aspects of native proteins.

Chapter 2. This chapter reports the development of two new Fe ArMs in which an endogenous glutamate amino acid residue is coordinated to the Fe center. The structure of [Fe^{II}(biot-et-dpa$(OH_2)_2$(κ^1-O_{E112})⊂2xM-S_{112}E-Sav] revealed an unusual bidentate coordination mode for the dipyridylmethylamine (dpa) ligand where only one pyridine coordinated to the Fe^{II} center. Additionally, two water molecules and the glutamate amino acid residue of Sav were observed to bind to the Fe^{II} center through κ^1-coordination of the

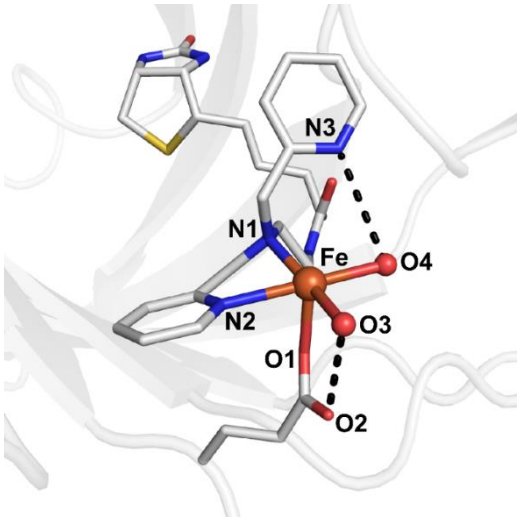

Figure 1.12 Molecular structure of a facial triad Fe^{II} ArM studied in Chapter 2.

carboxylate (Figure 1.12). Moreover, an extended H-bonding network that had structural aspects similar to those of native proteins was observed. The analogous Fe^{III} ArM was also developed, and used as a synthon to study exogenous ligand binding.

Chapter 3. This chapter details research using the Fe^{II} ArM as a synthon to study dioxygen activation with α-KG analog substrate phenylpyruvate. The addition of dioxygen to the Fe^{II} ArM in the presence of phenylpyruvate produced two new absorbance features at λ_{max} ~ 420 and 540 nm, and a high-spin mononuclear Fe^{III} Mössbauer signal was observed for this species. The molecular structure of this Fe^{III} species revealed that the phenylpyruvate

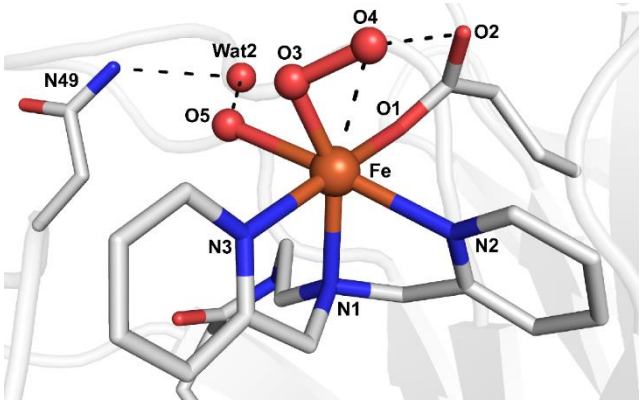

Figure 1.13 Molecular structure of an Fe^{III}–O_2 adduct in Sav studied in Chapter 3.

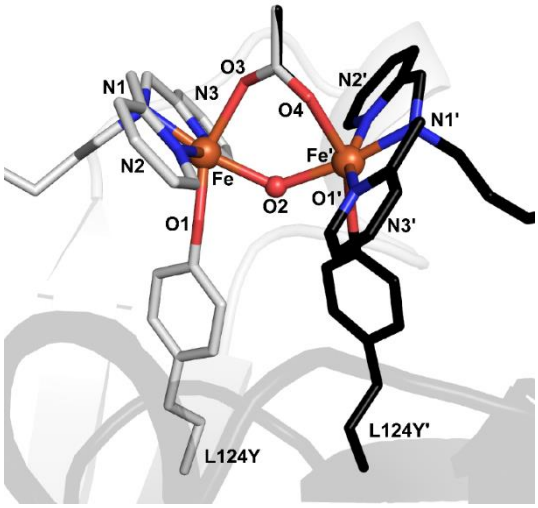

Figure 1.14 Molecular structure of a di-Fe ArM studied in Chapter 4.

docked via a π-stacking interaction between the two biotinylated Fe complexes and that the O_2 adduct is coordinated in an asymmetric side-on to the Fe center (Figure 1.13).

Chapter 4. The research detailed in this chapter sought to develop a di-Fe ArM. A series of biot-n-dpa (n = et, pr, bu) ligands were developed, and three variants of Sav ($S_{112}Y$, $K_{121}Y$, $K_{121}A/L_{124}Y$) were expressed and purified. An optical screen was then performed with the Fe^{III}-n-dpa complexes to determine the proper linker length and variant placement for achieving an Fe^{III}–phenolate interaction; the butyl linker and the $K_{121}A/L_{124}Y$ Sav variant allowed for coordination of the phenolate to the Fe center. The molecular structure revealed a di-Fe active site within Sav in which the Fe centers were bridged by a μ–oxo ligand, which highlights the fact that the Fe···Fe' distance falls within a range comparable to that in native proteins (Figure 1.14). Subsequent studies using three-atom and two-atom bridging ligands confirmed that the Fe···Fe' distance ranged between 3.7 and 4 Å.

CHAPTER 2

Modelling the Active Sites in Non-Heme Dioxygenases

Introduction

Mononuclear non-heme Fe oxygenases are enzymes that catalyze a wide range of oxidative transformations using dioxygen as the terminal oxidant.[3,6,8,139–142] Many of these enzymes share a common Fe binding site that is composed of side chains from two histidine amino acid residues, and either a glutamate or aspartate amino acid residue.[4,5,143] As described in Chapter 1, this endogenous binding site coordinates an Fe center in a facial orientation and is referred to as the 2-His-1-carboxylate facial triad.[2] Information learned from structural biology indicates that in the Fe^{II} resting state of these proteins and the absence of any exogenous cofactors, the remaining coordination sites are occupied by water molecules (Figure 2.1).[10,144,145] A common feature of these structures is the presence of an intramolecular hydrogen bond (H-bond) between one of the aqua ligands and the carbonyl group of the coordinated carboxylate ligand.

Attempts to model this type of coordination environment include synthetic systems that catalyze the epoxidation and/or cis-dihydroxylation of olefins with H_2O_2 and O_2,[146,147]

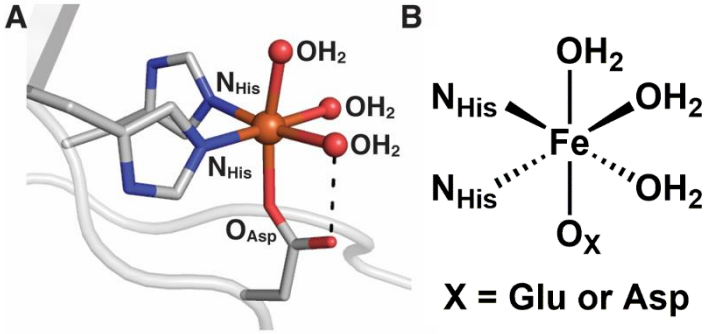

Figure 2.1 Fe binding site in cephalosporin synthase showing the 2-His-1-carboxylate facial triad (**A**, PDB: 1RXF) and ChemDraw representation of the active site (**B**).

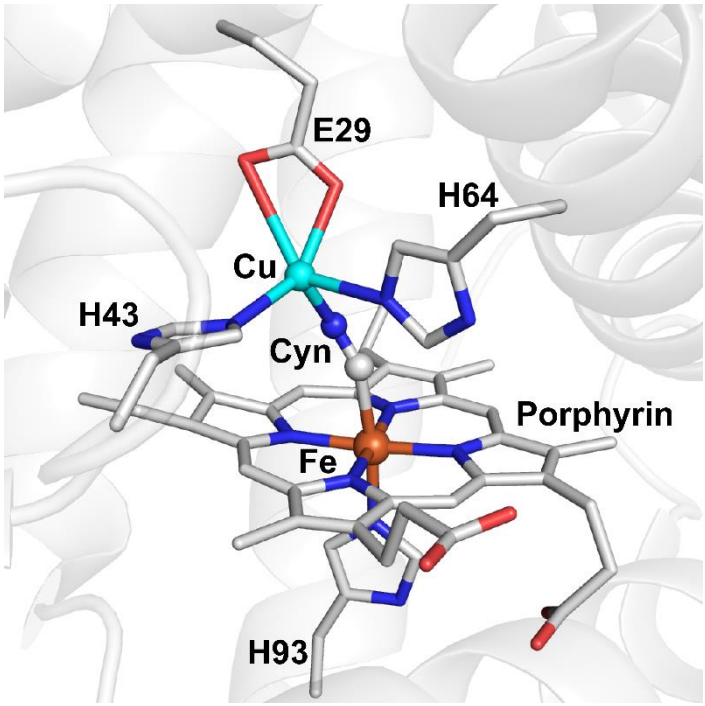

Figure 2.2 Engineered myoglobin with an Fe···Cu active site and a cyanido (cyn) ligand bound (PDB 3MN0).

and the intramolecular arene hydroxylation of benzoylformate with O_2.[148–150] However, it has proven challenging to develop synthetic complexes whose coordination spheres resemble those found within these proteins. For instance, reported complexes that emulate the facial triad have been derived from sterically hindered N-donors, terphenylcarboxylate ligands,[151] and tripodal ligands,[152–161] but these complexes lack the aqua ligands found within protein active sites. In addition, these systems do not replicate the control over the secondary coordination spheres that is seen in metalloproteins. One example of an engineered facial triad from the field of artificial metalloproteins was reported by Lu and coworkers, who engineered a 2-His-1-carboxylate facial triad binding site near the heme active site in sperm whale myoglobin. The facial triad site binds a variety of metal ions, including Fe, Cu, and Zn. Both the Fe and Cu forms of the engineered facial triad exhibited nitric oxide reductase (NOR) activity; however, only the Cu form of the protein was

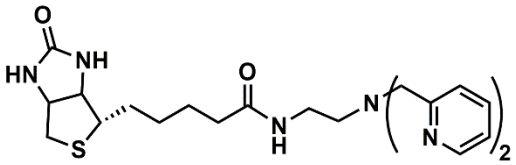

biot-et-dpa

Figure 2.3 Biotinylated ligand used in this study.

crystallographically characterized (Figure 2.2). Lu's artificial Fe myoglobin system highlights one example of how an engineered protein can establish control over the coordination environment around an Fe active site.

In this chapter, the design and development of new artificial mononuclear Fe proteins that simulate the 2-His-1-carboxylate facial triad are discussed. Fe^{II} and Fe^{III} artificial metalloproteins (ArMs) were designed utilizing the ligand bis(2-pyridylmethyl)amine (Figure 2.3: biot-et-dpa), and a new variant of streptavidin (Sav) was expressed and purified to introduce a $S_{112}E$ mutation; this mutation could promote Fe–$O_{carboxylate}$ bond formation. Additionally, the binding of an azide ion to the Fe^{III} ArM was performed to demonstrate exogenous ligand binding. The Fe^{II} and Fe^{III} ArMs were analyzed by electronic absorbance spectroscopy, perpendicular-mode (⊥-mode) and parallel-mode (∥-mode) electron paramagnetic resonance (EPR) spectroscopy, X-ray absorption spectroscopy (XAS), X-ray diffraction (XRD), and X-ray free electron laser (XFEL) diffraction methods. The data showed that three new mononuclear Fe ArMs with the classic 2-His-1-carboxylate facial triad motif known for mononuclear non-heme Fe oxygenases were formed within Sav. Both the primary and secondary coordination spheres of the Fe centers were influenced by the Sav host to produce new ArMs in which intramolecular hydrogen bonds (H-bonds) played a key structural role.

Results and Discussion

Design Concepts. A complementary approach that combines synthetic inorganic chemistry and protein engineering was utilized to develop bio-relevant Fe active sites within ArMs.[100,162–167] As explained in Chapter 1, the approach capitalizes on biotin-Sav technology to predictably insert biotinylated synthetic complexes into variants of Sav.[98,112,168,169] These protein hosts could provide ligands within the primary coordination sphere and simultaneously influence the secondary coordination sphere to better emulate natural active sites. Moreover, these constructs are stable in aqueous solution, thereby allowing water to act as a ligand as is found in natural metalloproteins. As discussed in Chapter 1, previous work in our group has shown how the primary coordination sphere can be manipulated to produce ArMs that model the properties of cupredoxins by introducing an endogenous thiolate ligand into Sav that forms a strong covalent bond to the Cu center.[137] This work on Type 1 Cu sites showed how Cu–$S_{thiolate}$ coordination could be achieved by using a relatively short ethylene linker between the biotin unit and the synthetic complex that positioned the Cu center close to the residue at position 112.[137] It was anticipated that Fe complexes prepared from a similar construct, biot-et-dpa (Figure 2.3), should also place the metal center near this residue. The introduction of a $S_{112}E$ mutation in Sav would produce a variant that could then promote Fe–$O_{carboxylate}$ bond formation. In addition, the Sav host was re-engineered to incorporate two additional mutations, $K_{121}A/E_{101}Q$, as described previously.[170] The parent protein host is referred to as 2xM-Sav, and the specific protein host used to develop mononuclear Fe sites is denoted 2xM-$S_{112}E$-Sav.

Synthesis and Characterization of Biotinylated Fe^{II} and Fe^{III} compounds. The biotinylated biot-et-dpa construct was prepared from dpa via a 3-step route (Scheme 2.1) using a modified literature procedure.[137] The formation of the Fe^{II} complex was achieved by treating biot-et-dpa with $FeBr_2$ in CH_3CN under an inert atmosphere to afford $[Fe^{II}(\text{biot-et-dpa})(OH_2)_2]Br_2$. The synthesis of the Fe^{III} complex was accomplished by allowing biot-et-dpa to react with $FeCl_3{\cdot}6H_2O$ in EtOH to yield $[Fe^{III}(\text{biot-et-dpa})(OH_2)_3]Cl_3$. Both Fe^{II} and Fe^{III} compounds were stored under an inert atmosphere. The $Fe^{II/III}$ complexes were analyzed by electrospray ionization mass spectrometry (ESI-MS), which gave molecular ion peaks corresponding to $[Fe^{II}(\text{biot-et-dpa})Br]^+$ and $[Fe^{III}(\text{biot-et-dpa})Cl_2]^+$. Elemental analysis showed that the Fe^{II} complex was a dihydrate with the form $[Fe^{II}(\text{biot-et-dpa})(OH_2)_2]Br_2$, and the Fe^{III} complex was a trihydrate with the form $[Fe^{III}(\text{biot-et-dpa})(OH_2)_3]Cl_3$.

Scheme 2.1 Synthetic route for the preparation of the biot-et-dpa ligand.

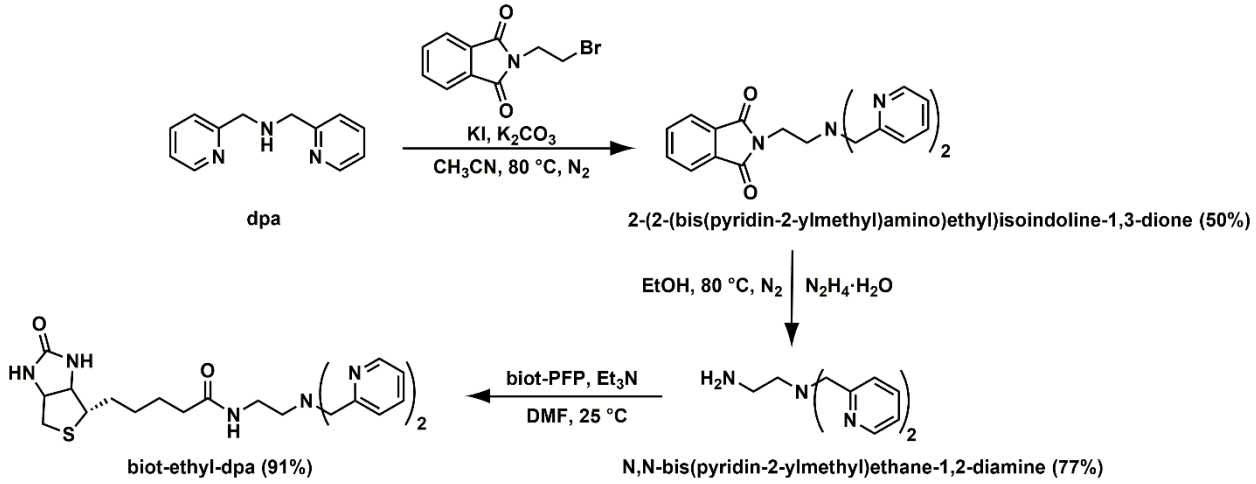

Equation 2.1 Preparation of Fe^{II} and Fe^{III} ArMs in solution.

$$[Fe^{II}(\text{biot-et-dpa})(OH_2)_2]Br_2 \xrightarrow[\substack{\text{phosphate buffer}\\ N_2,\ rt}]{\text{2xm-}S_{112}\text{E-Sav}} [Fe^{II}(\text{biot-et-dpa})(OH_2)_2(\kappa^1\text{-}O_{E_{112}}) \subset \text{2xm-}S_{112}\text{E-Sav}] \quad (1)$$
(**1**)

$$[Fe^{III}(\text{biot-et-dpa})(OH_2)_3]Cl_3 \xrightarrow[\substack{\text{acetate buffer}\\ rt}]{\text{2xm-}S_{112}\text{E-Sav}} [Fe^{III}(\text{biot-et-dpa})(X)_2(\kappa^1\text{-}O_{E_{112}}) \subset \text{2xm-}S_{112}\text{E-Sav}] \quad (2)$$
(**2**)

$X = OH_2,\ OAc^-$

The ArMs containing the Fe^{II} complex, [Fe^{II}(biot-et-dpa(OH_2)$_2$(κ^1-O_{E112})⊂2xM-S_{112}E-Sav] (**1**, eq 2.1), and the corresponding Fe^{III} complex, [Fe^{III}(biot-et-dpa(X)$_2$(κ^1-O_{E112})⊂2xM-S_{112}E-Sav] (**2**, eq 2.1), were prepared by incubating an aqueous solution of the complexes with 2xM-S_{112}E-Sav at pH 8 in phosphate buffer (50 mM) or at pH 6 in acetate buffer (100 mM). Titration experiments were done with 2-(4'-hydroxyazo-benzene)benzoic acid (HABA)[171] to determine the binding stoichiometry of **1** and **2** to Sav. For a HABA titration, a solution of Sav is loaded with an excess (150 equivalents) of HABA to ensure complete binding of HABA to the biotin-binding domains of Sav ($K_b \sim 10^4\ M^{-1}$). The HABA-Sav interaction has a characteristic absorbance feature at $\lambda_{max} \sim 506$ nm that is used to monitor the displacement of HABA by a biotinylated complex. Upon the addition of a biotinylated species, the absorbance feature at 506 nm decreases until the binding pockets of Sav are

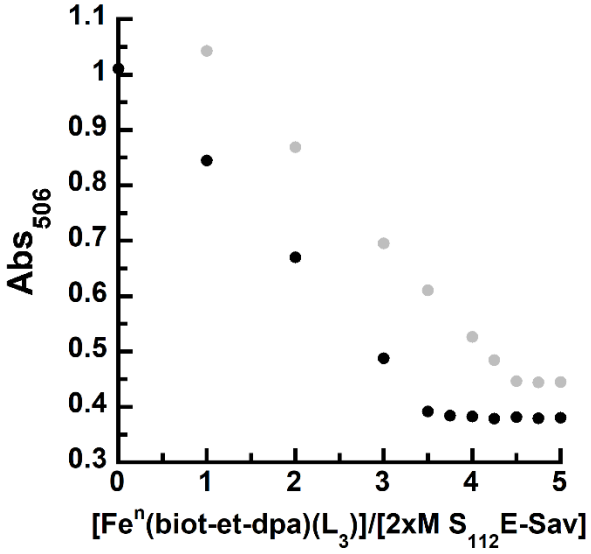

Figure 2.4 HABA Titrations of **1** (n: 2^+, grey) and **2** (n: 3^+, black).

saturated. The binding stoichiometry can then be calculated from the concentrations of Sav and complex added. In the current study of the two Fe complexes, no further spectroscopic changes were observed after approximately four equivalents of complex had been added. Thus, the HABA studies indicated a 4:1 bioinylated Fe^{II} and Fe^{III} complexes to protein host ratio and confirmed complete occupancy of the Sav binding pockets with the complexes (Figure 2.4).

Electronic absorbance and EPR spectroscopies were used to characterize **1** and **2** in solution. For **1**, a single feature observed at λ_{max} (ε_M, $M^{-1}cm^{-1}$) = 375 (700) nm was attributed to a pyridine-to-Fe^{II} ligand charge transfer (LMCT) transition (Figure 2.5A). For **2**, three absorbance bands were found at λ_{max} (ε_M, $M^{-1}cm^{-1}$) = 350 (2500), 485 (220), and 650 (50) nm (Figure 2.6A). The ∥-mode, X-band EPR spectrum for **1** displayed a broad signal with a *g* value at 8.8 that is consistent with a high-spin Fe^{II} species with an $S = 2$ spin ground state (Figure 2.5B). The ⊥-mode, X-band EPR spectrum of **2** revealed a weak signal with features at *g* values of 9.1 and 4.3, indicating the presence of a high-spin Fe^{III} species

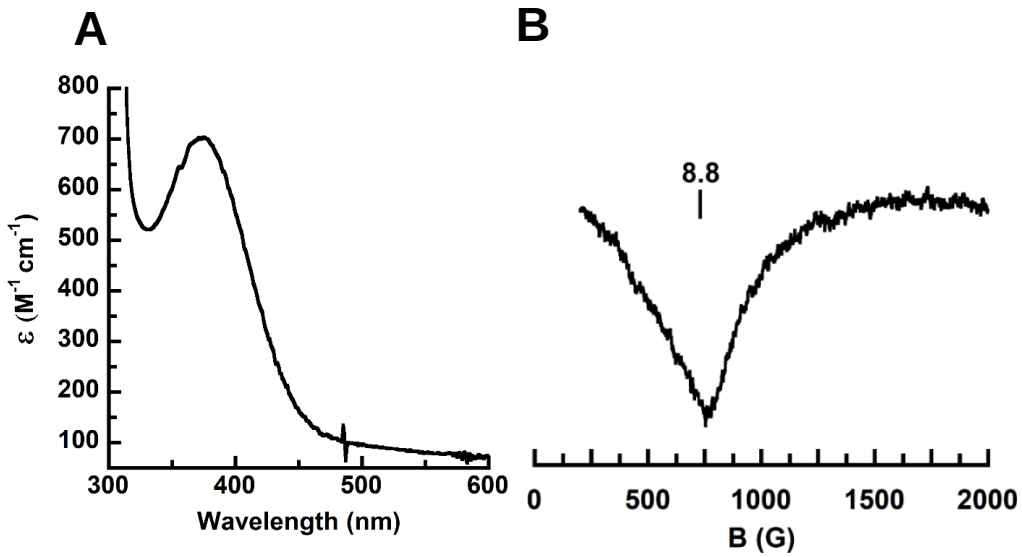

Figure 2.5 Electronic absorbance (**A**) and EPR (**B**) spectra of **1** recorded in 50 mM phosphate buffer pH 8.

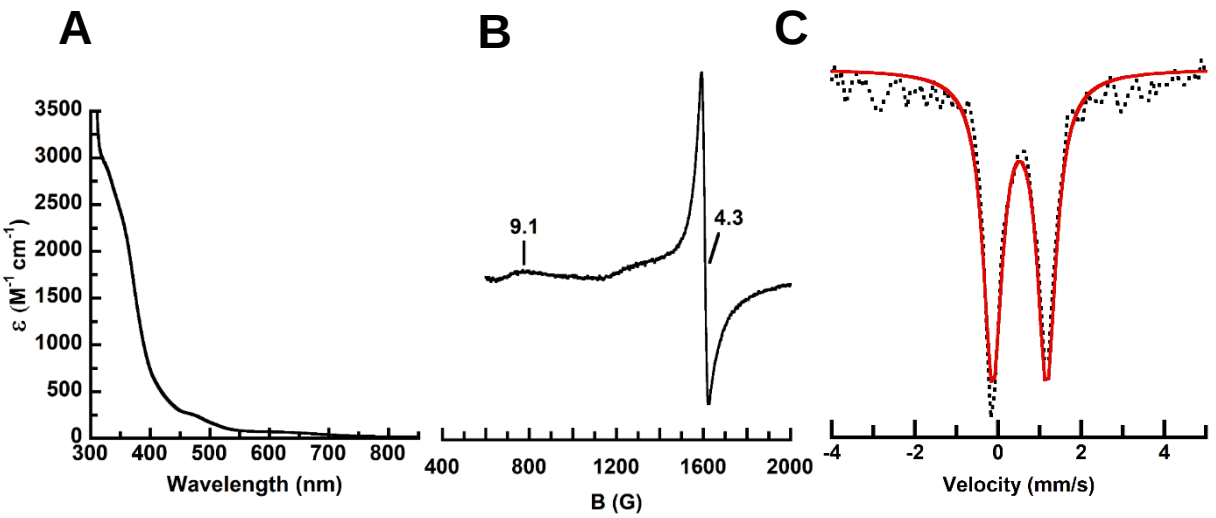

Figure 2.6 Electronic absorbance (**A**), EPR (**B**), and Mössbauer (**C**) spectra of **2** recorded in 100 mM acetate buffer pH 6. The simulation is shown as a red line.

with a rhombic coordination geometry (Figure 2.6B). Mössbauer studies of **2** produced a spectrum containing a quadrupole doublet associated with a coupled $Fe^{III}\cdots Fe^{III}$ system having an isomer shift (δ) of 0.52 mm/s and a quadrupole splitting (ΔE_Q) of 1.30 mm/s (Figure 2.6C). More experiments are necessary to determine what is causing the Fe centers to couple in solution.

*Structural Characterization of **1***. A significant advantage of utilizing biotin-Sav technology in the design of ArMs is the strong tendency of Sav to form single crystals, from which molecular structures can be determined using XRD methods. The general method uses the high affinity of Sav for biotin to form Fe ArMs *in crystallo* by incubating apo-Sav crystals with a solution of biotinylated Fe complex. For biotinylated complexes, this soaking method should generate single crystals of Sav that contain one complex per subunit. An added benefit of this approach is that it is possible to compare the chemistry occurring within a single crystal to that occurring in the analogous solution-based process.

Single crystals of **1** were prepared by soaking apo-2xM-S_{112}E-Sav crystals in a solution of $[Fe^{II}(biot\text{-}et\text{-}dpa)(OH_2)_2]Br_2$. The structure of **1** was solved to a resolution of

1.47 Å to reveal a mononuclear Fe complex immobilized within each subunit. The Fe center is coordinated by O atoms from the carboxylate group of $S_{112}E$ bound in a κ^1 fashion and two aqua ligands (Figure 2.7, Tables 2.3 and 2.4, Tables 2.5 and 2.6). Nitrogen donors N1 and N2 from dpa also bind to the Fe center with Fe–N1 and Fe–N2 bond lengths of 1.94 Å and 2.32 Å, respectively. Our structure shows two conformations for the pyridine ring containing N3 (Figure 2.7A). In the major complex (**1a**), modelled to 70% occupancy, this pyridine ring is not coordinated (unbound state); instead, N3 is H-bonded to the aqua ligand of O3. The resultant complex is 5-coordinate with a square pyramidal geometry and a τ-value of 0.05 (Figure 2.7B). The minor complex (**1b**) that was modelled to 30% occupancy is 6-coordinate with N3 bound to the Fe center (bound state) with an Fe–N3 bond length of 2.21 Å and N2–Fe–N3 and N3–Fe–O3 bond angles of 107° and 79°, respectively (Figure 2.7C). The carboxylate group at $S_{112}E$ also has two conformations; a major confirmation, modelled to 80% occupancy, places O1 in a position to coordinate to the Fe center (Figure 2.12A), whereas in the minor species with 20% occupancy, the carboxylate is not coordinated to the Fe center (Figure 2.12A).

In the molecular structure of **1a**, the Fe site is coordinated by two N-atom donors from dpa and the O atom from the residue of $S_{112}E$ in a facial arrangement that is similar to the 2-His-1-carboxylate facial triad observed in several nonheme monooxygenases.[4] In addition, the κ^1-coordination of the glutamate residue in **1a** and **1b** leaves O4 positioned to H-bond with the aqua ligand of O2, as gauged by the O4···O2 distance of 2.71 Å. This

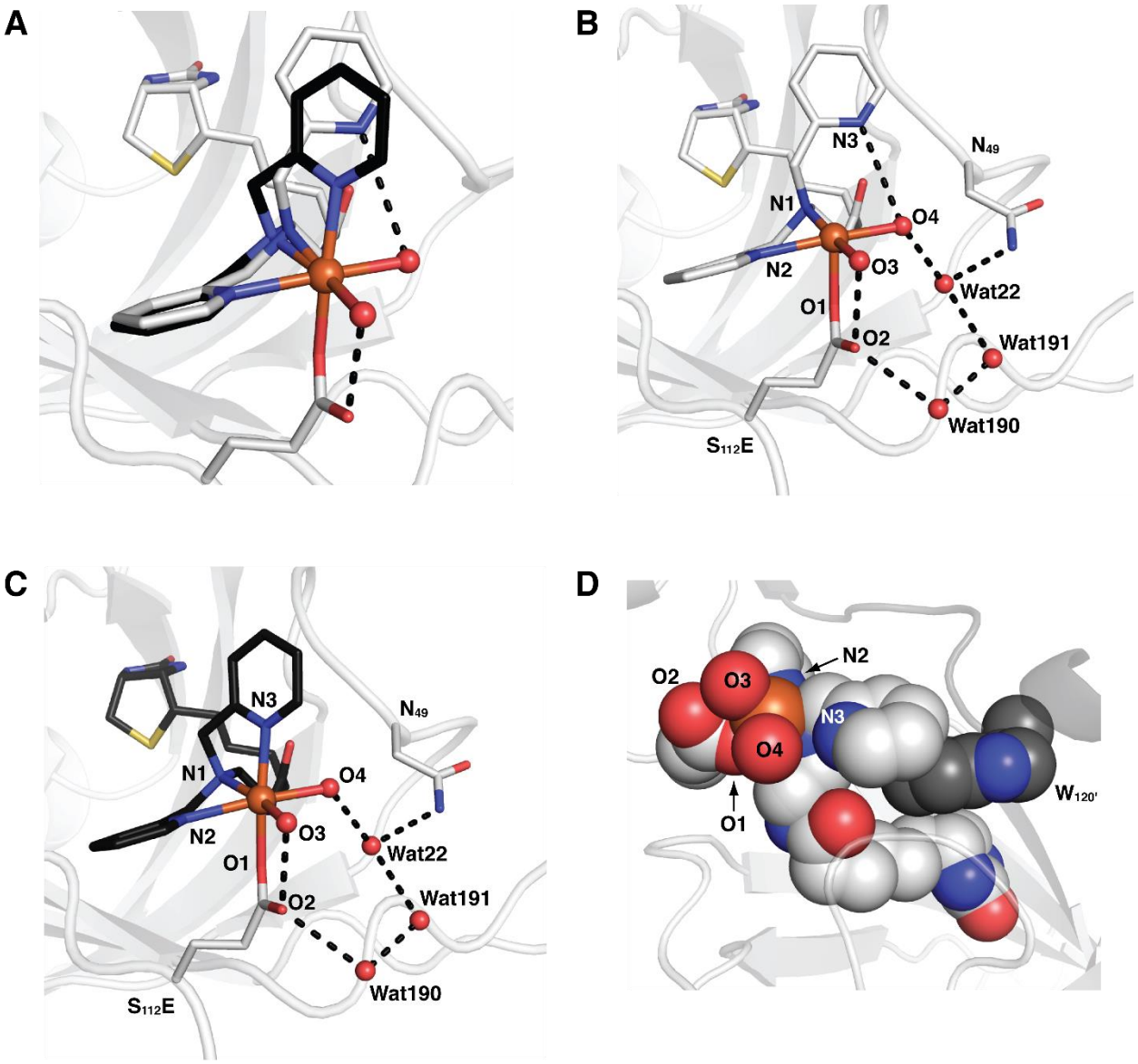

Figure 2.7 Overlay of the molecular structures of **1a** (grey) and **1b** (black) (**A**, PDB: 6UIY). The individual molecular structures of **1a** (**B**) and **1b** (**C**) and a partial space-filling representation of **1a** highlighting the π-stacking interaction of the biotinylated Fe^{II} complex that includes one of its pyridine rings with $W_{120'}$ from the neighboring subunit (**D**, dark grey). Fe ions are colored in orange, N atoms are in blue, and O atoms/water molecules are in red. H-bonds are shown as black dashed lines.

type of monodentate carboxylate coordination to Fe with an additional intramolecular H-bond is seen in several native nonheme enzymes, such as deacetoxy-cephalosporin C synthase (Figure 2.1A),[144] phenylalanine hydroxylase binary enzyme (PDB: 1J8U),[172] and soybean lipoxygenase (PDB: 1JNQ).[145] These enzymes have O···O distances that range

between 2.5 and 3.6 Å. The Fe^{II} complex in **1** and the Fe^{II} sites in natural enzymes also share the coordination of multiple water molecules.

The 2xM-S_{112}E-Sav host in **1** promotes other noncovalent interactions with the artificial Fe cofactor. For instance, the aqua ligand of O2 participates in an additional H-bond with a structural water molecule (Wat22) that is also H-bonded to the residue of N_{49} and the backbone carbonyl of A_{86}. This aqua ligand thus participates in two H-bonds, which could account for the slightly longer Fe–O3 bond length of 2.22 Å when compared to the Fe–O2 bond length (2.17 Å). These water molecules are also part of a larger H-bonding network that extends from N3 to the glutamate 112 side chain and help to stabilize its coordination to the Fe center (Figures 2.7B, C). Furthermore, the noncoordinating pyridine ring participates in an additional π-stacking interaction with the residue of W_{120} from the adjacent subunit with a $centroid_{py}$–$centroid_{trp}$ distance of 4.86 Å; the interaction likely contributes to the stabilization of this conformation (Figure 2.7D).

In synthetic complexes, dpa binds solely as a tridentate ligand to $Fe^{II/III}$ centers. In fact, analysis of all the structures in the Cambridge Structural Database[173] for complexes containing Fe(dpa) fragments (over 300 entries) found that both pyridine N atoms are bound to the Fe center in the crystalline phase. The confinement of $[Fe^{II}$(biot-et-dpa)$(OH_2)_2]Br_2$ within 2xM-S_{112}E-Sav appears to promote the unusual bidentate coordination of dpa. The trapping of this Fe^{II} species with a non-coordinating pyridine ligand highlights the importance of the local environment around a metal center and how it can influence the structure of the embedded metal complex.

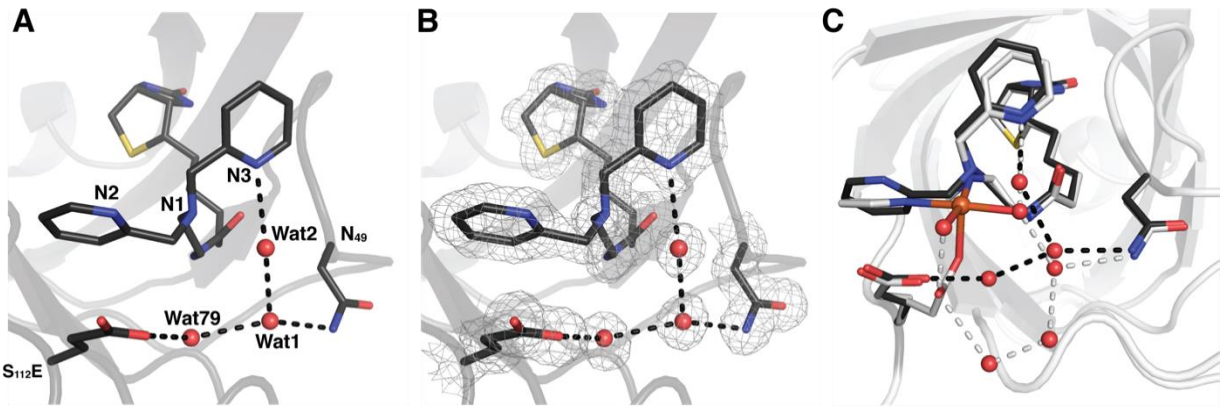

Figure 2.8 The molecule structure of biot-et-dpa⊂2xM-S_{112}E-Sav (**A**, PDB: 6UIU). The $2F_o$-F_c electron density map (grey, contoured at 1σ) is highlighted in **B** with same labelling as that in **A**. An overlay of biot-et-dpa⊂2xM-S_{112}E-Sav (black) and **1a** (grey) (**C**) shows the H-bonding networks associated with biot-et-dpa⊂2xM-S_{112}E-Sav (black dashes) and **1a** (grey dashes). Fe ions are colored in orange, N atoms are in blue, and O atoms/water molecules are in red. The number schemes in **B** and **C** are the same as those in **A**.

Structural Characterization of biot-et-dpa⊂2xM-S_{112}E-Sav. The unusual molecular structure of the Fe complexes in **1** prompted us to examine the structure of 2xM-S_{112}E-Sav containing just biot-et-dpa. We were interested in determining how the dpa ligand was positioned within the protein host in the absence of the Fe center and if any structural differences occurred upon coordination to Fe. The structure of biot-et-dpa ⊂ 2xM-S_{112}E-Sav was solved to a resolution of 1.35 Å, and both the dpa ligand and carboxylate group at position 112 were modelled with single conformations at 100% occupancy (Figure 2.8A and 2.8B, Tables 2.5 and 2.6). Both N1 and N2 are centered near the carboxylate group at position 112, and the pyridine ring containing N3 adopts a nearly identical confirmation to what is found in **1a**, including the same π-stacking interaction with W_{120} (Figure 2.8C). Additional noncovalent interactions are present in the form of an extended H-bonding network that includes N1 and N3, a series of water molecules, and the side chains of N_{49} and S_{112}E (Figure 2.8A). Atom N3 thus forms a H-bond as in **1a** but with a structural water molecule rather than an aqua ligand. Notice that the H-bonding network also links N3 to the carboxylate group at S_{112}E, which influences its orientation.

The structure of biot-et-dpa⊂2xM-S_{112}E-Sav provides insight into how the protein host influences both the primary and secondary coordination spheres in **1** (Figures 2.8A, B). The glutamate residue and the pyridine group containing N3 have two different conformations in the structure of **1** (Figure 2.7). For the glutamate residue, the carboxylate group in the minor state of **1** occupies the same position as that observed in biot-et-dpa⊂2xM-S_{112}E-Sav, and this position places the O atoms more than 3.0 Å away from the Fe center. In its bound state, the carboxylate group rotates toward the dpa ligand, enabling O1 to coordinate to the Fe center. Moreover, the unbound pyridine group in **1a** is displaced by only 0.6 Å from the position occupied by the same ring in biot-et-dpa ⊂ 2xM-S_{112}E-Sav. This change appears to be enough to promote intramolecular H-bonding of the pyridine group with the aqua ligand of O3, but not enough to enable its coordination to the Fe center (Figure 2.7C). For the bound state in **1b**, the position of the pyridylmethyl arm changes significantly, which moves N3 by over 2.0 Å and allows it to coordinate to the Fe^{II} center. There is also an extended H-bonding network like the one found in **1** that includes N3, several water molecules, and the S_{112}E side chain (Figure 2.8C).

*Structural Characterization of **2**.* To evaluate the effects of Fe oxidation on the molecular structure of the active site, we prepared single crystals of **2** by soaking crystals of apo 2xM-S_{112}E-Sav in a solution of $[Fe^{III}$(biot-et-dpa)$(OH_2)_3]Cl_3$. Analysis of crystals that diffracted to a 1.40 Å resolution revealed the formation of a six-coordinate mononuclear Fe complex within each subunit of Sav (Figure 2.9A and 2.12B, Tables 2.3 and 2.4, Tables 2.7 and 2.8). The primary coordination sphere is composed of an N_3O_3 donor set with an O-

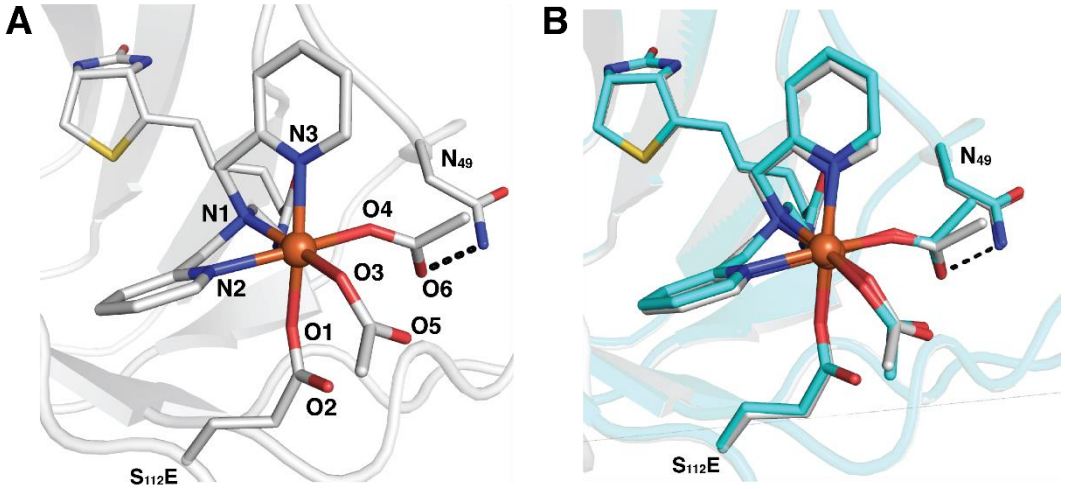

Figure 2.9 The molecular structure of **2** (**A**, PDB: 6UIO) and an overlay of the structure collected using XFEL (**B**, carbons colored in teal, PDB: 6US6). Fe ions are colored in orange, N atoms are in blue, and O atom/water molecules are in red. H-bonds are shown as black dashed lines. The number scheme in **B** is the same as that in **A**.

atom donor from the $S_{112}E$ residue that is bound in a similar κ^1 manner as observed in **1**. The other O-atom donors are from acetate ions (from the crystallization conditions) that also bind as monodentate ligands and occupy the same coordination sites as the aqua ligands in **1**. The dpa ligand binds facially to the Fe^{III} center, and all three N-donors are coordinated. Notice that the structural water molecule (Wat22) found in **1** is not present in **2**, which allows O6 of the acetato ligand to H-bond with the amide residue of N_{49} with a $N_{49}\cdots O6$ distance of 2.97 Å.

To evaluate if photoreduction occurred on the crystals of **2**, and determine the extent of change that photoreduction would cause on the resultant structure, XRD data were also collected using XFEL techniques in collaboration with the Yachandra/Yano group at Lawrence Berkeley National Lab. This method utilizes femtosecond X-ray pulses to collect XRD data in a serial fashion, with each diffraction image obtained from a new crystal.[174–177] Detection occurs before the diffusion of radicals or solvated electrons, which often causes X-ray-induced changes in protein structure. This method has therefore

provided structural data for metal centers in a non-damaged (that is, not photoreduced) state for several metalloproteins.[174–177] The molecular structure of **2** was obtained on room-temperature crystals using this method and resolved to 1.50 Å (Tables 2.7 and 2.8). The resulting structure of **2** and that obtained from frozen crystals examined by XRD were nearly identical (Figure 2.9B and 2.12D) with an average difference in the Fe–N/O bond lengths of 0.03 Å. Notice that there are slight differences in the orientations of the ligands in the two structures (Figure 2.9B), which could be caused by the different temperatures used for data collection. Nevertheless, these results suggest that the structure of **2** obtained using synchrotron radiation at cryogenic temperatures was minimally affected by radiation damage.

XAS. The properties of the Fe centers in **1** and **2** were further probed using XAS to gain a better understanding of the structure of the protein-embedded complexes in solution. X-ray absorption near edge structure (XANES) analysis provided energy edges at 7122.4 eV and 7123.1 eV for **1** and **2**, respectively (Figures 2.13 and 2.14, Table 2.13), which are consistent with the energy edges of other synthetic and biological $Fe^{II/III}$ systems.[178–180] These results indicate that in solution, **1** has a ferrous metal center and **2** has a ferric metal center. Extended X-ray absorption fine structure (EXAFS) analysis revealed the presence of five O/N scatterers at a distance of 2.15 Å for **1** (Table 2.1, Figure 2.15, Tables 2.9 and 2.10). Two additional shells from the Fe center were fit to four carbon scatterers at 3.01 Å and one at 2.63 Å. The longer-distance carbon scatterers could include the carbonyl C atom of the $S_{112}E$ side chain, which was found at an Fe···C distance of 3.12 Å by XRD. The shorter Fe···C distance of 2.63 Å matched that found by XRD between the Fe center and the methylene carbon of the unbound

Table 2.1 Comparison of metrical parameters for **1** obtained by XAS and XRD.

Bond	No. of Scatterers	XAS (Å)	XRD (Å)
Average Fe–O/N	5	2.15	2.16
Average Fe···C	4	3.01	3.01
Fe···$C_{methylene}$	1	2.63	2.60

Table 2.2 Comparison of metrical parameters for **2** obtained by XAS and XRD.

Bond	No. of Scatterers	XAS (Å)	XRD (Å)
Average Fe–O/N	5	2.07	2.15
Fe–O/N	1	1.81	
Average Fe···$C_{methylene}$	6	3.08	3.01

pyridylmethyl group. Taken together, these data suggest that the predominate species in solution for **1** is also the unbound state in which one pyridine ring of dpa is not coordinated (Figure 2.7B). Fits of the EXAFS region for **2** revealed 5 O/N scatterers at 2.07 Å and 1 O/N scatterer at 1.81 Å (Table 2.2, Figure 2.16, Tables 2.11 and 2.12). This pattern indicates a general shortening of the bond lengths when the metal is oxidized. An additional shell was fit to carbon scatterers at 3.08 Å from the Fe center.

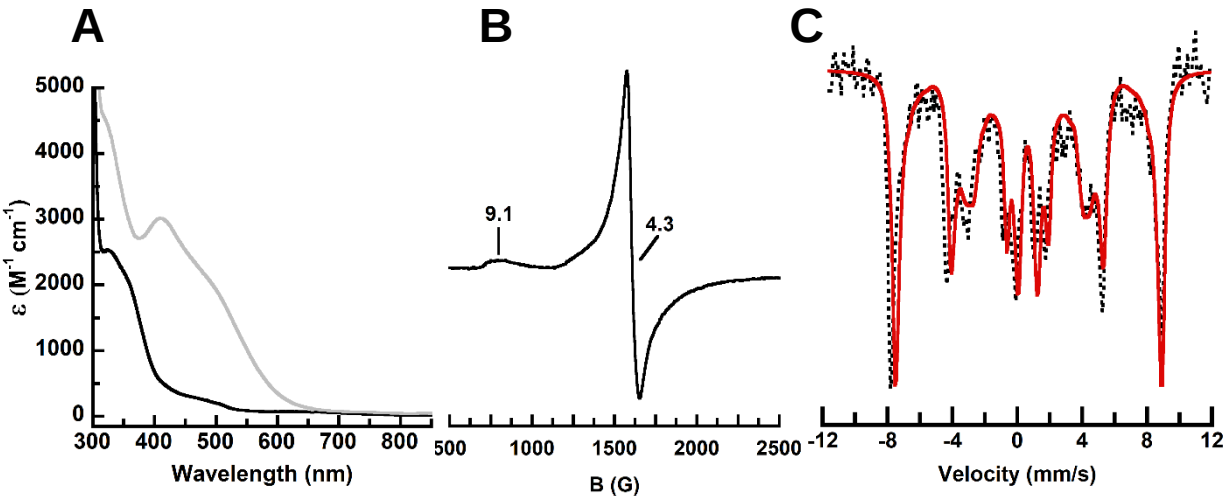

Figure 2.10 Electronic absorbance (**A**), EPR (**B**), and Mössbauer (**C**) spectra of **2–N_3** recorded in 100 mM acetate buffer pH 6. The initial electronic absorbance spectrum is shown as black line, and the final spectrum is shown as a grey line. The simulation is shown as a red line.

*Azide Binding to **2***. The binding of azide ions to **2** was examined in order to investigate how exogenous ligands bind to the Fe center. In solution studies, **2** was treated with a 100-fold excess of NaN_3 in acetate buffer pH 6 to afford a new spectrum with a band at λ_{max} (ε_M, $M^{-1}cm^{-1}$) = 405 (3000) nm that was assigned to an azido-to-Fe^{III} (LMCT) charge transfer transition (Figure 2.10A).[181] EPR and Mössbauer studies revealed 85% conversion to a paramagnetic Fe^{III} species with δ = 0.51 mm/s and ΔE_Q = 0.09 mm/s. The significant changes in the EPR and Mössbauer spectra from **2** to **2–N_3** support the coordination of the azido ligand to the Fe^{III} center (Figures 2.10B, 2.10C). Parallel *in crystallo* studies were performed by soaking crystals of **2** in a 100 mM solution of NaN_3 to afford **2–N_3**, whose structure was obtained to a resolution of 1.85 Å (Tables 2.3 and 2.4, Figure 2.12C, Tables 2.7 and 2.8). Analysis of the molecular structure of **2–N_3** revealed a monomeric Fe complex where the dpa ligand, the carboxylate side chain of $S_{112}E$, and one acetato ligand containing O3 are coordinated in the same positions as found in **2** (Figures 2.9A). However, the second acetato ligand is absent. In its place is electron density that was modelled as a terminal azido ligand with an Fe–N4 bond length of 2.15 Å. The azido ligand has an Fe–N4–N5 bond angle of 120.1°, which is comparable to bond angles found in previously reported Fe^{III}–N_3 complexes (Figure 2.11A and 2.11B).[182] The presence of the azido ligand in **2–N_3** causes a 0.29 Å elongation of the Fe–N2 bond over that observed in **2**, which is consistent with the stronger *trans* influence of an azido ligand than an acetate ion. The structural water molecule Wat1 was modelled at 100% occupancy and is part of an H-bonding network that

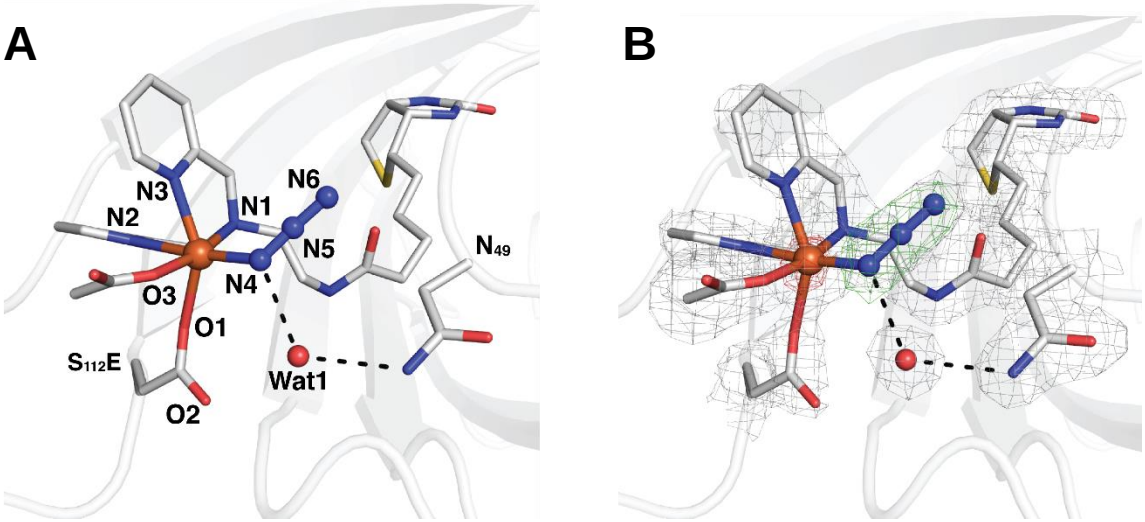

Figure 2.11 Molecular structure of **2**–N_3 (**A**, PDB: 6UIZ), and the $2F_o$-F_c electron density map (grey, contoured at 1σ), F_o-F_c omit map (green, contoured at 3σ) and anomalous difference density (red, contoured at 5 σ) are shown in **B**. Fe ions are colored in orange, N atoms are in blue, and O atoms/water molecules are in red. The numbering scheme in **B** is the same as in **A**.

includes the azido ligand. The H-bonding network extends from the proximal N4 atom of the azido ligand and includes Wat1 and the amide residue of N_{49} with N4···Wat1 and Wat1···N_{49} distances of 2.88 and 3.17 Å, respectively (Figures 2.11A and 2.11B).

Summary and Conclusions

In this chapter, the development of new mononuclear Fe proteins further illustrated the versatility of using biotin-Sav technology to engineer ArMs. Biotin-Sav technology leverages the proper placement of synthetic complexes proximal to endogenous functional groups to produce new biomimetic constructs. Following the design concept of previously developed Cu^{II} proteins, the Sav protein was re-engineered to produce the host 2xM-S_{112}E-Sav, which included a glutamate at position 112. When matched with the biotinylated complexes $[Fe^{II}$(biot-et-dpa)$(OH_2)_2]Br_2$ and $[Fe^{III}$(biot-et-dpa)$(OH_2)_3]Cl_3$, ArMs were produced with properties that resembled those found in mononuclear nonheme Fe enzymes. The positioning of the artificial cofactors within 2xM-S_{112}E-Sav allowed for monodentate

coordination of the carboxylate side chain in an identical manner, as found in the active sites of Fe monooxygenases. Moreover, the unusual structural feature of **1a**, in which one pyridine group of the dpa ligand was not coordinated, produced an Fe binding site that was similar to the 2-His-1-carboxylate facial triad found in the natural metalloproteins. The observation that only one pyridine group was coordinated to the Fe center in **1a** is unusual and has not been structurally observed in other Fe complexes with dpa. This difference is attributed to the confinement of the complex within a protein host, which helped to regulate the secondary coordination sphere around the Fe complex. In fact, the complexes participated in several noncovalent interactions, including with a pyridine ring of the dpa ligand that stabilized the unbound state found in **1a**. An additional H-bond was found between an aqua ligand and the non-coordinating O atom of a glutamate side chain, an interaction that is found in many nonheme Fe enzymes.

The structure of **2** also revealed κ^1–coordination of the carboxylate at position 112 to the Fe^{III} center. In **2**, the Fe complex was 6-coordinate, and the aqua ligands were replaced with acetato ligands to produce a primary coordination sphere that contained three monodentate carboxylate ligands. Again, H-bonds involving the carboxylate ligands appeared to stabilize this unusual coordination environment. Substitution of one of the acetato ligands was achieved by treating **2** with excess azide ion to produce **2–N_3**. The structure of **2–N_3**, along with those of **1** and **2**, also illustrated the importance of the amide side chain of N_{49} in maintaining H-bonding networks around the complexes. Taken together, the design of Fe ArMs supported by a 2-His-1-carboxylate facial triad highlights how the synergistic design of Sav and an artificial metallocofactor allows for the control of both the

primary and secondary coordination spheres of a confined metal complex within a protein host.

Experimental Details

General Methods. All commercially available reagents were obtained at the highest possible purity and used as received. Acetonitrile (CH_3CN), ethanol (EtOH), dimethylformide (DMF), methanol (CH_3OH), dimethylsulfoxide (DMSO), dichloromethane (DCM), chloroform ($CHCl_3$) and diethyl ether were degassed with argon and dried by vacuum filtration through activated alumina according to the procedure by Grubbs.[183] Triethylamine was distilled from KOH. Thin-layer chromatography (TLC) was performed on Merck 60 F254 aluminum-backed silica plates or Merck 60 F254 glass-backed basic aluminum oxide plates. Eluted plates were visualized using UV light. Silica or basic alumina gel chromatography was performed with the indicated solvent system using Fisher reagent silica gel 60 (230-400 mesh) or Sigma reagent Brockmann 1 basic aluminum oxide 58 (150 mesh). Biotin pentafluorophenol ester (biot-PFP)[184] and di-(2-picolyl)amine[185] were prepared according to literature procedures.

Physical Methods

Instrumentation. ^{1}H NMR spectra were recorded at 500 MHz. ^{1}H NMR spectra were reported in ppm on the δ scale and referenced to tetramethylsilane or solvent residual. The data are presented as follows: chemical shift, multiplicity (s = singlet, d = doublet, t = triplet, q = quartet, quin = quintet, m = multiplet, br = broad), and integration. Mass spectra were measured on a MicroMass AutoSpec E, a MicroMass Analytical 7070E, or a MicroMass LCT Electrospray instrument. Electronic absorbance spectra were recorded with a Cary 50 or 8453 Agilent UV-vis spectrophotometer. X-band (9.64 GHz and 9.32 GHz) EPR spectra were recorded on a Bruker spectrometer equipped with Oxford liquid helium cryostats.

The quantification of all signals is relative to a CuEDTA spin standard. The concentration of the standard was derived from an atomic absorption standard (Aldrich). For all instruments, the microwave frequency was calibrated with a frequency counter and the magnetic field with an NMR gaussmeter. A modulation frequency of 100 kHz was used for all EPR spectra. The EPR simulation software (SpinCount) was written by our collaborating author Michael P. Hendrich.[186] Mössbauer spectra were recorded with a Janis Research Super-Varitemp dewar. Isomer shifts are reported relative to Fe metal at 298 K.

Preparative methods

2-(2-(bis(pyridin-2-ylmethyl)amino)ethyl)isoindoline-1,3-dione.[137] Dpa (2.03 g, 10.0 mmol), *N*-(2-bromoethyl)phthalimide (2.93 g, 11.0 mmol), KI (0.339 g, 0.002 mol) and K_2CO_3 (5.6 g, 41 mmol) were dissolved in 60 mL CH_3CN and refluxed for 24 h. The solution was cooled to room temperature, filtered, and reduced to dryness. The maroon-brown residue was dissolved in 30 mL DCM and washed with 3 x 30 mL aqueous $NaHCO_3$ (with a small addition of brine) and 2 x 30 mL water. The maroon-brown organic layer was acidified with 20 mL 12 mM HCl dissolved in 10 mL water and washed with 5 x 30 mL DCM. The aqueous layer was carefully neutralized with solid $NaHCO_3$ and extracted with 4 x 30 mL DCM. The solution was dried with $MgSO_4$, filtered, and reduced to dryness to yield a reddish, brown oil. The crude product was purified via column chromatography with silica gel and CH_3OH:DCM:Et_3N (9:90:1) or with basic alumina and CH_3OH:DCM (10:90) as the eluent to yield pure product as a yellow oil (1.68 g, 44%-50%). ^1H (500 MHz, $CDCl_3$) δ 8.44 (d, 2H), 7.82 (dd, 2H), 7.74 (dd, 2H) 7.42 (t, 2H), 7.34 (d, 2H), 7.06 (t, 2H), 3.85 (m, 6H), 2.86 (t, 2H). MS (ESI, MeOH) *m/z* calcd $C_{22}H_{20}N_4O_2$ [M + (Na^+)] 395.15, found 395.09.

***N,N*-bis(pyridin-2-ylmethyl)ethane-1,2-diamine**.[137] Hydrazine monohydrate (1.10 mL, 0.020 mol) and **2-(2-(bis(pyridin-2-ylmethyl)amino)ethyl)isoindoline-1,3-dione** (1.7 g, 5.0 mmol) were dissolved in 60 mL EtOH and refluxed under N_2 for 3 h. The phthalhydrazide byproduct precipitated as a white solid after 15 min of reflux. The solution was filtered to remove the phthalhydrazide and washed with 3 x 5 mL chloroform. The solution was reduced to dryness, and the yellow oily residue was dissolved in 40 mL $CHCl_3$ and 40 mL of 1 M NaOH. The aqueous layer was extracted with 3 x 40 mL $CHCl_3$, dried over $MgSO_4$, filtered, and reduced to dryness. The product was recovered as a yellow oil (0.80 g, 77%). ^{1}H (500 MHz, $CDCl_3$) δ 8.53 (d, 2H), 7.66 (t, 2H), 7.50 (d, 2H) 7.15 (t, 2H), 3.85 (s, 4H), 2.80 (t, 2H), 2.66 (t, 2H). MS (ESI, MeOH) *m/z* calcd $C_{14}H_{18}N_4$ [M + (H^+)] 243.16, found 243.11.

biot-et-dpa.[137] A solution of biot-PFP (1.30 g, 3.01 mmol), ***N,N*-bis(pyridin-2-ylmethyl)ethane-1,2-diamine** (0.85 g, 3.0 mmol), and triethylamine (0.39 g, 3.0 mmol) in 20 mL DMF was stirred overnight. The DMF was removed under vacuum to yield a sticky tan residue. The residue was triturated with diethyl ether until a free-flowing solid formed (3-7 days). The light tan solid was filtered, washed with diethyl ether, and dried under vacuum (1.49 g, 91%). The solid was stored under an inert atmosphere. ^{1}H (500 MHz, DMSO) δ 8.44 (d, 2H), 7.75 (br, 1H), 7.71 (t, 2H) 7.50 (d, 2H), 7.21 (t, 2H), 6.40 (s, 1H), 6.33 (s, 1H), 4.27 (t, 1H), 4.07 (t, 1H), 3.72 (s, 4H), 3.16 (q, 2H), 3.04 (q, 1 H), 2.78 (dd, 1 H), 2.55 (s, 1H), 2.46 (t, 2H), 2.02 (t, 2H), 1.45 (m, 6H). MS (ESI, MeOH) *m/z* calcd $C_{24}H_{32}N_6O_2S$ [M + (Na^+)] 491.22, found 491.17.

Preparation of Metal Complexes

[Fe^{II}(biot-et-dpa)(OH_2)$_2$]Br_2.[187] [Fe^{II}(biot-et-dpa)(OH_2)$_2$]Br_2 was prepared by the addition of **biot-et-dpa** (53 mg, 0.24 mmol) in 10 mL CH_3CN to $FeBr_2$. A pale yellow solid immediately precipitated from the solution. The suspension was stirred under N_2 for 30 min, after which the pale-yellow solid was collected via filtration, washed with CH_3CN:diethyl ether (1:1), and dried under vacuum (0.125 g, 75%). The solid was stored under an inert atmosphere. HR-MS (ESI, 1% DMF:CH_3CN) m/z calcd for $C_{24}H_{32}FeN_6O_2SBr$ [M – (Br^-)] 603.08, found 603.08. Elem. Anal. Calcd for ($C_{24}H_{36}N_6SO_4FeBr_2$): C, 40.02; H, 5.04; N, 11.67. Found: C, 39.67; H, 4.52; N, 11.38.

[Fe^{III}(biot-et-dpa)(OH_2)$_3$]Cl_3.[188] [Fe^{III}(Biot-ethyl-DPA)(OH_2)$_3$]Cl_3 was prepared by the addition of **biot-et-dpa** (0.09 g, 0.2 mmol) in 3 mL EtOH to $FeCl_3 \cdot 6H_2O$ (0.10 g, 0.38 mmol) in 3 mL EtOH. A yellow solid immediately precipitated from the solution. The suspension was stirred under N_2 for 15 min, after which the yellow solid was isolated via filtration. The solid was washed with 10 mL chilled EtOH:diethyl ether (4:1) and dried under vacuum (0.10 g, 86%). The solid was stored under an inert atmosphere. HR-MS (ESI, MeOH) *m/z* calcd for $C_{24}H_{32}Cl_2FeN_6O_2S$ [M – (Cl^-)] 594.10, found 594.08. Elem. Anal. Calcd for ($C_{24}H_{38}N_6SO_5FeCl_3$): C, 42.09; H, 5.59; N, 12.27. Found: C, 42.28; H, 5.12; N, 12.23.

Spectroscopic Methods.

HABA Titrations. To 2.4 mL of 8 μM Sav in 200 mM sodium phosphate buffer at pH 7 was added 300 μL of a 10 mM 2-(4′-hydroxyazobenzene)benzoic acid (HABA) in 200 mM phosphate buffer pH 7. After 5 min of equilibration, the absorbance at 506 nm was recorded. A solution of 1 mM Fe complex in nanopure water was added in 4-20 μL portions until approximately 4 equivalents had been added. The absorbance at 506 nm was recorded until no further changes in intensity were observed.

Electronic Absorption Studies. A solution of lyophilized protein (50-250 μM) was prepared in nanopure water. Four equivalents of Fe complex (0.2-1 mM) in nanopure water were added to the protein solution. Samples were prepared in a final volume of 500 μL containing 50 mM potassium phosphate or 100 mM sodium acetate buffer at the indicated pH.

EPR Studies. A solution of protein (500 μM) was prepared in nanopure water. Four equivalents of Fe complex (2 mM) in nanopure water were added to the protein solution. Samples were prepared in a final volume of 200 μL containing 50 mM potassium phosphate or 100 mM sodium acetate buffer at the indicated pH. The sample was transferred to an EPR tube, frozen at 77 K in liquid nitrogen, and run at 10 K.

Mössbauer studies. A solution of protein (500 μM) was prepared in nanopure water. Four equivalents of Fe complex (2 mM) in nanopure water were added to the protein solution. Samples were prepared in a final volume of 300 μL containing 100 mM sodium acetate buffer at the indicated pH. The sample was prepared in a solution Mössbauer cup, frozen at 77 K in liquid nitrogen, and run at 4 K.

XAS Studies. A solution of protein (750 μM) was prepared in nanopure water. Four equivalents of Fe complex (3 mM) in nanopure water were added to the protein solution. Samples were prepared in a final volume of 250 μL with nanopure water. The sample was then poured in liquid ethane to freeze and packed as a solid into a pre-cooled XAS sample holder.

XAS data collection and processing. XAS experiments were performed at the Stanford Synchrotron Radiation Laboratory (SSRL) on beam line 7-3 at 13 K. Fe K-edge data were collected using a Si(220) φ=0° double-crystal monochromator with a 9.0 keV cutoff for

harmonic rejection. Data were collected in fluorescence mode with a Canberra 30-element Ge solid-state detector. To limit photoreduction of the samples, only first scans were averaged into the final data sets (exposure time ~35 minutes). Fe K-edge data for all species were comprised of 14 first scans. Energies were calibrated using an Fe foil (7111.2 eV) and edge energies were obtained from the first derivative of the data with 1.0 eV smoothing and a third order polynomial in the program EXAFSPAK.[189] The Fe K-edge data sets were fit over the region k = 3-15 Å^{-1} using EXAFSPAK with *ab initio* phases and amplitudes generated with the program FEFF v8.40.[190] The Fe K-edge fits for the Fe species were comprised of the first and second shell atoms. All Debye-Waller factors were treated as free parameters. The scale factor, S_0, was set to 0.9. Monochromator glitches in the Fe K-edge data sets at approximately k = 12.5 Å^{-1} were removed using a cubic polynomial fit to the data. No other modifications to the raw data were performed.

Protein Preparation and Crystallography

Protein Expression and Purification

Preparation of Sav variants. The construction of E_{101}Q-K_{121}A-S_{112}E-Sav and other variants was achieved by site-directed mutagenesis (SDM) using the codon optimized K_{121}A-pET24a-Sav plasmid,[191] the following primers and, and Q5 polymerase.

E_{101}Q_fwd: 5'-GGTGCACAAGCACGCATTAATACCC-3'

E_{101}Q _rev: 5'-GTGCTTGTGCACCACCAACATACTG-3'

S_{112}E_fwd: 5'-GACCTACGGCACCACCGAAGCAAATGC-3'

S_{112}E_rev: 5'-GTGCCGTAGGTCAGCAGCCACTGG-3'

Amplification of pET24a-Sav mutant plasmids was accomplished by the transformation of SDM reaction mixtures into DH5α ultracompetent cells. Plasmids were isolated using a

Miniprep kit from Qiagen, eluting the final plasmid with distilled deionized-water (ddH_2O, 18 MΩ cm^{-1}). DNA sequencing was performed by Genewiz.

Sav Expression. Transformation of 4 µL amplified plasmids into 50 µL Rosetta cells or bl21 cells was followed by rescue with 450 µL LB media. Of this solution, 200 µL was spread aseptically onto LB/Kanamycin agar plates and incubated overnight at 37 °C. Inoculation of a starter culture containing 500 mL LB media and the same antibiotic from a single colony was followed by incubation overnight at 37 °C and shaking at 225 rpm. From this starter culture, 25 mL was used to inoculate each 2L flask containing 500 mL LB media, 25 mL each of 20x sugar (12% glycerol, 1% glucose, 10% lactose) and salt (1 M Na_2HPO_4, 1 M KH_2PO_4, 0.5 M $(NH_4)_2SO_4$) stocks, 1 mL of 1 M $MgSO_4$, 100 µL 5000x trace metal mix (containing 1 M $CaCl_2$, 100 mM $FeCl_3$, 10 mM $MnCl_2$, 10 mM $ZnSO_4$, 2 mM $CoCl_2$, 2 mM $CuCl_2$, 2 mM $NiCl_2$, 2 mM Na_2MoO_4, and 2 mM H_3BO_3 all in 60 mM HCl), and 250 µL of 100 mg/mL Kanamycin. Incubation at 37 °C and 225 rpm was continued until cells reached OD_{600} = 0.6–0.8, at which point the temperature was dropped to 25 °C and cultures incubated another 24 h.

Sav purification. Cultures were centrifuged at 4000 x *g* for 20 min at 4 °C. The resulting cell pellet was resuspended in lysis buffer (50 mL per 1 L expressed) containing 20 mM Tris buffer pH 7.4, 1 mg/mL lysozyme, and a spatula tip of DNase I. The suspension was then allowed to shake at 25 °C and 225 rpm for 6-8 h followed by one overnight freeze-thaw cycle. Dialysis against 6 M guanidinium hydrochloride pH 1.5 for 24 h was followed by neutralization via dialysis against 20 mM Tris buffer pH 7.4 for 24 h, and against nanopure H_2O for another 24 h. Dialysis overnight against iminobiotin (IB) buffer containing 500 mM NaCl and 50 mM $NaHCO_3$ at pH 10.5 afforded the crude, biotin-free lysate. This material was centrifuged at 10,000 x *g* for 1 h at 4 °C and the soluble portion loaded onto an iminobiotin-

agarose column pre-equilibrated with IB buffer. The column was washed with 6 column volumes (CVs) of IB buffer or until the absorbance at 280 nm (A_{280}) dropped to zero. Elution with 1% acetic acid in nanopure H_2O, and pooling fractions by A_{280}, provided highly pure (>95%) Sav as assessed by 18% SDS-PAGE. Pooled fractions were dialyzed against 10 mM Tris pH 7.4 for 24 h followed by dialysis in ddH_2O for an additional 72 h and were then lyophilized. Yields of lyophilized protein were typically 100 mg per L expressed, and the solid protein was stored at 4 °C.

Protein Crystallization

*Crystallization of [Fe^{II}(biot-et-dpa(OH_2)$_2$(κ^1-O_{E112})⊂2xM-S_{112}E-Sav] (**1**).* Apo-Sav protein was crystallized by the sitting drop vapor diffusion method under an inert atmosphere. Diffraction-quality crystals were grown at room temperature by mixing 3.5 µL of protein solution (26 mg/mL lyophilized protein in water) and 1.5 µL of crystallization buffer (2.0 ammonium sulfate, 0.1 M sodium acetate, pH 4). The droplet was equilibrated against a reservoir solution of 100 µL crystallization buffer. Single crystals of Sav were prepared by soaking apo-crystals in a soaking buffer (2.6 ammonium sulfate, 0.1 M sodium acetate, pH 8) with a 10 mM stock solution of [Fe^{II}(biot-et-dpa)(OH_2)$_2$]Br_2 in nanopure water (9 µL crystallization buffer, 1 µL [Fe^{II}(biot-et-dpa)(OH_2)$_2$]Br_2) overnight. After the soaking process, crystals were transferred to cryo-protectant for 1 min (30% glycerol in crystallization buffer) and shock-frozen in liquid nitrogen.

*Crystallization of [Fe^{III}(biot-et-dpa(OAc)$_2$(κ^1-O_{E112})⊂2xM-S_{112}E-Sav] (**2**).* Apo-Sav protein was crystallized by the sitting drop vapor diffusion method. Diffraction-quality crystals were grown at room temperature by mixing 3.5 µL of protein solution (26 mg/mL lyophilized protein in water) and 1.5 µL of crystallization buffer (2.0 ammonium sulfate, 0.1 M sodium

acetate, pH 4). The droplet was equilibrated against a reservoir solution of 100 µL crystallization buffer. Single crystals of Sav were prepared by soaking apo-crystals in a soaking buffer (2.6 ammonium sulfate, 0.1 M sodium acetate, pH 6) with a 10 mM stock solution of $[Fe^{III}(biot\text{-}et\text{-}dpa)(OH_2)_3]Cl_3$ in nanopure water (9 µL crystallization buffer, 1 µL $[Fe^{III}(biot\text{-}et\text{-}dpa)(OH_2)_3]Cl_3$) overnight. After the soaking process, crystals were transferred to cryo-protectant for 1 min (30% glycerol in crystallization buffer) and shock-frozen in liquid nitrogen. Crystals were prepared in the same manner for data collected using XFEL.

Crystallization of biot-et-dpa⊂2xM-S_{112}E-Sav. Apo-Sav protein was crystallized by the sitting drop vapor diffusion method. Diffraction-quality crystals were grown at room temperature by mixing 3.5 µL of protein solution (26 mg/mL lyophilized protein in water) and 1.5 µL of crystallization buffer (2.0 ammonium sulfate, 0.1 M sodium acetate, pH 4). The droplet was equilibrated against a reservoir solution of 100 µL crystallization buffer. Single crystals of Sav were prepared by soaking apo-crystals in a soaking buffer (2.6 ammonium sulfate, 0.1 M sodium acetate, pH 6) with a 10 mM stock solution of biot-et-dpa in nanopure water (9 µL crystallization buffer, 1 µL biot-et-dpa) overnight. After the soaking process, crystals were transferred to cryo-protectant for 1 min (30% glycerol in crystallization buffer) and shock-frozen in liquid nitrogen.

*Crystallization of $[Fe^{III}(biot\text{-}et\text{-}dpa)(OAc)(N_3)(\kappa^1\text{-}O_{E112})$⊂2xM-$S_{112}$E-Sav] (**2–$N_3$**).* Apo-Sav protein was crystallized by the sitting drop vapor diffusion method. Diffraction-quality crystals were grown at room temperature by mixing 3.5 µL of protein solution (26 mg/mL lyophilized protein in water) and 1.5 µL of crystallization buffer (2.0 ammonium sulfate, 0.1 M sodium acetate, pH 4). The droplet was equilibrated against a reservoir solution of 100

uL crystallization buffer. Single crystals of Sav were prepared by soaking apo-crystals in a soaking buffer (2.6 ammonium sulfate, 0.1 M sodium acetate, pH 6) with a 10 mM stock solution of $[Fe^{III}(biot\text{-}et\text{-}dpa)(OH_2)_3]Cl_3$ in nanopure water (9 µL crystallization buffer, 1 µL $[Fe^{III}(biot\text{-}et\text{-}dpa)(OH_2)_3]Cl_3$) overnight. After this initial soaking step, the crystals were soaked in a soaking buffer (2.6 ammonium sulfate, 0.1 M sodium acetate, pH 6) with a 1 M stock solution of NaN_3 in nanopure water for 5-10 min (9 µL crystallization buffer, 1 µL NaN_3). After the second soaking process, the crystals were transferred to cryo-protectant for 1 min (30% glycerol in crystallization buffer) and shock-frozen in liquid nitrogen.

X-ray diffraction data collection and processing. X-ray diffraction data were collected at the Stanford Synchrotron Radiation Lightsource (BL 12.2, 9.2, or MFX LCLS) and the Advanced Light Source (BL 8.2.1 or 8.2.2) at a wavelength of 1 Å. Data for **2–N$_3$** were collected with helical data collection using exposure time/frame 0.2/0.2 s/deg. X-ray diffraction data were processed with XDS[192] or iMosflm[193] and scaled with AIMLESS (CCP4 Suite).[193] The structures were solved by molecular replacement using program PHASER (CCP4 Suite)[193] and the structure 2QCB from the PDB as input model ligand with water molecules removed. For structure refinement, REFMAC5 (CCP4 Suite)[194] and PHENIX.REFINE[195] were used. Ligand manipulation was carried out with program REEL using the small molecule crystal structure RAGQEV01 from the Cambridge Structural Database as an input model.[196] For water picking, electron density, and structure visualization, the software COOT[197] was used. Figures were drawn with PyMOL (the PyMOL Molecular Graphics System, Version 1.8.2.3, Schrödinger, LLC). Crystallographic details, processing and refinement statistics are given in Supplementary Table 2.5-2.8.

XFEL data collection and processing. XFEL data were collected at the MFX instrument (Sierra

2019) of the LCLS facility (SLAC National Accelerator Lab, Menlo Park, CA) using X-ray pulses of ~35 fs length at an energy of 9.5 keV and with an average pulse power of 2.5 mJ and a beam size of 4 μm (FWHM), obtained by compound refractive lenses. A suspension of microcrystals of **2** (50-80 μm in the longest dimension, 1 x 10^6 Crystals•mL^{-1}) was delivered into the X-ray interaction region by the Drop-On-Demand method described by Fuller et al.[198] utilizing a flow rate of 8 μL•min^{-1}. The 4.4-nL droplets were deposited on a Kapton tape traveling at 300 mm•sec^{-}1 and transversed a helium enclosure for 0.8 sec before the X-ray pulse. Diffraction data were collected at a rate of 30 Hz on a Rayonix MX 340HS detector with 2x2 binning at a distance of 144 mm from the interaction point. XFEL data from 6010 images were processed and indexed using *cctbx.xfel* and DIALS.[199,200] The images were merged using *cxi.merge* within the *cctbx.xfel* package[201] using a per-image resolution cutoff (based on resolution-binned I/σ(I) estimates), including post-refinement by applying a partiality correction to inflate the unmerged partially-recorded reflections from the still images to their full equivalent values. The final dataset was merged to 1.50 Å resolution based on multiplicity and $CC_{1/2}$ criteria.

Structural Results.

Crystal Color. All crystals of Sav soaked with complexes $[Fe^{II}$(biot-et-dpa)$(OH_2)_2]Br_2$ and $[Fe^{III}$(biot-et-dpa)$(OH_2)_3]Cl_3$ changed from colorless to pale yellow and dark yellow, respectively. Crystals soaked with NaN_3 changed from dark yellow to red. There was no color change for crystals soaked with only biot-et-dpa ligand.

Structural Refinement. Apo-crystals of proteins 2xM-S_{112}E-Sav soaked with either biot-et-dpa, $[Fe^{II}$(biot-et-dpa)$(OH_2)_2]Br_2$, or $[Fe^{III}$(biot-et-dpa)$(OH_2)_3]Cl_3$ constituted space group $I4_122$ with unit cell parameters reported in Tables 2.5-2.8. A single Sav monomer was

obtained per asymmetric unit after molecular replacement. Protein residues 2-10 and 135-159 of the N- and C-terminus, respectively, were not resolved in the electron density, presumably due to disorder. Starting from the Sav monomer the biological homotetramer is generated by application of crystallographic C_2-symmetry axes along the x-, y- and z-axes of the unit cell. The overall protein structures are virtually identical to structure biotin ⊂ WT-Sav (PDB 1STP, see Tables 2.5 and 2.7).

General Complex Modeling. For all structures of apo-protein crystals soaked with the corresponding Fe-complexes, the following general observations were made: i) residual electron density in the F_o-F_c map was observed in the biotin binding pocket, ii) in the biotin vestibule which is flanked by protein residues of loop-3,4^A (the superscript number indicates Sav monomer within tetramer) loop-4,5^C, loop-5,6^A loop-7,8^A and loop-7,8^B, and iii) an anomalous dispersion density map indicated a significant peak in the biotin vestibule superimposed with the electron density peak. The residual electron density was fit with the corresponding Fe-complexes, which projected Fe to the position of the strong anomalous density peak.

*Structural refinement of **1**.* In the $I4_122$ symmetry solution, the dpa ligand is modelled at 70% uncoordinated and 30% coordinated to the Fe center. The Fe center was modelled at 80% occupancy; the decrease in occupancy could be because of this disorder within the active site. It is possible that the occupancy is higher for uncoordinated dpa ligand; however, the B factors did not significantly change between 70-90% occupancy and the final solution was decided based on modelling less to ensure a more correct model with less bias. The glutamate residue was also modelled with 80% coordinated and 20% uncoordinated to the Fe center.

*Structural refinement of **2**.* In the $I4_122$ symmetry solution, the dpa ligand is modelled 100% coordinated to the Fe center; whereas the glutamate residue is modelled at 80% coordinated, and 20% uncoordinated to the Fe center. The Fe center is modelled at 80% because of the significant negative density in the F_o-F_c map. The decrease in occupancy can be possible because of disorder in the structure. Additionally, at the density that was modelled for the acetato ligand (O3), there was density in the anomalous map to ~4 σ. It was attempted to model a sulfate ligand in the density to account for the anomalous density with a sulfur atom; however, negative density in the F_o-F_c map appeared after refinement with a sulfate ligand. Moreover, the biotin sulfur had anomalous density to ~ 8 σ, which could mean that whatever ligand is causing the anomalous density at O3 cannot be significant. Rather than a sulfate ligand, the O3 density was fit to an acetato ligand, and a Poulder map confirmed that acetate is a reasonable fit to the density. It is unknown why the anomalous density is present at O3 but the data fits well to an acetato ligand and was thus modelled for the final solution. Lastly, the comparable symmetry solution with the XFEL data also fit the density at O3 reasonably to an acetato ligand.

*Structural Refinement of **2–N$_3$**.* In the $I4_122$ symmetry solution, there was significant disorder in the Fe complex, presumably to accommodate the coordination of the azido ligand. The dpa ligand, Fe center, and azide ligand were modelled with 100% occupancy; whereas, the glutamate residue was modelled 80% coordinated and 20% uncoordinated to the Fe center. The glutamate residue was disordered, and fitting the uncoordinated conformation was determined to be necessary because there was negative density around the coordinated residue side chain without the second confirmation. Additionally, the first location of the azido ligand was obvious; however, it was thought to be possible that in the

density where an acetato ligand (O3) was fit, there could also be some amount of azido ligand present as well. Modelling with 50/50 acetato/azido ligand or 100% occupancy azido ligand did not fit the data as well as with one acetato ligand at 100% occupancy. A Poulder map also confirmed that an acetato ligand was a reasonable fit. However, there is some amount of disorder that surrounds the acetato ligand because there is some extra density in the F_o-F_c map around the acetato ligand. At the final solution, the best fit that was modelled was one acetato ligand. However, it might be possible that the disorder within the structure is due to the competition between an acetato and a second azido ligand binding to the second coordination site.

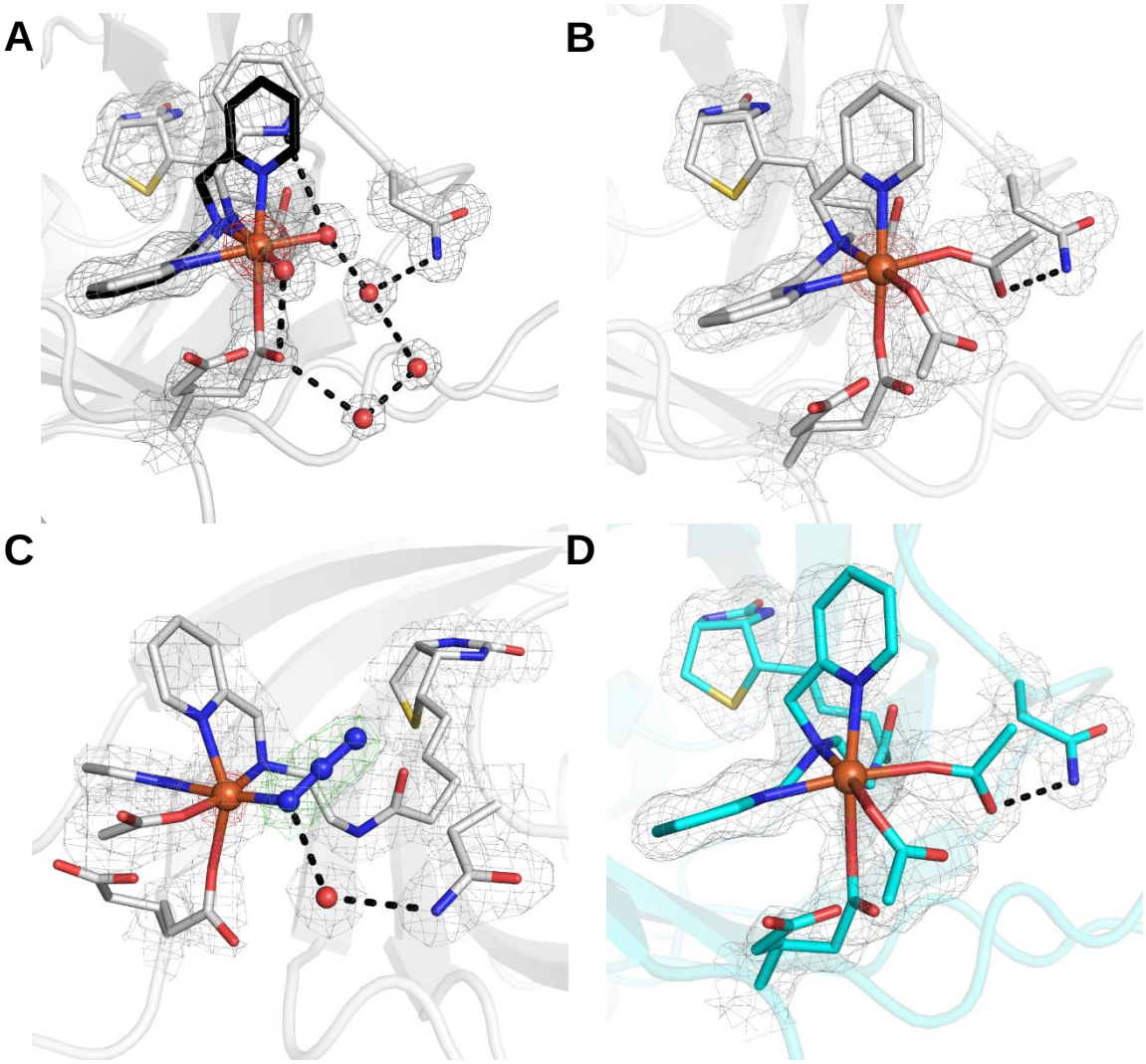

Figure 2.12 Close-up views of the Fe sites in the molecular structures of complex **1** (**A**), **2** (**B**–XRD; **D**–XFEL), and **2–N$_3$** (**C**). For clarity, only one Sav monomer is displayed. The protein is displayed in surface representation, and the Fe complex and residues 112 and 49 are displayed as sticks. The position of the ligand molecules is indicated by the $2F_o$-F_c electron density (grey, contoured at 1 σ) and anomalous difference density (red, contoured at 4 σ; for C, contoured at 3 σ). Fe is colored in orange, N atoms are in blue, and O atoms/water molecules are in red. H-bonding interactions are displayed as dashed black lines. The numbering scheme is the same as in Figures 2.7, 2.9, and 2.11.

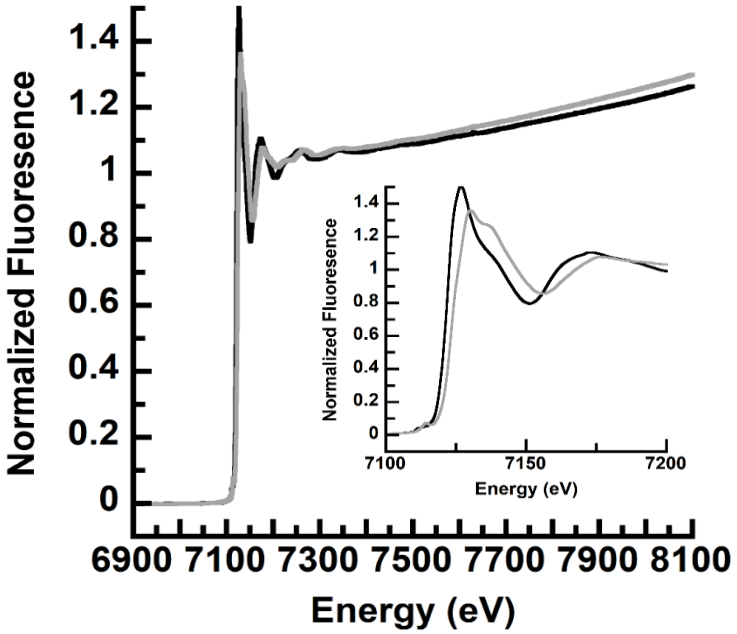

Figure 2.14 Normalized fluorescence spectra of **1** (black) and **2** (grey). The insert is an expansion of the XANES region.

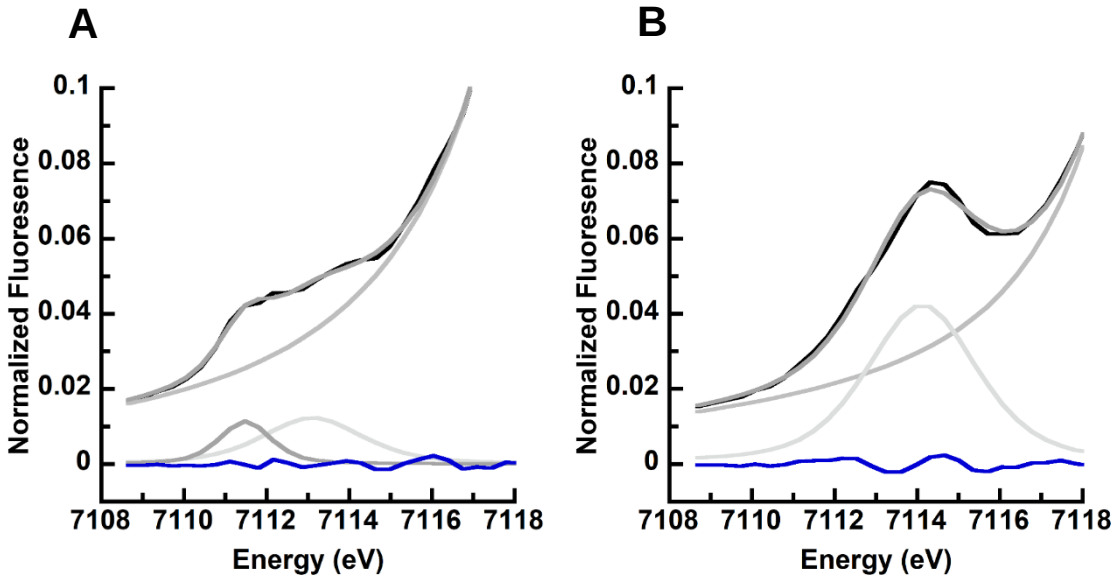

Figure 2.13 Pre-edge region analysis of **1** (**A**) and **2** (**B**) showing the experimental data (black), baseline (grey), pre-edge peak componenets (grey), residuals (blue), and total fit (dark grey).

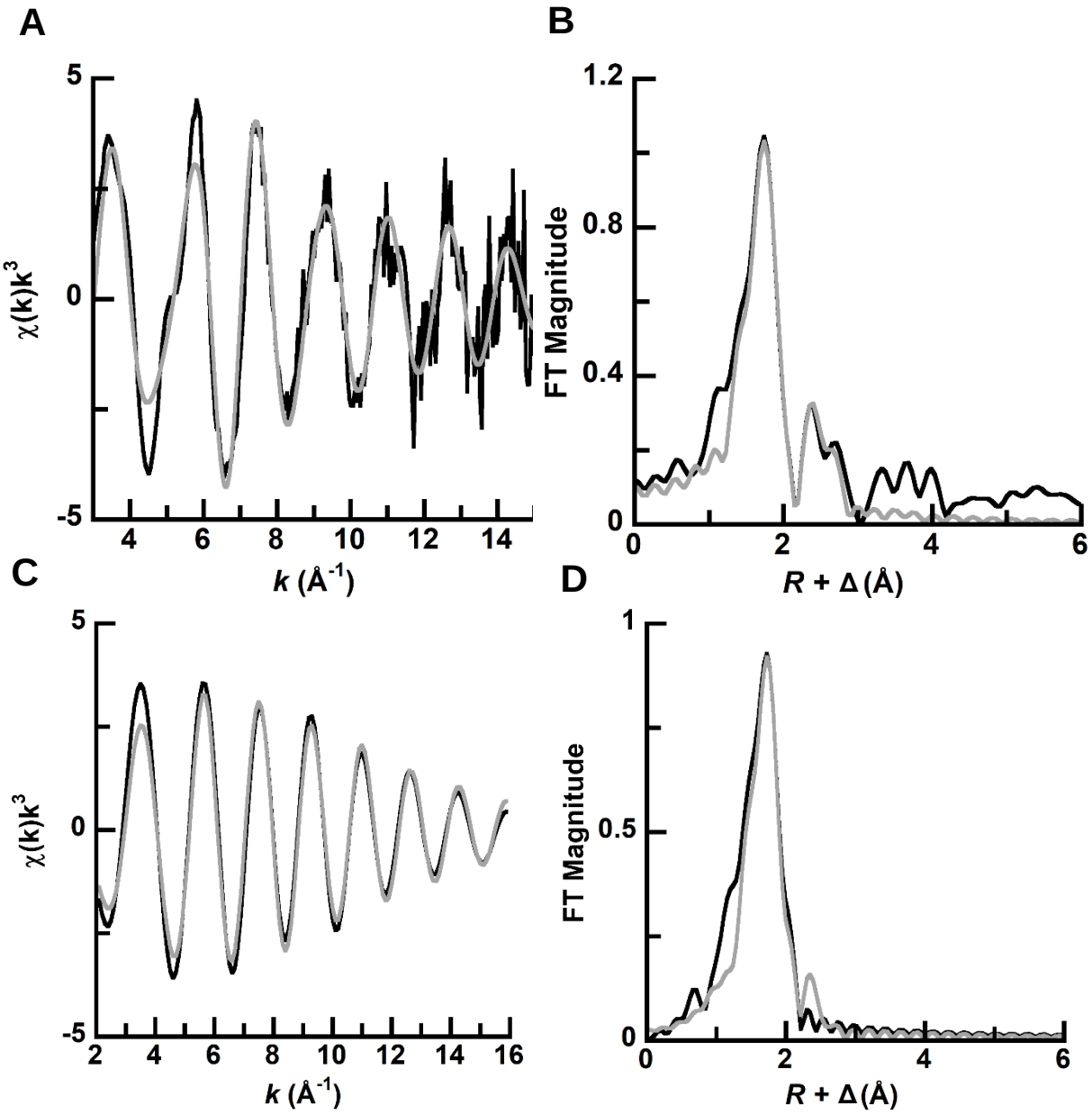

Figure 2.15 Fit (grey) of the unfiltered (black) EXAFS data (**A**) and the corresponding Fourier transform (FT) (**B**) of **1**. Fit (grey) of the filtered (black) EXAFS data (**C**) and the corresponding FT (**D**) of **1**.

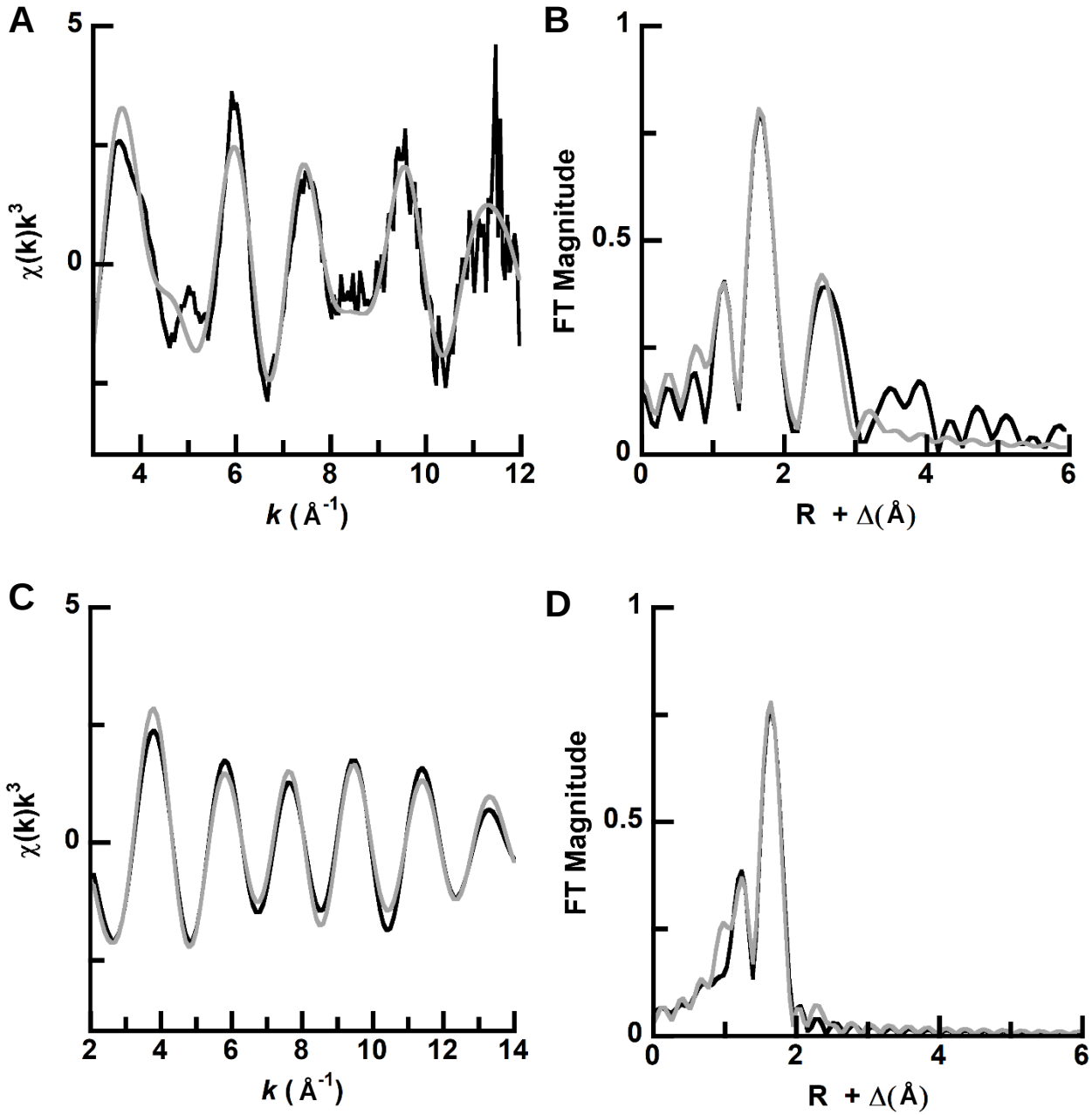

Figure 2.16 Fit (grey) of the unfiltered (black) EXAFS data (**A**) and the corresponding FT (**B**) of **2**. Fit (grey) of the filtered (black) EXAFS data (**C**) and the corresponding FT (**D**) of **2**.

Table 2.3 Selected bond lengths (Å) and angles (°) for the ArMs from XRD measurements for **1**, **2**, **2–N_3**.

Bond lengths and angles	**1a**	**1b**	**2**	**2–N_3**
Fe–O1	2.16	2.16	2.11	2.35
Fe–O3	2.17	2.17	2.17	2.00
Fe–O4	2.22	2.22	2.15	–
Fe–N1	1.94	2.31	2.15	2.27
Fe–N2	2.32	2.36	2.23	2.52
Fe–N3	–	2.21	2.18	2.27
Fe–N4	–	–	–	2.15
N1–Fe–O3	167	167	168	169
N1–Fe–N2	79	67	70	79
N2–Fe–O4	170	164	164	–
N2–Fe–O3	96	101	100	91
N1–Fe–O4	95	101	95	–
O3–Fe–O4	91	91	95	–
O1–Fe–N1	100	91	90	95
O1–Fe–N2	82	78	78	75
O1–Fe–N3	–	166	163	146
O1–Fe–O3	91	91	95	87
O1–Fe–O4	92	92	94	–
N1–Fe–N3	–	79	75	83
N2–Fe–N3	–	107	104	71
N3–Fe–O3	–	101	101	89
N3–Fe–O4	–	79	79	–
O1–Fe–N4	–	–	–	110
O3–Fe–N4	–	–	–	89
N1–Fe–N4	–	–	–	101
N2–Fe–N4	–	–	–	175
N3–Fe–N4	–	–	–	103
Fe–N4–N5	–	–	–	120

Table 2.4 Selected H-bonds (Å) for the ArMs from XRD measurements for **1**, **2**, **2–N_3**.

Distances	**1**	**2**	**2–N_3**
N3···O4	3.51	–	–
O4···Wat22	2.54	–	–
Wat22···N_{49}	3.00	–	–
Wat22···Wat191	3.05	–	–
Wat191···Wat190	2.34	–	–
Wat190···O2	3.12	–	–
O2···O3	2.71	–	–
O6···N_{49}	–	2.97	–
N4···Wat1	–	–	2.88
Wat1···N_{49}	–	–	3.17

Table 2.5 X-ray Crystallography Data Processing and Refinement Statistics for biot-et-dpa and **1**.

Identification		
Sav Mutant	2xM S112E	2xM S112E
Fe complex/biotinylated Ligand	**biot-et-dpa**	$[Fe^{II}(\text{biot-et-dpa}(OH_2)_2(\kappa^1\text{-}O_{E_{112}})]^+$ (**1**)
PDB Code	6UIU	6UIY
Fe complex PDB 3-letter code	QG7	QGI
Data Processing		
Unit Cell	a, b, c = 57.9 Å, 57.9 Å, 184.3 Å α, β, γ = 90°	a, b, c = 57.7 Å, 57.7 Å, 184.3 Å α, β, γ = 90°
Space Group	$I4_122$	$I4_122$
Resolution (Å)	37.4 – 1.35	55.10 – 1.47
Highest resolution shell (Å)	1.40 – 1.35	1.49– 1.47
R_{merge} (%)	24 (246)	6.9 (50)
No. of unique reflections	35163 (1647)	27259 (1317)
Multiplicity	13.1 (11.5)	12.9 (9.6)
I/Sig(I)	5.6 (1.1)	21.6 (4.0)
Completeness	99.8 (96.4)	100.0 (100)
CC(1/2)	0.992 (0.91)	0.99 (0.93)
Beamline	SSRL 12.2	ALS 8.2.1
Structure Refinement		
R_{work}	0.21	0.15
R_{free}	0.23	0.18
Rmsd bond length (Å)	0.015	0.018
Rmsd bond angle (°)	3.027	2.434
Rmsd compared to biotin-Sav WT (PDB 1STP) (Å)	0.67	0.62
No. ligands		
Fe complex	1	1
Water	116	118
Acetate	0	2

Table 2.6 Summary of structural details for biot-et-dpa and **1**.

PDB Code	6UIU	6UIY
Complex	**biot-et-dpa**	**1**
Electron density at Fe in F_o–F_c omit map (σ)	–	36
Anomalous dispersion density at Fe (σ)	–	20
Geometry of Fe complex	–	70%: square pyramidal 30%: distorted octahedral
Coordination number of Fe complex	–	70%: 5 30%: 6
Occupancy of Fe complex (%)	–	80
B-factor (Å²)		
Overall protein	16	17
S112E	16	(80/20): 18/10
K121A	12	12
E101Q	40	49
Fe complex	–	(70/30): 19/19
DPA	15	(70/30): 19/19
Fe	–	28
Distance Fe–Fe (Å)	–	10

Table 2.7 X-ray Crystallography Data Processing and Refinement Statistics for **2** and **2–N_3**.

Identification			
Sav Mutant	2xM S112E	2xM S112E	2xM S112E
Fe complex	[Fe^{III}(biot-et-dpa$(OAc)_2$(κ^1-O_{E112})] (**2-XRD**)	[Fe^{III}(biot-et-dpa$(OAc)_2$(κ^1-O_{E112})] (**2-XFEL**)	[Fe^{III}(biot-ethyl-dpa)(OAc)(N_3)(κ^1-O_{E112})] (**2–N_3**)
PDB Code	6UIO	6US6	6UIZ
Fe complex PDB 3-letter code	QFY	QFY	QG4
Data Processing			
Unit Cell	a, b, c = 57.9 Å, 57.9 Å, 184.7 Å α, β, γ = 90º	a, b, c = 58.1 Å, 58.1 Å, 185.7 Å α, β, γ = 90º	a, b, c = 57.8 Å, 57.8 Å, 184.5 Å α, β, γ = 90º
Space Group	$I4_122$	$I4_122$	$I4_122$
Resolution (Å)	37.42 – 1.40	23.21 – 1.50	37.34 – 1.85
Highest resolution shell (Å)	1.42 – 1.40	1.55 – 1.50	1.89 – 1.85
R_{merge} (%)	6.5 (233)	–	22 (140)
No. of unique reflections	31551 (1533)	26030 (2514)	13859 (827)
No. of merged images	–	6011	–
Multiplicity	25.9 (26.3)	99.98 (13.24)	10.9 (11.3)
I/Sig(I)	30.6 (1.7)	27.544 (0.967)	10.1 (2.3)
Completeness	100.0 (100)	99.8 (99.5)	99.9 (100)
CC(1/2)	1.00 (0.68)	0.977 (2.4)	0.996 (0.793)
Beamline	ALS 8.2.2	SSRL MFX LCLS	SSRL 9.2
Structure Refinement			
R_{work}	0.16	0.17	0.18
R_{free}	0.18	0.18	0.23
Rmsd bond length (Å)	0.014	0.015	0.017
Rmsd bond angle (°)	2.072	1.996	2.994
Rmsd compared to biotin-Sav WT (PDB 1STP) (Å)	0.61	0.74	0.62
No. ligands			
Fe complex	1	1	1
Water	105	63	107
Acetate	6	3	3

Table 2.8 Summary of structural details for **2** and **2–N_3**.

PDB Code	6UIO	6US6	6UIZ
Complex	**2–XRD**	**2–XFEL**	**2–N_3**
Electron density at Fe in F_o–F_c omit map (σ)	37	35	32
Anomalous dispersion density at Fe (σ)	20	–	7
Geometry of Fe complex	Distorted octahedral	Distorted octahedral	Distorted octahedral
Coordination number of Fe complex	6	6	6
Occupancy of Fe complex (%)	80	80	100
B-factor (Å^2)			
Overall protein	22	22	20
S112E (80/20)	20/16	23/16	25/15
K121A	17	17	14
E101Q	49	60	48
Fe complex	23	27	24
DPA	23	27	23
Fe	26	29	27
Distance Fe–Fe (Å)	10	10	10

Table 2.9 Best fits for EXAFS data for **1**. Fit k = 3–15 Å^{-1}

	Fe–N			Fe–O			Fe···C			GOF		
Fit	**N**	**R (Å)**	**σ²**	**N**	**R (Å)**	**σ²**	**N**	**R (Å)**	**σ²**	**ΔE$_o$**	**F**	**F'**
1	5	2.15	0.00386				4	3.01	0.00919	-9.63	145	38
							1	2.63	0.00612			

Table 2.10 Best fits for Fourier filtered EXAFS data for **1**. Fit k = 2–16 Å^{-1}

	Fe–N			Fe–O			Fe···C			GOF		
Fit	**N**	**R (Å)**	**σ²**	**N**	**R (Å)**	**σ²**	**N**	**R (Å)**	**σ²**	**ΔE$_o$**	**F**	**F'**
1	5	2.15	0.00403							-9.60	24	–

Table 2.11 Best fits for EXAFS data of **2**. Fit k = 3–12 Å^{-1}

	Fe–N			Fe–O			Fe···C			GOF		
Fit	**N**	**R (Å)**	**σ²**	**N**	**R (Å)**	**σ²**	**N**	**R (Å)**	**σ²**	**ΔE$_o$**	**F**	**F'**
1	5	2.07	0.00950				6	3.08	0.00639	-4.72	61	39
	1	1.81	0.00267									

Table 2.12 Best fits for Fourier filtered EXAFS data of **2**. Fit k = 2–14 Å^{-1}

	Fe–N			Fe–O			Fe···C			GOF		
Fit	**N**	**R (Å)**	**σ²**	**N**	**R (Å)**	**σ²**	**N**	**R (Å)**	**σ²**	**ΔE$_o$**	**F**	**F'**
1	5	2.07	0.00991							-5.11	47	–
	1	1.81	0.00294									

Table 2.13 K-edge and pre-edge area fits for **1** and **2**.

ArM	K-edge (eV)	Pre-edge area
1	7122.4	5.9
2	7123.1	13.0

CHAPTER 3

SEEING RED

Introduction

The binding of dioxygen and subsequent oxidation of substrates is a pivotal process in biology that is accomplished by several metalloproteins.[46,53,139,202,203] As discussed in Chapter 1, the mechanism of taurine dioxgenase (TauD) provides a clear example of how monooxygenases bind dioxygen, form an Fe^{IV}–oxido oxidant, and perform substrate oxidation.[9,142] While the formation of the Fe^{IV}–oxido species is well established, much less is known about the Fe–O_2 adducts that are formed upon initial dioxygen activation. In the postulated pathway for nonheme Fe proteins, the initial binding and reduction of dioxygen produces an Fe^{III}–superoxido species, after which the superoxido ligand is reduced once more to form an $Fe^{III/IV}$–peroxido species (details in Chapter 1: Figure 1.1B).[142] As further support for this mechanism, Ramaswamy and coworkers successfully trapped dioxygen bound side-on to Fe in the active site of napthalene dioxygenase (NDO), which is one of the only known details about this step.[204] In the absence of substrate, the dioxygen ligand

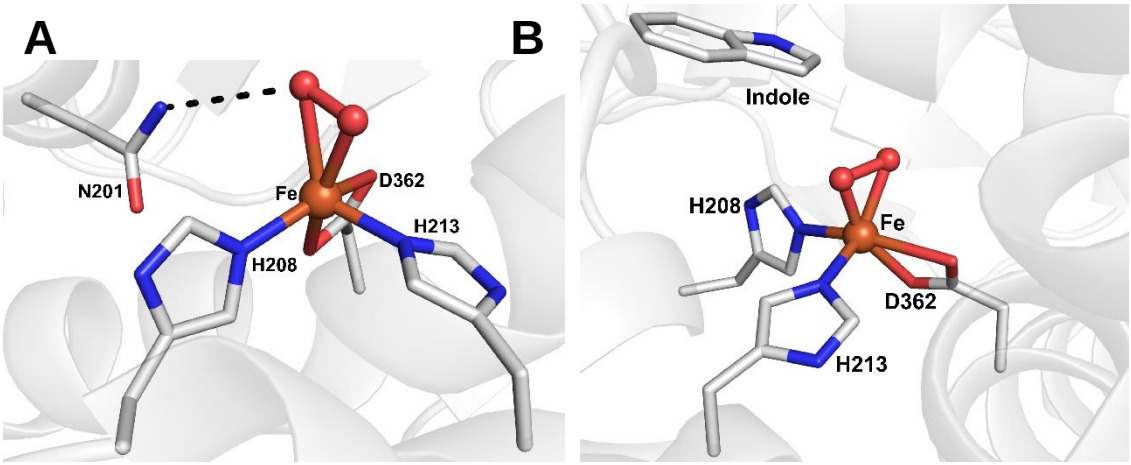

Figure 3.1 Molecular structures of side-on O_2 binding (**A**: PDB 1O7M) and asymmetric O_2 binding with substrate indole present (**B**: 1O7N) to the Fe active site in NDO. Possible H-bonding interaction is shown as a dashed black line.

coordinated in a symmetric fashion to the Fe center; however, when the substrates indole or naphthalene were present, the coordination mode of the Fe–O_2 unit changed slightly to asymmetric coordination (Figure 3.1). The dioxygen species was postulated to be a peroxido ligand based on an O–O bond distance of 1.4 Å, but there is no other data to support this claim. An asparagine residue (N_{201}) was also located within H-bonding distance to the bound dioxygen species and thus, could be involved in a water channel that delivers protons to the O_2 species (Figure 3.1).[204] Additionally, Lipscomb and coworkers successfully trapped three different intermediates in different subunits of the homotetrameric homoprotocatechuate 2,3-dioxgenase enzyme (2,3-HPCD).[205] In one subunit, dioxygen coordinated through symmetric side-on binding to the Fe center. This O_2 unit was proposed to be a superoxido ligand with an O–O bond distance of 1.34 Å (Figure 3.2).[205] In the next subunit, a bond formed between the substrate 4-nitrocatechol (4-NC) and the O_2 ligand to form an alkylperoxido intermediate with an O–O bond distance of 1.5 Å (Figure 3.2).[205] It is important to note that most of the evidence for initial dioxygen binding step in mononuclear nonheme Fe metalloproteins comes from structural work with little

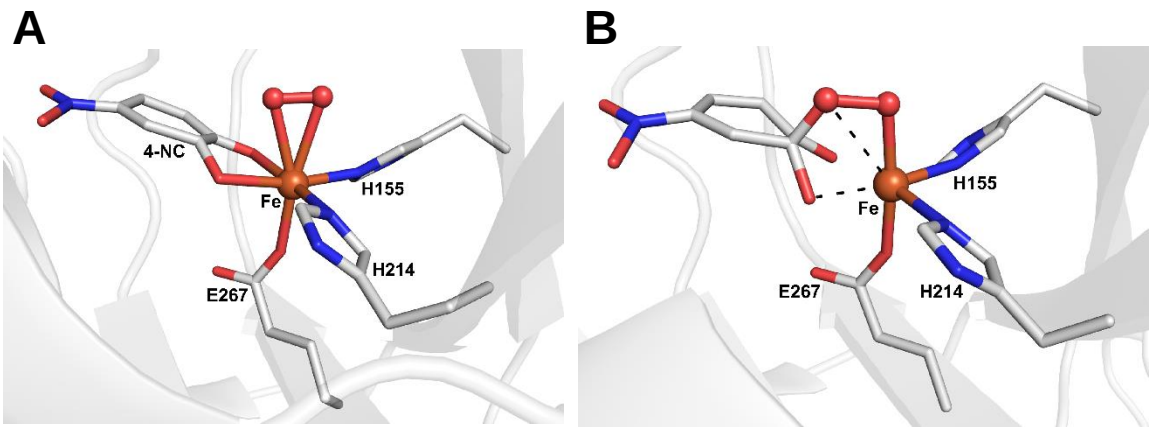

Figure 3.2 Molecular structures of side-on O_2 binding (**A**: PDB 2IGA-subunit C) and alkylperoxido binding (**B**: PDB 2IGA-subunit D) to the Fe active site in 2,3-HPCD.

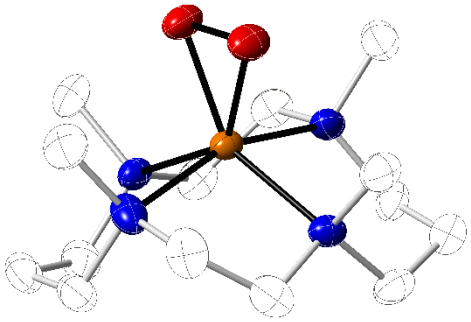

Figure 3.3 Molecular structure of the Fe^{III}–peroxido species from Nam.

spectroscopic evidence to corroborate the formation of Fe–O_2 adducts. As noted by Lipscomb, these structural findings make the assignment of the O_2 species as a peroxido or superoxido ligand difficult.

In addition to the work done in native proteins, synthetic complexes have been used to elucidate spectroscopic and structural features of dioxygen binding to an Fe center.[32,51,202,206–215,215–227] For example, Nam and coworkers crystallographically and spectroscopically characterized a mononuclear nonheme Fe^{III}–peroxido complex using the ligand TMC (1,4,8,11-tetramethyl-1,4,8,11-tetraazacyclotetradecane) and H_2O_2.[228] The molecular structure revealed an O–O bond distance of 1.463(6) Å and an average Fe–O bond distance of 1.910 Å (Figure 3.3). Nam reported that the addition of acid caused the absorbance feature of the Fe^{III}–peroxido complex at $\lambda_{max} \sim 782$ nm to convert to an absorbance feature at $\lambda_{max} \sim 526$ nm, corresponding to an Fe^{III}–hydroperoxido complex. The subsequent addition of base rapidly converted the species back to the Fe^{III}–peroxido complex.[228]

Artificial metalloproteins (ArMs) have also been utilized to study the initial stages of dioxygen activation. As mentioned in Chapter 1, Ménage and coworkers redesigned the nickel-binding protein NikA to include a synthetic Fe complex, FeL (L = *N*-benzyl-*N*'-(2-

hydroxybenzyl)-*N*,*N*'-ethylenediaminediacetic acid), that was able to catalyze intramolecular arene hydroxylation.[165] The FeL complex was stabilized in the NikA binding site by several H-bonding interactions and electrostatic interactions with nearby amino acid residues. Ménage used diffraction methods (X-ray diffraction, XRD) to monitor the reaction of single crystals of the FeL–NikA ArM with dioxygen at different time intervals, and structurally characterized four intermediates in the catalytic cycle, including an Fe–O_2 adduct (Figure 3.4).[165] The Fe–O_2 adduct bond distances are consistent with an end-on Fe–(hydro)peroxido species, but solution studies could not definitively elucidate the identity of the O_2 adduct as either a peroxido or hydroperoxido ligand.

To further investigate the nature of biologically relevant dioxygen binding to Fe, the Fe^{II}–ArM described in Chapter 2, [Fe^{II}(biot-et-dpa(OH_2)$_2$(κ^1-O_{E112})⊂2xM-S_{112}E-Sav] (**1**), was used as a synthon because the primary coordination sphere matches the 2-His-1-carboxylate facial triad found in α-ketoglutarate-dependent nonheme monooxygenases. This chapter describes the crystallographic and spectroscopic characterization of dioxygen binding to the Sav-based Fe^{II}–ArM in the presence of substrate.

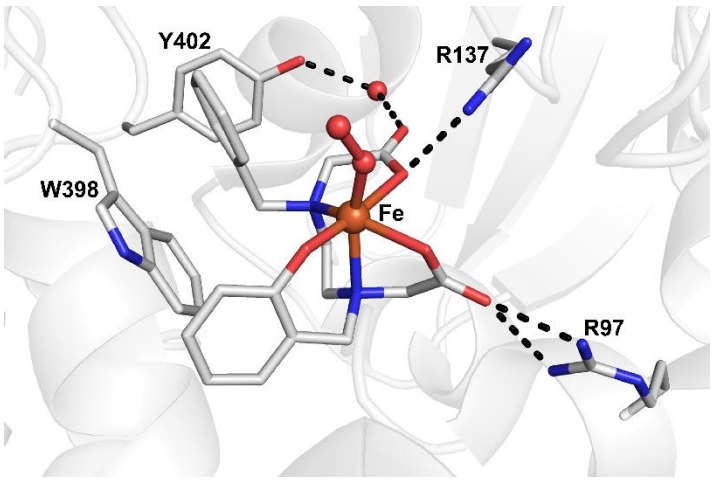

Figure 3.4 Molecular structure of the Fe–O_2 adduct in NikA (PDB 3MVY). H-bonds are shown as dashed lines.

Results and Discussion

Design Concepts. As described in Chapter 1, previous work in our group demonstrated the ability to trap a Cu^{II}–hydroperoxido species within Sav and regulate its reactivity or stability by modifying the H-bonding network that surrounds the Cu active site. Based on those Cu studies, the above Fe^{II}–ArM could analogously model the initial α-ketoglutarate cofactor and dioxygen binding stages that are seen in α-ketoglutarate-dependent monooxygenases. For these studies, a modified protein host, $K_{121}A$-$S_{112}E$-Sav, was used instead of the original protein 2xM-$S_{112}E$-Sav because the $E_{101}Q$ surface mutation of the original protein was not necessary to form the Fe^{II}–ArM.

Structural and solution studies of Fe^{II}–ArM. Initial attempts to prepare the Fe^{II}–ArM began with the biotinylated complex $[Fe^{II}(biot\text{-}et\text{-}dpa)(OH_2)_2]Br_2$ and the variant $K_{121}A$-$S_{112}E$-Sav to ensure that the coordination environment was the same that was found in in **1** (Chapter 2). The ArM containing the Fe^{II} complex, $[Fe^{II}(biot\text{-}et\text{-}dpa(OH_2)_2(\kappa^1\text{-}O_{E112})\subset K_{121}A\text{-}S_{112}E\text{-Sav}]$ (**3**), was prepared by incubating a solution of the complex in nanopure water with $K_{121}A$ -$S_{112}E$-Sav at pH 8 in phosphate buffer (50 mM). A 2-(4'-hydroxyazo-

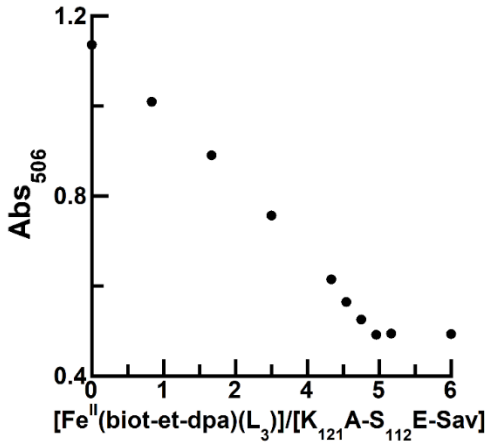

Figure 3.5 HABA titration of Fe^{II}-et-dpa in $K_{121}A$-$S_{112}E$-Sav.

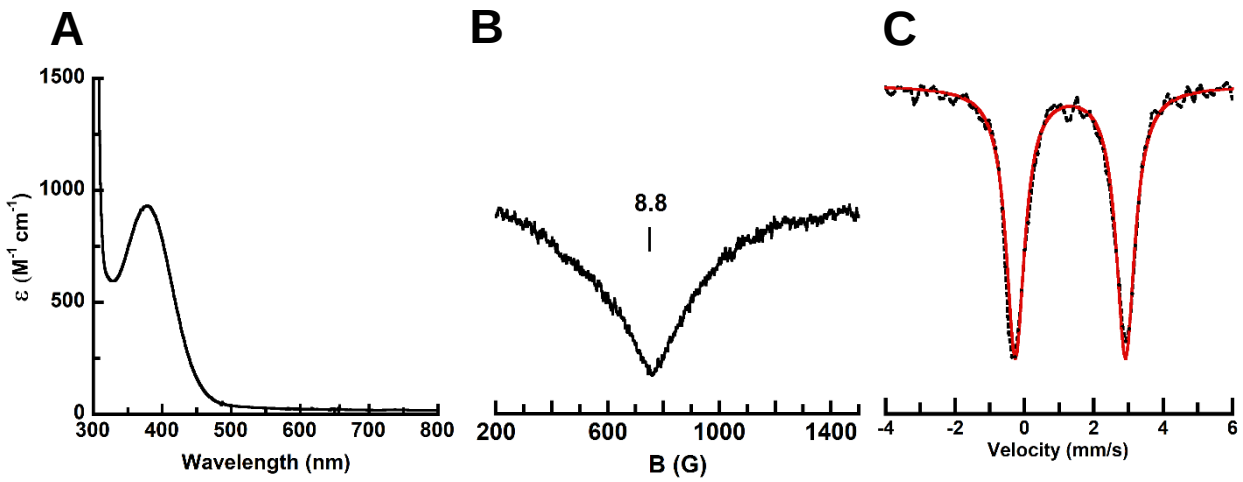

Figure 3.6 Electronic absorbance (**A**), EPR (**B**), and Mössbauer (**C**) spectra of **3** recorded in 50 mM phosphate buffer pH 8 at 4 °C, 10 K, and 4 K, respectively. Simulation is shown as a red line.

benzene)benzoic acid (HABA) assay, performed as described in Chapter 2, revealed stoichiometric binding of the biotinylated Fe^{II} complex to the protein host (Figure 3.5). The electronic absorbance spectrum revealed the same absorbance band at λ_{max} = 375 nm as seen in **1** (Figure 3.6A). Moreover, the parallel-mode (‖-mode) EPR spectrum of **3** exhibited

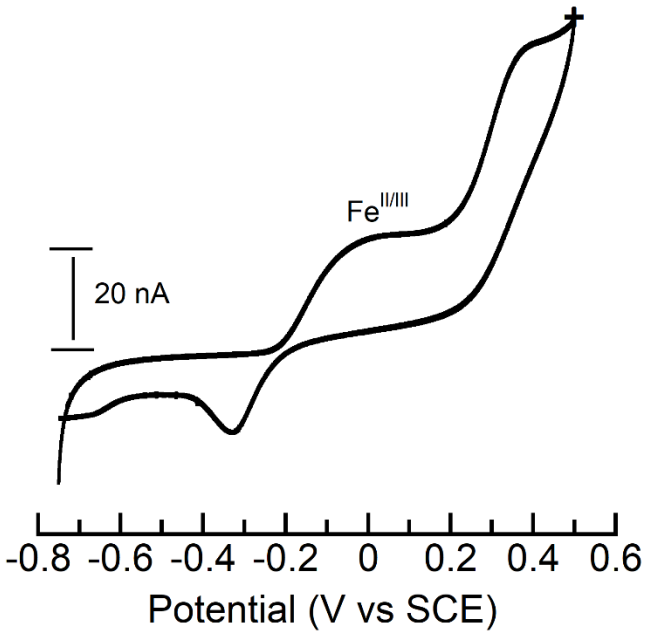

Figure 3.7 Cylic voltammagram of **3** recorded in 50 mM phosphate buffer pH 8: $Fe^{II/III}$ couple. Measurements were collected at room temperature with a scan rate of 2.5 mV/s.

a broad signal with a *g* value at 8.8, which is consistent with a high-spin Fe^{II} species with an *S* = 2 spin ground state and the same *g* value as seen in **1** (Figure 3.6B). Mössbauer spectroscopy was also used to characterize **3**, though it was not used to characterize **1**. The Mössbauer spectrum revealed an isomer shift (δ) of 1.32 mm/s and a quadrupole splitting (ΔE_Q) of 3.20 mm/s, which are also indicative of a high-spin Fe^{II} species (Figure 3.6C). Electrochemical data revealed a potentially quasi-reversible one electron redox couple at -163 mV vs SCE. The one electron event is thought to be the $Fe^{II/III}$ redox couple. The additional peak at more positive potentials could come from the phosphate buffer or a contaminant on the electrode (Figure 3.7). Additionally, the molecular structure, resolved to 1.40 Å, revealed that the coordination environment of **3** was similar to that in **1**, as predicted (Figure 3.8, Tables 3.1, 3.4, and 3.5).

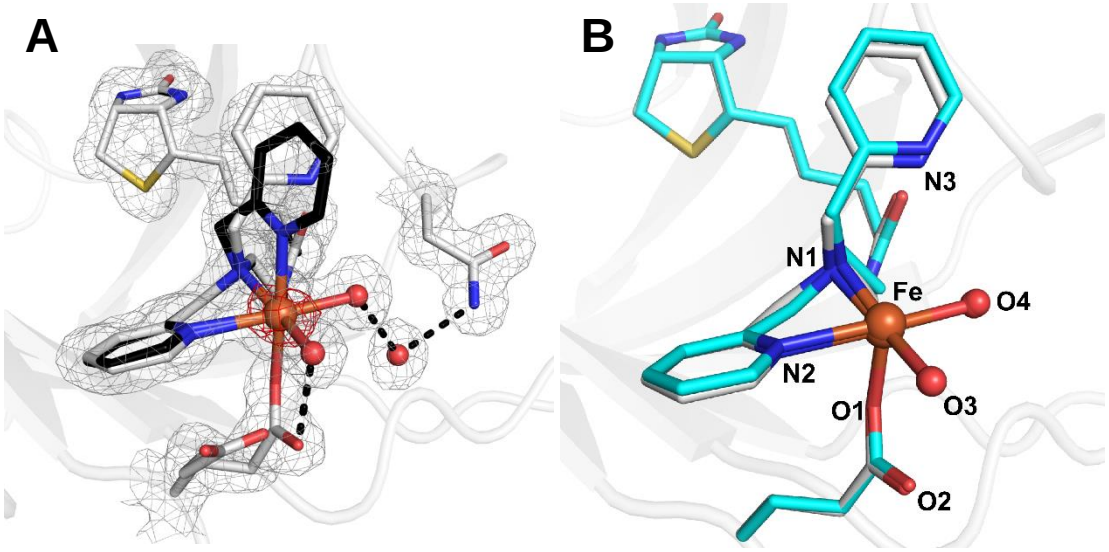

Figure 3.8 The molecular structures of **3** (**3a**: unbound, grey; **3b**: bound, black) (**A**) and the overlay of the molecular structures of **3a** (grey) and **1a** (cyan) (B). Fe ions are colored in orange, N atoms are in blue, and O atoms/water molecules are in red. H-bonds are shown as dashed black lines. The position of the Fe complex is indicated by the $2F_O$-F_C electron density map (grey, contoured at 1 σ) and anomalous difference density (red, contoured at 3 σ). H-bonds are shown in black dashed lines. The number schemes in **B** are the same as those in **A**.

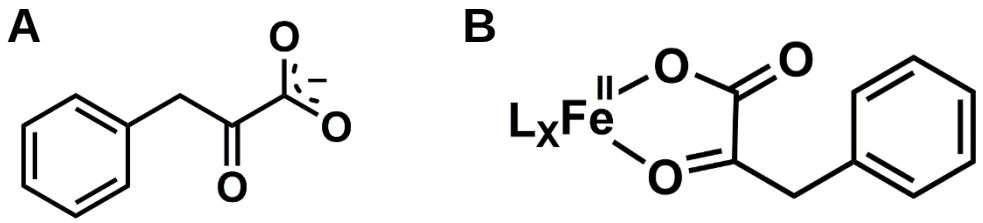

Figure 3.9 ChemDraw representation of phenylpyruvate (**A**) and common bidentate coordination of phenylpyruvate to an FeL complex (L = ligand) (**B**).

*Solution studies of phenylpyruvate binding to **3** (**3–phenylpyruvate**).* As described in Chapter 1, in the first step of the accepted mechanism of TauD, the cofactor α-ketoglutarate (α-KG) coordinates to the Fe^{II} center and the substrate taurine docks near the active site. To visualize this initial binding of α-KG in synthetic systems, many groups have utilized analogues of α-ketoglutarate that have an aromatic ring appended near the keto acid functional group. When the aromatic cofactor coordinates in a similar bidentate fashion as α-KG (Figure 3.9B), this appended aromatic ring gives rise to a distinct color change, with an absorbance feature between $\lambda_{max} \sim$ 400-650 nm caused by a low-energy Fe^{II}–α-keto carboxylate metal-to-ligand charge-transfer (MLCT) transition.[149,223,229–243] Thus, sodium phenylpyruvate (Figure 3.8A) was chosen as the cofactor for the current studies because the color change would provide a spectroscopic handle with which to monitor the binding of the keto acid analogue. In addition, phenylpyruvate contains a benzylic carbon that could be activated if **3** was able to perform the same type of oxidative chemistry as TauD.

Initial studies began by monitoring the addition of 20 equivalents of phenylpyruvate in a nanopure water solution to **3** in 50 mM phosphate buffer at pH 8. The only change that was observed in the spectrum was an increase in absorption intensity at 300 nm, which can be attributed to the absorbance associated with the addition of phenylpyruvate. No absorbance bands that could be associated with the coordination of phenylpyruvate to the Fe^{II} center, in the manner shown above, were observed (Figure 3.9B, 3.10A). EPR and

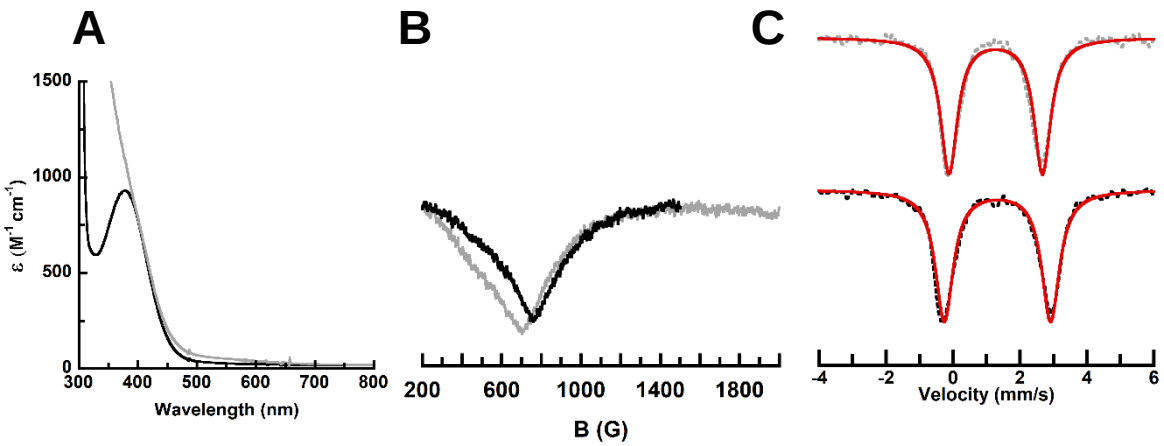

Figure 3.10 Electronic absorbance (**A**), EPR (**B**), and Mössbauer (**C**) spectra of **3–phenylpyruvate** recorded in 50 mM phosphate buffer pH 8 at 4 °C, 10 K, and 4 K, respectively. The initial spectrum is shown as a black line, and the final spectrum is shown as a grey line. Simulation is shown as a red line.

Mössbauer spectroscopies were then employed to investigate the fate of the added phenylpyruvate. In the ‖-mode EPR spectrum, the g = 8.8 feature shifted slightly to g = 9.4, suggesting a change in the primary coordination sphere around the Fe^{II} center, but this result still did not provide clarity about the location of the phenylpyruvate in **3** (Figure 3.10B). The Mössbauer spectrum showed a similar δ value of 1.28 mm/s as **3** but a slight change in the ΔE_Q value from 3.20 mm/s to 2.79 mm/s, which also indicates a small but not significant change to the Fe^{II} center (Figure 3.10C). These solution studies suggested that the addition of phenylpyruvate had a modest effect on **3** but did not correlate those effects to the location of phenylpyruvate within **3**.

*Structural characterization of **3–phenylpyruvate**.* XRD was performed to determine how phenylpyruvate interacted with the Fe^{II} complex in Sav. Single crystals were prepared by soaking crystals of **3** in a 20 mM solution of sodium phenylpyruvate. Analysis of the resulting crystals, which diffracted to a 1.31 Å resolution, revealed the formation of a mononuclear Fe complex where the dpa ligand, the carboxylate side chain of $S_{112}E$, and the two *cis* aquo ligands coordinated in the same positions as found in **1b** in the bound state (Chapter 2, Figure 2.7C). No additional density was observed near the Fe center to indicate that the phenylpyruvate was coordinated. However, as described in Chapter 1, Sav is a tetramer that assembles as a dimer of dimers. Examination of the full space formed by the dimer of Sav revealed new electron density at the interface of the dimer vestibule. This electron density was modelled as a disordered phenylpyruvate molecule (Figure 3.11, Table 3.1, 3.4, and 3.5). Thus, the structure revealed that phenylpyruvate docked between the two Fe complexes within a Sav dimer. A π-stacking interaction with an average $centroid_{py}\cdots centroid_{ph}$ distance of ~4.60 Å occurred between the pyridine rings of the dpa

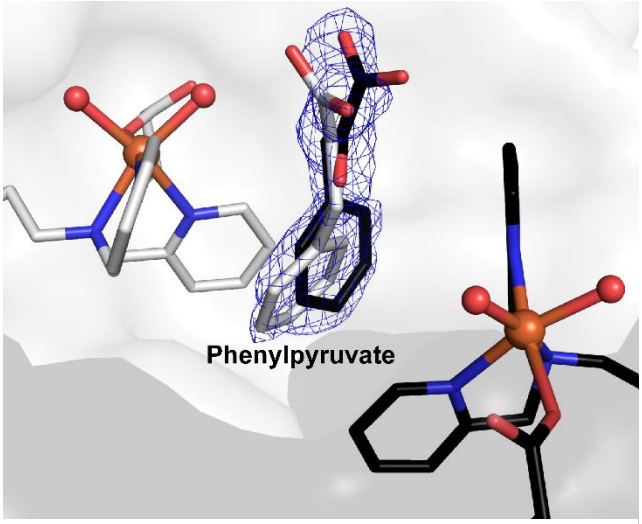

Figure 3.11 Molecular structure of **3–phenylpyruvate**. Fe ions are shown in orange, N atoms are in blue, and O atoms/water molecules are colored in red. The position of the phenylpyruvate is indicated by the $2F_o$-F_c electron density map (blue, contoured at 1 σ).

ligand and the phenyl ring of phenylpyruvate. Moreover, these π-stacking interactions involve the pyridine groups that were unbound in **1a**; the addition of phenylpyruvate appears to promote complete coordination of the dpa ligands. Furthermore, the crystallography data offers an explanation for the subtle changes in the solution spectroscopy data, in which phenylpyruvate docking does result in a structural change to the Fe^{II} species from 5- to 6-coordinate.

The molecular structure revealed that although phenylpyruvate does not coordinate to the Fe center within Sav, it docks ~4 Å from it. However, this distance does not preclude further reactivity, as shown in TauD, where the substrate taurine docks through noncovalent interactions ~ 5 Å from the Fe center and still undergoes C–H bond activation. Thus, while phenylpyruvate does not coordinate to the Fe center, it is possible that phenylpyruvate is poised to undergo C–H oxidation.

*Solution studies of dioxygen binding to **3–phenylpyruvate (3–phenylpyruvate–O$_2$).*

In order to test whether **3–phenylpyruvate** could bind dioxygen or perform C–H bond

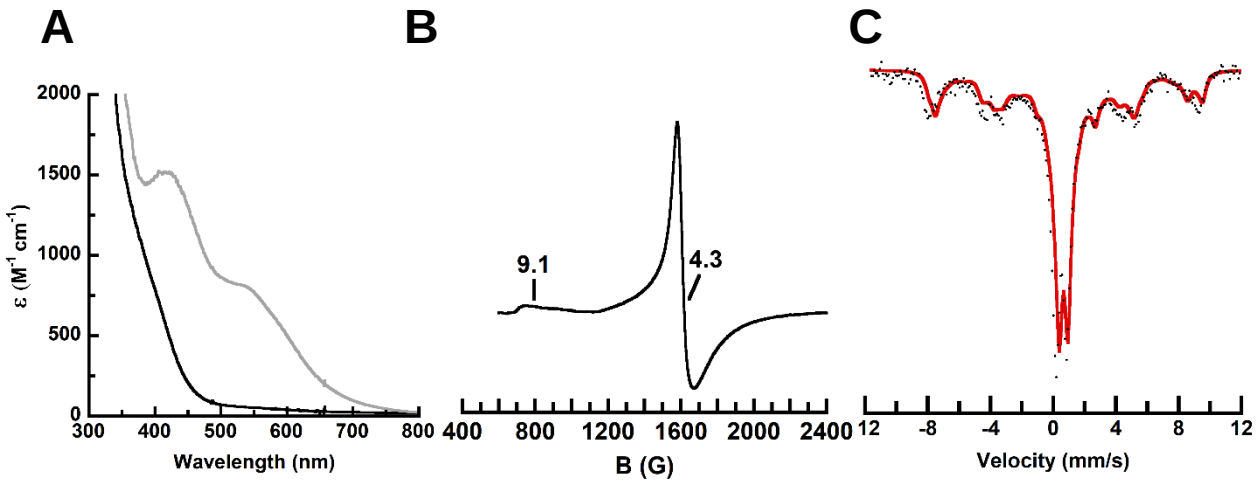

Figure 3.12 Electronic absorbance (**A**), EPR (**B**), and Mössbauer (**C**) spectra of **3–phenylpyruvate** recorded in 50 mM phosphate buffer pH 8 at 4 °C, 10 K, and 4 K, respectively. For the electronic absorbance spectra, the initial spectrum is shown as a black line, and the final spectrum is shown as a black line. Simulation is shown as a red line.

activation similar to that seen in native nonheme Fe monooxygenases, excess dioxygen was added to **3–phenylpyruvate** and the resulting changes were monitored by electronic abosrbance, EPR, and Mössbauer spectroscopies. It is worth noting that without phenylpyruvate present, the reaction of adding excess dioxygen to **3** gives different spectroscopic results than described below (details in Appendix B). The addition of excess dioxygen to **3–phenylpyruvate** at 4 °C produced a red solution with two new absorbance features at $\lambda_{max} \sim 420$ and 540 nm (Figure 3.12A). EPR spectroscopy revealed the loss of the $g = 9.4$ signal in the ∥-mode EPR spectrum and the evolution of a new ⊥-mode EPR spectrum with g values at 9 and 4.3, indicative of a high-spin Fe^{III} species with a ground spin state of $S = 5/2$ (Figure 3.12B). The disappearance of the ∥-mode EPR signal was complete after 120 minutes. Quantitation of the ⊥-mode EPR spectrum indicated that the $g = 9$ and 4.3 signal accounted for 15% of the reported Fe concentration, suggesting there could be an EPR-silent species present. Mössbauer spectroscopy was then performed on the completed reaction to investigate the identity of the Fe species present. The resulting spectrum showed that 55% of the Fe was represented by a 6-line hyperfine splitting pattern with $\delta = 0.56$ mm/s and $\Delta E_Q = 0.53$ mm/s, indicative of a high-spin mononuclear Fe^{III} species (Figure 3.12C). These Mössbauer parameters are comparable to those of known high-spin Fe^{III}–peroxo complexes in the literature, such as the side-on Fe^{III}–(η^2)–peroxo prepared by Latour and coworkers, which had the parameters $\delta = 0.65$ mm/s and $\Delta E_Q = 0.72$ mm/s.[224] Thus, the Mössbauer and EPR parameters for the high-spin mononuclear Fe^{III} species could be suggestive of the formation of an Fe^{III}–peroxido species within Sav. An additional doublet signal corresponding to 40% of a coupled $Fe^{III}\cdots Fe^{III}$ species was observed in the Mössbauer spectrum with an $\delta = 0.53$ mm/s and $\Delta E_Q = 0.70$

mm/s. (Figure 3.12C). High-field Mössbauer studies showed weak antiferromagnetic coupling between the two Fe centers across the Sav dimer with a *J* value less than 1 cm^{-1}. One possible explanation for the doublet signal in the Mössbauer spectrum is that the Fe centers are coupled through the phenylpyruvate π-stacking interaction across the Sav dimer. A Mössbauer time course study was done to understand why the reaction takes 120 min to complete and if there were any intermediates formed during the course of the reaction. The time course revealed that upon dioxygen addition, two new species formed: one with parameters indicative of a high spin mononuclear Fe^{III} and one for a weakly coupled $Fe^{III}\cdots Fe^{III}$ species. During the time course, these two species continued to grow in while the Fe^{II} starting complex decreased. At 120 min the reaction completed and the Fe^{II} species completely disappeared. The final Mössbauer spectrum from the time course (120

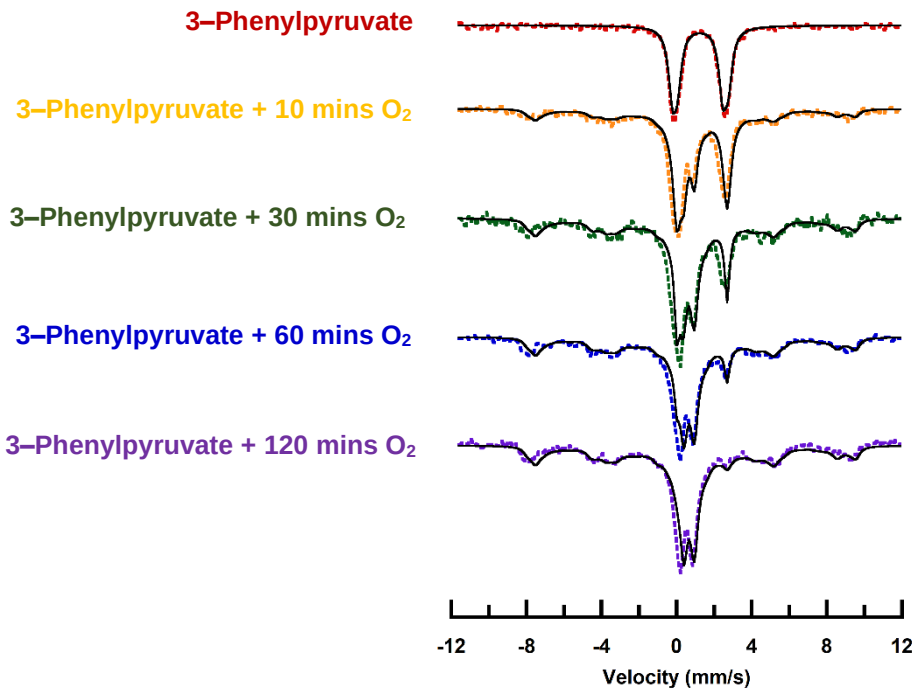

Figure 3.13 Timecourse Mössbauer study on **3–phenylpyruvate** with different exposure times to O_2.

min) was comparable to the independently prepared sample (Figure 3.12C, 3.13: purple); however, no other intermediates were observed.

Another spectroscopic study was performed to determine the effects of additional phenylpyruvate on the reaction of **3–phenylpyruvate** and dioxygen. From the studies with 20 equivalents of phenylpyruvate, the spectroscopic and crystallographic data supports that phenylpyruvate docks weakly near the Fe complexes. Additionally, phenylpyruvate is important for the reaction because adding dioxygen without phenylpyruvate present gives different spectroscopic results (details in Appendix B). Electronic absorbance, EPR, and Mössbauer spectroscopies were utilized to study the changes in **3–phenylpyruvate–O_2** in the presence of varying equivalents of phenylpyruvate. Electronic absorbance experiments performed with increasing equivalents of phenylpyruvate and constant amounts of **3** and dioxygen revealed significant increases in the two absorbance bands at $\lambda_{max} \sim 420$ and 540 nm (Figure 3.14A). Using 100 equivalents of phenylpyruvate showed the largest absorbance, suggesting more phenylpyruvate is necessary to drive the equilibrium of the reaction. Because 100 equivalents of phenylpyruvate was observed to have the largest effect on the reaction, EPR and Mössbauer spectroscopy were also used to the analyze this reaction. EPR spectroscopy again revealed a $\perp$-mode EPR spectrum with g values at 9 and 4.3, indicative of a high-spin mononuclear Fe^{III} species with a ground spin state of $S = 5/2$. In comparison to the EPR spectrum using 20 equivalents, the g values are the same but the quantification of the high-spin mononuclear Fe^{III} species increased from 15% to 50% (Figure 3.14B). Similarly, the Mössbauer spectrum revealed a high-spin mononuclear Fe^{III} species with $\delta = 0.55$ mm/s and $\Delta E_Q = 0.52$ mm/s and a weakly coupled $Fe^{III}\cdots Fe^{III}$ species with $\delta = 0.50$ mm/s and $\Delta E_Q = 0.85$ mm/s. The Mössbauer parameters are comparable

between the reactions with 20 and 100 equivalents of phenylpyruvate, but the quantitation of the species is different. With 100 equivalents of phenylpyruvate, the mononuclear Fe^{III} species increased from 55% to 84% and the weakly coupled $Fe^{III}\cdots Fe^{III}$ species decreased from 44% to 12% (Figure 3.14C). These experiments indicated that the red color produced after the addition of O_2 became more intense with increasing amounts of phenylpyruvate, and the Fe center became mostly a high-spin mononuclear Fe^{III} species. Based on the EPR and Mössbauer studies performed, phenylpyruvate weakly docks within Sav via π-stacking interactions, and more phenylpyruvate is necessary to drive the equilibrium of **3** towards the proposed Fe^{III}–O_2 species.

In collaboration with the Möenne-Loccoz lab, resonance Raman (rR) spectroscopy was utilized to further elucidate the identity of an O_2 species within Sav. Samples were prepared analogously to those prepared for the previously described EPR and Mössbauer studies. The rR studies showed no resonance-enhanced vibrations at any of the excitation wavelengths used, indicating that the absorbance features causing the red color of the

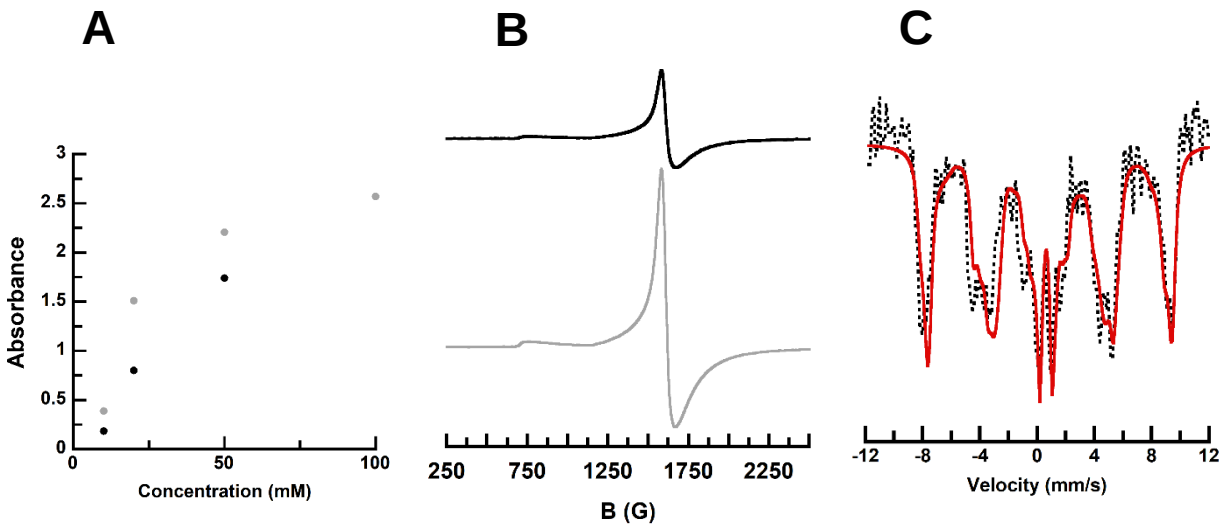

Figure 3.14 Plot of absorbance (420 nm – grey; 540 nm – black) versus increasing concentration of phenylpyruvate (**A**), EPR spectra with 20 (black) and 100 (grey) equivalents of phenylpyruvate (**B**), and Mössbauer spectra of **3–phenylpyruvate–O_2** with 100 equivalents of phenylpyruvate. Simulation is shown in red.

solution may not be associated with an Fe^{III}–peroxido species. Because the absorbance bands that gave rise to the red color were not resonance enhanced, it is possible that those absorbance bands are not associated with an Fe–O_2 adduct. Fe^{III}–(hydro)peroxo complexes often have absorbance features between λ_{max} ~ 500-600 nm and are resonance enhanced with vibrations near ν_{O-O} ~ 800 cm^{-1}.[51,203,206,215,219,228,244–247] One explanation is that the red color is not associated with the Fe species, and rather, it is associated with a product from a reaction. With this idea, the absorption data collected, as detailed above, is limited to 30 second intervals; if an intermediate was formed before 30 seconds when the red color is present, stopped-flow electronic absorbance spectroscopy would be able to detect it. Therefore, stopped-flow electronic absorbance experiments were performed to monitor the addition of dioxygen to **3–phenylpyruvate** on the millisecond time scale. Monitoring the reaction by stopped-flow spectroscopy at room temperature showed the growth of two new absorbance bands at λ_{max} ~ 320 and 535 nm at 500 ms (Figure 3.15). After 1 second, the absorbance bands seen previously at λ_{max} ~ 420 and 540 nm begin to grow in over the λ_{max} ~ 320 and 535 nm absorbance bands. Based on the results of the stopped-flow

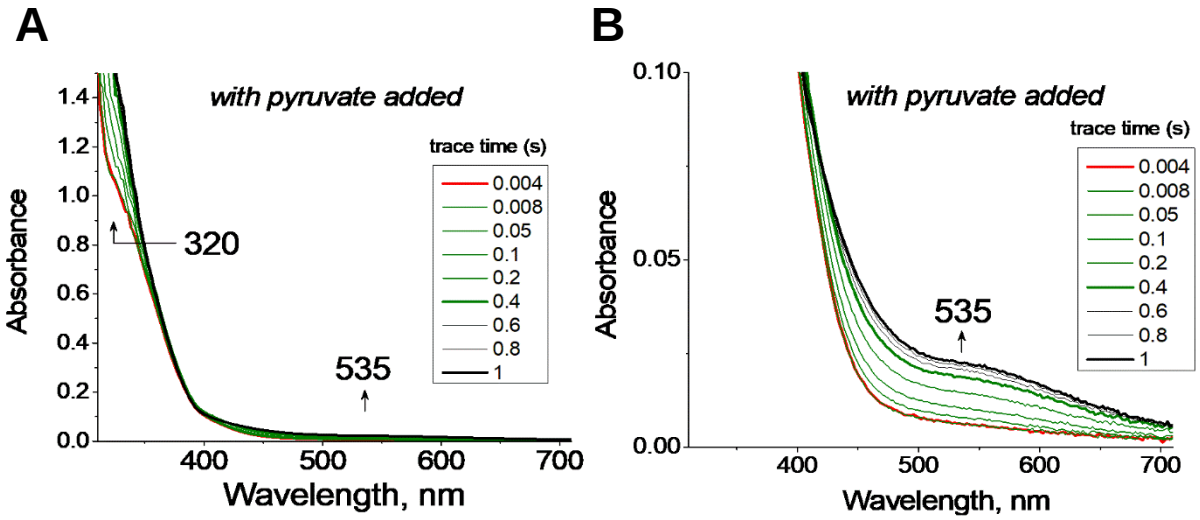

Figure 3.15 Stopped flow electronic absorption spectra of reaction of **3–phenylpyruvate** with O_2 (**A**) and zoom of low-energy region (**B**). Recorded in 50 mM phosphate buffer pH 8 at room temperature (RT).

experiment, freeze-quench samples for rR experiments were prepared at various millisecond-to-second timepoints to form the first species (λ_{max} ~ 320 and 535 nm) without forming the second red species (λ_{max} ~ 420 and 540 nm). Additionally, ^{16}O- and ^{18}O-labelled samples were prepared at ~0.5 mM Fe at room temperature (RT). However, analysis of these samples by rR in search of an isotopically sensitive resonance-enhanced vibration is still ongoing.

In crystallo studies of ***3–phenylpyruvate–O2.*** To provide further evidence that an Fe^{III}–peroxido species forms, single crystals of **3–phenylpyruvate** were soaked in an O_2-saturated buffer. The molecular structures of several different crystals indicated that O_2 can coordinate to the Fe center; however, different soaking times of the **3–phenylpyruvate** crystals produced different modes and places of O_2 coordination to the Fe center.

Analysis of the crystals subjected to short soaking times (0-30 minutes: **Structure 3C**, resolved to 1.70 Å) revealed a similar primary coordination sphere to that of **3**. There were two confirmations for the dpa ligand modelled, 70% bound and 30% unbound to the

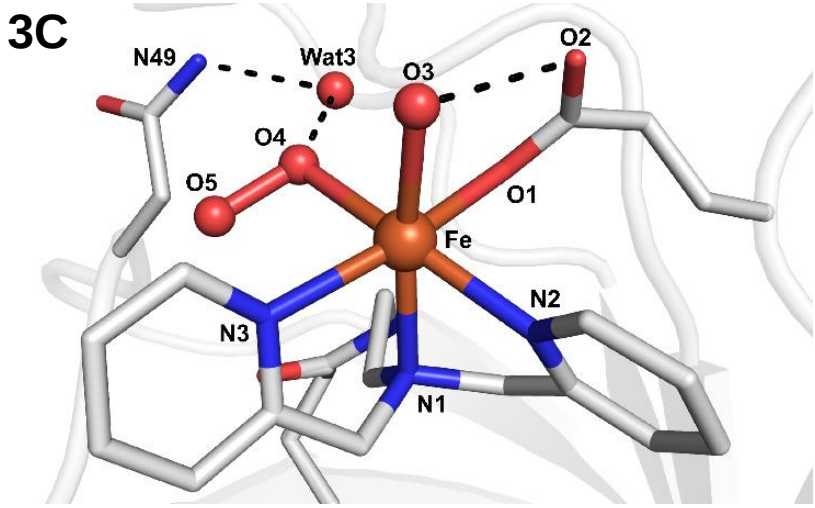

Figure 3.16 Molecular structure of **3–phenylpyruvate–O_2** (**3C**). Fe ions are shown in orange, N atoms are in blue, and O atoms/water molecules are colored in red. H-bonds are shown as black dashed lines.

Fe center. Additionally, there were two confirmations modelled with the glutamate residue side chain, with 80% bound and 20% unbound to the Fe center. However, elongated density was observed in the place of one of the aquo ligands, and was modelled as an O_2 unit with 90% occupancy. The O_2 ligand is coordinated end-on to the Fe center with Fe–O4 and Fe–O5 bond distances of 2.29 Å and 2.94 Å, respectively, and an O3–O4 bond distance of 1.47 Å. Additional H-bonding interactions formed between O3 and a nearby structural water molecule (Wat2) that is also H-bonded to the residue associated with N_{49}. O2 also participates in a H-bond to O5 of the carboxylate of $S_{112}E$, as seen in **3** (Figures 3.16 and 3.21, Tables 3.2, 3.6, and 3.7).

At intermediate soaking times (30-60 minutes: **Structure 3D**), the Fe structures in the four subunits of the tetrameric Sav are not equivalent with a mixture of aquo and

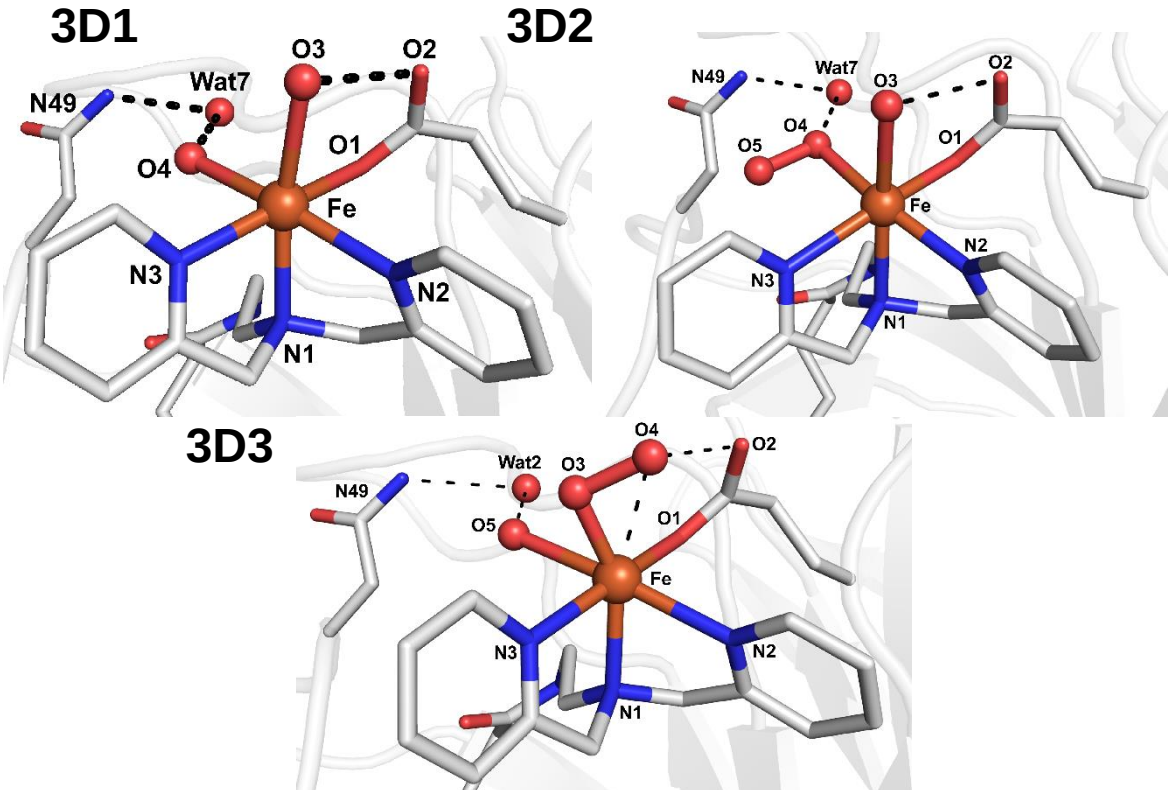

Figure 3.17 Molecular structure of **3–phenylpyruvate–O_2** (**3D1; 3D2**; **3D3**). Fe ions are shown in orange, N atoms are in blue, and O atoms/water molecules in red. H-bonds are shown as black dashed lines.

dioxygen ligands. As an example, one crystal resolved to 1.45 Å (Figure 3.17, 3.22, and 3.23, Tables 3.3, 3.8, and 3.9), the one subunit (**Structure 3D1**) contained a similar primary coordination sphere as **3–phenylpyruvate**, with two *cis* aquo ligands coordinated to the Fe center. In the next subunit (**Structure 3D2**), the density was fit to an end-on O_2 species similar to that in **Structure 3C** with 80% occupancy. In the final two Sav subunits (**Structures 3D3 and 3D4**), elongated density was observed in the equatorial plane of the Fe center and was modelled to an O_2 unit. This O_2 unit is asymmetrically coordinated to the Fe center with average Fe–O3 and Fe–O4 bond distances of 1.85 and 2.48 Å, respectively. Additionally, O3 is displaced towards O2 of the carboxylate side chain of $S_{112}E$ with an O2···O4 average distance of 2.80 Å. It is possible that the O_2 unit is displaced towards the carboxylate side chain because it is participating in a H-bonding interaction. The new electron density in this structure was modelled with a peroxido ligand, but it is not possible to further assign it as a hydroperoxido or peroxido ligand based on crystallography alone. Both types of ligand are possible, but if the O_2 species does indeed participate in a H-bonding interaction with the carbonyl of the glutamate residue as suggested by the displacement of O4 towards O2 in the molecular structure, it is reasonable to suspect that the O_2 species is likely a hydroperoxido ligand. The primary coordination sphere of the Fe center is completed by an aqua ligand (O5), causing the Fe active site to be 7-coordinate. Additionally, O5 participates in a H-bonding interaction with Wat2, which H-bonds to the residue group of N_{49}.

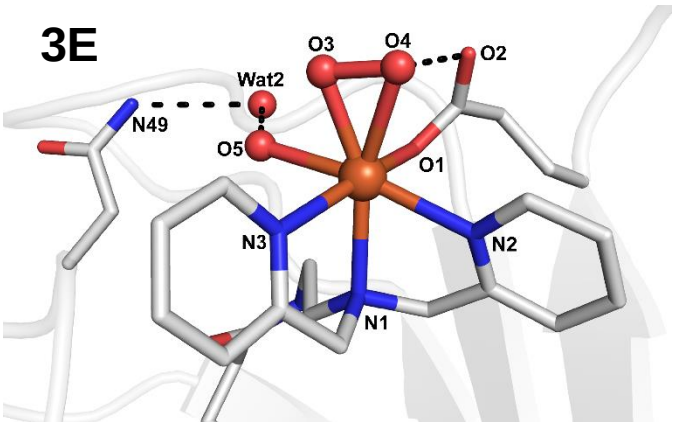

Figure 3.18 Molecular structure of **3–phenylpyruvate–O_2** (**Structure 3E)**. Fe ions are shown in orange, N atoms are in blue, and O atoms/water molecules in red.

After longer soaking times (60-180 minutes: **Structure 3E**), the molecular structure, resolved to 1.55 Å, revealed an O_2 unit coordinated asymmetrically to the Fe center, similar to the confirmation observed in **Structure 3D3** (Figure 3.18 and 3.26, Tables 3.2, 3.6, and 3.7). However, unlike in the Sav tetramer of **3D** in which a mixture of O_2 coordination modes was observed, all four subunits of Sav in **Structure 3E** have an asymmetrically coordinated O_2 unit that is displaced towards O5 of the carboxylate group from $S_{112}E$ (**Structure 3E**: Figure 3.18). The Fe–O3 and Fe–O4 bond distances are 2.09 Å and 2.32 Å, respectively, and the O3–O4 bond distance is 1.44 Å. The other open coordination site is occupied by a water ligand (O5) that participates in a H-bonding interaction with Wat2 and the residue group of N_{49}. Finally, the O_2 unit is skewed out of the equatorial plane with an O2···O4 distance of 2.78 Å. In each of these structures, there is electron density in the F_o-F_c map that could be modelled to phenylpyruvate in the same location as where it was found in **3–phenylpyruvate**; however, because of the disorder in the density, it is not possible to determine if the phenylpyruvate has been chemically modified. Regardless of if phenylpyruvate has been chemically modified, the density was found in the same location

as was found in **3–phenylpyruvate**, which can support the Mössbauer results that indicate the presence of an $Fe^{III}\cdots Fe^{III}$ species with weak coupling.

The reason for the change in binding modes and location of the O_2 unit to the Fe center are still under investigation. However, one possible reason is because that the initial location of O_2 binding is sterically controlled. The phenylpyruvate is docked between the two Fe complexes and blocking the coordination site in the equatorial plane of the Fe complex (Figure 3.19). If a reaction is occurring, it is possible that the O_2 unit is involved in the reaction and then once it is completed, the phenylpyruvate is no longer blocking the final coordination site. Furthermore, there is a significant amount of disorder present in the shorter exposure time structures with the dpa ligand and the glutamate residue having two confirmations modelled; whereas, at the longer exposure times, there is not disorder in the

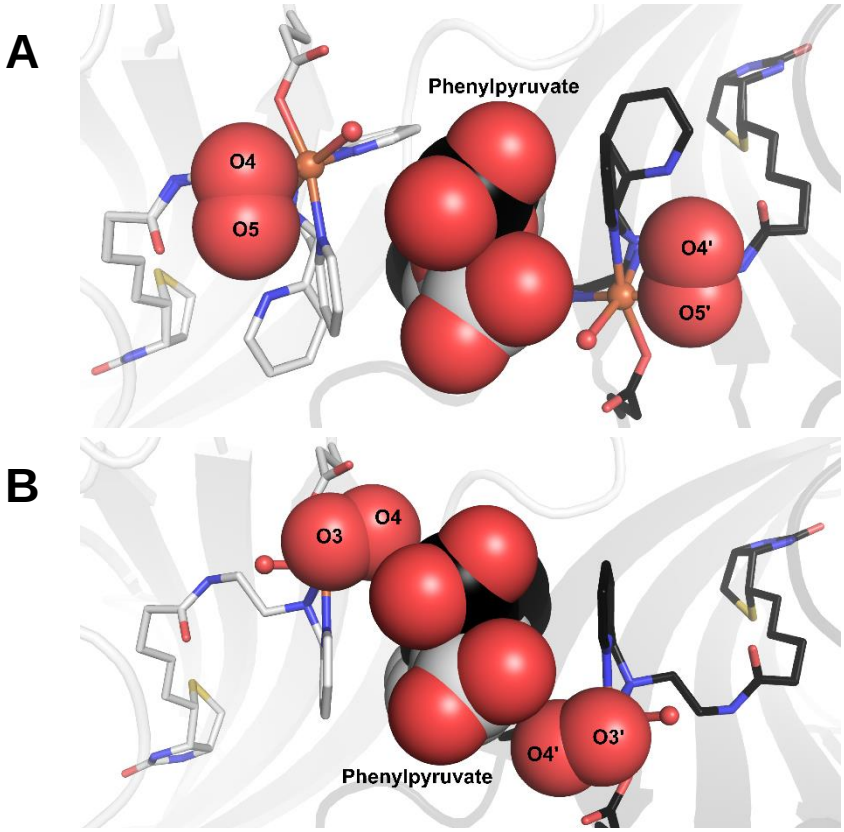

Figure 3.19 Space-filling model of **3C** (**A**) and **3E** (**B**). Fe ions are colored in orange, N atoms are in blue, and O atoms/water molecules are in red.

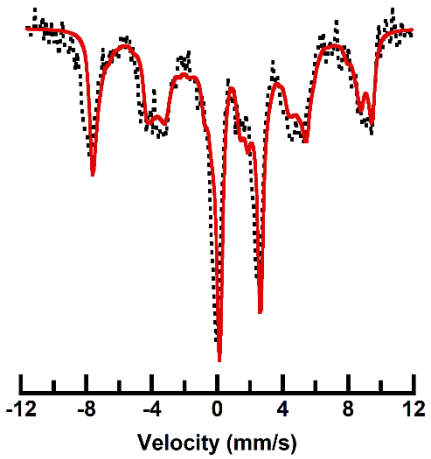

Figure 3.20 Mossbauer spectrum of crystalline **3–phenylpyruvate–O_2.** The spectrum was recorded at 4 K in 50 mM phosphate buffer pH 8.

active site, the dpa ligand and the glutamate are coordinated 100% to the Fe center. It is possible that as the O_2 ligand moves to the final coordination site, the Fe active site becomes more ordered.

To help elucidate the identity of the O_2 unit produced at long soaking times, *in crystallo* Mössbauer studies were performed. The crystalline Mössbauer sample was prepared by soaking crystals of **3–phenylpyruvate** in O_2-saturated buffer for 2 hours. The Mössbauer spectrum showed a 6-line hyperfine splitting pattern with parameters $\delta = 0.56$ mm/s and $\Delta E_Q = 0.53$ mm/s that accounted for 70% of the sample (Figure 3.20). The remaining 30% of the sample was unreacted Fe^{II} complex. The Mössbauer spectrum of the crystalline sample had similar parameters to those obtained from the solution studies; however, no coupled $Fe^{III}\cdots Fe^{III}$ species was present in the crystalline sample. It is possible that during sample preparation, extensive washing steps of the crystals removed the weakly coordinating phenylpyruvate/product. The major species in the crystalline sample was a high-spin Fe^{III} species with comparable parameters to those of a high-spin Fe^{III}–peroxo species.

To assess the red color, the protein was separate from the solution using centrifugal filtration. The filtrate was red in color, indicating it may not be associated with the Fe species in **3–phenylpyruvate–O2**. Nuclear magnetic resonance (NMR) and mass spectrometry analyses of the red filtrate indicated that phenylpyruvate is the major species present. More experiments are necessary to better determine the identity of the red species, as well as the cause of the observed changes with variable amounts of phenylpyruvate.

Summary and Conclusions

In this chapter, phenylpyruvate was shown to dock in the Sav vestibule in **3** via a π-stacking interaction, and the resulting mononuclear Fe^{II} ArM **3–phenylpyruvate** was shown to bind dioxygen. Molecular structures from XRD measurements revealed that dioxygen coordinates to the Fe center and that its binding confirmation is dependent on the length of exposure. At shorter dioxygen exposure times, dioxygen coordinates end-on to the Fe center. At intermediate dioxygen exposure times, a mixture of aqua, end-on dioxygen, and asymmetrically bound dioxygen ligands are observed on the Fe center. At longer dioxygen exposure times, the dioxygen exclusively coordinates asymmetrically to the Fe center. Mössbauer studies of solution-based samples showed that the reaction is complete at approximately 120 min, and thus, the species giving rise to the final spectrum may correspond to the molecular structure obtained from longer exposure times (**Structure 3E**) where dioxygen is coordinated asymmetrically to the Fe center. Additionally, ΔE_Q values of 0.53 and 0.52 mm/s measured for Mössbauer samples prepared with 20 and 100 equivalents of phenylpyruvate, respectively, are comparable to the ΔE_Q value of known high-spin Fe^{III}–peroxo species in the literature.[224] The EPR results also

support the formation of a high-spin mononuclear Fe^{III} species. The O–O bond length further supports the Fe^{III}–peroxo assignment of the Fe–O_2 species. However, future experiments are needed to determine the fate of phenylpyruvate and the origin of the red species.

Experimental Details

General Methods. All commercially available reagents were obtained in the highest possible purity and used as received. Acetonitrile (CH_3CN) and diethyl ether were degassed with argon and dried by vacuum filtration through activated alumina according to the procedure by Grubbs.[183] Triethylamine was distilled from KOH. Thin-layer chromatography (TLC) was performed on Merck 60 F254 aluminum-backed silica plates or Merck 60 F254 glass-backed basic aluminum oxide plates. Eluted plates were visualized using UV light. Silica or basic alumina gel chromatography was performed with the indicated solvent system using Fisher reagent silica gel 60 (230-400 mesh) or Sigma reagent Brockmann 1 basic aluminum oxide 58 (150 mesh). Biotin pentafluorophenol ester (biot-PFP)[184] and di-(2-picolyl)amine[185] were prepared according to literature procedures.

Physical Methods

Instrumentation. Mass spectra were measured on a MicroMass AutoSpec E, a MicroMass Analytical 7070E, or a MicroMass LCT Electrospray instrument. Electronic absorbance spectra were recorded with a Cary 50 or 8453 Agilent UV-vis spectrophotometer. X-band (9.64 GHz and 9.32 GHz) EPR spectra were recorded on a Bruker spectrometer equipped with Oxford liquid helium cryostats. The quantification of all signals is relative to a CuEDTA spin standard. The concentration of the standard was derived from an atomic absorption standard (Aldrich). For all instruments, the microwave frequency was calibrated with a

frequency counter and the magnetic field with an NMR gaussmeter. A modulation frequency of 100 kHz was used for all EPR spectra. The EPR simulation software (SpinCount) was written by our collaborating author, Michael P. Hendrich.[186] Mössbauer spectra were recorded with a Janis Research Super-Varitemp dewar. Isomer shifts are reported relative to Fe metal at 298 K. Stopped-flow experiments were performed with an SX20 apparatus (Applied Photophysics) with a 1-cm path length cell at room temperature inside an anaerobic glovebox. Stock solutions of the Fe^{II} protein were prepared to obtain a final concentration of 0.5 mM in phosphate buffer, pH 8. Oxygenated solutions at 50 mM in the same buffer were prepared in 1.2 mL glass vials capped with septa and were used immediately. After each experiment, remaining premixed solutions were recovered from the stopped-flow apparatus to confirm the concentration of the reactants. Cyclic voltammetry was performed on a Pine WaveDriver 10 potentiostat and the data was analyzed using After Math.

Preparative methods

biot-et-dpa and $[Fe^{II}(\text{biot-et-dpa})(OH_2)_2]Br_2$ were prepared as described in Chapter 2.

Spectroscopic methods

HABA Titrations. To 2.4 mL of 8 μM Sav in 200 mM sodium phosphate buffer at pH 7 was added 300 μL of a 10 mM 2-(4′-hydroxyazobenzene)benzoic acid (HABA) solution in 200 mM phosphate buffer pH 7. After 5 min of equilibration, the absorbance at 506 nm was recorded. A solution of 1 mM Fe complex in nanopure water was added in 4-20 μL portions until approximately 4 equivalents had been added. The absorbance at 506 nm was recorded until no further changes in intensity were observed.

Electronic Absorption Studies. A solution of lyophilized protein (250 μM) was prepared in nanopure water. Four equivalents of Fe complex (1 mM) in nanopure water were added to the protein solution. Samples were prepared in a final volume of 500 μL containing 50 mM potassium phosphate buffer at the indicated pH. For phenylpyruvate samples, 10, 20, 50, or 100 equivalents of phenylpyruvate (10, 20, 50, or 100 mM) in nanopure water were added to the sample after **3** was prepared. For O_2 samples, 5 mL of O_2 was added by gas-tight syringe after the sample was prepared.

EPR Studies. A solution of protein (500 μM) was prepared in nanopure water. Four equivalents of Fe complex (2 mM) in nanopure water were added to the protein solution. Samples were prepared in a final volume of 200 μL containing 50 mM potassium phosphate buffer at the indicated pH. For phenylpyruvate samples, 20 or 100 equivalents of phenylpyruvate (40 mM or 200 mM) in nanopure water were added to the sample after **3** was prepared. For O_2 samples, 5 mL of O_2 was added by gas-tight syringe after the sample was prepared. The sample was prepared in a solution Mössbauer cup, frozen at 77 K in liquid nitrogen, and run at 10 K.

Mössbauer studies. A solution of protein (500 μM) was prepared in nanopure water. Four equivalents of Fe complex (2 mM) in nanopure water were added to the protein solution. Samples were prepared in a final volume of 300 μL containing 50 mM potassium phosphate buffer at the indicated pH. For phenylpyruvate samples, 20 or 100 equivalents of phenylpyruvate (40 mM or 200 mM) in nanopure water were added to the sample after **3** was prepared. For O_2 samples, 5 mL of O_2 was added by gas-tight syringe after the sample was prepared. The sample was prepared in a solution Mössbauer cup, frozen at 77 K in liquid nitrogen, and run at 4 K.

Electrochemical Measurements. A solution of protein (500 μM) was prepared in nanopure water. Four equivalents of Fe complex (2 mM) in nanopure water were added to the protein solution. Samples were prepared to their final volume of 300 μL containing 100 mM potassium phosphate buffer at the indicated pH. Experiments were conducted using a Pine Wavedriver 10 potentiostat under an N_2 atmosphere. Measurements were obtained using a 1 mm diameter glassy carbon disc working electrode, a glassy carbon rod counter electrode, and a saturated calomel reference electrode. **3** was sampled between 2.5 and 50 mV/s.

Stopped-Flow Spectroscopy. A solution of protein (250 μM) was prepared in nanopure water. Four equivalents of Fe complex (1 mM) in nanopure water were added to the protein solution. Twenty equivalents of phenylpyruvate (20 mM) were added in nanopure water. Samples were prepared in a final volume of 600 μL containing 50 mM potassium phosphate buffer at the indicated pH. Samples were run on the stopped-flow electronic abosrbance spectrophotometer by rapidly mixing the prepared ArM sample and O_2-saturated buffer, collecting at 1 ms (500 points) for 1 s. Initial kinetic analysis indicates that the kinetics are biphasic and follow a A>B model.

Rapid Freeze-Quench Resonance Raman spectroscopy. Rapid freeze-quench samples were prepared with three syringes. One syringe was filled with a protein solution (250 uM), four equivalents of Fe complex (1 mM), and 20 equivalents of phenylpyruvate (20 mM), and prepared in a final volume of 2 mL containing 50 mM potassium phosphate buffer at the indicated pH. The second and third syringes were filled with ^{16}O- and ^{18}O-saturated 50 mM potassium phosphate buffer at the indicated pH. The samples were then prepared using these rapid freeze-quench instrument parameters: reactor 400, velocity of 0.8 cm/s,

displacement of 12 mm, and at 645 s. Resonance Raman spectra were obtained at room temperature on samples in glass capillaries (1 mM concentration in Fe) using a 90° geometry with a custom McPherson 2061/207 spectrograph equipped with a liquid-N_2-cooled CCD detector (LN-1100PB, Princeton Instruments). The 650-nm excitation was derived from an Ar laser (Innova 302, Coherent). A long-pass filter (RazorEdge, Semrock) was used to attenuate Rayleigh scattering. Comparison of rapid acquisitions with a range of laser powers and continuous sample translation with longer data acquisitions provided no evidence of photosensitivity for all the streptavidin samples. The integrity of the rR samples was confirmed by direct monitoring of their electronic abosrbance spectra in Raman capillaries before and after laser exposure. Frequencies were calibrated relative to indene and are accurate to ±1 cm^{-1}. Polarization conditions were optimized using CCl_4 and indene.

Protein Preparation and Crystallography

Protein Expression and Purification

Preparation of Sav variants. The construction of K_{121}A-S_{112}E-Sav and other variants was achieved by site-directed mutagenesis (SDM) using the codon optimized K_{121}A-pET24a-Sav plasmid,[191] the following primers and, and Q5 polymerase.

S_{112}E_fwd: 5'-GACCTACGGCACCACCGAAGCAAATGC-3'

S_{112}E_rev: 5'-GTGCCGTAGGTCAGCAGCCACTGG-3'

Amplification of pET24a-Sav mutant plasmids was accomplished by the transformation of SDM reaction mixtures into DH5α ultracompetent cells. Plasmids were isolated using a Miniprep kit from Qiagen, eluting the final plasmid with distilled deionized-water (ddH_2O, 18 MΩ cm^{-1}). DNA sequencing was performed by Genewiz.

Sav Expression. Transformation of 4 µL amplified plasmids into 50 µL Rosetta cells or bl21 cells was followed by rescue with 450 µL LB media. Of this solution, 200 µL was spread aseptically onto LB/Kanamycin agar plates and incubated overnight at 37 °C. Inoculation of a starter culture containing 500 mL LB media and the same antibiotic from a single colony was followed by incubation overnight at 37 °C and shaking at 225 rpm. From this starter culture, 25 mL was used to inoculate each 2L flask containing 500 mL LB media, 25 mL each of 20x sugar (12% glycerol, 1% glucose, 10% lactose) and salt (1 M Na_2HPO_4, 1 M KH_2PO_4, 0.5 M $(NH_4)_2SO_4$) stocks, 1 mL of 1 M $MgSO_4$, 100 µL 5000x trace metal mix (containing 1 M $CaCl_2$, 100 mM $FeCl_3$, 10 mM $MnCl_2$, 10 mM $ZnSO_4$, 2 mM $CoCl_2$, 2 mM $CuCl_2$, 2 mM $NiCl_2$, 2 mM Na_2MoO_4, and 2 mM H_3BO_3 all in 60 mM HCl), and 250 µL of 100 mg/mL Kanamycin. Incubation at 37 °C and 225 rpm was continued until cells reached OD_{600} = 0.6–0.8, at which point the temperature was dropped to 25 °C and cultures incubated another 24 h.

Sav purification. Cultures were centrifuged at 4000 x *g* for 20 min at 4 °C. The resulting cell pellet was resuspended in lysis buffer (50 mL per 1 L expressed) containing 20 mM Tris buffer pH 7.4, 1 mg/mL lysozyme, and a spatula tip of DNase I. The suspension was then allowed to shake at 25 °C and 225 rpm for 6-8 h followed by one overnight freeze-thaw cycle. Dialysis against 6 M guanidinium hydrochloride pH 1.5 for 24 h was followed by neutralization via dialysis against 20 mM Tris buffer pH 7.4 for 24 h, and against nanopure H_2O for another 24 h. Dialysis overnight against iminobiotin (IB) buffer containing 500 mM NaCl and 50 mM $NaHCO_3$ at pH 10.5 afforded the crude, biotin-free lysate. This material was centrifuged at 10,000 x *g* for 1 h at 4 °C and the soluble portion loaded onto an iminobiotin-agarose column pre-equilibrated with IB buffer. The column was washed with 6 column volumes (CVs) of IB buffer or until the absorbance at 280 nm (A_{280}) dropped to zero. Elution

with 1% acetic acid OH in nanopure H_2O, and pooling fractions by A_{280}, provided highly pure (>95%) Sav as assessed by 18% SDS-PAGE. Pooled fractions were dialyzed against 10 mM Tris pH 7.4 for 24 h followed by dialysis in ddH_2O for an additional 72 h and were then lyophilized. Yields of lyophilized protein were typically 100 mg per L expressed, and the solid protein was stored at 4 °C.

Protein Crystallization

*Crystallization of [Fe^{II}(biot-et-dpa$(OH_2)_2$(κ^1-O_{E112})⊂K_{121}A-S_{112}E-Sav] (**3**).* Apo-Sav protein was crystallized by the sitting drop vapor diffusion method under an inert atmosphere. Diffraction-quality crystals were grown at room temperature by mixing 3.5 µL of protein solution (26 mg/mL lyophilized protein in water) and 1.5 µL of crystallization buffer (2.0 ammonium sulfate, 0.1 M sodium acetate, pH 4). The droplet was equilibrated against a reservoir solution of 100 µL crystallization buffer. Single crystals of Sav were prepared by soaking apo-crystals in a soaking buffer (2.6 ammonium sulfate, 0.1 M sodium acetate, pH 8) with a 10 mM stock solution of [Fe^{II}(biot-et-dpa)$(OH_2)_2$]Br_2 in nanopure water (9 µL crystallization buffer, 1 µL [Fe^{II}(biot-et-dpa)$(OH_2)_2$]Br_2 overnight. After soaking, the crystals were transferred to cryo-protectant for 1 min (30% glycerol in soaking buffer) and shock-frozen in liquid nitrogen.

*Crystallization of [Fe^{II}(biot-et-dpa$(OH_2)_2$(κ^1-O_{E112})⊂K_{121}A-S_{112}E-Sav] + phenylpyruvate (**3–phenylpyruvate**).* Apo-Sav protein was crystallized by the sitting drop vapor diffusion method under an inert atmosphere. Diffraction-quality crystals were grown at room temperature by mixing 3.5 µL of protein solution (26 mg/mL lyophilized protein in water) and 1.5 µL of crystallization buffer (2.0 ammonium sulfate, 0.1 M sodium acetate, pH 4). The droplet was equilibrated against a reservoir solution of 100 µL crystallization buffer.

Single crystals of Sav were prepared by soaking apo-crystals in a soaking buffer (2.6 ammonium sulfate, 0.1 M sodium acetate, pH 8 or 3 M ammonium sulfate) with a 10 mM stock solution of $[Fe^{II}(biot\text{-}et\text{-}dpa)(OH_2)_2]Br_2$ in nanopure water (9 µL crystallization buffer, 1 µL $[Fe^{II}(biot\text{-}et\text{-}dpa)(OH_2)_2]Br_2$ overnight. After this initial soaking, the crystals were again soaked in a soaking buffer (2.6 ammonium sulfate, 0.1 M sodium acetate, pH 8 or 3.0 M ammonium sulfate) with a 200 mM stock solution of sodium phenylpyruvate in nanopure water for 5-10 min (9 µL soaking buffer, 1 µL sodium phenylpyruvate). After the second soaking period, the crystals were transferred to cryo-protectant for 1 minute (30% glycerol in soaking buffer) and shock-frozen in liquid nitrogen.

*Crystallization of $[Fe^{II}(biot\text{-}et\text{-}dpa(OH_2)_2(\kappa^1\text{-}O_{E112})(O_2)\subset K_{121}A\text{-}S_{112}E\text{-}Sav]$ + phenylpyruvate (**3–phenylpyruvate–O_2**).* Apo-Sav protein was crystallized by the sitting drop vapor diffusion method under an inert atmosphere. Diffraction-quality crystals were grown at room temperature by mixing 3.5 µL of protein solution (26 mg/mL lyophilized protein in water) and 1.5 µL of crystallization buffer (2.0 ammonium sulfate, 0.1 M sodium acetate, pH 4). The droplet was equilibrated against a reservoir solution of 100 µL crystallization buffer. Single crystals of Sav were prepared by soaking apo-crystals in a soaking buffer (2.6 ammonium sulfate, 0.1 M sodium acetate, pH 8 or 3.0 M ammonium sulfate) with a 10 mM stock solution of $[Fe^{II}(biot\text{-}et\text{-}dpa)(OH_2)_2]Br_2$ in nanopure water (9 µL crystallization buffer, 1 µL $[Fe^{II}(biot\text{-}et\text{-}dpa)(OH_2)_2]Br_2$ overnight. After this initial soaking, the crystals were again soaked in a soaking buffer (2.6 ammonium sulfate, 0.1 M sodium acetate, pH 6) with a 200 mM stock solution of sodium phenylpyruvate in nanopure water for 5-10 mins (9 µL soaking buffer, 1 µL sodium phenylpyruvate). After the second soaking period, the crystals were transferred to O_2-saturated soaking buffer (10 uL) for a period ranging from

30 s-3 h. Then, the crystals were transferred to cryo-protectant for 1 minute (30% glycerol in soaking buffer) and shock-frozen in liquid nitrogen.

X-ray diffraction data collection processing. X-ray diffraction data were collected at the Stanford Synchrotron Radiation Lightsource (BL 12.2) and the Advanced Light Source (BL 8.2.1) at a wavelength of 1 Å. Data were collected with helical (SSRL) or vector (ALS) data collection using exposure time/frame 0.2/0.2 s/deg or 1/0.5 s/deg. Helical or vector collection was used because it decreases the amount of radiation damage on the crystal, which ensures better quality data. Additionally, using these collection techniques helps ensure that the exogenous ligands are not dissociated during the collection time. X-ray diffraction data were processed with XDS[192] or iMosflm[193] and scaled with AIMLESS (CCP4 Suite).[193] The structures were solved by molecular replacement using program PHASER (CCP4 Suite)[193] and the structure 2QCB from the PDB as input model ligand with water molecules removed. For structure refinement, REFMAC5 (CCP4 Suite)[194] and PHENIX.REFINE[195] were used. Ligand manipulation was carried out with program REEL using the small molecule crystal structure RAGQEV01 from the Cambridge Structural Database as an input model.[248] For water picking, electron density, and structure visualization, the software COOT[197] was used. Figures were drawn with PyMOL (the PyMOL Molecular Graphics System, Version 1.8.2.3, Schrödinger, LLC). Crystallographic details, processing and refinement statistics are given in Supplementary Table 3.4-3.9.

Structural Results.

Crystal Color. All crystals of Sav soaked with $[Fe^{II}(biot\text{-}ethyl\text{-}dpa)(OH_2)_2]Br_2$ changed from colorless to pale yellow. Crystals soaked with sodium phenylpyruvate still remained yellow. Crystals soaked with O_2 and phenylpyruvate changed from yellow to dark red. It is

important to note that sometimes a green color can be observed before the dark red color begins to form for crystals that are soaked with phenylpyruvate and O_2.

Structural Refinement. Apo-crystals of protein K_{121}A-S_{112}E-Sav soaked with [Fe^{II}(biot-et-dpa)$(OH_2)_2$]Br_2 constituted space group $I4_122$ with unit cell parameters reported in Tables SX. A single Sav monomer was obtained per asymmetric unit after molecular replacement. Protein residues 2-10 and 135-159 of the N- and C-terminus, respectively, were not resolved in the electron density, presumably due to disorder. Starting from the Sav monomer, the biological homotetramer is generated by application of crystallographic C_2-symmetry axes along the x-, y- and z-axes of the unit cell. The overall protein structures are virtually identical to structure biotin ⊂ WT Sav (PDB 1STP, see Tables 3.4 and 3.6).

Because the crystals soaked with phenylpyruvate and O_2 showed disordered density, it was important to also solve the structures in reduced C121 symmetry to ensure the correct assignment of the O_2 coordination to the Fe center. Additionally, because the phenylpyruvate is located at the crystallographic C_2-symmetry axis, the structures with phenylpyruvate were also solved in reduced C121 symmetry to ensure that the phenylpyruvate density was not an artifact of symmetry. The unit cell parameters are reported in Table 3.8. A single Sav tetramer was obtained per asymmetric unit after molecular replacement.

General Complex and O_2 ligand Modeling. For all structures of apo-protein crystals soaked with the corresponding Fe-complexes, the following general observations were made: i) residual electron density in the F_o-F_c map was observed in the biotin binding pocket, ii) the biotin vestibule is flanked by protein residues of loop-$3,4^A$ (the superscript number indicates Sav monomer within tetramer) loop-$4,5^C$, loop-$5,6^A$ loop-$7,8^A$ and loop-$7,8^B$, and

iii) an anomalous dispersion density map indicated a significant peak in the biotin vestibule superimposed with the electron density peak. The residual electron density was fit with the corresponding Fe-complexes, which projected Fe to the position of the strong anomalous density peak.

The O_2 ligand was modelled using the PDB PEO for hydrogen peroxide. Each density that was modelled for an O_2 ligand was only done so after attempting to model with one or two water molecules and determining through B-factors, negative density in the F_o-F_c map, or distances between atoms that were not chemically reasonable that water was not a reasonable fit for the density. Additionally, the PDB OXY for dioxygen was also used to determine if the O_2 unit was more similar to a superoxido rather than a peroxido ligand. However, the O–O bond distance was contracted to ~1.2 Å, which is shortened from known Fe–O_2 complexes. Additionally, the O_2 unit would not fit the full span of unmodelled density, and there was some additional density in the F_o-F_c map, indicating that OXY was not a reasonable fit. Designing a ligand to incorporate an O_2 ligand with restraints on the O_2 ligand was done and the solutions were similar with similar O–O bond distances. However, the final solution was not determined using a model with O_2 restraints because the Fe complex was synthesized, placed into Sav, then phenylpyruvate, and dioxygen were added, respectively; it was not a pre-synthesized complex that would have provided knowledge of where the O_2 ligand was coordinating or the bond distances. Because of this, PEO was added after fitting the Fe complex to ensure the most accurate fit of the O_2 ligand that would match how the experiment was conducted. Lastly, using PEO instead of a restraints file allowed for the refinement to indicate what the O–O bond distance was, rather than a bias being placed by designating restraints.

*Structural refinement of **3**.* The refinement of **3** was similar to that of **1** (from Chapter 2).

*Structural refinement of **3–phenylpyruvate**.* In both the $I4_122$ and C121 symmetry solutions, the dpa ligand, glutamate residue, and *cis* water ligands were modelled with 100% occupancy. The dpa ligand was fully coordinated to the Fe center (similar to **1b**: Figure 2.7B). In the $I4_122$ symmetry solution, the phenylpyruvate was modelled with 50% occupancy because phenylpyruvate lies directly at the center of symmetry. In the C121 symmetry solution (Figure 3.24, Tables 3.8, 3.9, and 3.10), the phenylpyruvate was modelled in the same location as was found in the $I4_122$ solution, but with 100% occupancy. The presence of the phenylpyruvate in the C121 symmetry solution supports that the docking of phenylpyruvate is not an artifact of symmetry. The higher B-factors for the phenylpyruvate are likely because it is disordered, docked in place by weak noncovalent interactions, and is at the interface of Sav pointing towards the solvent. There is some density in the F_o-F_c map near the glutamate side chain that is present at 3 σ, but disappears at 4 σ. The second confirmation (as seen in **3**) was not modelled because the density is likely not more than 1%-5% of the total density.

*Structural refinement of **3C**.* The $I4_122$ symmetry solution revealed a disordered active site. The dpa ligand still showed two conformations – the major conformation is the pyridine-bound species modelled to 70% occupancy, and the minor conformation is the pyridine-unbound species modelled to 30% occupancy. Additionally, there is disorder in the glutamate side chain $S_{112}E$, modelled to 80% glutamate coordinated to the Fe center, and 20% uncoordinated to the Fe center. The O_2 binds in an end-on fashion to the Fe center with 90% occupancy. A possible reason for the disorder observed in this structure is because it is an intermediate species along the pathway towards a stable O_2 conformation.

Also, the phenylpyruvate molecule has been modelled in the same conformation as that seen in **3–phenylpyruvate**; however, there are significantly higher B-factors. Possible reasons for high B-factors are that the phenylpyruvate is disordered and the α-keto carboxylate chain at the surface of the protein is facing the solvent.

In the C121 symmetry solution (Figure 3.25, Tables 3.8, 3.9, and 3.11), density for phenylpyruvate was found in the same location as in the $I4_122$ symmetry solution with significantly high B factors. The high B factors again are likely due to the disorder of phenylpyruvate and that is located at the surface of the protein. In one dimer, the O_2 ligand is modelled with 100% occupancy for both Fe complexes; however, in the second dimer, the O_2 ligand is modelled with 80% occupancy for both Fe complexes. This is a possible reason why the O_2 ligand is modelled at 90% occupancy in the $I4_122$ symmetry solution. *Structural refinement of **3D**.* The $I4_122$ symmetry solution showed a mixture that made it difficult to determine the O_2 conformations. Because of this difficulty, the C121 symmetry solution was the primary solution for this structure. The Fe center was modelled to 80% occupancy; this decrease can be caused by disorder in the structure. Each of the O_2 conformations was modelled with 80% occupancy. There are two possible reasons for the occupancy decrease: 1) the O_2 units are disordered and 2) this is also an intermediate structure that was trapped before the final conformation was stabilized. There is some density in the F_o–F_c map that could be modelled to the unbound pyridine conformation of the dpa ligand; however, it was left unmodelled because it is likely to be less than 5%. Lastly, there is some density in the F_o–F_c map at the location where phenylpyruvate is typically found. Most of the phenyl ring density and the carboxylate chain were only

observable at 0.7 σ. Because of this, phenylpyruvate was not modelled into the density. It is likely that phenylpyruvate is too disordered too be able to model.

*Structural refinement of **3E**.* The $I4_122$ symmetry solution revealed 100% occupancy for the dpa ligand in the fully bound conformation, the glutamate residue, and the O_2 unit coordinated to the Fe center. Phenylpyruvate was modelled at 50% occupancy because it is at the center of symmetry. The C121 symmetry solution was not of efficient quality to be able to assess the O_2 coordination.

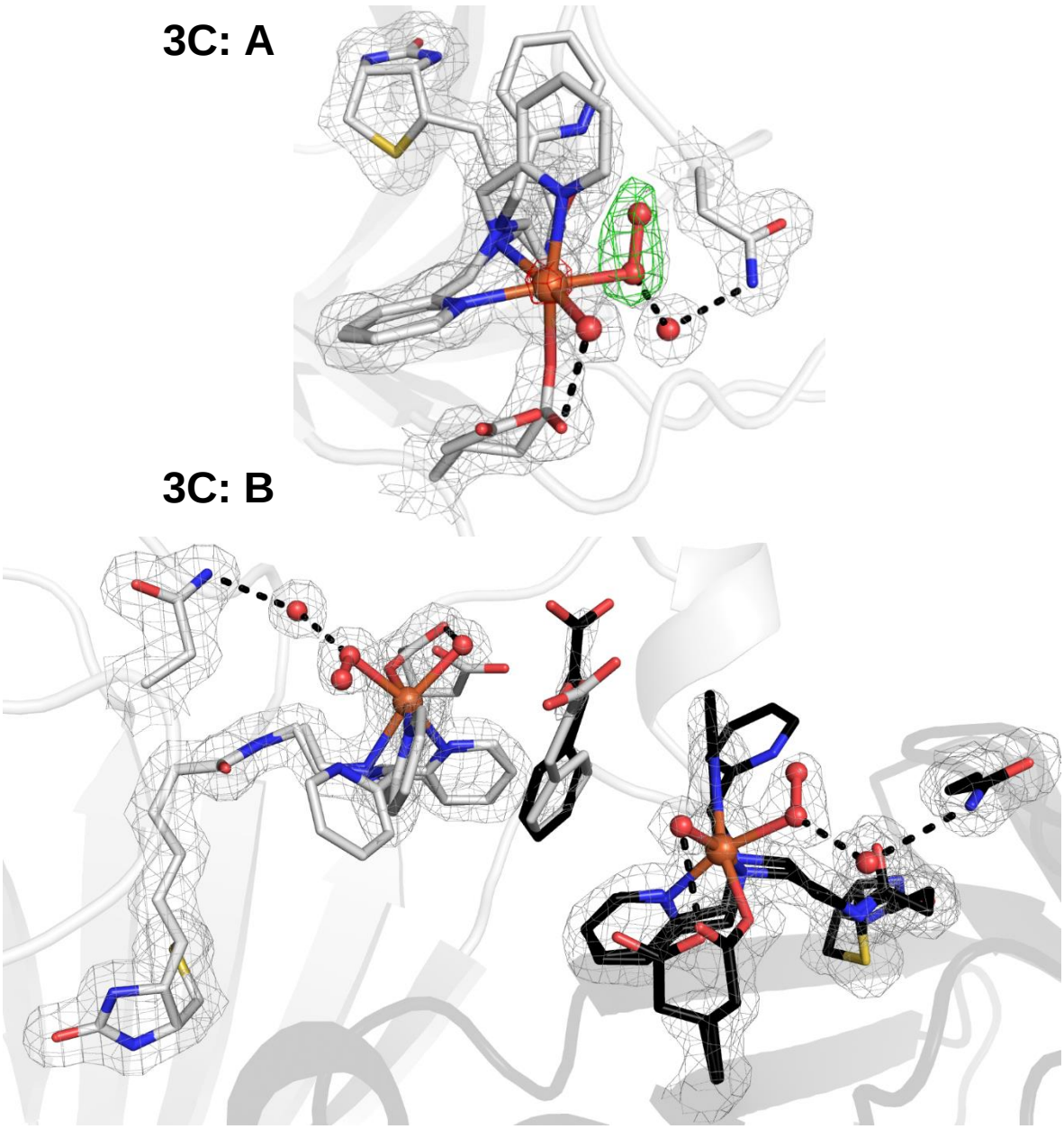

Figure 3.21 Molecular structure of **3–phenylpyruvate–O_2** (**3C**) (**A**: monomer; **B**: dimer). The position of the cofactor is shown by the $2F_o$-F_c electron density (grey, contoured at 1 σ), the omit map (green, contoured at 3 σ), and the anomalous map (red, contoured at 3 σ). Fe ions are shown in orange, N atoms are in blue, and O atoms/water molecules are in red. The number schemes in **3C** are the same as those in Figure 3.16. H-bonds are shown as black dashed lines.

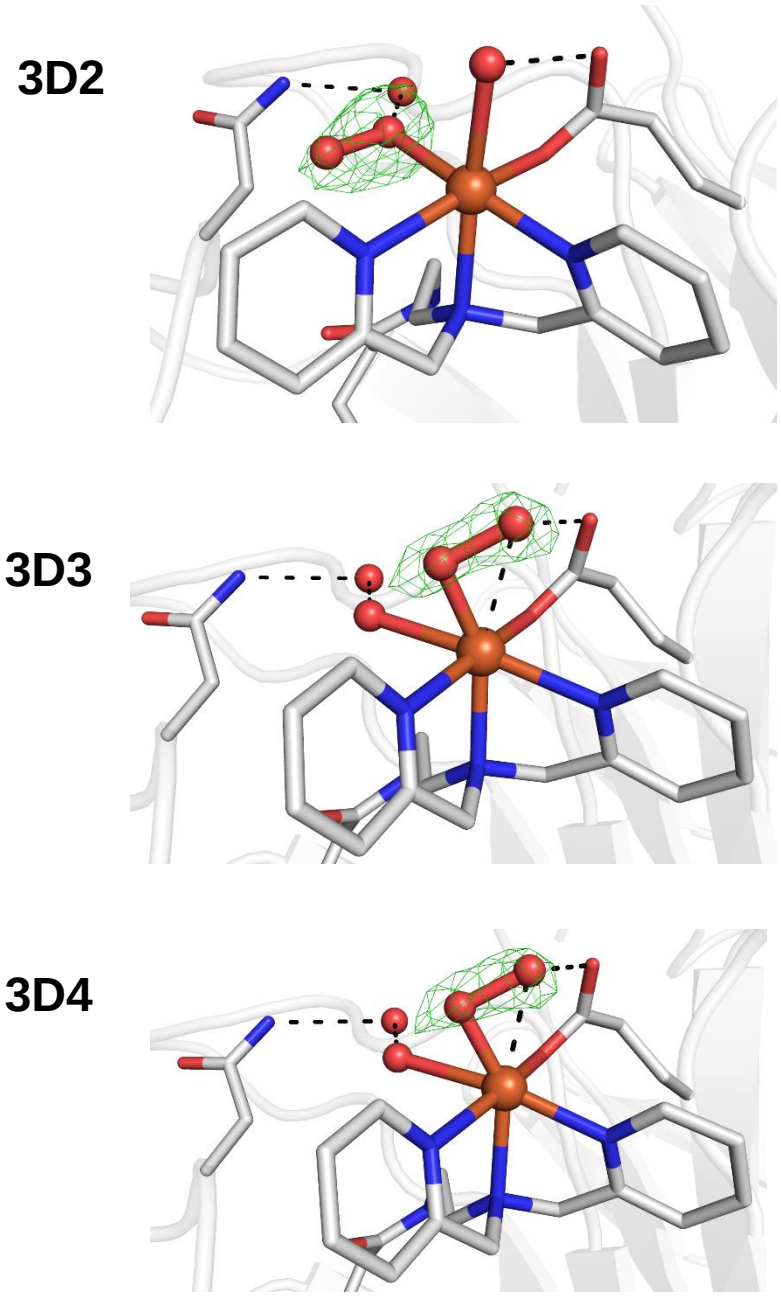

Figure 3.22 Molecular structure of **3–phenylpyruvate–O_2** (**3D2**; **3D3**; **3D4**) and the position of the O_2 ligand is shown by the omit map (green, contoured at 3 σ). Fe ions are shown in orange, N atoms are in blue, and O atoms/water molecules in red. The number schemes in **3D2, 3D3, 3D4** are the same as those in Figure 3.17. H-bonds are shown as black dashed lines.

Dimer A

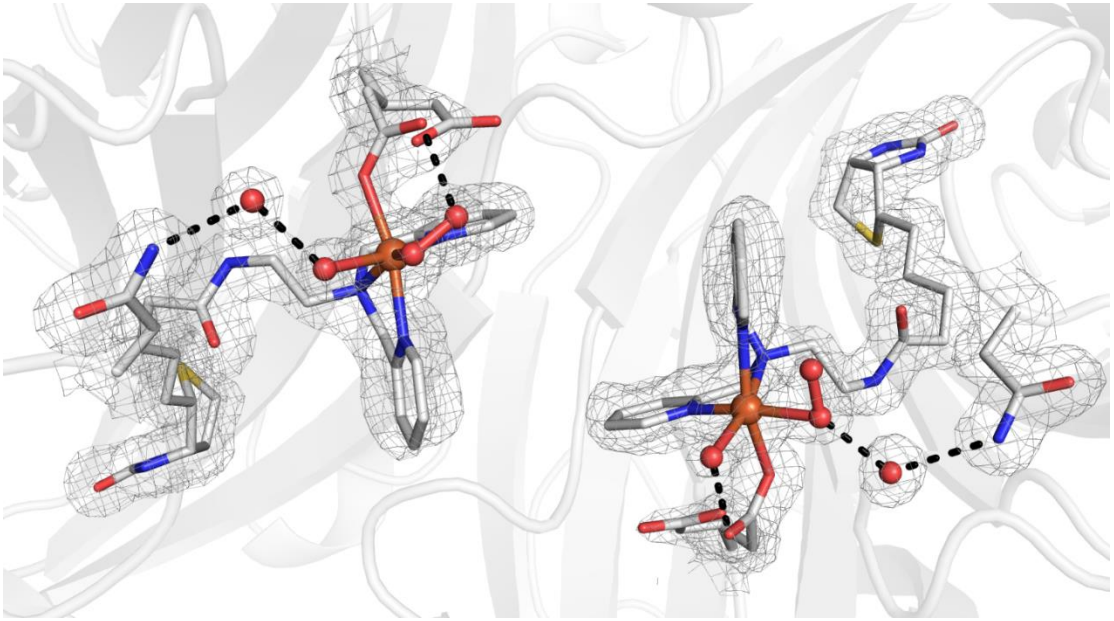

Dimer B

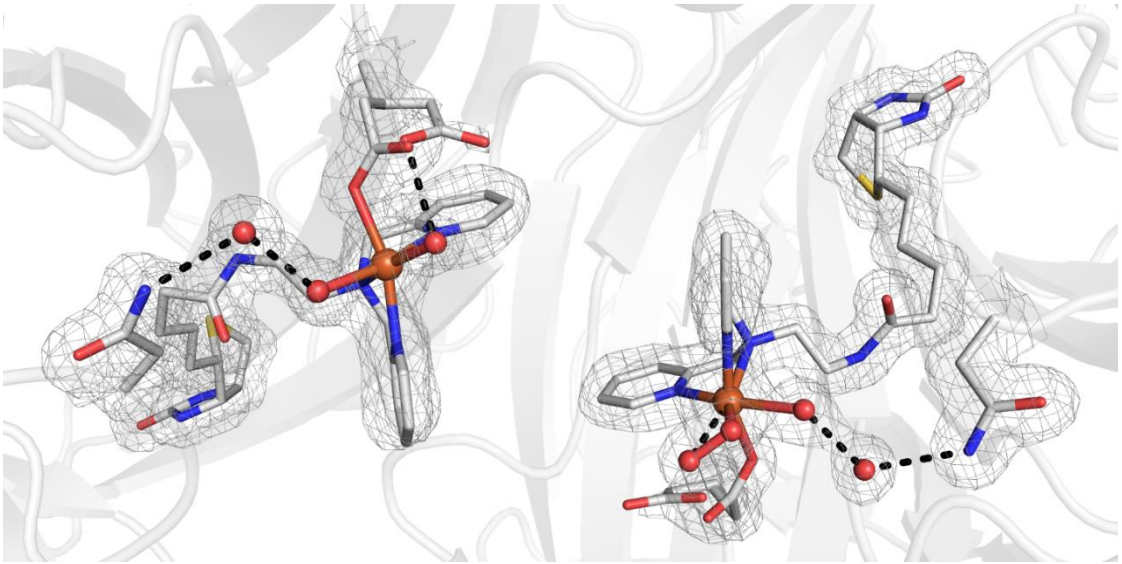

Figure 3.23 Close-up views of the Fe sites in the molecular structure of **3D1**, **3D2**, **3D3**, and **3D4** solved in C121 symmetry. Dimers A and B of the tetrameric Sav are shown for clarity. The protein is displayed in cartoon representation, and the Fe complex and residues 112 are displayed as sticks. The position of the ligand molecules is indicated by the $2F_o$-F_c electron density (grey, contoured at 1 σ). Fe ions are colored in orange, N atoms are in blue, and O atoms/water molecules are in red. The number schemes in **3D2, 3D3, 3D4** are the same as those in Figure 3.17. H-bonds are shown as black dashed lines.

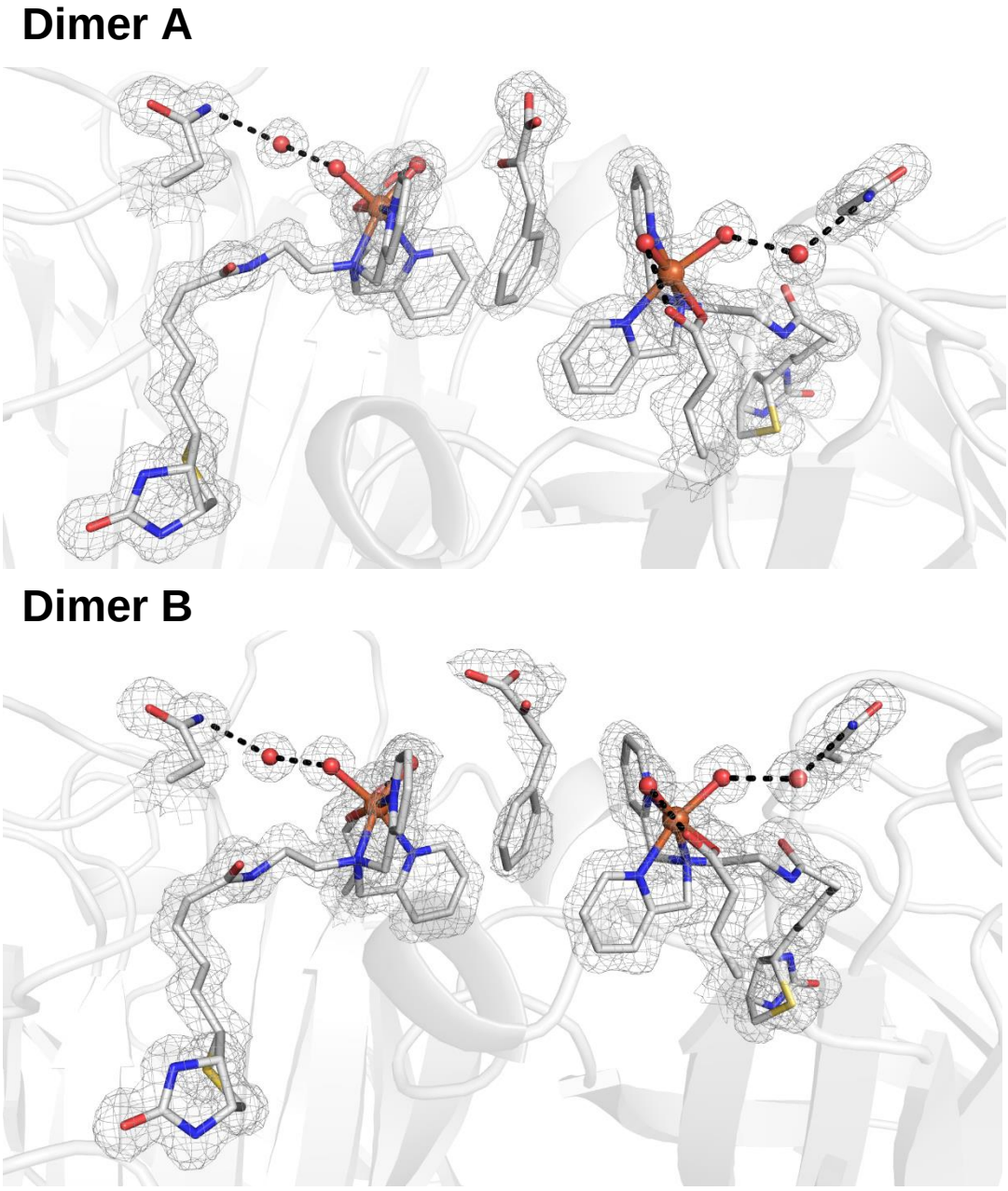

Figure 3.24 Close-up views of the Fe sites in the molecular structure of **3–phenylpyruvate** solved in C121 symmetry. Dimers A and B of the tetrameric Sav are shown for clarity. The protein is displayed in cartoon representation, and the Fe complex and residues 112 are displayed as sticks. The position of the ligand molecules is indicated by the $2F_o$-F_c electron density (grey, contoured at 1 σ). Fe ions are colored in orange, N atoms are in blue, and O atoms/water molecules are in red. The number schemes in **3–phenylpyruvate** are the same as those in Figure 3.8 and 3.11. H-bonds are shown as black dashed lines.

Dimer A

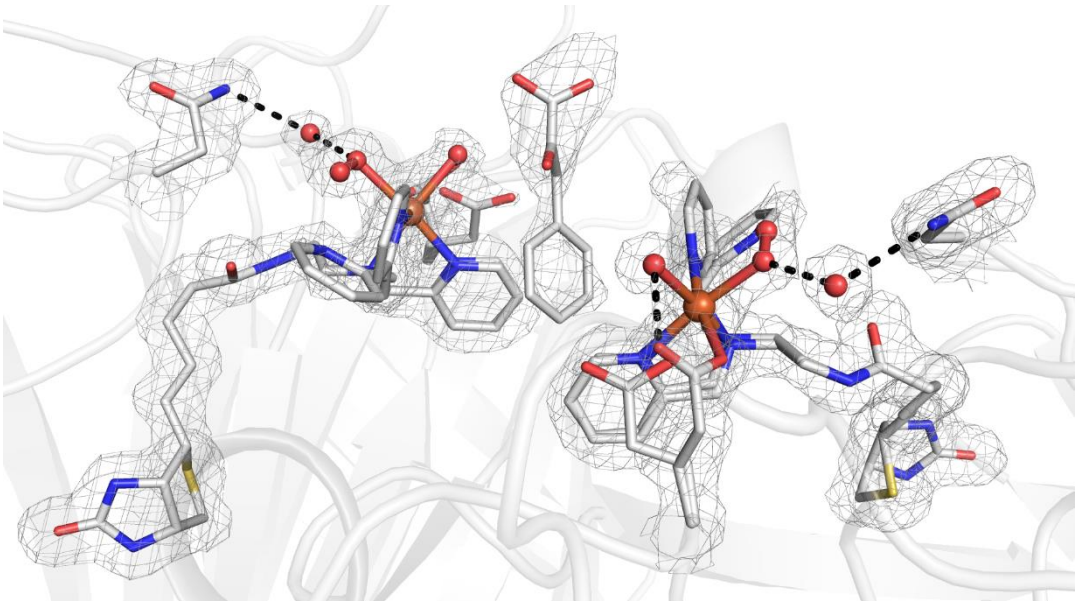

Dimer B

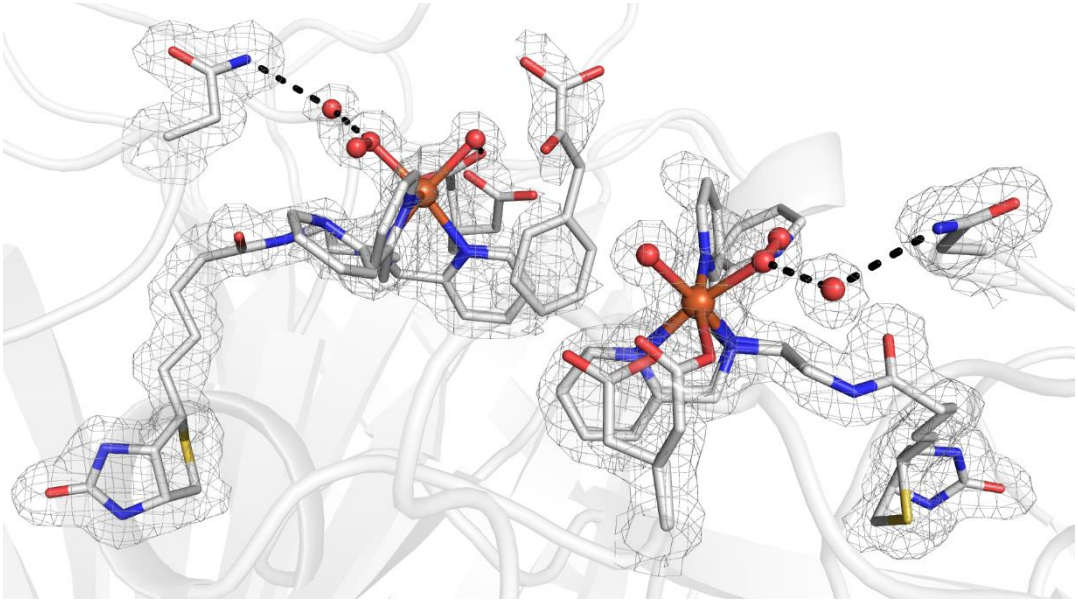

Figure 3.25 Close-up views of the Fe sites in the molecular structure of **3C** solved in C121 symmetry. Dimers A and B of the tetrameric Sav are shown for clarity. The protein is displayed in cartoon representation, and the Fe complex and residues 112 are displayed as sticks. The position of the ligand molecules is indicated by the $2F_o$-F_c electron density (grey, contoured at 1 σ). Fe ions is colored in orange, N atoms are in blue, and O atoms/water molecules are in red The number schemes in **3C** are the same as those in Figure 3.16. H-bonds are shown as black dashed lines.

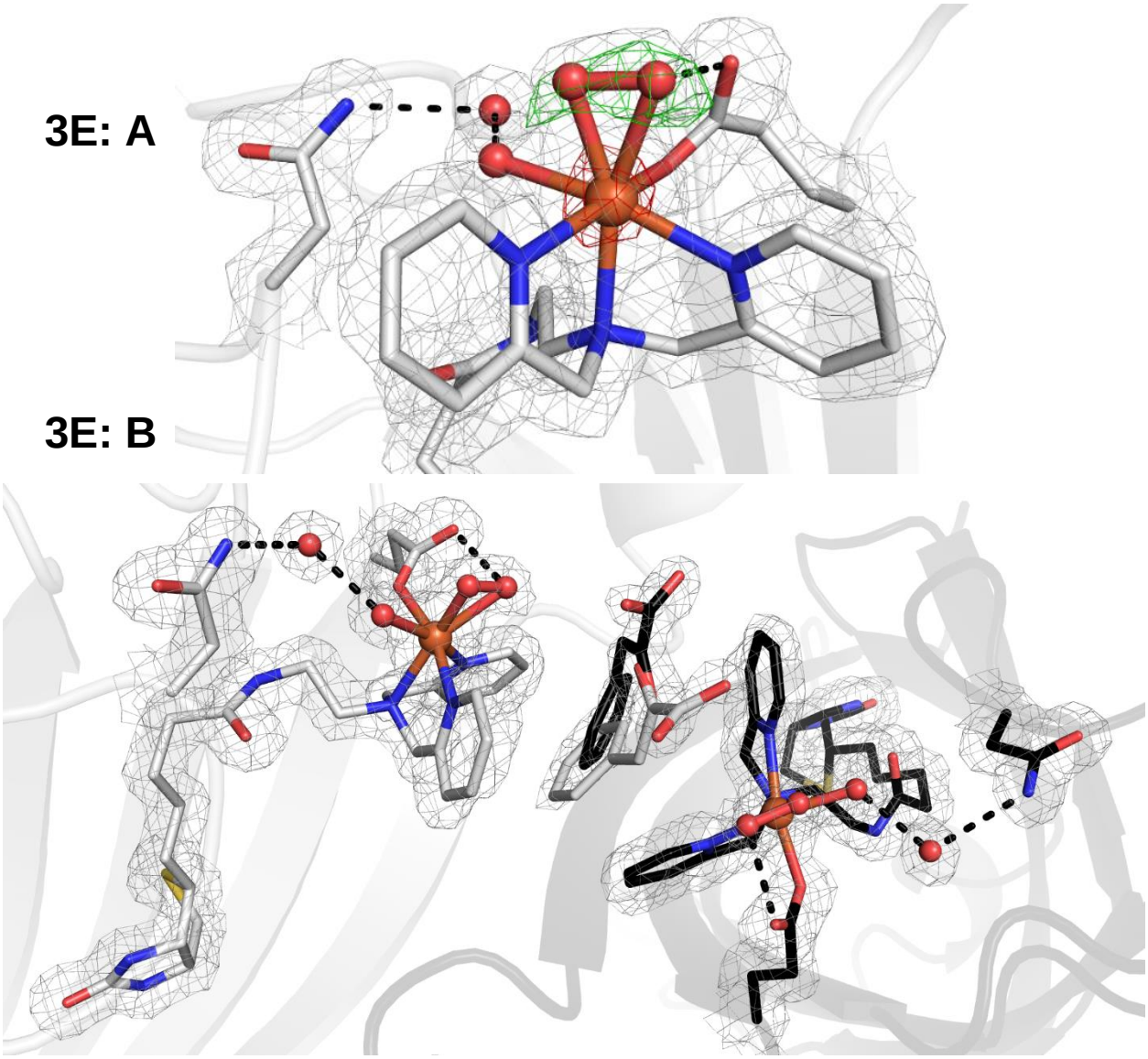

Figure 3. 26 Close-up views of the Fe sites in the molecular structure of **3E** (**A**: monomer; **B**: dimer) The position of the ligand molecules is indicated by the $2F_o$-F_c electron density (grey, contoured at 1 σ), the omit map (green, contoured at 3 σ), and the anomalous map (red, contoured at 3 σ). The protein is displayed in cartoon representation, and the Fe complex and residues 112 are displayed as sticks. Fe ions are colored in orange, N atoms are in blue, and O atoms/water molecules are in red. The number schemes in **3D2, 3D3, 3D4** are the same as those in Figure 3.18. H-bonds are shown as black dashed lines.

Table 3.1 Selected bond lengths and (Å) and angles (°) for **3a**, **3b**, **3–phenylpyruvate.**

Bond lengths (Å) and angles (°)	**3a**	**3b**	**3–phenylpyruvate**
Fe–O1	2.15	2.15	2.10
Fe–O3	2.22	2.22	2.06
Fe–O4	2.18	2.18	2.10
Fe–N1	2.07	2.14	2.23
Fe–N2	2.33	2.36	2.23
Fe–N3	–	2.24	2.11
N1–Fe–O3	164	167	164
N1–Fe–N2	73	71	71
N1–Fe–O4	98	99	100
N2–Fe–O3	100	99	96
N2–Fe–O4	168	168	165
O3–Fe–O4	91	91	95
O1–Fe–N1	98	94	94
O1–Fe–N2	79	82	81
O1–Fe–N3	–	172	168
O1–Fe–O3	94	94	94
O1–Fe–O4	95	95	90
N1–Fe–N3	–	79	78
N2–Fe–N3	–	98	104
N3–Fe–O3	–	93	96
N3–Fe–O4	–	84	84
O3···O2	2.84	2.84	2.66
O4···Wat3	2.59	2.59	2.68
Wat3···N49	3.02	3.02	3.17
$centroid_{py}$···$centroid_{Trp}$	4.86	–	–
Average $centroid_{py}$···$centroid_{ph}$	–	–	4.60

Table 3.2 Selected bond lengths and (Å) and angles (°) for **3C1**, **3C2**, **3E.**

Bond lengths (Å) and angles (°)	**Structure 3C1**	**Structure 3C2**	**Structure 3E**
Fe–O1	2.25	2.25	2.13
Fe–O3	2.31	2.31	2.09
Fe–O4	2.29	2.29	2.32
Fe–O5	2.94	2.94	2.24
Fe–N1	2.31	2.35	2.30
Fe–N2	2.24	2.24	2.29
Fe–N3	2.29	–	2.26
N1–Fe–O3	168	161	158
N1–Fe–N2	69	76	69
N1–Fe–O4	99	100	–
N2–Fe–O4	162	168	–
O3–Fe–O5	–	–	65
O3–Fe–O4	92	92	–
O1–Fe–N1	95	106	95
O1–Fe–N2	83	86	82
O1–Fe–N3	165	–	163
O1–Fe–O3	90	90	99
O1–Fe–O4	85	85	–
O1–Fe–O5	–	–	90
N2–Fe–O3	101	95	130
N1–Fe–N3	80	–	74
N2–Fe–N3	107	–	105
N3–Fe–O3	98	–	88
N3–Fe–O4	82	–	–
N3–Fe–O5	–	–	79
N2–Fe–O5	–	–	164
N1–Fe–O5	–	–	98
Fe–O3–O4	–	–	80
O3–O4	–	–	1.44
Fe–O4–O5	101	101	–
O4–O5	1.47	1.47	–
O3···O2	2.79	2.79	–
O4···O2	–	–	2.78
O5···Wat2	–	–	2.58
Wat2···N49	–	–	3.04
O4···Wat3	2.41	2.41	–
Wat3···N49	3.04	3.04	–
Average $centroid_{py}\cdots centroid_{ph}$	4.53	–	4.79

Table 3.3 Selected bond lengths and (Å) and angles (°) for **3D1**, **3D2**, **3D3**, **3D4**.

Bond lengths (Å) and angles (°)	**Structure 3D1**	**Structure 3D2**	**Structure 3D3**	**Structure 3D4**
Fe–O1	2.28	2.19	2.25	2.27
Fe–O3	2.35	2.40	1.85	1.86
Fe–O4	2.30	2.20	2.48	2.39
Fe–O5	–	2.66	2.34	2.37
Fe–N1	2.23	2.34	2.20	2.29
Fe–N2	2.32	2.17	2.34	2.21
Fe–N3	2.19	2.37	2.26	2.36
N1–Fe–O3	166	168	154	149
N1–Fe–N2	70	70	72	70
N1–Fe–O4	100		–	–
N2–Fe–O4	167	166	–	–
O1–Fe–N1	94	96	97	96
O1–Fe–N2	83	83	82	84
O1–Fe–N3	163	163	168	162
O1–Fe–O3	90	92	105	102
O1–Fe–O4	89	84	–	–
N1–Fe–N3	76	71	75	73
N2–Fe–N3	105	102	104	105
N3–Fe–O3	103	103	82	82
N2–Fe–O3	97	102	127	136
O4–Fe–O3	93	86	–	–
N3–Fe–O4	80	89	–	–
O1–Fe–O5	–	–	91	87
O2–Fe–O5	–	–	64	59
N2–Fe–O5	–	–	168	164
N1–Fe–O5	–	–	100	97
N3–Fe–O5	–	–	82	80
Fe–O4–O5	–	91	–	–
Fe–O3–O4	–	–	96	91
O4–O5	–	1.46	–	–
O3–O4	–	–	1.47	1.47
O3···O2	2.70	2.80	–	–
O4···Wat7	2.47	–	–	–
Wat7···N49	2.99	–	–	–
O4···O2	–	–	2.80	2.71
O5···Wat5	–	–	–	2.49
Wat5···N49	–	–	–	3.08
O5···Wat2	–	–	2.49	–
Wat2···N49	–	–	3.00	–
O4···Wat3	–	2.43	–	–
Wat3···N49	–	3.04	–	–

Table 3.4 X-ray Crystallography Data Processing and Refinement Statistics for $I4_122$ symmetry solutions of **3** and **3–phenylpyruvate**.

Identification		
Sav Mutant	$K_{121}A\text{-}S_{112}E$	$K_{121}A\text{-}S_{112}E$
Fe complex	$[Fe^{II}(biot\text{-}et\text{-}dpa(OH_2)_2(\kappa^1\text{-}O_{E_{112}})]^+$ (**3**)	$[Fe^{II}(biot\text{-}et\text{-}dpa(OH_2)_2(\kappa^1\text{-}O_{E_{112}})]^+$ + phenylpyruvate (**3–phenylpyruvate**)
PDB Code	Unpublished	Unpublished
Fe complex PDB 3-letter code	QGI	QGI
Data Processing		
Unit Cell	a, b, c = 57.7 Å, 57.7 Å, 184.2 Å α, β, γ = 90°	a, b, c = 57.8 Å, 57.8 Å, 183.7 Å α, β, γ = 90°
Space Group	$I4_122$	$I4_122$
Resolution (Å)	54.99 – 1.40	55.10 – 1.31
Highest resolution shell (Å)	1.42 – 1.40	1.33– 1.31
R_{merge} (%)	9 (132)	9.4 (75)
No. of unique reflections	31049 (1498)	38377 (1832)
Multiplicity	11.5 (11.3)	20.1 (19.9)
I/Sig(I)	14.6 (1.9)	18.6 (4.1)
Completeness	100 (100)	100.0 (100)
CC(1/2)	0.999 (0.587)	0.99 (0.92)
Beamline	ALS 8.2.1	SSRL 12.2
Structure Refinement		
R_{work}	0.17	0.17
R_{free}	0.20	0.18
Rmsd bond length (Å)	0.018	0.019
Rmsd bond angle (°)	2.434	2.508
Rmsd compared to biotin-Sav WT (PDB 1STP) (Å)	0.62	0.81
No. ligands		
Fe complex	1	1
Water	106	115
Phenylpyruvate	–	1

Table 3.5 Summary of structural details for **3** and **3–phenylpyruvate**.

PDB Code	Unpublished	Unpublished
Complex	**3**	**3–phenylpyruvate**
Electron density at Fe in F_o–F_c omit map (σ)	35	56
Anomalous dispersion density at Fe (σ)	12	37
Geometry of Fe complex	70%: square pyramidal 30%: distorted octahedral	Distorted octahedral
Coordination number of Fe complex	70%: 5 30%: 6	6
Occupancy of Fe complex (%)	90	100
B-factor (Å²)		
Overall protein	17	15
S112E	(80/20): 17/11	13
K121A	13	10
Fe complex	(70/30): 21/14	14
DPA	(70/30): 21/13	14
Fe	26	17
Phenylpyruvate	–	32
Distance Fe–Fe (Å)	10	10

Table 3.6 X-ray Crystallography Data Processing and Refinement Statistics for $I4_122$ symmetry solutions of **Structure 3C** and **Structure 3E**.

Identification		
Sav Mutant	$K_{121}A\text{-}S_{112}E$	$K_{121}A\text{-}S_{112}E$
Fe complex	$[Fe^{II}(biot\text{-}et\text{-}dpa(OH_2)_2(\kappa^1\text{-}O_{E_{112}})]^+$ + phenylpyruvate + O_2 (**Structure 3C**)	$[Fe^{II}(biot\text{-}et\text{-}dpa(OH_2)_2(\kappa^1\text{-}O_{E_{112}})]^+$ + phenylpyruvate + O_2 (**Structure 3E**)
PDB Code	Unpublished	Unpublished
Fe complex PDB 3-letter code	QGI	QGI
Data Processing		
Unit Cell	a, b, c = 57.5 Å, 57.5 Å, 183.5 Å α, β, γ = 90°	a, b, c = 57.7 Å, 57.7 Å, 183.6 Å α, β, γ = 90°
Space Group	$I4_122$	$I4_122$
Resolution (Å)	37.18 – 1.70	45.89 – 1.55
Highest resolution shell (Å)	1.73 – 1.70	1.58 – 1.55
R_{merge} (%)	9.3 (62)	12 (84)
No. of unique reflections	17481 (913)	23070 (1121)
Multiplicity	8.9 (9.4)	10.2 (8.8)
I/Sig(I)	15.0 (3.4)	11.7 (2.1)
Completeness	99.9 (100.0)	99.9 (99.0)
CC(1/2)	0.997 (0.932)	0.997 (0.809)
Beamline	SSRL 12.2	ALS 8.2.1
Structure Refinement		
R_{work}	0.18	0.21
R_{free}	0.21	0.25
Rmsd bond length (Å)	0.016	0.013
Rmsd bond angle (°)	2.622	2.296
Rmsd compared to biotin-Sav WT (PDB 1STP) (Å)	0.63	0.83
No. ligands		
Fe complex	1	1
Water	79	104
Phenylpyruvate	1	1

Table 3.7 Summary of structural details for **Structure 3C** and **Structure 3E**.

PDB Code	Unpublished	Unpublished
Complex	**3C**	**3E**
Electron density at Fe in F_o–F_c omit map (σ)	29	29
Anomalous dispersion density at Fe (σ)	5	10
Geometry of Fe complex	70% Distorted octahedral 30% Square pyramidal	Distorted octahedral
Coordination number of Fe complex	70%: 6 30%: 5	7
Occupancy of Fe complex (%)	90	100
Occupancy of O_2 (%)	90	
B-factor (Å^2)		
Overall protein	21	16
S112E	80/20: 21/13	16
K121A	17	12
Fe complex	80/20: 23/19	17
DPA	80/20: 23/19	17
Fe	32	22
Phenylpyruvate	74	35
O_2	34	36
Distance Fe–Fe (Å)	10	10

Table 3.8 X-ray Crystallography Data Processing and Refinement Statistics for C121 symmetry solutions of **Structure 3D**, **3–phenylpyruvate**, and **Structure 3C**.

Identification			
Sav Mutant	$K_{121}A$-$S_{112}E$	$K_{121}A$-$S_{112}E$	$K_{121}A$-$S_{112}E$
Fe complex	$[Fe^{II}$(biot-et-dpa$(OH_2)_2$ (κ^1-$O_{E_{112}}$)$]^+$ + phenylpyruvate + O_2 (**Structure 3D**)	$[Fe^{II}$(biot-et-dpa$(OH_2)_2$(κ^1-$O_{E_{112}}$)$]^+$ + phenylpyruvate (**3–phenylpyruvate**)	$[Fe^{II}$(biot-et-dpa$(OH_2)_2$ (κ^1-$O_{E_{112}}$)$]^+$ + phenylpyruvate + O_2 (**Structure 3C**)
PDB Code	Unpublished	Unpublished	Unpublished
Fe complex PDB 3-letter code	QGI	QGI	QGI
Data Processing			
Unit Cell	a, b, c = 192.9 Å, 57.8 Å, 57.8 Å α, β, γ = 90°, 107.4°, 90°	a, b, c = 192.6 Å, 57.8 Å, 57.8 Å α, β, γ = 90°, 107.5°, 90°	a, b, c = 192.2 Å, 57.5 Å, 57.5 Å α, β, γ = 90°, 107.4°, 90°
Space Group	C121	C121	C121
Resolution (Å)	37.32 – 1.45	55.10 – 1.31	37.18 – 1.76
Highest resolution shell (Å)	1.47 – 1.45	1.33 – 1.31	1.79 – 1.76
R_{merge} (%)	8.1 (68)	8.3 (69)	6.9 (40)
No. of unique reflections	100858 (4997)	137517 (6751)	56252 (3299)
Multiplicity	3.8 (3.8)	5.6 (5.4)	2.5 (2.5)
I/Sig(I)	8.1 (1.7)	10.1 (2.0)	6.4 (1.9)
Completeness	94.3 (94.4)	93.9 (95.3)	94.6 (96.5)
CC(1/2)	0.996 (0.772)	0.994 (0.724)	0.994 (0.850)
Beamline	SSRL 12.2	SSRL 12.2	SSRL 12.2
Structure Refinement			
R_{work}	0.20	0.19	0.18
R_{free}	0.23	0.17	0.20
Rmsd bond length (Å)	0.014	0.017	0.015
Rmsd bond angle (°)	2.232	2.443	2.382
Rmsd compared to biotin-Sav WT (PDB 1STP) (Å)	0.65	0.61	0.65
No. ligands			
Fe complex	4	4	4
Water	280	442	243
Phenylpyruvate	Disordered	2	2
O_2	2	–	4

Table 3.9 Summary of structural details of **Structure 3D**, **3–phenylpyruvate**, and **Structure 3C**.

PDB Code	Unpublished	Unpublished	
Complex	**3D**	**3–phenylpyruvate**	**3C**
Electron density at Fe in F_o–F_c omit map (σ)	28	50	25
Anomalous dispersion density at Fe (σ)	–	–	–
Geometry of Fe complex	Distorted octahedral	Distorted octahedral	70% Distorted octahedral 30% Square pyramidal
Coordination number of Fe complex	D1-D2: 6-coordinate D3-D4: 7-coordinate	6-coordinate	70%: 6-coordinate 30%: 5-coordinate
Occupancy of Fe complex (%)	80	100	90
Occupancy of O_2 (%)	80	–	100 (2 subunits) 80 (2 subunits)
B-factor (Å²)			
Overall protein	20	15	20
S112E	19	14	16
K121A	17	10	16
Fe complex	25	15	19
DPA	25	15	19
Fe	28	18	33
Phenylpyruvate	–	59	92
O_2	33	–	39
Distance Fe–Fe (Å)	10	10	10

*B-factors were averaged from the tetrameric Sav

Table 3.10 3–phenylpyruvate bond lengths and distances from C121 symmetry solution.

Bond lengths (Å)	**Monomer 1**	**Monomer 2**	**Monomer 3**	**Monomer 4**
Fe–O1	2.15	2.11	2.10	2.11
Fe–O3	2.05	2.05	2.08	2.05
Fe–O4	2.10	2.14	2.12	2.10
Fe–N1	2.24	2.23	2.22	2.24
Fe–N2	2.26	2.23	2.23	2.24
Fe–N3	2.13	2.16	2.12	2.16
O3···O2	2.63	2.67	2.68	2.66
O4···Wat3	2.64	–	–	–
Wat3···N49	3.23	–	–	–
O4···Wat6	–	2.65	–	–
Wat6···N49	–	3.23	–	–
O4···Wat12	–	–	2.72	–
Wat12···N49	–	–	3.22	–
O4···Wat9	–	–	–	2.70
Wat9···N49	–	–	–	3.26
Distances (Å)	**Dimer A (1 & 2)**		**Dimer B (3 & 4)**	
Average $centroid_{py}$···$centroid_{ph}$	4.58		4.66	
Fe···Fe'	10		10	

Table 3.11 3C bond lengths and distances from C121 symmetry solution.

Bond lengths (Å)	**Monomer 1A**	**Monomer 1B**	**Monomer 2A**	**Monomer 2B**	**Monomer 3A**	**Monomer 3B**	**Monomer 4A**	**Monomer 4B**
Fe–O1	2.29	2.29	2.31	2.31	2.32	2.32	2.27	2.27
Fe–O3	2.30	2.30	2.35	2.35	2.25	2.25	2.20	2.20
Fe–O4	2.25	2.25	2.23	2.23	2.20	2.20	2.17	2.17
Fe···O5	2.85	2.85	2.82	2.82	2.70	2.70	2.74	2.74
Fe–N1	2.16	2.20	2.20	2.33	2.19	2.23	2.12	2.16
Fe–N2	2.19	2.27	2.26	2.25	2.22	2.26	2.27	2.32
Fe–N3	2.21	–	2.19	–	2.18	–	2.16	–
O3···O2	2.51	2.51	2.60	–	2.84	2.84	2.80	2.80
O4···Wat190	2.41	2.41	–	–	–	–	–	–
Wat190···N49	2.99	2.99	–	–	–	–	–	–
O4···Wat155	–	–	2.47	2.47	–	–	–	–
Wat155···N49	–	–	2.95	2.95	–	–	–	–
O4···Wat144	–	–	–	–	2.35	2.35	–	–
Wat144···N49	–	–	–	–	3.00	3.00	–	–
O4···Wat146	–	–	–	–	–	–	2.42	2.42
Wat146···N49	–	–	–	–	–	–	2.96	2.96
Distances (Å)	**Dimer A (1 & 2)**				**Dimer B (3 & 4)**			
Average $centroid_{py}$··· $centroid_{ph}$	4.63				4.58			
Fe···Fe'	10				10			

CHAPTER 4

The Hunt for Blue Precious

Introduction

As discussed in Chapter 1, several dinuclear Fe metalloenzymes are capable of binding and/or activating dioxygen.[249] For example, hemerythrin (Hr) reversibly binds dioxygen, while soluble methane monooxygenase (sMMO) and the β-subunit of ribonucleotide reductase (RNR-R2) activate dioxygen to perform the hydroxylation of methane and the conversion of ribonucleotides to deoxyribonucleotides, respectively.[249–253] In native di-Fe enzymes, the primary coordination sphere is commonly occupied by

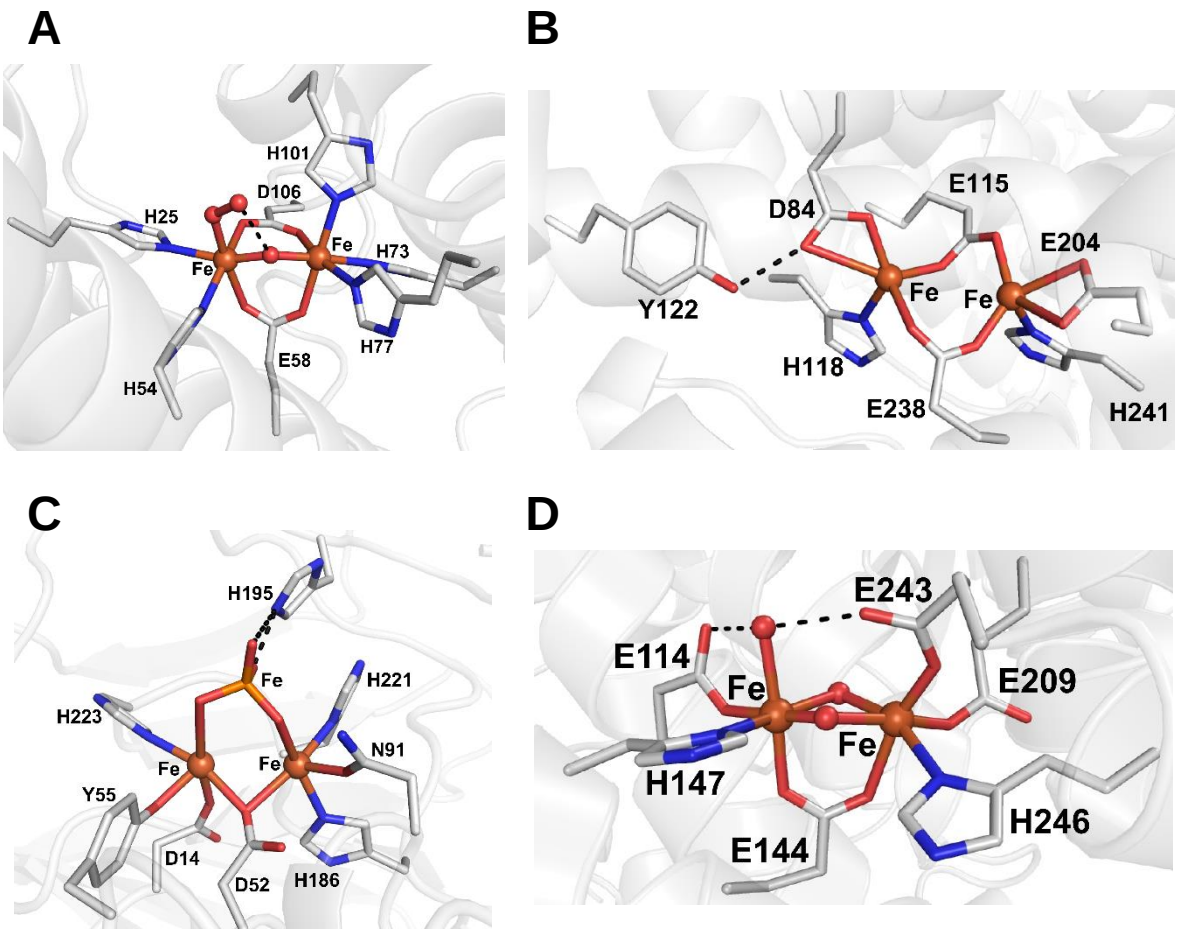

Figure 4.1 Molecular structures of the active sites of di-Fe proteins Hr (**A**: PDB 1HMD), RNR-R2 (**B**: PDB 1PFR), purple acid phosphatase (**C**: PDB 1QCF), and sMMO (**D**: PDB 1HMY).

amino acid residues and aqua, hydroxido, or oxido ligands.[249] For example, the Fe centers in Hr, RNR, sMMO, and purple acid phosphatase are coordinated by histidine amino acid residues and carboxylate-containing amino acid residues that bridge the two Fe centers via a 1,3- or 1,1-carboxylate bridge; in Hr and sMMO, an additional aqua or hydroxido ligand further couples the two metal centers (Figure 4.1).[249] In purple acid phosphatase, a tyrosine amino acid residue coordinates the Fe center, which gives the protein a diagnostic color ($\lambda_{max} \sim 500$ nm) at the Fe^{III} oxidation state.[254–257] In di-Fe proteins, the distance between the two Fe centers is often between 3.0 and 4.2 Å, which gives rise to diagnostic coupling that can typically be identified by various spectroscopic techniques, such as electronic absorbance, Mössbauer, and electron paramagnetic resonance (EPR) spectroscopies and superconducting quantum interference device (SQUID) magnetometry.[249] Additionally, noncovalent interactions in the secondary coordination sphere play an integral role in the progression of substrate oxidation. For example, in RNR, a nearby tyrosine amino acid residue is known to generate a relatively stable tyrosyl radical that is required for initiating ribonucleotide reduction,[249,258–260] and in Hr, a

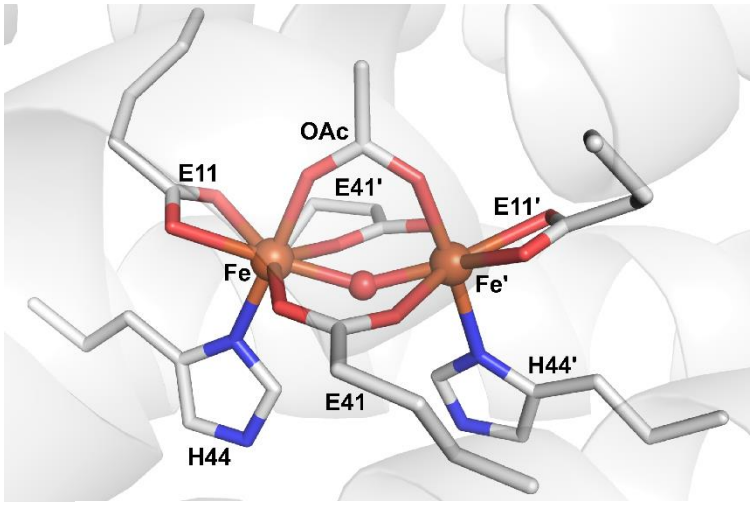

Figure 4.2 Molecular structure of di-Fe^{III} DFT2.

hydrogen bond (H-bond) from the hydroxido bridge stabilizes the dioxygen ligand bound to the coordinatively unsaturated Fe center.[16,22,249,261]

Bioinorganic chemists have used several approaches to further understand the structures of di-Fe proteins and how these structures control the impressive chemical competencies. For example, in the field of artificial metalloproteins, DeGrado has utilized DF2t from the due-ferri (DF) family of de novo-designed peptides to develop a 4-helix bundle that assembles a di-Fe binding site containing a 4-Glu, 2-His motif (Figure 4.2).[107] The two Fe^{III} ions are bridged by a μ-oxido ligand and a μ-(1,3)-acetato ligand which positions the Fe centers 3.6 Å apart.[107] Many synthetic chemists have sought to achieve similar Fe-Fe separations by designing binucleating ligands capable of supporting discrete di-Fe complexes to further study their electronic and structural properties.[42,86,101,249,262–268] Kodera and coworkers used the ligand 1,2-bis[2-{bis(2-pyridylmethyl)amino-methyl}-6-pyridyl]ethane (6-HPA) to form a di-Fe complex with a μ–oxido bridging atom that was able to epoxidize alkenes with H_2O_2 (Figure 4.3A).[269,270] Our lab has also designed the ligand $[MST]^{3-}$, which contains sulfonamido groups that can both act as H-bond acceptors

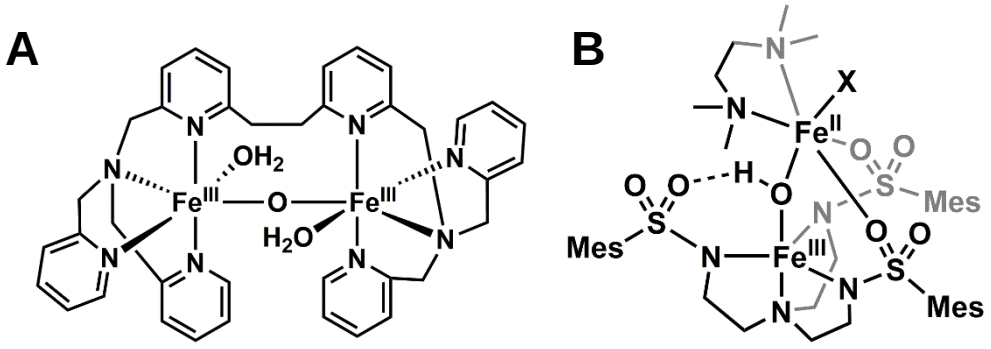

Figure 4.3 ChemDraw structures of synthetic model complexes of di-Fe protein active sites from Kodera (**A**) and Borovik (**B**).

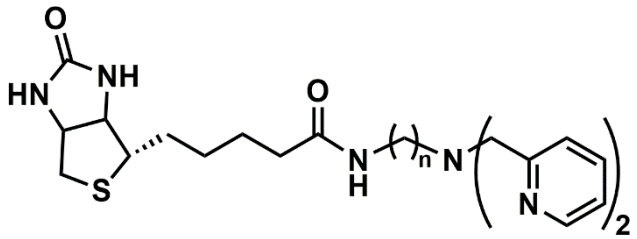

Figure 4.4 ChemDraw representation of biotinylated ligands used in this chapter (n = 2, biot-et-dpa; n = 3, biot-pr-dpa; n = 4, biot-bu-dpa).

and establish an auxiliary metal binding site that has produced several discrete di-Fe systems (Figure 4.3B).[78–81]

To further explore the properties of di-Fe cores in proteins, new artificial metalloproteins (ArMs) with a di-Fe^{III} active site have been developed. To accomplish this goal, several design elements had to be established, which are discussed. Within this study, two new ligands analogous to biot-et-dpa (Chapter 2), biot-pr-dpa and biot-bu-dpa (Figure 4.4), were prepared, and three new variants of Sav, S_{112}Y-Sav, K_{121}Y-Sav, and K_{121}A-L_{124}Y-Sav were expressed and purified. Fe^{III} complexes supported by the family of dpa ligands were synthesized, and the di-Fe^{III} ArMs were characterized by electronic absorbance, perpendicular-mode (⊥-mode) EPR, Mössbauer, resonance Raman (rR), and X-ray absorption (XAS) spectroscopies. The combined data showed that new di-Fe^{III} ArMs were formed within Sav.

Results and Discussion

Design Concepts. Previous work in our lab utilizing biot-et-dpea (Chapter 1) and biot-et-dpa[271] successfully produced mononuclear Cu sites immobilized within Sav; however, the design of dinuclear sites proved to be increasingly difficult. A dpa ligand with a longer linker, biot-bu-dpa (Figure 4.5A), was employed in an attempt to bring the Cu centers closer together. However, crystallographic characterization of the resulting Cu ArM

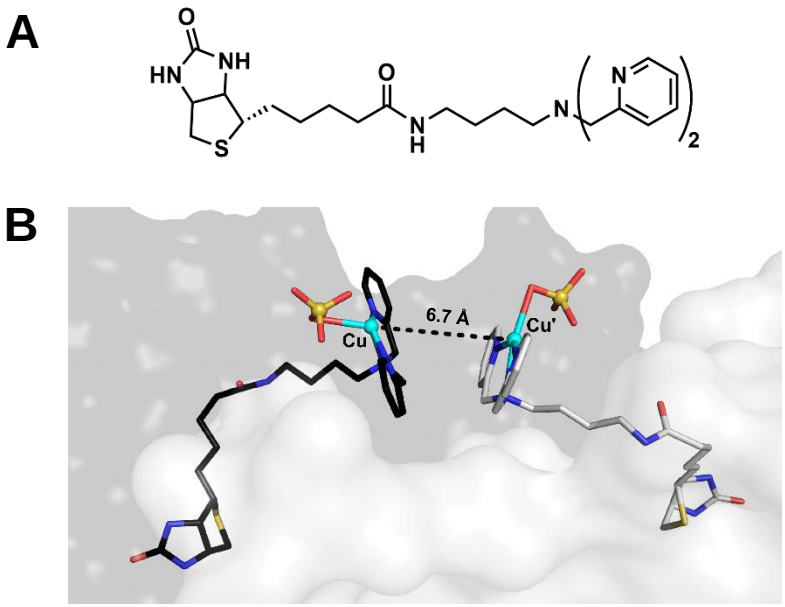

Figure 4.5 ChemDraw representation of biot-bu-dpa (**A**) and molecular structure displaying the binding interface of $[Cu(biot\text{-}bu\text{-}dpa)]^{2+}\subset$WT-Sav (**B**).

revealed that the two Cu centers could come no closer than 6.7 Å, too long of a distance for the Cu centers to undergo any identifiable magnetic coupling.[271] The structure of $[Cu(biot\text{-}bu\text{-}dpa)]^{2+}\subset$WT-Sav (wild-type) also revealed that the Cu centers extended towards the open solvent channel of the protein vestibule (Figure 4.5B).[271] With the knowledge that the butyl linker alone was not sufficiently long to bring the Cu centers close enough together, we turned to the idea of utilizing an endogenous ligand of Sav that would facilitate covalent attachment of the metal complexes to Sav, and aid in establishing dinuclear cores. The binding of the complexes to an endogenous ligand would potentially allow them to span across the Sav dimer, rather than puckering outward

Previous studies in our group have indicated that endogenous ligand binding relies on the correct match between the linker on the biotinylated metal complex and the position of the amino acid residue within Sav. Analogous to the noted artificial cupredoxins in Chapter 1, several native nonheme mononuclear and dinuclear proteins have a

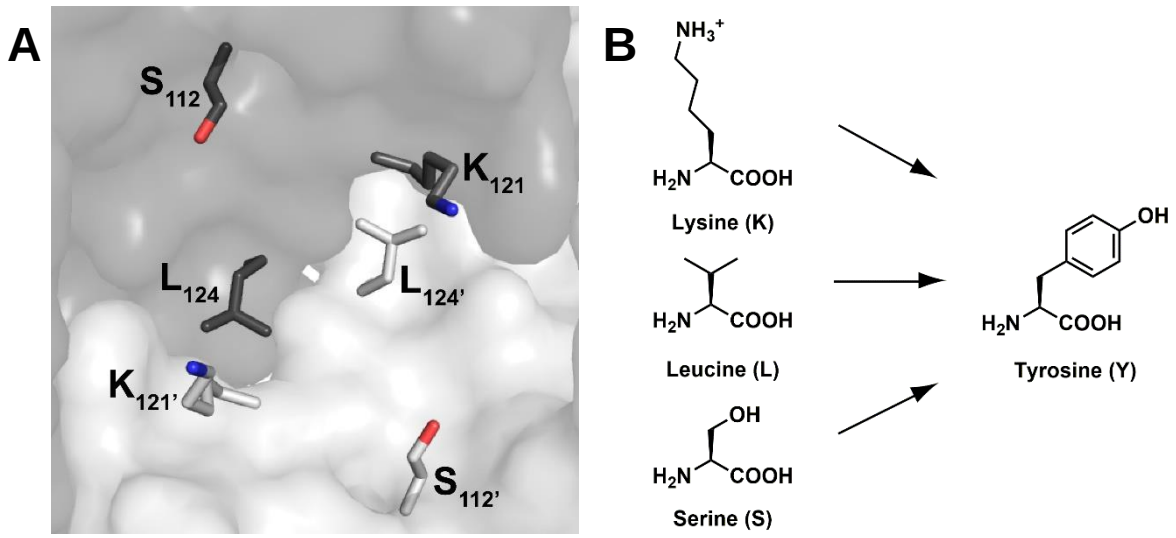

Figure 4.6 Surface representation of amino acid residues in the vestibule of Sav (**A**) and ChemDraw structures of amino acid residues subjected to site-directed mutagenesis (**B**).

spectroscopic handle associated with the coordination of an amino acid residue to an Fe^{III} center. In particular, phenolate coordination to an Fe^{III} center is spectroscopically observable as a ligand-to-metal charge transfer (LMCT) transition in the range $\lambda_{max} \sim 400$-700 nm ($\varepsilon_M \sim 1000$-4000 $M^{-1}cm^{-1}$).[257] In the mononuclear protein protocatechuate 3,4 dioxygenase and the dinuclear protein purple acid phosphatase, phenolate coordination to the Fe^{III} center is observed as an absorbance band at $\lambda_{max} = 435$ nm ($\varepsilon_M \sim 2900$ $M^{-1}cm^{-1}$) and 550 nm ($\varepsilon_M \sim 2500$ $M^{-1}cm^{-1}$), respectively.[256,272] The premise of our approach was to vary both the linker length (et, pr, bu) and the placement of the tyrosine mutation within the Sav vestibule (S_{112}Y-Sav, K_{121}Y-Sav, and K_{121}A-L_{124}Y-Sav: Figure 4.6) to identify conditions that would give an observable color change. This optical screen would allow us to monitor endogenous ligand coordination by absorption rather than solely relying on crystallography.

Synthesis and Characterization of Biotinylated Fe^{III} compounds. The ligands biot-pr-dpa and biot-bu-dpa were prepared analogously to biot-et-dpa (Chapter 1). The ligands of the biot-n-dpa series (n = et, pr, bu) were hygroscopic and therefore stored under an inert atmosphere. The Fe^{III} complexes were prepared by the treatment of biot-n-dpa with $FeCl_3 \cdot 6H_2O$ in ethanol, which resulted in the immediate precipitation of yellow solids. The Fe^{III} complexes were also stored under an inert atmosphere. The Fe^{III} complexes were analyzed by ESI-MS, giving molecular ion peaks corresponding to $[Fe^{III}(\text{biot-n-dpa})Cl_2]^+$. Elemental analysis showed that the Fe^{III} complexes were trihydrates with the assigned formation of $[Fe^{III}(\text{biot-n-dpa})(OH_2)_3]Cl_3$. The three complexes also showed similar absorption spectra with broad absorbance bands with a $\lambda_{max} \sim 260$, 320, and 480 nm (Figure 4.7A). The $\perp$-mode EPR spectra of the three Fe^{III} complexes showed weak signals centered around $g = 9$ and 4.3, consistent with an $S = 5/2$ mononuclear Fe^{III} center (Figure 4.7B). Titration experiments were done with 2-(4'-hydroxyazo-benzene)benzoic acid

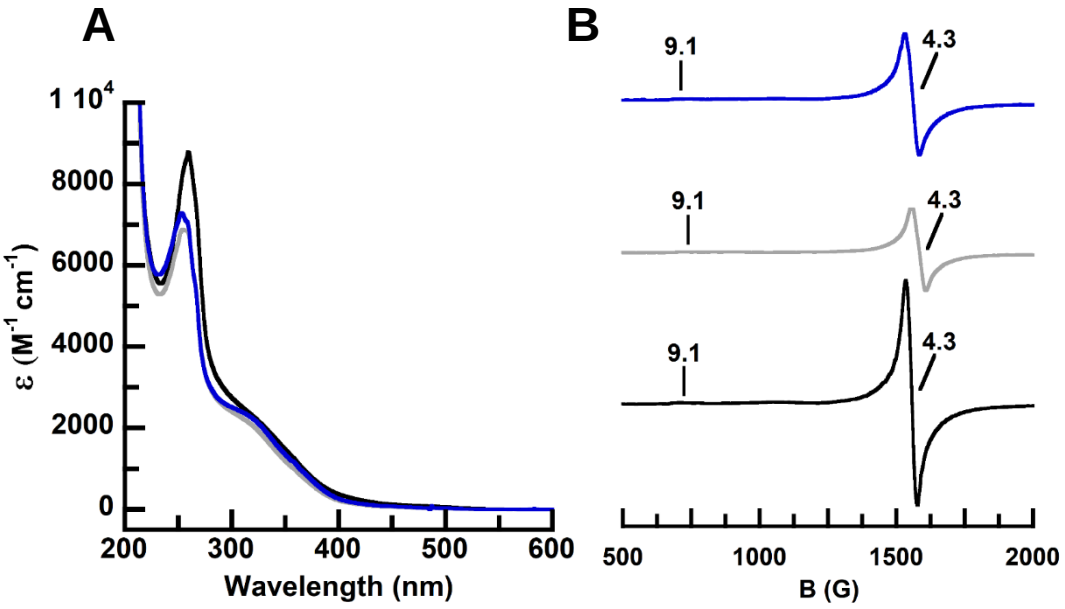

Figure 4.7 Electronic absorbance (**A**) and EPR (**B**) spectra of Fe^{III}-n-dpa. Absorbance data were collected in nanopure H_2O at RT, and EPR data were collected in CH_3OH at 10 K. n = 2 (black), et; 3, pr (grey); 4, bu (blue).

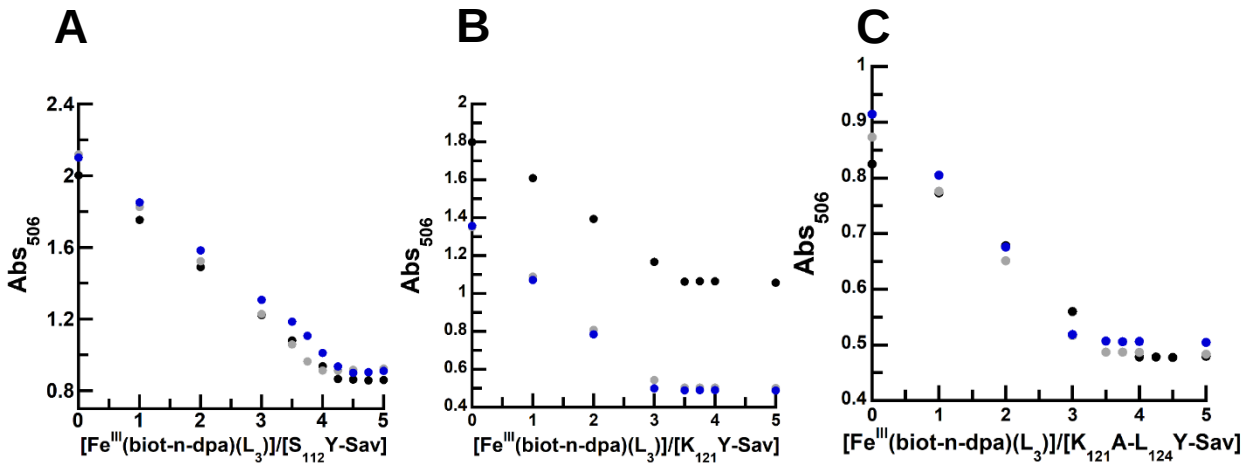

Figure 4.8 HABA titrations of Fe^{III}-n-dpa in S_{112}Y-Sav (**A**), K_{121}Y-Sav (**B**), and $K_{121}A/L_{124}$Y-Sav (**C**). n = 2 (black), et; 3, pr (grey); 4, bu (blue).

(HABA) to determine the binding stoichiometry of the $[Fe^{III}(biot\text{-}n\text{-}dpa)(OH_2)_3]Cl_3$ complexes to each Sav variant. The HABA studies indicated a 4:1 bioinylated Fe^{III} complex to protein host ratio, confirming complete occupancy within the three Sav variants (Figure 4.8).

Development of an optical screen. Initial studies were done using a 96-well plate to visually monitor for a color change with the addition of the Fe^{III}-n-dpa complexes to solutions of the three Sav variants (S_{112}Y-Sav, K_{121}Y-Sav, and $K_{121}A$-L_{124}Y-Sav). The Fe^{III} complexes in nanopure H_2O were pale yellow (Figure 4.9). In the variant S_{112}Y, the three Fe^{III} complexes remained yellow, indicating that tyrosine did not coordinate to the Fe center. Similarly, in the variant K_{121}Y, Fe^{III}-et-dpa remained yellow, while Fe^{III}-pr-dpa and Fe^{III}-bu-dpa changed color to light green. In the variant $K_{121}A$-L_{124}Y, Fe^{III}-et-dpa remained yellow, Fe^{III}-pr-dpa converted to a light blue-purple, and Fe^{III}-bu-dpa produced an immediate intense color change to dark blue (Figure 4.9). Thus, the optical screen provided an immediate assessment of the best linker and variant combination for phenolate coordination to the Fe complex. Of the ArMs screened in this study, the ArM with the $K_{121}A$-

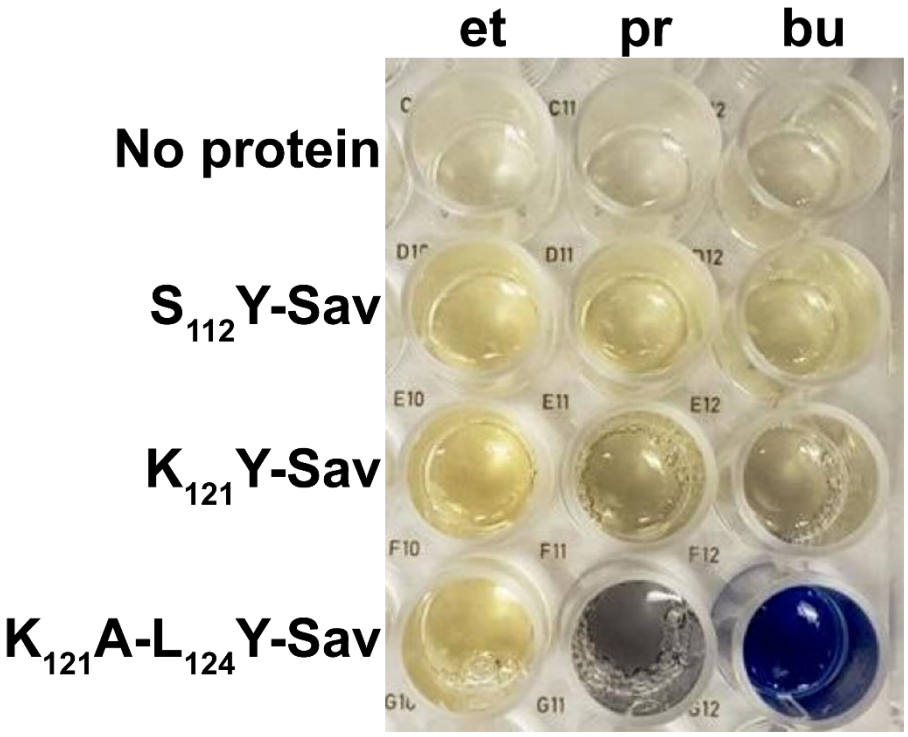

Figure 4.9 Optical screen of Fe^{III}-n-dpa and tyrosine variants of Sav.

$L_{124}Y$ variant and butyl linker length is the combination that extends farthest into the Sav vestibule. Thus, the optical screen highlighted which ArM to pursue for the possible formation of a di-Fe ArM. For the remainder of the chapter, the ArM Fe^{III}-bu-dpa⊂$K_{121}A$-$L_{124}Y$-Sav will be referred to as **Precious**.

*Spectroscopic Characterization of **Precious**.* As illustrated in the optical screen, **Precious** had a distinct blue color in nanopure water at room temperature (RT). The optical properties observed by electronic absorbance spectroscopy supported the formation of an artificial Fe^{III}-tryosinate protein with an absorbance feature at λ_{max} = 605 nm ($\varepsilon_M \sim 2800\ M^{-1}cm^{-1}$) (Figure 4.10A). The rR spectrum also supported the presence of an Fe–O_{Y124} interaction with a vibration at 590 cm^{-1}, consistent with the assignment of previously characterized Fe–tyrosine interactions in the literature.[257] Additional features in the rR spectrum revealed a strong resonance enhancement of the phenol ring vibrations in

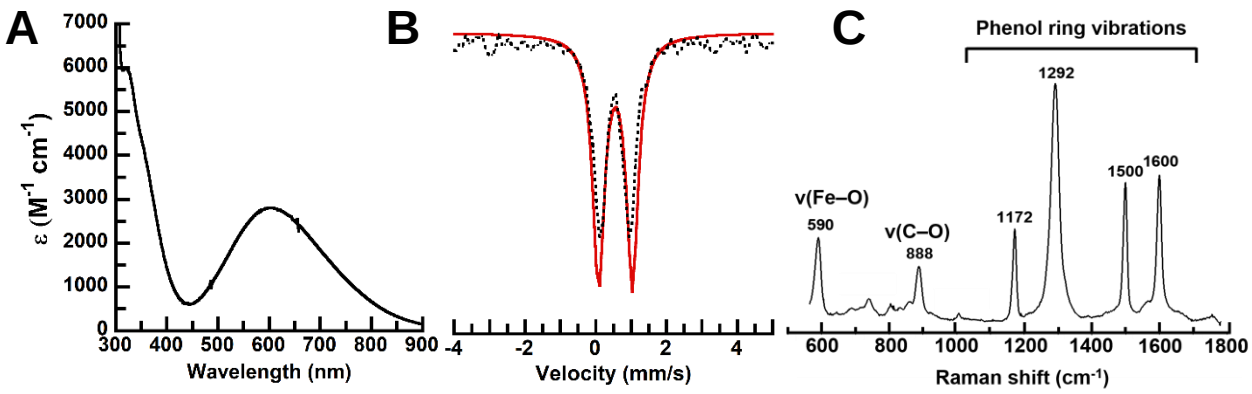

Figure 4.10 Electronic absorbance (**A**), Mössbauer (**B**), and rR spectra (**C**) of **Precious**. Recorded in nanopure H_2O at RT for absorbance and rR spectra (647-nm excitiaton wavelength) and 4 K for Mössbauer spectrum. Simulation is shown as a red line.

the 800-1600 cm^{-1} region, which were assigned as follows: 1600 and 1500 cm^{-1}, C=C breathing; 1292 cm^{-1}, ring/C–O stretch; 1172 cm^{-1}, C–H bend; and 888 cm^{-1}, C–C breathing mode (Figure 4.10C). Although both the UV-vis and rR data are consistent with coordination of the phenolate to a Fe^{III} center, neither is indicative of the formation of a di-Fe species. To address the goal of the design, EPR and Mössbauer spectroscopies were utilized to determine if the Fe centers interacted with one another. The ⊥-mode EPR spectrum for **Precious** was silent tentatively supports assignment as a dinuclear Fe^{III} species within Sav. The Mössbauer spectrum was more conclusive, as it revealed parameters indicative of a coupled di-Fe^{III} species with an isomer shift (δ) of 0.54 mm/s and quadrupole splitting (ΔE_Q) of 0.86 mm/s (Figure 4.10B). High-field Mössbauer studies were conducted and demonstrated strong antiferromagnetic coupling suggestive of a μ-oxido atom bridging the di-Fe^{III} species in Sav. Oxido bridged species are known to facilitate stronger coupling (J > 100 cm^{-1}) than hydroxido (J < 100 cm^{-1}) or aqua bridging atoms. More extensive high-field studies are required to obtain an accurate J value, but at this time, the magnitude of coupling was estimated to be large enough to support antiferromagnetic coupling through an oxido bridging ligand.[249,273,274]

Structural Characterization of Precious:

Crystallographic Structural Characterization. Single crystals of **Precious** were prepared by soaking apo-$K_{121}A$-$L_{124}Y$-Sav crystals in a solution of [Fe^{III}(biot-bu-dpa)$(OH_2)_3$]Cl_3. Uptake of the Fe complex was observed as a change in the color of the

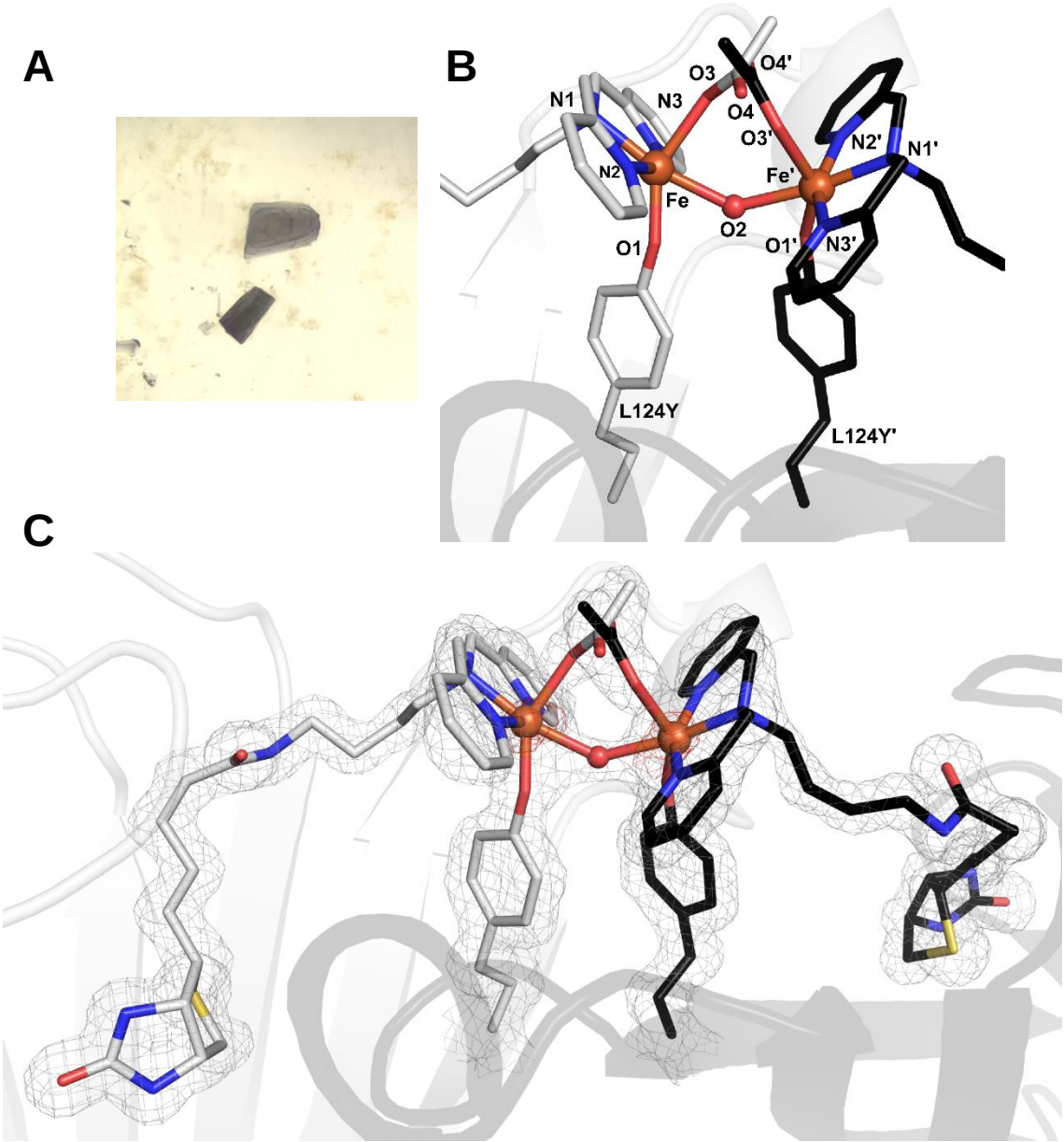

Figure 4.11 Photograph of crystals of **Precious** (**A**) and the molecular structure of **Precious** (**B** & **C**). For the structure in **C**, the position of the Fe^{III}-bu-dpa complex is indicated by the $2F_o$-F_c electron density map (grey, contoured at 1 σ) and anomalous difference density (red, contoured at 4 σ). Fe ions are colored in orange, N atoms are in blue, and O atoms/water molecules are in red. Two subunits are shown (grey and black).

crystals from colorless to blue (Figure 4.11A). The molecular structure was resolved to 1.30 Å, revealing a dinuclear Fe complex immobilized within each Sav dimer. Nitrogen donors N1, N2, and N3 from dpa coordinated to each Fe center in a meridional fashion with an average bond distance of 1.97 Å. Additionally, the O-atom donors from the phenolate group of $L_{124}Y$ were bound to each Fe center with a bond length of 1.78 Å, which supports the observable color change. Additional density was observed between the two Fe centers that was modelled to as O-atom bridge with a bond length of 2.10 Å to each Fe center and an Fe–O2–Fe' bond angle of 141°. A disordered acetato ligand, provided by the crystallization conditions, docked between the two Fe centers with differing Fe–O3 and Fe'–O4 bond lengths of 2.17 Å and 3.39 Å. The two distinct bond lengths suggest that the acetato ligand was coordinated to one Fe center and weakly interacting with the other Fe center. The Fe···Fe' distance was 3.96 Å, which is at the longer end of the range of distances known for di-Fe proteins; however, this distance is most comparable to the bond distance of 3.93 Å observed in the XRD structure of RNR-R2 (Figures 4.11B and 4.11C, and 4.22A, Tables 4.1, 4.2 and 4.3).

XAS. In order to gain a better understanding of the coordination environment of **Precious**, XAS studies were performed. On frozen solution samples, X-ray absorption near edge structure (XANES) analysis provided a K-edge energy of 7124.4 eV for **Precious**. This value of the K-edge energy falls well within the range found for other diferric enzymes, including CmlI, R2lox, and frog M ferritin, supporting the assignment as a diferric species.[249] Additional analysis of the XANES region revealed that the pre-edge area value for **Precious** is 8.1 units (Figure 4.12A). The area of the pre-edge falls well below the average value of ~14 units for $Fe(III)_2(\mu\text{-}O)$ species, the species hypothesized to be the

bridging motif based on Mössbauer spectroscopy. The value is more consistent with the pre-edge area of Fe(III)$_2$(μ-OH) species, which have an average area of ~7 units.[249] The conflicting XAS pre-edge data and Mössbauer studies make it difficult to conclusively assign an identity to the bridging ligand.

Data from extended X-ray absorption fine structure (EXAFS) analysis of **Precious**

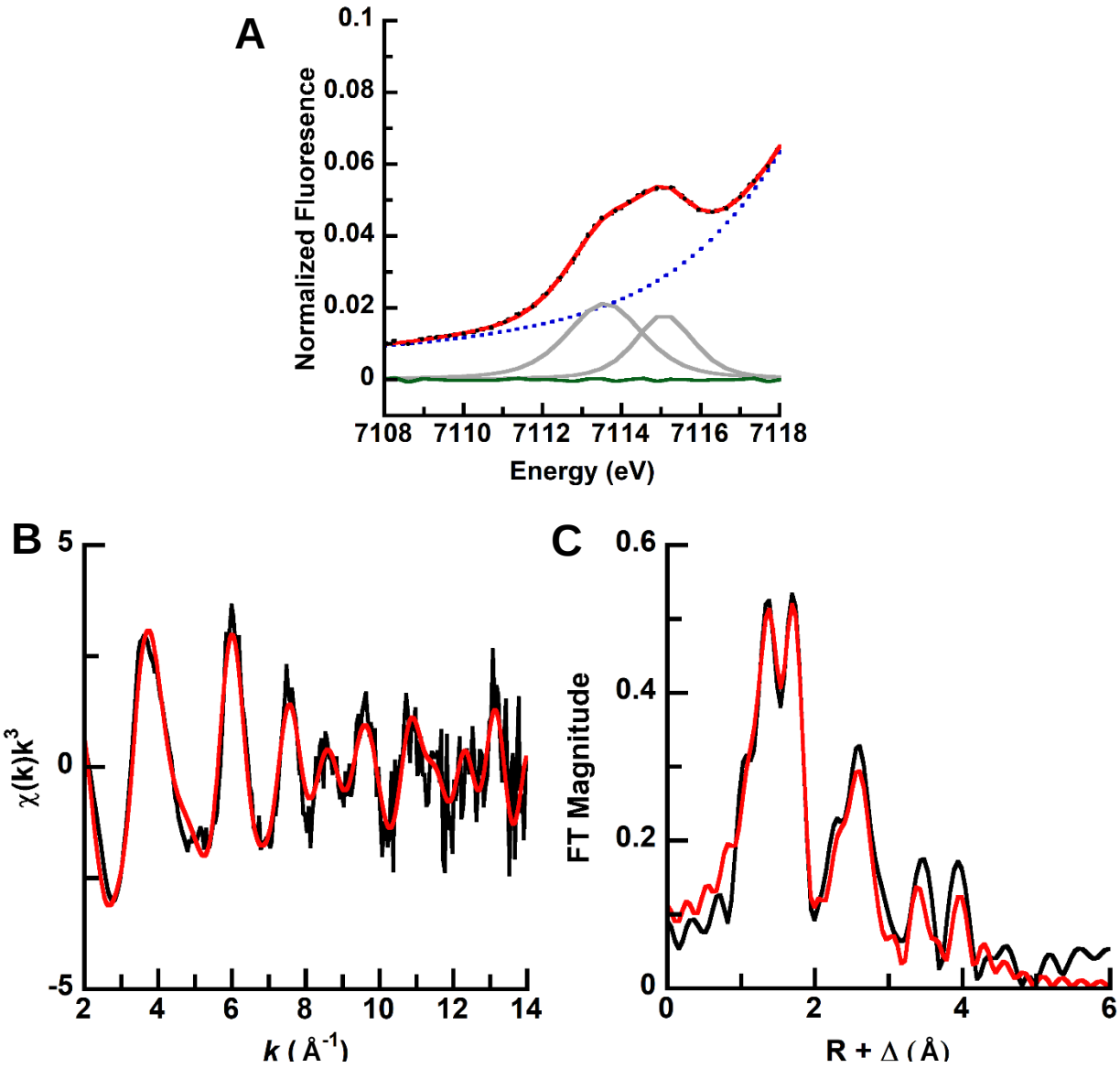

Figure 4.12 Pre-edge region analysis of **Precious**. The experimental data (black dotted), baseline (blue dashed), pre-edge peak componenets (grey solid), residuals (green solid), and total fit (red solid) are shown (**A**). Fit (red solid) of the unfilted (black solid) EXAFS data (**B**) and corresponding Fourier transform (FT) (**C**) of **Precious**. Data were fit in the range k = 2–14 Å^{-1}.

were fit with two sets of scatterers in the primary coordination sphere: Fe–N/O at 1.89 Å and 2.10 Å. The longer distance was fit with four scatterers and had a relatively high mean-squared deviation (σ^2) value of ~8×10^{-3} Å^2. Attempts to split the shell resulted in a set of shorter (~2.05 Å) and longer (~2.15 Å) scatterers with reasonable σ^2 values, but the resolution of the data ($\Delta R = 0.13$ Å) did not justify the inclusion of the split shell in the best fit. The Fe–N/O bond distance at 1.89 Å is consistent with the tyrosine residue binding to the di-Fe complex. Carbon scatterers were required at 3.05 Å; these scatterers are consistent with the alkyl linkages between the pyridyl arms of the ligand as well as the carbon atoms adjacent to the N atoms of the pyridyl groups. The Fe···Fe distance was fit at 4.02 Å, consistent with the distance found from the molecular structure obtained from XRD. The Fe···Fe fit had a primary contribution in the Fourier transformed (FT) data at R+Δ ~3.5 Å that only fit the feature when Fe···C scatterers that contributed intensity to the FT feature at R+Δ ~4 Å were included at 4.20 Å. This long carbon scatterer can be assigned to the carbon atoms in the planar pyridyl rings of the ligand, as well as the aromatic rings of the tyrosine residues. The removal of either the Fe···Fe or the Fe···C scatterers prevented an appropriate fit of the corresponding FT features to be obtained. In addition, fitting these features exclusively with carbon scatterers also resulted in an inadequate fit of the data (Figures 4.12B and 4.12C, Table 4.12).

Binding of additional bridging ligands to Precious:

*Acetate (**Precious–OAc**).* The discovery of a disordered acetato ligand in the structure of **Precious** prompted examination of the ability to purposefully bind other exogenous ligands to the Fe centers. Since the structure of **Precious** indicated that an acetato ligand could dock nearby and interact with the Fe centers, initial studies were done with the

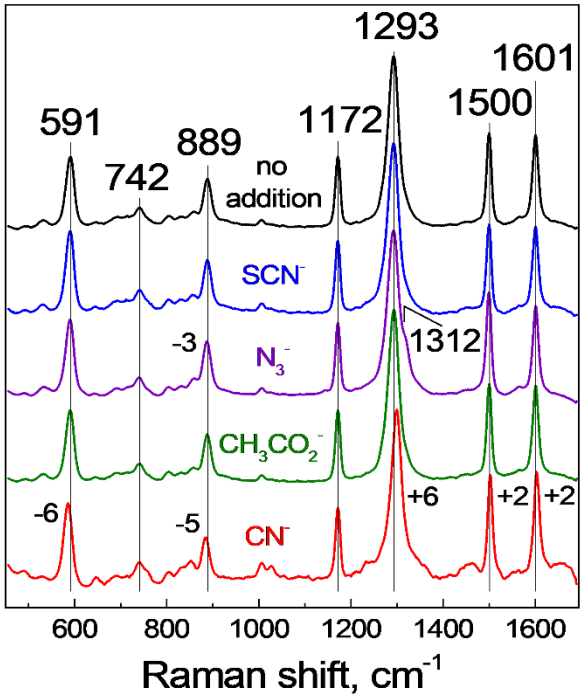

Figure 4.13 rR spectra of **Precious** (black), **Precious–OAc** (green), **Precious–N_3** (purple), **Precious–SCN** (blue), and **Precious–CN** (red). Recorded at RT using 647-nm excitation wavelength.

addition of sodium acetate (NaOAc). The fact that several native di-Fe proteins, such as RNR-R2 and Hr, contain active sites with carboxylato-bridged Fe centers further motivated

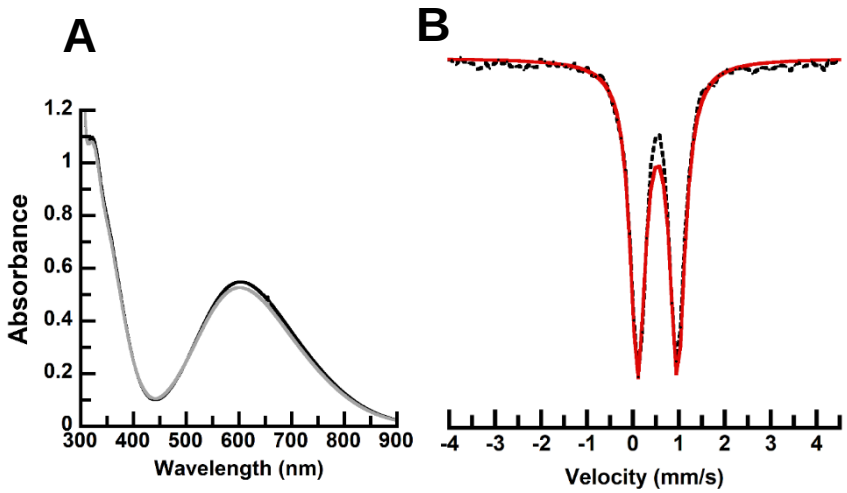

Figure 4.14 Electronic absorbance (**A**) and Mössbauer spectra (**B**) of **Precious–OAc** in nanopure H_2O at RT and 4 K, respectively. Initial spectrum of **Precious** (black) and spectrum after treatment with NaOAc (grey) for absorbance spectra. Simulation is shown as red line.

this initial course of action.

The binding of acetate was first examined in solution. **Precious** was treated with 10 equivalents of NaOAc in nanopure water at room temperature, which afforded a spectrum with a change in the absorbance band at λ_{max} = 600 nm (Figure 4.14A). In addition, the treatment of **Precious** with excess NaOAc showed no significant change in the EPR, Mössbauer, and rR spectra (Figure 4.13: green, 4.14B).

Single crystals of **Precious–OAc** were prepared by soaking crystals of **Precious** in a 100 mM solution of NaOAc. The resulting **Precious-OAc** crystals diffracted to a resolution of 1.50 Å, and the solution of their structure revealed the formation of a dinuclear Fe active site within each dimer of Sav. The primary coordination spheres around the Fe centers in this active site were similar to those found in **Precious**. One distinct difference between the structures of **Precious** and **Precious-OAc** was the clear addition of a new bridging ligand. In place of the previously disordered acetato ligand in **Precious**, an ordered acetato ligand

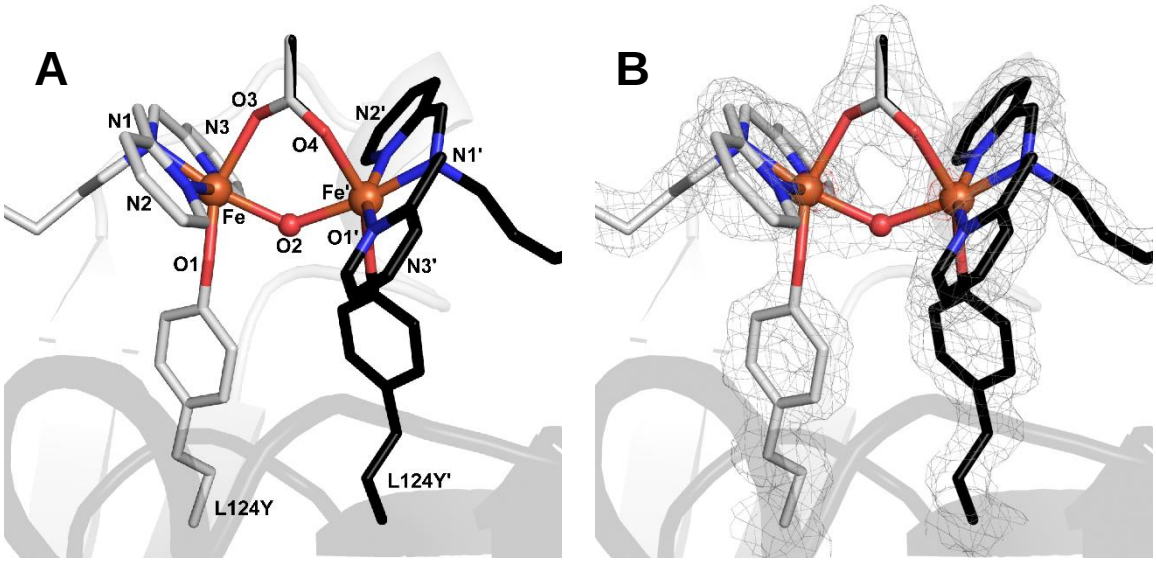

Figure 4.15 Molecular structure of **Precious–OAc** (**A**), the position of the cofactor is indicated by the $2F_o$-F_c electron density map (**B**: grey, contoured at 1 σ) and anomalous difference density (red, contoured at 3 σ). Fe ions are colored in orange, N atoms are in blue, and O atoms/water molecules are colored in red. Two subunits are shown (grey and black).

was resolved in **Precious-OAc** with a bond distance of 2.20 Å to each Fe center. The μ-(1,3) coordination of the acetato ligand to the two Fe centers offers a stabilization effect because of the formation of a 6-membered chelate ring. Further analysis showed a minimal shortening of the Fe···Fe' distance from 3.96 Å in **Precious** to 3.91 Å in **Precious-OAc** but a significant change in the Fe–O2–Fe' bond angle to 134° (Figures 4.15A, 4.15B, and 4.22B, Tables 4.1, 4.2, and 4.3).

*Azide (**Precious–N_3**).* The structure of **Precious–OAc** provided a proof of concept that a bridging ligand can be purposefully added to **Precious**. However, the carboxylate bridge did not substantially decrease the distance between the Fe centers. In further efforts to bring the two metal centers closer together, other bridging ligands were explored. This study investigated the binding of azide ions to **Precious**. Solution studies of azide produced a species with similar electronic properties as **Precious** and **Precious–OAc** by UV-vis, EPR, and rR spectroscopies (Figure 4.16A, 4.14: purple). However, in the Mössbauer spectrum,

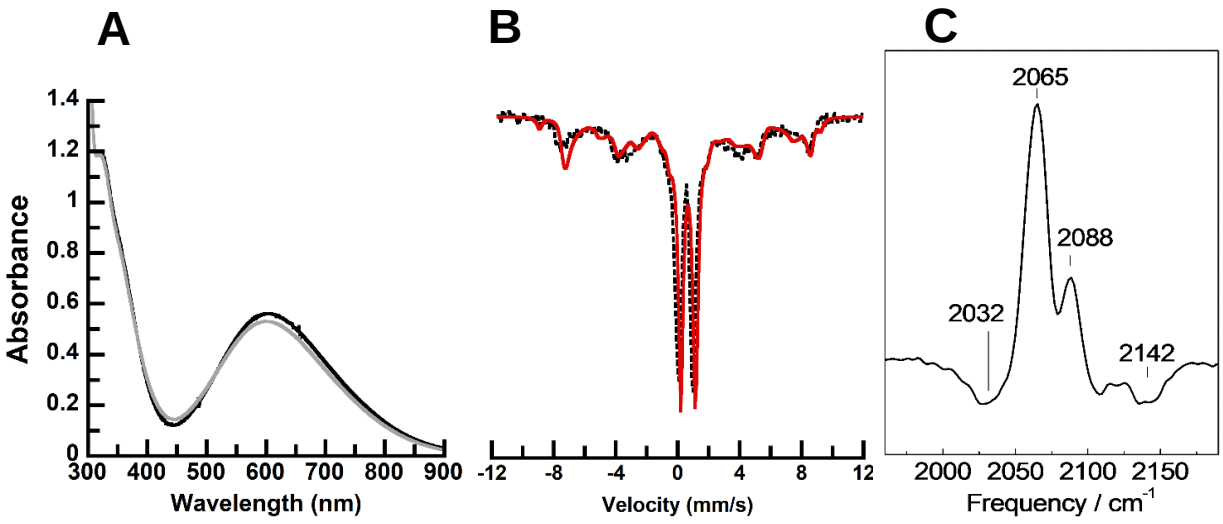

Figure 4.16 Electronic absorbance (**A**) and Mössbauer spectra (**B**) of **Precious–N_3** collected in nanopure H_2O at RT and 4 K, respectively. FTIR photolysis difference spectrum of **Precious–N_3** collected at 30 K (**C**). Initial shown as black line and final shown as black line for absorbance spectra. Simulation is shown as red line.

two species were found: 1) 60% mononuclear Fe^{III} and 2) 40% of the same coupled species that was found in **Precious**. In contrast, the EPR studies produced a different estimate of 90% of the coupled species and 10% mononuclear Fe^{III} present in the **Precious–N_3** solution sample (Figure 4.16B). It is possible that adding an azide ligand disrupted the μ-oxido bridging ligand, but this scenario is not consistent with the EPR results. However, azide bridging ligands have an added benefit of possessing distinct vibrations that can be observed by infrared spectroscopy. Therefore, in collaboration with the Möenne-Loccoz group, Fourier-transform infrared spectroscopy (FTIR) studies were conducted to determine if the azido ligand was coordinated in solution. The FTIR data revealed two peaks (ν(NNN) = 2065 cm^{-1} and 2088 cm^{-1}) attributed to the Fe–azido interaction, suggesting that the azido complex exists as two conformers.[275] Photolysis experiments were conducted to determine if the azido ligand could be photodissociated from the di-Fe complex, and these experiments resulted in a negative band at 2032 cm^{-1}. This feature is marginally lower than the vibration of free azide (2048 cm^{-1}) and can still be attributed to photodissociation of the azido ligand from the di-Fe complex. The photolytic process was shown to be fully reversible by annealing the samples at 130 K and then changing the temperature to 30 K to generate the same spectrum with a vibration at 2032 cm^{-1},

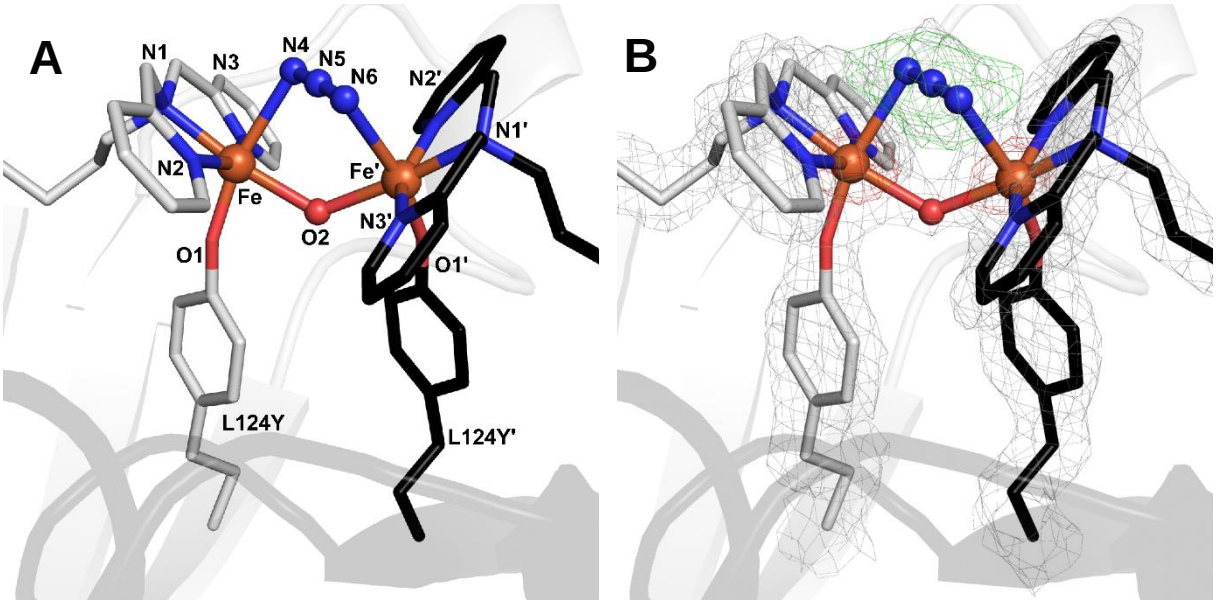

Figure 4.17 Molecular structure of **Precious–N_3** (**A** & **B**). For the structure in **B**, the position of the Fe^{III}-bu-dpa complex is indicated by the $2F_o$-F_c electron density map (grey, contoured at 1 σ), and anomalous difference density (red, contoured at 3 σ), and the azido ligand position is indicated with the F_o-F_c omit map (green, contoured at 3 σ). Fe ions are colored in orange, N atoms are in blue, and O atoms/water molecules are in red. Two subunits are shown (grey and black).

supporting that, in solution, the azido ligand is coordinated to the Fe complex (Figure 4.16C).

Single crystals of **Precious–N_3** were prepared in the same manner as **Precious–OAc** but a 100 mM solution of NaN_3 was used instead of NaOAc. The molecular structure was solved to a resolution of 1.70 Å and revealed a similar primary coordination sphere as those of **Precious–OAc** and **Precious**. One important difference is the presence of additional electron density for another bridging ligand between the two Fe centers, which was modelled as an azido ligand. The azido ligand binds in a μ-(1,3) fashion to the Fe centers with a distance of 2.45 Å and an Fe–N4–N5 bond angle of 96°. Moreover, the Fe···Fe' distance has shortened to 3.82 Å relative to that in **Precious–OAc** and **Precious** with an Fe–O2–Fe' bond angle of 126° (Figures 4.17A,4.17B, and 4.22C, Tables 4.1, 4.2, and

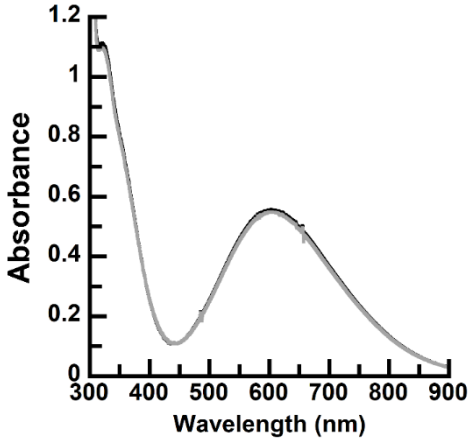

Figure 4.18 Electronic absorbance spectrum of **Precious–SCN**. Recorded at RT in nanopure H_2O. Initial is shown as black line and final is shown as grey line.

4.3). The bridging O atom was modelled with 100% occupancy when the azido ligand is present, which directly contrasts the solution Mössbauer studies that showed 60% of a mononuclear Fe^{III} species. This discrepancy could be explained by differences in solution and crystallographic studies; however, because the EPR results support the structural work, more work is necessary to determine the difference in the quantification of the Mössbauer results. The shortening of the Fe⋯Fe' distance shows that it is possible to decrease the distance between the two Fe centers in **Precious** with the aid of an exogenous bridging ligand.

*Isothiocyanate (**Precious–SCN**).* The isothiocyanate ion was chosen as an additional three-atom bridging ligand due to its ability to coordinate to the Fe centers in a similar μ-(1,3) fashion as an azide ion. Initial spectroscopic studies showed that when Precious was treated with 10 equivalents of NaSCN in nanopure water, the new species had similar electronic properties by UV-vis, EPR, and rR as **Precious**, **Precious–OAc**, and **Precious–N_3** (Figure 4.18, 4.13: blue)

Single crystals of **Precious–SCN** were prepared by the same method as described above with a 100 mM solution of NaSCN. Analysis of the molecular structure, resolved to 1.90 Å, again revealed similar coordination of the dpa ligand, the phenolate group, and the O-atom bridge to the Fe centers found for **Precious**. Additional electron density between the two Fe centers was apparent and was fit to a bridging isothiocyanato ligand. With the limitations of crystallography, the coordination of the S/N atoms to a specific Fe center could not be determined, and thus, both conformations were modelled. The isothiocyanato ligand binds in a μ-(1,3) fashion to the Fe centers with an Fe–S/N distance of 2.42 Å and an Fe–S/N–C bond angle of 89°. The bound isothiocyanato ligand also forms a 6-membered chelate ring with the two Fe centers and the μ-oxo bridging atom. Additionally, the Fe···Fe' distance further shortened to 3.77 Å with an Fe–O2–Fe' bond angle of 122° (Figures 4.19A, 4.19B, and 4.23A, Tables 4.1, 4.6, and 4.7). Similar to the results of the azide studies, the

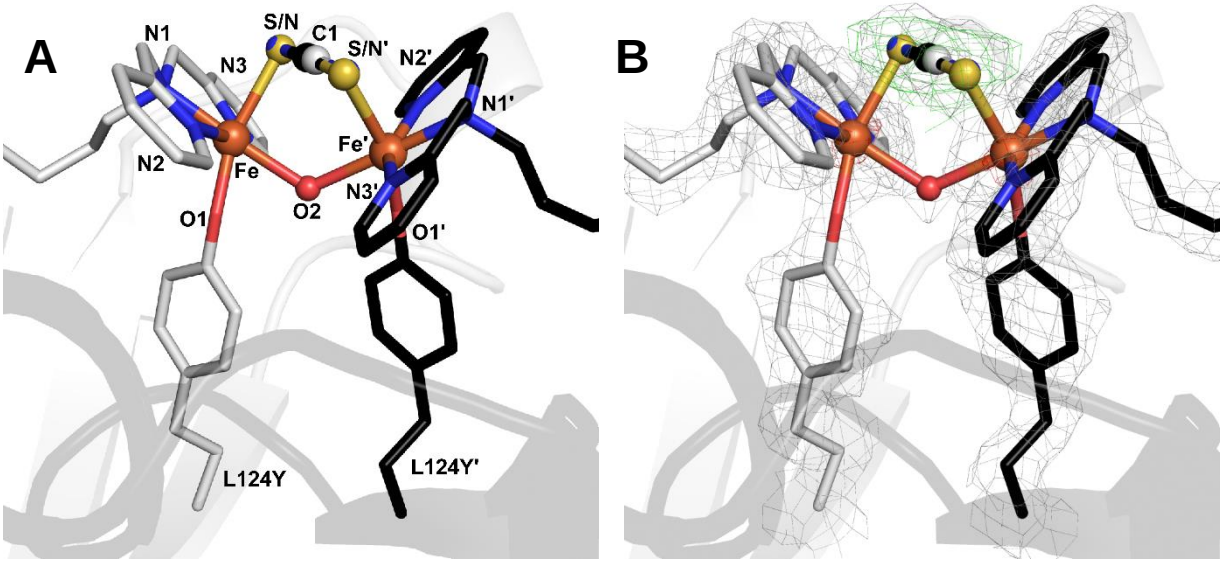

Figure 4.19 Molecular structure of **Precious–SCN** (**A** & **B**). For the structure in **B**, the position of the Fe^{III}-bu-dpa complex is indicated by the $2F_o$-F_c electron density map (grey, contoured at 1 σ), and anomalous difference density (red, contoured at 3 σ), and the isothiocyanato ligand position is indicated with the F_o-F_c omit map (green, contoured at 3 σ). Fe ions are colored in orange, N atoms are in blue, S atoms are in blue, and O atoms/water molecules are in red. Two subunits are shown (grey and black).

studies involving isothiocyanate successfully showed that exogenous three-atom bridging ligands can be used to bind two Fe centers and cause a slight decrease in the distance between them.

*Cyanide (**Precious–CN**).* The success of adding three-atom bridging ligands to decrease the distance between the two Fe centers in **Precious** prompted further studies using cyanide ions which could serve as a two-atom bridging ligand. The treatment of **Precious** with 10 equivalents of NaCN in nanopure water was monitored spectroscopically and revealed an initial shift in the UV-vis spectrum to a band at $\lambda_{max} \sim 500$ nm. At room temperature, the absorbance band slowly decreased over a period of 30 minutes to give a featureless spectrum (Figure 4.20). **Precious–CN** was also examined by EPR and rR spectroscopies and there were no significant changes from those of **Precious**. (Figure 4.13: red)

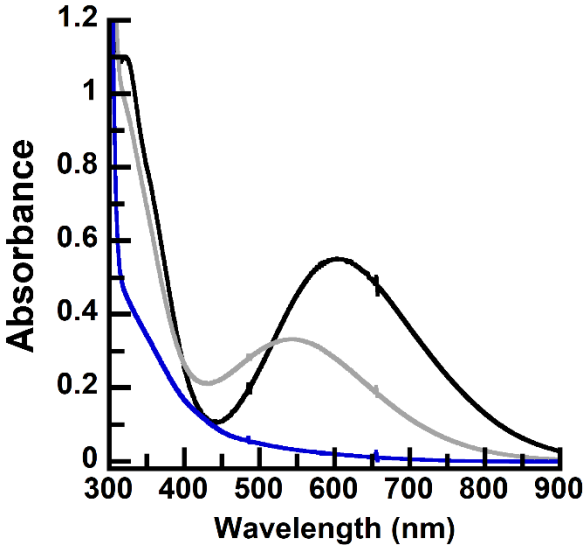

Figure 4.20 Electronic absorbance spectrum of **Precious–CN**. Recorded at RT in nanopure H_2O. Initial is shown as black line and final is shown as blue line.

Single crystals of **Precious–CN** were prepared in a similar manner as described above using a 100 mM solution of NaCN. The molecular structure was resolved to a 1.70 Å resolution to reveal a similar primary coordination sphere as that of **Precious** with a bridging cyanido ligand. Again, due to the limitations of crystallography, the coordination of the C/N atoms to a specific Fe center could not be determined, and thus, both conformations were modelled. There is no difference in the bond metrics for either confirmation. The cyanido ligand binds in a μ-(1,2) fashion to the Fe centers with a distance of 2.47 Å and an Fe–C/N–C/N bond angle of 109°. The bound cyanido ligand also forms a 5-membered chelate ring with the two Fe centers and the μ-oxido bridging atom. It is important to note that the Fe···Fe' distance shortened to 3.73 Å with an Fe–O2–Fe' bond angle of 132° (Figure 4.21A, 4.21B, and 4.23B, Tables 4.1, 4.6, and 4.7). Thus, the cyanide studies highlight that using two-atom bridging ligands also successfully decreases the

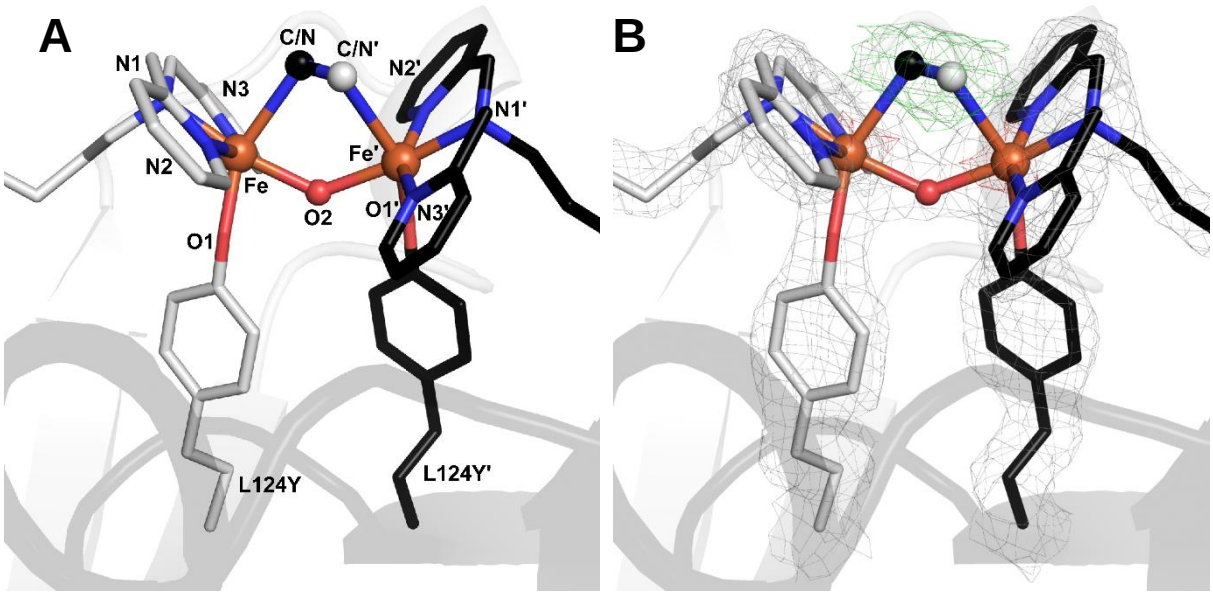

Figure 4.21 Molecular structure of **Precious–CN** (**A** & **B**). For the structure in **B**, the position of the Fe^{III}-bu-dpa complex is indicated by the $2F_o$-F_c electron density map (grey, contoured at 1 σ), and anomalous difference density (red, contoured at 3 σ), and the cyanido ligand position is indicated with the F_o-F_c omit map (green, contoured at 3 σ). Fe ions are colored in orange, N atoms are in blue, and O atoms/water molecules are colored in red. H-bonds are displayed as dashed black lines. Two subunits are shown (grey and black).

distance between the two Fe centers, and forms a di-Fe ArM with an Fe⋯Fe' distance that is comparable to that in native di-Fe proteins.

Summary and Conclusions

In this chapter, new di-Fe ArMs were constructed, and an optical screen was developed to help elucidate the placement of the Fe^{III} complexes within Sav. The optical screen employed three new protein variants, S_{112}Y-Sav, K_{121}Y-Sav, and K_{121}A-L_{124}Y-Sav, in conjunction with two analogous ligands to biot-et-dpa (Chapter 2), biot-pr-dpa and biot-bu-dpa. The optical study suggested that the optimal linker length to form an Fe^{III}–O_{Tyr} bond was butyl. The combination of biot-bu-dpa with K_{121}A-L_{124}Y-Sav resulted in the controlled formation of a di-Fe species within Sav. Mössbauer spectroscopy suggested that the O-atom bridge between the two Fe centers was a μ-oxo atom, and UV-vis and rR studies supported the coordination of the phenolate group from the tyrosine amino acid residue at position 124 to the Fe centers. Further studies varied the Fe⋯Fe' distance from 3.7-4 Å by adding various bridging ligands (OAc, N_3, SCN, or CN).

The structural results indicate that it is difficult for the Fe⋯Fe distance to contract below 3.7 Å. In fact, all doubly bridged centers had a small variation in the Fe⋯Fe distance (3.9-3.7 Å) and only a slight change was observed in **Precious–CN**. One explanation for why the Fe centers could be brought no closer together than 3.7 Å is the two anchor points in the di-Fe ArMs: the biotin moiety and the tyrosine amino acid residue. The biotin anchor on the synthetic complex is locked into place by a series of H-bonds and cannot move. The tyrosine amino acid residue cannot move significantly because of a steric interaction with a second tyrosine amino acid residue in the opposing subunit of the Sav dimer. The phenyl rings of the tyrosine amino acid residues have a $centroid_{ph}$-$centroid_{ph}$ distance of ~5 Å,

which allows for a π-stacking interaction that positions them pointing directly up towards the open solvent channel of the Sav vestibule. The new di-Fe ArMs with phenolate coordination and the optical screen described in this chapter provide a foundation from which to design more biologically relevant di-Fe ArMs that have a resting state of Fe^{II} and that are capable of activating dioxygen and oxidizing substrates.

Experimental Details

General Methods. All commercially available reagents were obtained in the highest purity and used as received. Ethanol (EtOH) and diethyl ether were degassed with argon and dried by vacuum filtration through activated alumina according to the procedure by Grubbs.[183] Triethylamine was distilled from KOH. Thin-layer chromatography (TLC) was performed on Merck 60 F254 aluminum-backed silica plates or Merck 60 F254 glass-backed basic aluminum oxide plates. Eluted plates were visualized using UV light. Silica or basic alumina gel chromatography was performed with the indicated solvent system using Fisher reagent silica gel 60 (230-400 mesh) or Sigma reagent Brockmann 1 basic aluminum oxide 58 (150 mesh). Biotin pentafluorophenol ester (biot-PFP)[184] and di-(2-picolyl)amine[185] were prepared according to literature procedures. The ligand biot-et-dpa and Fe^{III} complex $[Fe^{III}(\text{biot-et-dpa})(OH_2)_3]Cl_3$ were prepared as described in Chapter 2. The ligands biot-pr-dpa and biot-bu-dpa and Fe^{III} complexes $[Fe^{III}(\text{biot-pr-dpa})(OH_2)_3]Cl_3$ and $[Fe^{III}(\text{biot-bu-dpa})(OH_2)_3]Cl_3$ were prepared with slight modifications to the procedures detailed in Chapter 2.

Physical Methods

Instrumentation. ^1H NMR spectra were recorded at 500 MHz. ^1H NMR spectra were reported in ppm on the δ scale and referenced to tetramethylsilane or solvent residual. The

data are presented as follows: chemical shift, multiplicity (s = singlet, d = doublet, t = triplet, q = quartet, quin = quintet, m = multiplet, br = broad), and integration. Mass spectra were measured on a MicroMass AutoSpec E, a MicroMass Analytical 7070E, or a MicroMass LCT Electrospray instrument. Electronic absorbance spectra were recorded with a Cary 50 or 8453 Agilent UV-vis spectrophotometer. X-band (9.64 GHz and 9.32 GHz) EPR spectra were recorded on a Bruker spectrometer equipped with Oxford liquid helium cryostats. The quantification of all signals was performed relative to a CuEDTA spin standard. The concentration of the standard was derived from an atomic absorption standard (Aldrich). For all instruments, the microwave frequency was calibrated with a frequency counter and the magnetic field with an NMR gaussmeter. A modulation frequency of 100 kHz was used for all EPR spectra. The EPR simulation software (SpinCount) was written by our collaborating author, Michael P. Hendrich.[186] Mössbauer spectra were recorded with a Janis Research Super-Varitemp dewar. Isomer shifts are reported relative to Fe metal at 298 K.

Preparative Methods

2-(2-(bis(pyridin-2-ylmethyl)amino)propyl)isoindoline-1,3-dione.[137] **2-(2-(bis(pyridin-2-ylmethyl)amino)propyl)isoindoline-1,3-dione** was prepared analogously to literature procedures to yield a yellow oil (42%). ^{1}H (500 mHz, $CDCl_3$) δ 8.48 (d, 2H), 7.82 (dd, 2H), 7.71 (dd, 2H) 7.63 (t, 2H), 7.54 (d, 2H), 7.11 (t, 2H), 3.85 (m, 4H), 3.70 (t, 2H), 2.63 (t, 2H), 1.91 (m, 4H). MS (ESI, MeOH) *m/z* calcd $C_{23}H_{22}N_4O_2$ [M + (H^+)] 386.17, found 386.92.

***N,N*-bis(pyridin-2-ylmethyl)propane-1,2-diamine**.[137] ***N,N*-bis(pyridin-2-ylmethyl)propane-1,2-diamine** was prepared analogously to literature procedures to yield a yellow oil (55%). ^{1}H (500 mHz, $CDCl_3$) δ 8.53 (d, 2H), 7.65 (t, 2H), 7.52 (d, 2H) 7.14

(t, 2H), 3.81 (s, 4H), 2.70 (t, 2H), 2.60 (t, 2H), 1.68 (q, 2H). MS (ESI, MeOH) *m/z* calcd $C_{15}H_{20}N_4$ [M + (Na^+)] 279.16, found 279.14.

biot-pr-dpa.[137] **biot-pr-dpa** was prepared analogously to literature procedures to yield a tan solid (83%). ^1H (500 mHz, DMSO) δ 8.48 (d, 2H), 7.77 (br, 1H), 7.75 (t, 2H) 7.50 (d, 2H), 7.25 (t, 2H), 6.42 (s, 1H), 6.35 (s, 1H), 4.31 (t, 1H), 4.11 (t, 1H), 3.71 (s, 4H), 3.03 (m, 1H), 3.01 (q, 2H), 2.81 (dd, 1 H), 2.57 (d, 1 H), 2.46 (t, 1H), 2.46 (s, 2H), 2.00 (t, 2H), 1.62 (m, 8H). MS (ESI, MeOH) *m/z* calcd $C_{25}H_{34}N_6O_2S$ [M + (Na^+)] 505.24, found 505.17.

2-(2-(bis(pyridin-2-ylmethyl)amino)butyl)isoindoline-1,3-dione.[137] **2-(2-(bis(pyridin-2-ylmethyl)amino)butyl)isoindoline-1,3-dione** was prepared according to literature procedure to yield a yellow oil. The crude product was purified via column chromatography with silica gel and CH_3OH:DCM (0.5:9.5) as the eluent (44%). ^1H (500 mHz, $CDCl_3$) δ 8.49 (d, 2H), 7.82 (dd, 2H), 7.71 (dd, 2H) 7.63 (t, 2H), 7.53 (d, 2H), 7.12 (t, 2H), 3.79 (m, 4H), 3.63 (t, 2H), 2.57 (t, 2H), 1.67 (m, 2H), 1.57 (m, 2H). MS (ESI, MeOH) *m/z* calcd $C_{24}H_{24}N_4O_2$ [M + (H^+)] 401.2, found 401.3.

***N,N*-bis(pyridin-2-ylmethyl)butane-1,2-diamine**.[137] ***N,N*-bis(pyridin-2-ylmethyl)butane-1,2-diamine** was prepared according to literature procedure to yield a yellow oil (65%). ^1H (500 mHz, $CDCl_3$) δ 8.52 (d, 2H), 7.65 (t, 2H), 7.52 (d, 2H) 7.14 (t, 2H), 3.81 (s, 4H), 2.62 (t, 2H), 2.55 (t, 2H), 1.57 (m, 2H), 1.41 (m, 2H), 1.41 (br, 2H). MS (ESI, MeOH) *m/z* calcd $C_{16}H_{22}N_4$ [M + (H^+)] 271.2, found 271.4.

biot-bu-dpa.[137] **biot-bu-dpa** was prepared according to literature procedure to yield a light tan solid (64%). ^1H (500 mHz, DMSO) δ 8.47 (d, 2H), 7.77 (br, 1H), 7.75 (t, 2H) 7.51 (d, 2H), 7.25 (t, 2H), 6.40 (s, 1H), 6.34 (s, 1H), 4.29 (t, 1H), 4.11 (t, 1H), 3.70 (s, 4H), 3.07 (m,

2H), 2.97 (q, 1 H), 2.78 (dd, 1 H), 2.57 (d, 1H), 2.43 (t, 2H), 2.03 (t, 2H), 1.33 (m, 10H). MS (ESI, MeOH) *m/z* calcd $C_{26}H_{36}N_6O_2S$ [M + (Na^+)] 519.18, found 519.19.

Preparation of Metal Complexes

[Fe^{III}(biot-pr-dpa)(OH_2)$_3$]Cl_3.[187] [Fe^{III}(biot-pr-dpa)(OH_2)$_3$]Cl_3 was prepared according to literature procedure to yield a yellow solid (77%). HRMS (ESI, MeOH) *m/z* calcd for $C_{27}H_{40}Cl_2FeN_6O_2S$ [M – ($3Cl^-$) + (OCH_3)$_2$] 600.22, found 600.21. Elem. Anal. Calcd for ($C_{25}H_{40}N_6SO_5FeCl_3$): C, 42.96; H, 5.77; N, 12.03. Found: C, 42.56; H, 5.07; N, 11.89.

[Fe^{III}(biot-bu-dpa)(OH_2)$_3$]Cl_3.[187] [Fe^{III}(biot-bu-dpa)(OH_2)$_3$]Cl_3 was prepared according to literature procedure to yield a yellow solid (96%). HRMS (ESI, MeOH) *m/z* calcd for $C_{28}H_{42}Cl_2FeN_6O_2S$ [M – ($3Cl^-$) + (OCH_3)$_2$] 614.23, found 614.21. Elem. Anal. Calcd for ($C_{26}H_{42}N_6SO_5FeCl_3$): C, 43.80; H, 5.94; N, 11.79. Found: C, 43.69; H, 5.49; N, 11.65.

Spectroscopic methods

HABA Titrations. To 2.4 mL of 8 μM Sav in 200 mM sodium phosphate buffer at pH 7 was added 300 μL of a 10 mM 2-(4′-hydroxyazobenzene)benzoic acid (HABA) solution in 200 mM phosphate buffer pH 7. After 5 min of equilibration, the absorbance at 506 nm was recorded. A solution of 1 mM Fe complex in nanopure water was added in 4-20 μL portions until approximately 4 equivalents of the appropriate Fe complex had been added. The absorbance at 506 nm was recorded until no further changes in intensity were observed.

Electronic Absorption Studies. A solution of lyophilized protein (50-250 μM) was prepared in nanopure water. Four equivalents of Fe complex (0.2-1 mM) in nanopure water were added to the protein solution. Samples were prepared in a final volume of 500 μL with nanopure water. It is **important** to note that all solution experiments had to be performed in nanopure water. Any buffer that was used (Good's, phosphate, >100 mM acetate) or the

organic solvent DMF disrupted the Fe–phenolate interaction and **Precious** could not be made.

EPR Studies. A solution of protein (500 μM) was prepared in nanopure water. Four equivalents of Fe complex (2 mM) in nanopure water were added to the protein solution. Samples were prepared in a final volume of 200 μL with nanopure water. The sample was transferred to an EPR tube and frozen at 77 K in liquid nitrogen, and data were collected at 10 K.

Mössbauer studies. A solution of protein (500 μM) was prepared in nanopure water. Four equivalents of Fe complex (2 mM) in nanopure water were added to the protein solution. Samples were prepared in a final volume of 300 μL with nanopure water. The sample was prepared in a solution Mössbauer cup, frozen at 77 K in liquid nitrogen, and run at 4 K.

XAS Studies. A solution of protein (750 μM) was prepared in nanopure water. Four equivalents of Fe complex (3 mM) in nanopure water were added to the protein solution. Samples were prepared in a final volume of 250 uL with nanopure water and 30% glycerol. The sample was pipetted into a small delrin solution cell and frozen at 77 K in liquid nitrogen.

XAS data collection and processing. In collaboration with Dr. Andrew Jasniewski, Fe K-edge X-ray absorption spectra were collected on SSRL beam line 9-3 using a 100-element Ge monolith solid-state detector (Canberra) with a SPEAR3 storage ring current of ~500 mA at an energy of 3.0 GeV. The beam line 9-3 optics consist of a flat, bent, harmonic rejection vertically collimating Rh-coated Si M_0 mirror as well as a cylindrical, bent, Rh-coated focusing M_1 mirror. A total of six Fe K-edge scans were taken between 6882 and 8000 eV at ~10 K using an Oxford Instruments CF1208 continuous flow liquid helium cryostat using an

open-cycle liquid He dewar (BL 9-3). An Fe foil was placed in the beam pathway prior to the ionization chamber I_0 and scanned concomitantly for an energy calibration, with the first inflection point of the edge assigned to 7112.0 eV. A Soller slit with a 3 μm Mn filter was used to increase the signal to noise ratio of the spectra. Photoreduction was monitored by scanning the same spot on the sample twice and comparing the first derivative peaks associated with the edge energy during data collection.

The detector channels from the scans were examined, calibrated, averaged, and processed using EXAFSPAK.[189] Theoretical phase and amplitude parameters for a given absorber-scatterer pair were calculated using FEFF 8.40[190] and subsequently applied to the nonlinear least squares 'opt' fitting program of the EXAFSPAK package during curve fitting. Parameters for each species were calculated using an appropriate model derived from the crystal structure. In all analyses, the coordination number of a given shell (N) was a fixed parameter and was varied iteratively in integer steps, whereas the bond lengths (R) and mean-square deviation (σ^2) were allowed to freely float. The estimated uncertainties in R, σ^2, and N are 0.02 Å, 0.1 × 10^{-3} Å^2, and 20%, respectively. The amplitude reduction factor S_0 was fixed at 1.0 for the Fe K-edge data, whereas the edge-shift parameter ΔE_0 was allowed to float as a single value for all shells. Thus, in any given fit, the number of floating parameters was typically equal to 2 × number of shells + 1. The goodness of fit (GOF) parameters are calculated as follows:

$$F = \sqrt{\sum k^6 \left(\chi_{\exp} - \chi_{calc}\right)^2}$$

$$F' = \sqrt{\sum k^6 \left(\chi_{\exp} - \chi_{calc}\right)^2 / \sum k^6 \chi_{\exp}{}^2}$$

Pre-edge analysis was performed on the Fe K-edge fluorescence data normalized to have an edge jump of 1.0 at 7130 eV in the "process" program of the EXAFSPAK package. The pre-edge features were fit as described elsewhere[3] between 7108 eV to 7118 eV using the Fityk[276] program with pseudo-Voigt functions composed of 50:50 Gaussian/Lorentzian functions.

rR studies. A solution of protein (1.25 mM) was prepared in nanopure water. Four equivalents of Fe complex (5 mM) in nanopure water were added to the protein solution. Samples were prepared in a final volume of 300 μL with nanopure water. The sample was prepared in an Eppendorf tube, frozen at 195 K in dry ice (for shipping purposes), and run at room temperature.

rR data collection and processing. In collaboration with the Möenne-Loccoz lab, rR spectra were obtained at room temperature on samples in glass capillaries (3-5 mM concentration in Fe) using a 90° geometry with a custom McPherson 2061/207 spectrograph equipped with a liquid N_2-cooled CCD detector (LN-1100PB, Princeton Instruments). The 647-nm excitation was derived from a Kr laser (Innova 302, Coherent). A long-pass filter (RazorEdge, Semrock) was used to attenuate Rayleigh scattering. Comparison of rapid acquisitions with a range of laser power and continuous sample translation with longer data acquisitions provided no evidence of photosensitivity for all the Sav samples. The integrity of the rR samples was confirmed by direct monitoring of their UV-vis absorption spectra in Raman capillaries before and after laser exposure. Frequencies were calibrated relative to indene and are accurate to ±1 cm^{-1}. Polarization conditions were optimized using CCl_4 and indene.

FTIR studies. In collaboration with the Möenne-Loccoz lab, low-temperature FTIR photolysis with the azido complex was performed as previously described with slight modifications.[277–

[279] Approximately 15 μL of protein solution (5 mM in Fe) was deposited as a droplet on a CaF_2 window, and a second CaF_2 window was gently dropped on the sample to form an optical cell with a pathlength controlled by a 15-μm Teflon spacer. The FTIR cell was mounted to a closed-cycle cryogenic system (Displex, Advanced Research System). The unit was placed inside the sample compartment of the FTIR and kept in the dark during cooling down to 30 K. The temperature of the sample was monitored and controlled with a Cryo-Con 32 unit. FTIR spectra were obtained on a Bruker Vertex 80 equipped with a liquid N_2-cooled MCT detector. Sets of 1000-scan accumulations were acquired at 4-cm^{-1} resolution. Photolysis of the azido ligand was performed by continuous illumination of the sample directly in the FTIR sample chamber using a 300-W arc lamp after filtering out heat and NIR emissions. The complete reversibility of the photolysis process was confirmed by reproducing the same FTIR difference spectra after raising the sample temperature above 120 K, allowing rebinding of the photolyzed group to the Fe site.

Protein Preparation and Crystallography

Protein Expression and Purification

Preparation of Sav variants. The construction of K_{121}A-L_{124}Y-Sav and other variants was achieved by site-directed mutagenesis (SDM) using the codon optimized K_{121}A-pET24a-Sav plasmid,[191] the following primers and, and Q5 polymerase.

L_{124}Y_fwd: 5'-CAGCACCTATGTTGGTCATGATACCTTTC-3'

L_{124}Y_rev: 5'-CACCAACATAGGTGCTTTTCCAGGCATTC-3'

Amplification of pET24a-Sav mutant plasmids was accomplished by the transformation of SDM reaction mixtures into DH5α ultracompetent cells. Plasmids were isolated using a

Miniprep kit from Qiagen, eluting the final plasmid with distilled deionized-water (ddH_2O, 18 MΩ cm^{-1}). DNA sequencing was performed by Genewiz.

Sav Expression. Transformation of 4 µL amplified plasmids into 50 µL Rosetta cells or bl21 cells was followed by rescue with 450 µL LB media. Of this solution, 200 µL was spread aseptically onto LB/Kanamycin agar plates and incubated overnight at 37 °C. Inoculation of a starter culture containing 500 mL LB media and the same antibiotic from a single colony was followed by incubation overnight at 37 °C and shaking at 225 rpm. From this starter culture, 25 mL was used to inoculate each 2L flask containing 500 mL LB media, 25 mL each of 20x sugar (12% glycerol, 1% glucose, 10% lactose) and salt (1 M Na_2HPO_4, 1 M KH_2PO_4, 0.5 M $(NH_4)_2SO_4$) stocks, 1 mL of 1 M $MgSO_4$, 100 µL 5000x trace metal mix (containing 1 M $CaCl_2$, 100 mM $FeCl_3$, 10 mM $MnCl_2$, 10 mM $ZnSO_4$, 2 mM $CoCl_2$, 2 mM $CuCl_2$, 2 mM $NiCl_2$, 2 mM Na_2MoO_4, and 2 mM H_3BO_3 all in 60 mM HCl), and 250 µL of 100 mg/mL Kanamycin. Incubation at 37 °C and 225 rpm was continued until cells reached OD_{600} = 0.6–0.8, at which point the temperature was dropped to 25 °C and cultures incubated another 24 h.

Sav purification. Cultures were centrifuged at 4000 x *g* for 20 min at 4 °C. The resulting cell pellet was resuspended in lysis buffer (50 mL per 1 L expressed) containing 20 mM Tris buffer pH 7.4, 1 mg/mL lysozyme, and a spatula tip of DNase I. The suspension was then allowed to shake at 25 °C and 225 rpm for 6-8 h followed by one overnight freeze-thaw cycle. Dialysis against 6 M guanidinium hydrochloride pH 1.5 for 24 h was followed by neutralization via dialysis against 20 mM Tris buffer pH 7.4 for 24 h, and against nanopure H_2O for another 24 h. Dialysis overnight against iminobiotin (IB) buffer containing 500 mM NaCl and 50 mM $NaHCO_3$ at pH 10.5 afforded the crude, biotin-free lysate. This material was centrifuged at 10,000 x *g* for 1 h at 4 °C and the soluble portion loaded onto an iminobiotin-

agarose column pre-equilibrated with IB buffer. The column was washed with 6 column volumes (CVs) of IB buffer or until the absorbance at 280 nm (A_{280}) dropped to zero. Elution with 1% acetic acid in nanopure H_2O, and pooling fractions by A_{280}, provided highly pure (>95%) Sav as assessed by 18% SDS-PAGE. Pooled fractions were dialyzed against 10 mM Tris pH 7.4 for 24 h followed by dialysis in ddH_2O for an additional 72 h and were then lyophilized. Yields of lyophilized protein were typically 100 mg per L expressed, and the solid protein was stored at 4 °C.

Protein Crystallization

*Crystallization of [Fe_2^{III}(biot-bu-dpa)$_2$(OAc)(μ–O)($O_{Y_{124}}$)$_2$⊂K_{121}Y-L_{124}Y-Sav] (**Precious**).* Apo-Sav protein was crystallized by the sitting drop vapor diffusion method. Diffraction-quality crystals were grown at room temperature by mixing 4 μL of protein solution (26 mg/mL lyophilized protein in water) and 1 μL of crystallization buffer (2.0 ammonium sulfate, 0.1 M sodium acetate, pH 4). The droplet was equilibrated against a reservoir solution of 100 μL crystallization buffer. Single crystals of Sav were prepared by soaking apo-crystals in a soaking buffer (3.0 ammonium sulfate) with a 10 mM stock solution of [Fe^{III}(biot-bu-dpa)$(OH_2)_3$]Cl_3 in nanopure water (9 μL crystallization buffer, 1 μL [Fe^{III}(biot-bu-dpa)$(OH_2)_3$]Cl_3 overnight. After the soaking, crystals were transferred to cryo-protectant for 1 min (30% glycerol in crystallization buffer) and shock-frozen in liquid nitrogen. An **important** note is that the 0.1 M sodium acetate must be removed for successfully soaking the [Fe^{III}(biot-bu-dpa)$(OH_2)_3$]Cl_3 complex into K_{121}Y-L_{124}Y-Sav. If acetate is present in the soaking step, the crystals will not turn blue.

*Crystallization of [Fe_2^{III}(biot-bu-dpa)$_2$(μ–1,3–OAc)(μ–O)($O_{Y_{124}}$)$_2$⊂K_{121}Y-L_{124}Y-Sav] (**Precious–OAc**).* Apo-Sav protein was crystallized by the sitting drop vapor diffusion method.

Diffraction-quality crystals were grown at room temperature by mixing 4 µL of protein solution (26 mg/mL lyophilized protein in water) and 1 µL of crystallization buffer (2.0 ammonium sulfate, 0.1 M sodium acetate, pH 4). The droplet was equilibrated against a reservoir solution of 100 µL crystallization buffer. Single crystals of Sav were prepared by soaking apo-crystals in a soaking buffer (3.0 ammonium sulfate) with a 10 mM stock solution of $[Fe^{III}(biot\text{-}bu\text{-}dpa)(OH_2)_3]Cl_3$ in nanopure water (9 µL crystallization buffer, 1 µL $[Fe^{III}(biot\text{-}bu\text{-}dpa)(OH_2)_3]Cl_3$ overnight. Once the crystals turned blue, they were soaked in the soaking buffer (3 M ammonium sulfate) with a 1 M stock of NaOAc in nanopure water for 1-5 min (9 µL soaking buffer, 1 µL NaOAc). After the second soaking, the crystals were transferred to cryo-protectant for 1 minute (30% glycerol in soaking buffer) and shock-frozen in liquid nitrogen.

*Crystallization of $[Fe_2^{III}(biot\text{-}bu\text{-}dpa)_2(\mu\text{–}1,3\text{–}N_3)(\mu\text{–}O)(O_{Y_{124}})_2 \subset K_{121}Y\text{-}L_{124}Y\text{-}Sav$ (**Precious–N_3**)].* Apo-Sav protein was crystallized by the sitting drop vapor diffusion method. Diffraction-quality crystals were grown at room temperature by mixing 4 µL of protein solution (26 mg/mL lyophilized protein in water) and 1 µL of crystallization buffer (2.0 ammonium sulfate, 0.1 M sodium acetate, pH 4). The droplet was equilibrated against a reservoir solution of 100 µL crystallization buffer. Single crystals of Sav were prepared by soaking apo-crystals in a soaking buffer (3.0 ammonium sulfate) with a 10 mM stock solution of $[Fe^{III}(biot\text{-}bu\text{-}dpa)(OH_2)_3]Cl_3$ in nanopure water (9 µL crystallization buffer, 1 µL $[Fe^{III}(biot\text{-}bu\text{-}dpa)(OH_2)_3]Cl_3$ overnight. Then, the crystals were soaked in the soaking buffer (3 M ammonium sulfate) with a 1 M stock of NaN_3 in nanopure water for 1-5 min (9 µL soaking buffer, 1 µL NaOAc). After the second soaking, the crystals were transferred to

cryo-protectant for 1 minute (30% glycerol in soaking buffer) and shock-frozen in liquid nitrogen.

*Crystallization of [Fe_2^{III}(biot-bu-dpa)$_2$(μ–1,3–SCN)(μ–O)(O_{Y124})$_2$⊂K_{121}Y-L_{124}Y-Sav (**Precious–SCN**)].* Apo-Sav protein was crystallized by the sitting drop vapor diffusion method. Diffraction quality crystals were grown at room temperature by mixing 4 μL of protein solution (26 mg/mL lyophilized protein in water) and 1 μL of crystallization buffer (2.0 ammonium sulfate, 0.1 M sodium acetate, pH 4). The droplet was equilibrated against a reservoir solution of 100 μL crystallization buffer. Single crystals of Sav were prepared by soaking apo-crystals in a soaking buffer (3.0 ammonium sulfate) with a 10 mM stock solution of [Fe^{III}(biot-bu-dpa)(OH_2)$_3$]Cl_3 in nanopure water (9 μL crystallization buffer, 1 μL [Fe^{III}(biot-bu-dpa)(OH_2)$_3$]Cl_3 overnight. Then, the crystals were soaked in the soaking buffer (3 M ammonium sulfate) with a 1 M stock of NaSCN in nanopure water for 1-5 min (9 μL soaking buffer, 1 μL NaOAc). After the second soaking, the crystals were transferred to cryo-protectant for 1 minute (30% glycerol in soaking buffer) and shock-frozen in liquid nitrogen.

*Crystallization of [Fe_2^{III}(biot-bu-dpa)$_2$(μ–1,3–SCN)(μ–O)(O_{Y124})$_2$⊂K_{121}Y-L_{124}Y-Sav (**Precious–CN**)].* Apo-Sav protein was crystallized by the sitting drop vapor diffusion method. Diffraction quality crystals were grown at room temperature by mixing 4 μL of protein solution (26 mg/mL lyophilized protein in water) and 1 μL of crystallization buffer (2.0 ammonium sulfate, 0.1 M sodium acetate, pH 4). The droplet was equilibrated against a reservoir solution of 100 μL crystallization buffer. Single crystals of Sav were prepared by soaking apo-crystals in a soaking buffer (3.0 ammonium sulfate) with a 10 mM stock solution of [Fe^{III}(biot-bu-dpa)(OH_2)$_3$]Cl_3 in nanopure water (9 μL crystallization buffer, 1

μL $[Fe^{III}(biot\text{-}bu\text{-}dpa)(OH_2)_3]Cl_3$ overnight. Then, the crystals were soaked in the soaking buffer (3 M ammonium sulfate) with a 1 M stock of NaCN in nanopure water for 1-5 min (9 μL soaking buffer, 1 μL NaOAc). After the second soaking, the crystals were transferred to cryo-protectant for 1 minute (30% glycerol in soaking buffer) and shock-frozen in liquid nitrogen.

X-ray diffraction data collection processing. X-ray diffraction data were collected at the Stanford Synchrotron Radiation Lightsource (BL 12.2) and the Advanced Light Source (BL 5.0.2. and 8.2.1) at a wavelength of 1 Å. Data were collected with helical (SSRL) or vector (ALS) data collection using exposure time/frame 0.2/0.2 s/deg or 0.5/1 s/deg. Helical or vector collection was used because it decreases the amount of radiation damage on the crystal, which ensures better quality data. Additionally, using these collection techniques helps ensure that the exogenous ligands are not dissociated during the collection time. X-ray diffraction data were processed with XDS[192] or iMosflm and scaled with AIMLESS (CCP4 Suite). The structures were solved by molecular replacement using program PHASER (CCP4 Suite) and the structure 2QCB from the PDB as input model ligand with water molecules removed. For structure refinement, REFMAC5 (CCP4 Suite) and PHENIX.REFINE were used. Ligand manipulation was carried out with program REEL using the small molecule crystal structure RAGQEV01 from the Cambridge Structural Database as an input model. For water picking, electron density, and structure visualization, the software COOT[197] was used. Figures were drawn with PyMOL (the PyMOL Molecular Graphics System, Version 1.8.2.3, Schrödinger, LLC). Crystallographic details, processing and refinement statistics are given in Supplementary Table 4.2-4.7.

Structural Results.

Crystal Color. All crystals of Sav soaked with the complex $[Fe^{III}(biot\text{-}bu\text{-}dpa)(OH_2)_3]Cl_3$ changed from colorless to dark blue. Crystals soaked with NaOAc remained dark blue. Crystals soaked with NaN_3 changed from dark blue to dark red. Crystals soaked with NaSCN changed to a greenish, blue color. Crystals soaked with NaCN changed to a purple-blue color.

Structural Refinement. Apo-crystals of proteins $K_{121}A\text{-}L_{124}Y$-Sav soaked with $[Fe^{III}(biot\text{-}bu\text{-}dpa)(OH_2)_3]Cl_3$ constituted space group $I4_122$ with unit cell parameters reported in Tables 4.2 and 4.6. A single Sav monomer was obtained per asymmetric unit after molecular replacement. Protein residues 2-10 and 135-159 of the N- and C-terminus, respectively, were not resolved in the electron density, presumably due to disorder. Starting from the Sav monomer, the biological homotetramer is generated by application of crystallographic C_2-symmetry axes along the x-, y- and z-axes of the unit cell. The overall protein structures are virtually identical to structure biotin ⊂ WT-Sav (PDB 1STP, see Tables 4.2, 4.4, and 4.6).

Because the crystallographic C_2-symmetry axis lies directly at the interface where the two monomers of Sav connect, the apo-crystals of proteins $K_{121}A\text{-}L_{124}Y$-Sav soaked with $[Fe^{III}(biot\text{-}bu\text{-}dpa)(OH_2)_3]Cl_3$ were also solved in reduced C121 symmetry to ensure that the bridging atoms were not artifacts of symmetry. The unit cell parameters are reported in Table 4.4 and 4.6. A single Sav tetramer was obtained per asymmetric unit after molecular replacement.

General Complex Modeling. For all structures of apo-protein crystals soaked with the corresponding Fe-complexes, the following general observations were made: i) residual electron density in the $F_o\text{-}F_c$ map was observed in the biotin binding pocket, ii) the biotin vestibule is flanked by protein residues of loop-$3,4^A$ (the superscript number indicates Sav

monomer within tetramer) loop-4,5^{C}, loop-5,6^{A} loop-7,8^{A} and loop-7,8^{B}, and iii) an anomalous dispersion density map indicated a significant peak in the biotin vestibule superimposed with the electron density peak. The residual electron density was fit with the corresponding Fe-complexes, which projected Fe to the position of the strong anomalous density peak.

Structural Refinement of ***Precious***. In the $I4_122$ symmetry solution, the biot-bu-dpa ligand, μ-oxo bridging ligand, and tyrosine amino acid residues are modelled with 100% occupancy. The Fe center is modelled with 60% occupancy due to a large amount of negative density. There are several reasons there could be negative density around the Fe center: 1) the crystal was collected at an energy of 1 Å, which is far from the 1.7 Å Fe edge energy, 2) at a higher symmetry, the Fe centers are close to the center of symmetry for the monomer of Sav, and 3) there is disorder associated with the entire chelator portion of the biotinylated complex [Fe^{III}(biot-bu-dpa)]. Due to the disorder associated with the pyridine groups of the biotinylated ligand, there could be movement of the pyridyl groups and Fe center, which would cause negative density to arise around the Fe center.

In the C121 symmetry solution (Figure 4.24, Table 4.4, 4.5, 4.8), the biot-bu-dpa ligands, μ-oxo bridging ligand, and tyrosine amino acid residues are modelled with 100% occupancy. However, the Fe center is modelled with 80% occupancy. The increase of the occupancy of the Fe center can be possibly explained by the change in the asymmetric unit. In the lower symmetry solution, the asymmetric unit is the tetramer of Sav, which means that the center of symmetry is no longer between the two monomers of Sav that constitute one dimer. Without this center of symmetry, it is possible that the negative density around the Fe center lessened as it is being contributed to by the disorder of the pyridyl rings still.

Structural Refinement of ***Precious–OAc***. For the solution of **Precious–OAc**, the biot-bu-dpa ligands, μ-oxo bridging ligand, Fe centers, and tyrosine amino acid residues are modelled with 100% occupancy. However, there is a discrepancy between the $I4_122$ and the C121 symmetry solution (Figure 4.25, Tables 4.4, 4.5, and 4.9). In the higher symmetry structure, the μ-oxo bridging ligand is fit with 100% occupancy. In contrast, in the lower symmetry solution, the resolved structure revealed that one Sav dimer had all the components that the higher symmetry solution had, the acetate and μ-oxo bridging ligand. In the opposite Sav dimer, the acetato bridging ligand was present with similar bond distances to the Fe centers and Fe···Fe' bond distance but the μ-oxo bridging ligand was missing. When solving a molecular structure with a lower symmetry (C121) than what the symmetry of the crystal is actually ($I4_122$), the resolution of the structure is decreased (1.50 to 1.65 Å). One possible reason for the missing density of the μ-oxo bridging ligand is because there is not sufficient resolution to see the atom. With the bond distances of the di-Fe active site remaining similar between the two dimers, this is a likely reason for the discrepancy between the two structures. Two solutions were attempted to determine if the occupancy of the μ-oxo bridging ligand was assigned correctly. First, In the $I4_122$ symmetry solution, the occupancy was decreased to 25% from 50%. In the higher symmetry solution, the symmetry mate of the monomer reveals that the bridging ligands are in the same x,y,z coordinates as the solved structure. For this reason, the occupancy is initially decreased to 50% when solving $I4_122$ structures. The solution gave an increased amount of density in the F_o-F_c map, indicating that the occupancy was incorrect. Second, in the C121 symmetry, the occupancy was decreased to 50% from 100% for the μ-oxo bridging ligand that was present. The solution showed no new F_o-F_c density in the opposite dimer where there was

no μ-oxido bridging ligand, indicating that the occupancy was incorrect. With the results from the two occupancy tests, it is likely that the μ-oxo bridging ligand density is not present because of resolution restraints.

Structural Refinement of ***Precious–N$_3$***. For the solution of **Precious–N$_3$**, the biot-bu-dpa ligands, μ-oxo bridging ligand, Fe centers, and tyrosine amino acid residues are modelled with 100% occupancy. However, there is a discrepancy in bond distances to the azido bridging ligand between the I4$_1$22 and C121 symmetry solutions (Figure 4.26, Tables 4.4, 4.5, 4.10). In the I4$_1$22 symmetry solution, the bond distance between Fe–N4 of the azido ligand is 2.45 Å; however, in the C121 symmetry solution, the bond distance Fe–N4/Fe'–N6 is 2.32 Å as an average of the Sav tetramer. One possible reason for the 0.13 Å difference in bond distance is because the azido ligand is located at the center of symmetry in the I4$_1$22 symmetry solution. If a ligand is directly on the center of symmetry in a molecular structure, it can be difficult to determine accurate bond distances because of symmetry artifacts in the F_o-F_c map. Additionally, there is density above the azido ligand that is present until ~5 σ in the F_o-F_c map. Another conformation of the azido or an acetato ligand was attempted to fit in the extra density. The azido ligand was modelled as binding to only one Fe center rather than bridging. Any fit attempted resulted in increased density in the F_o-F_c map around the bridging azido ligand and negative density around the second conformation of the azido ligand. Additionally, the position of the bridging azido ligand would change and not fit the $2F_o$-F_c density well to allow for the placement of the second azido ligand conformation. Similar results were found when attempting to place an acetato ligand with the bridging azido ligand. If there is an additional ligand present that fits the F_o-F_c density well, the ligand will only have ~1-10% occupancy.

Structural refinement of ***Precious–SCN***. For the solution of **Precious–SCN**, the biot-bu-dpa ligands, μ-oxo bridging ligand, Fe centers, and tyrosine amino acid residues are modelled with 100% occupancy. Only the $I4_122$ symmetry solution was obtained for **Precious–SCN** because attempts to solve in the C121 symmetry decreased the resolution of the structure to ~2.2 Å, and it was difficult to determine the location of both the isothiocyanato and μ-oxo bridging ligands. From the $I4_122$ symmetry solution, it is not possible to determine the location of the S atom or the N atom of the isothiocyanato ligand by XRD. For this reason, the molecular structure shows both conformations of the bridged isothiocyanato ligand.

Structural refinement of ***Precious–CN***. For the solution of **Precious–CN**, the biot-bu-dpa ligands, μ-oxo bridging ligand, Fe centers, and tyrosine amino acid residues are modelled with 100% occupancy. For both the $I4_122$ and C121 symmetry solutions, there is extra density in the F_o-F_c map above the cyanido ligand (Figure 4.27, Tables 4.6, 4.7, 4.11). In the $I4_122$ symmetry solution, it is possible that there is a second conformation of the cyanido ligand, where instead of bridging in a μ-(1,2) fashion to the two Fe centers, the cyanido ligand instead binds one cyanido ligand to one Fe center. The solution of this second conformation was attempted. However, the cyanido ligands are less than 1 Å apart, which makes this solution chemical unreasonable. In the C121 symmetry solution, placing the cyanido ligand bridging in a μ-(1,2) fashion between the two Fe centers matches the F_o-F_c density well and does not support a second conformation. With the C121 symmetry solution, it is possible that the second conformation of the cyanido ligand might be a symmetry artifact because again, the cyanido ligand is lies on the center of symmetry for the monomeric Sav.

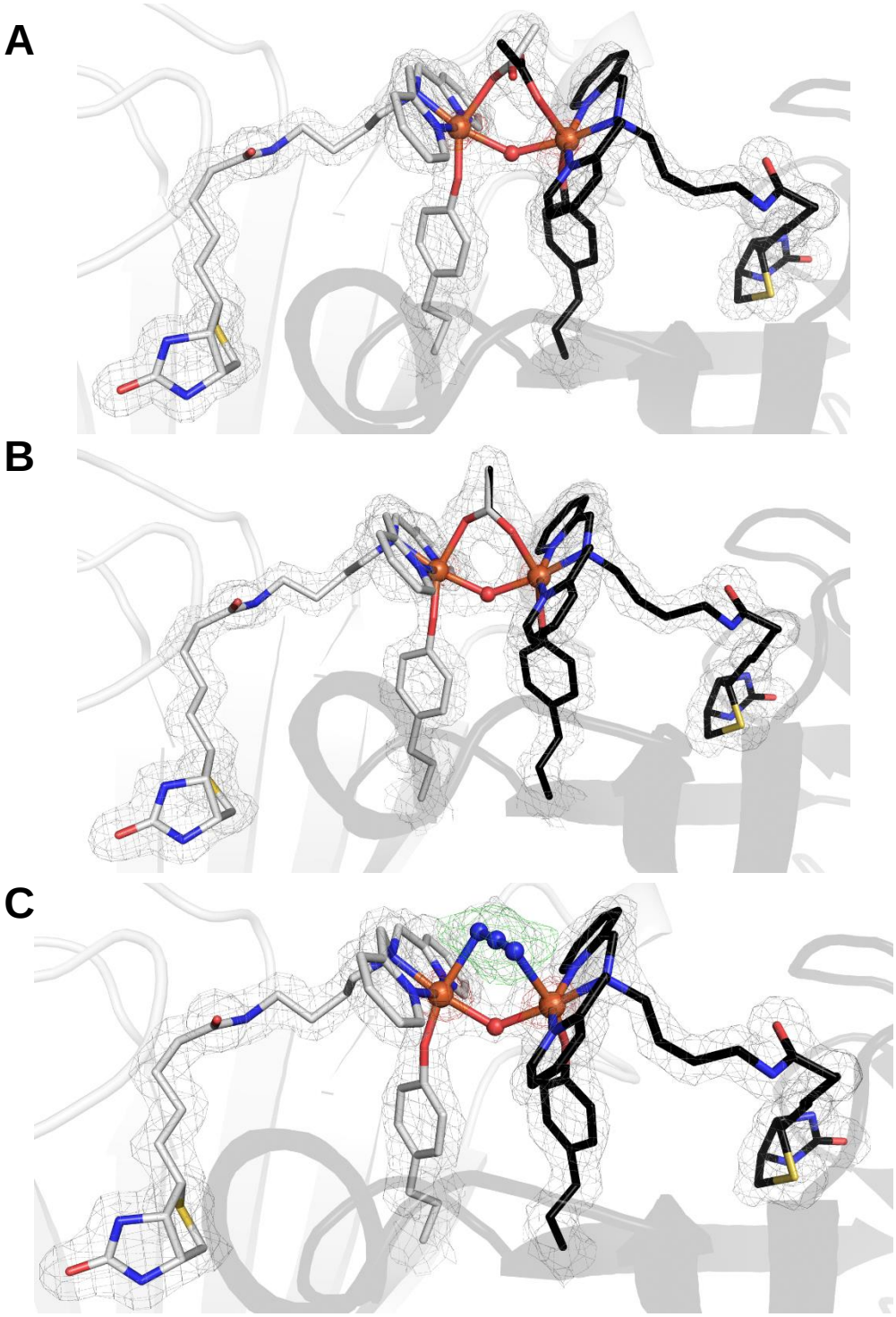

Figure 4.22 Close-up views of the Fe sites in the molecular structure of **Precious** (**A**), **Precious–OAc** (**B**), and **Precious–N_3** (**C**). For clarity, only one Sav dimer is displayed. The protein is displayed in cartoon representation, and the Fe complex and residues 124 are displayed as sticks. The position of the ligand molecules is indicated by the $2F_o$-F_c electron density (grey, contoured at 1 σ) and anomalous difference density (red, contoured at 4 σ; for C, contoured at 3 σ). Fe is colored in orange, N atoms are in blue, and O atoms/water molecules are in red. The number schemes in **A**, **B,** and **C** are the same as those in Figure 4.11B, 4.15A, and 4.17A.

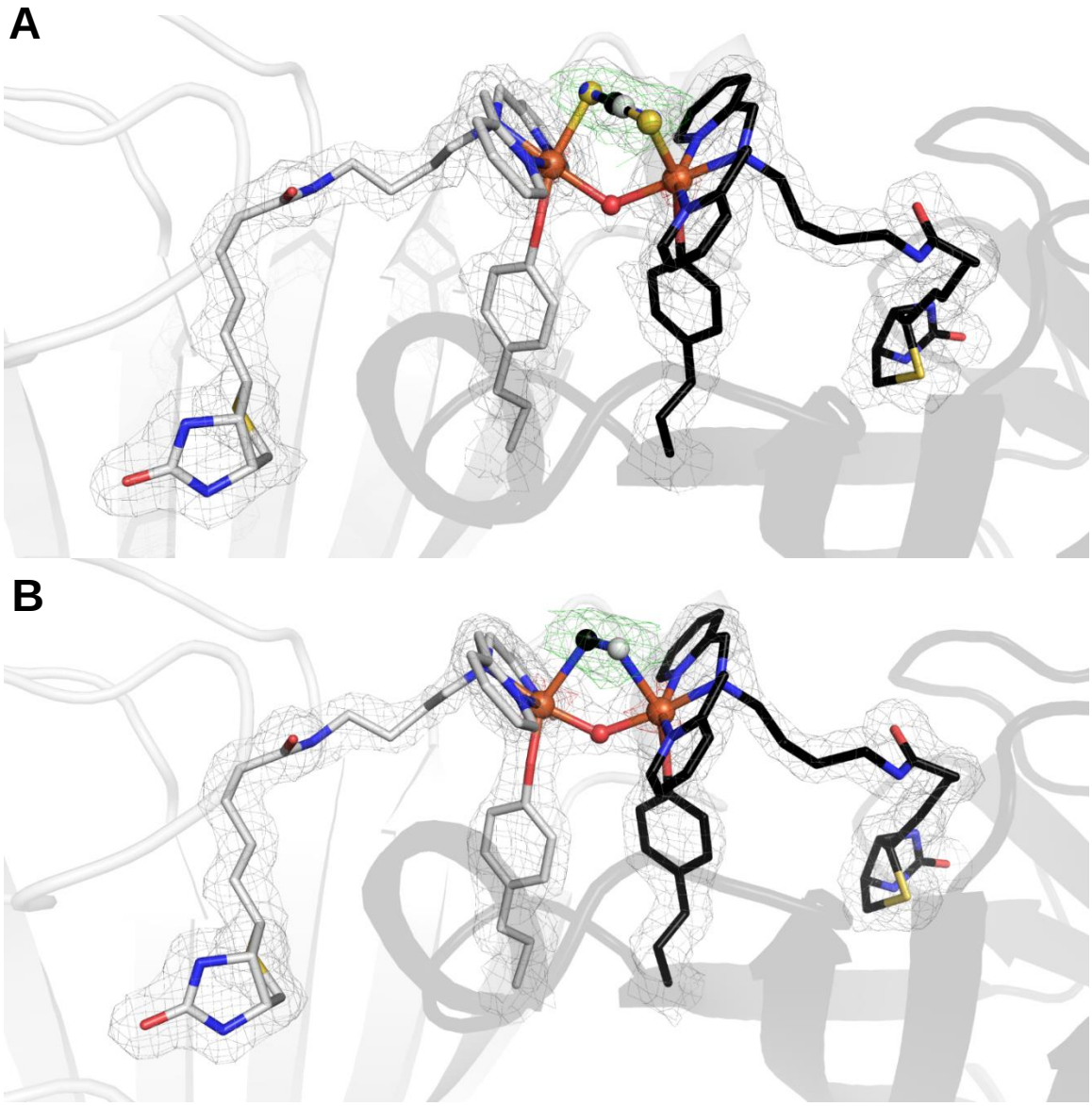

Figure 4.23 Close-up views of the Fe sites in the molecular structures of **Precious–SCN** (**A**) and **Precious–CN** (**B**). For clarity, only one Sav dimer is displayed. The protein is displayed in cartoon representation, and the Fe complex and residues 124 are displayed as sticks. The position of the ligand molecules is indicated by the $2F_o$-F_c electron density (grey, contoured at 1 σ) and anomalous difference density (red, contoured at 4 σ; for C, contoured at 3 σ). Fe is colored in orange, N atoms are in blue, S atoms are in yellow, and O atoms/water molecules are in red. The number schemes in **A** and **B** are the same as those in Figure 4.19A and 4.21A.

Dimer A

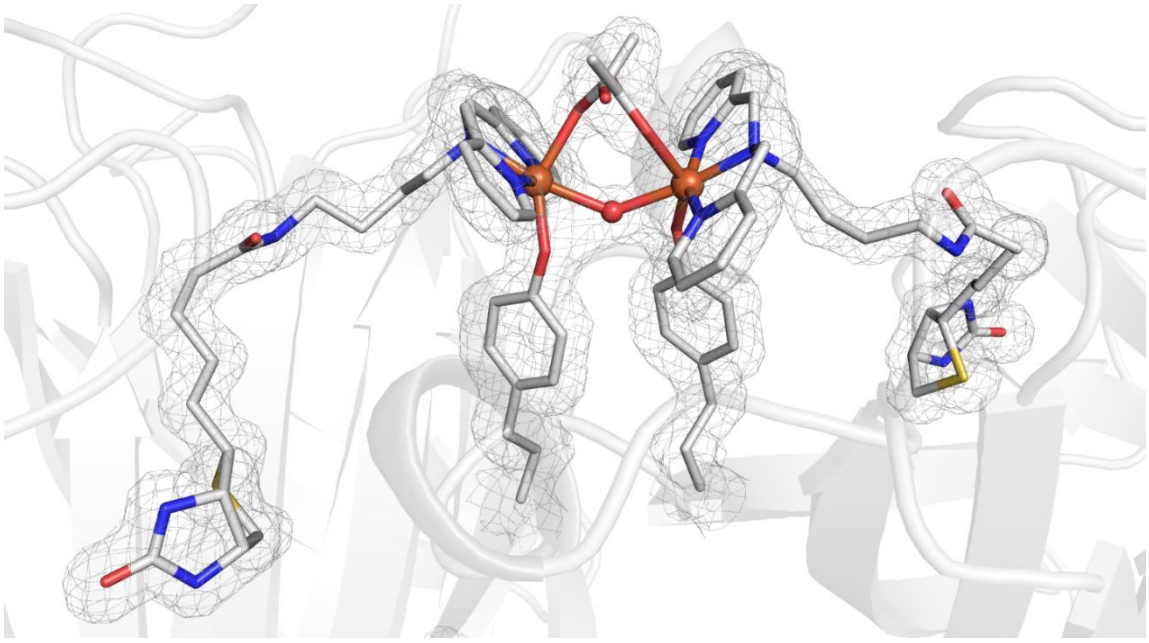

Dimer B

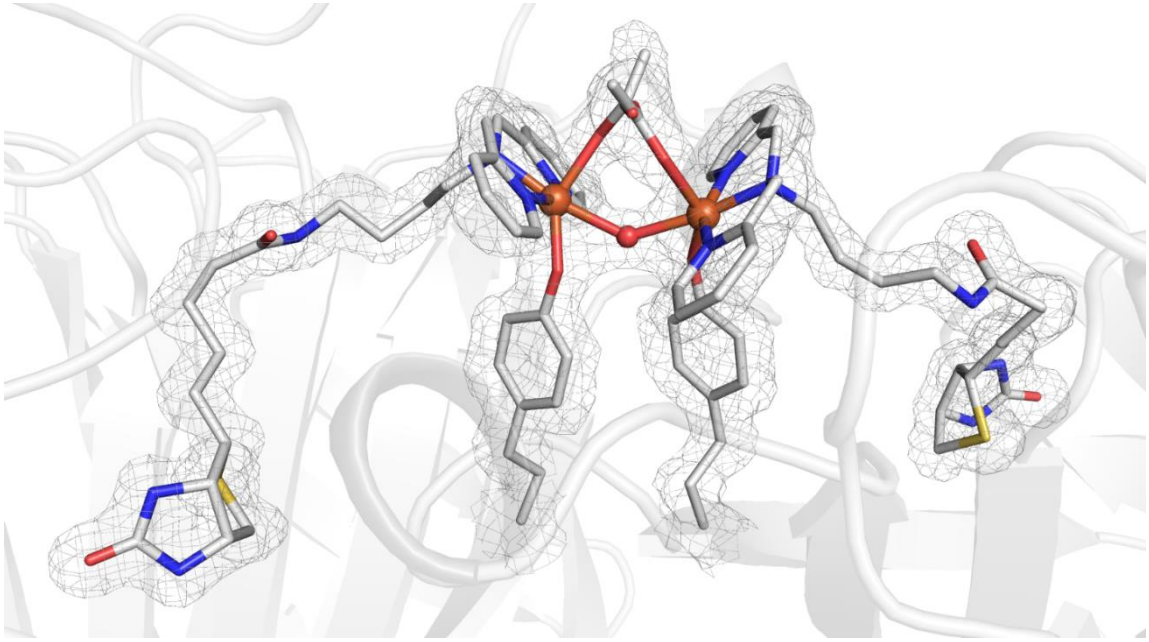

Figure 4.24 Close-up views of the Fe sites in the molecular structure of **Precious** solved in C121 symmetry. **Dimers A** and **B** of the tetrameric Sav are shown for clarity. The protein is displayed in cartoon representation, and the Fe complex and residues 124 are displayed as sticks. The position of the ligand molecules is indicated by the $2F_o$-F_c electron density (grey, contoured at 1 σ). Fe is colored in orange, N atoms are in blue, and O atoms/water molecules are in red. The number schemes in **Dimer A** and **Dimer B** are the same as those in Figure 4.11B.

Dimer A

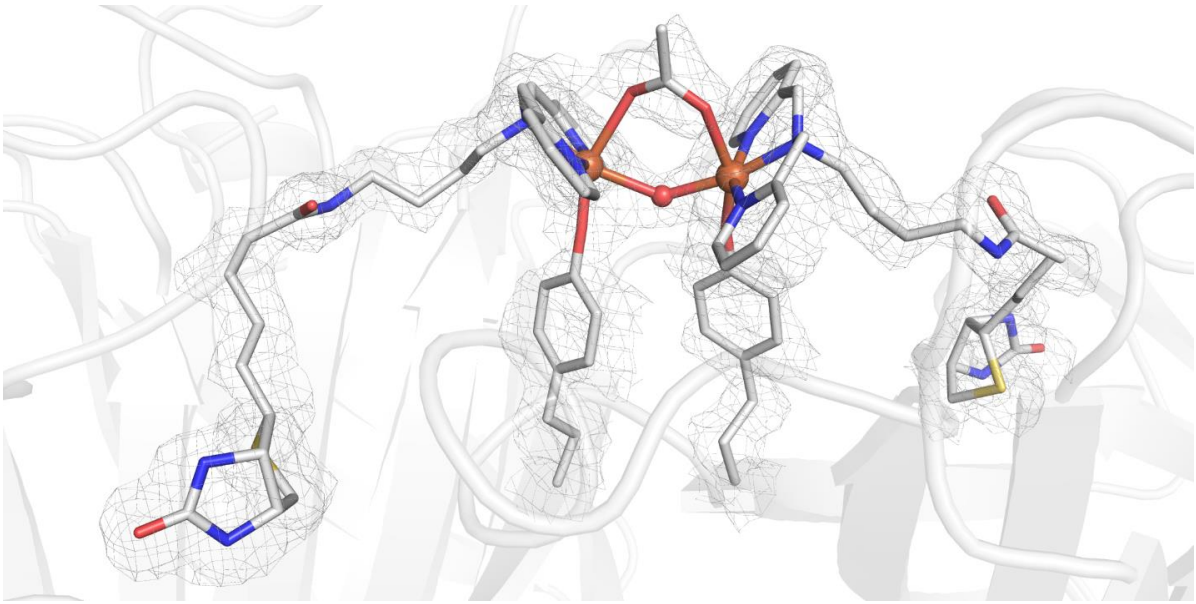

Dimer B

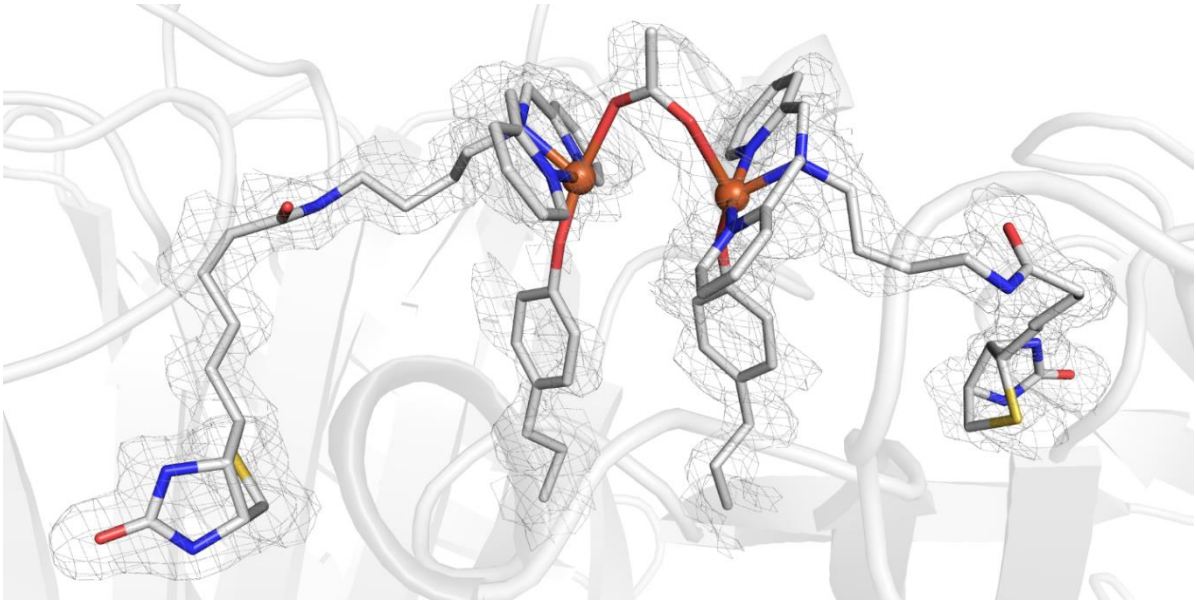

Figure 4.25 Close-up views of the Fe sites in the molecular structure of **Precious–OAc** solved in C121 symmetry. **Dimers A** and **B** of the tetrameric Sav are shown for clarity. The protein is displayed in cartoon representation, and the Fe complex and residues 124 are displayed as sticks. The position of the ligand molecules is indicated by the $2F_o$-F_c electron density (grey, contoured at 1 σ). Fe is colored in orange, N atoms are in blue, and O atoms/water molecules are in red. The number schemes in **Dimer A** and **Dimer B** are the same as those in Figure 4.15A.

Dimer A

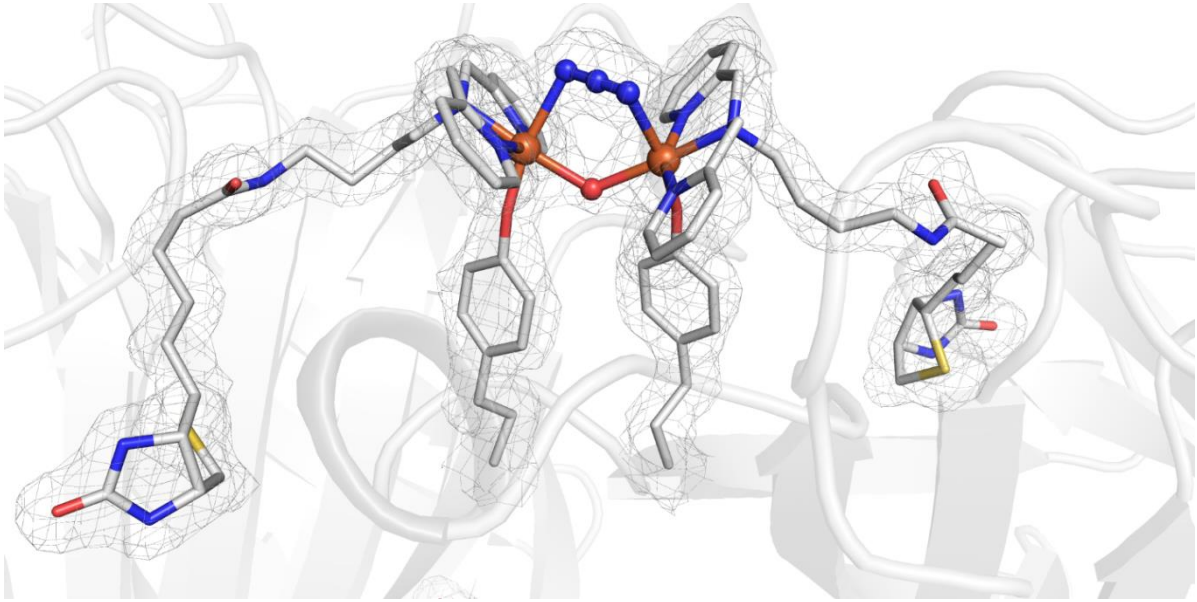

Dimer B

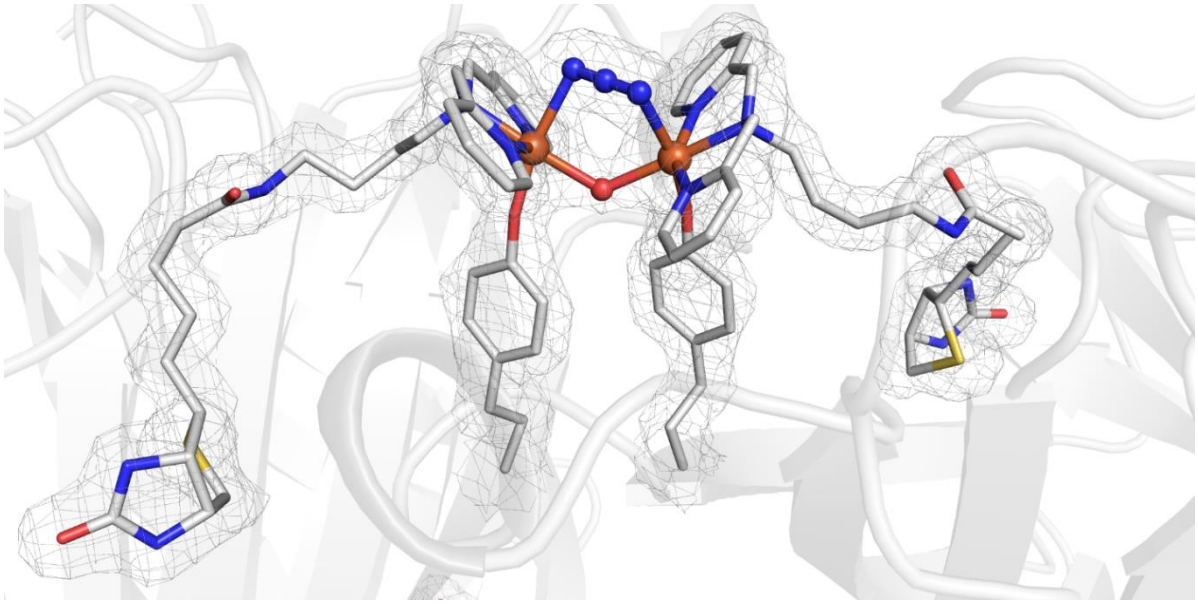

Figure 4.26 Close-up views of the Fe sites in the molecular structure of **Precious–N_3** solved in C121 symmetry. **Dimers A** and **B** of the tetrameric Sav are shown for clarity. The protein is displayed in cartoon representation, and the Fe complex and residues 124 are displayed as sticks. The position of the ligand molecules is indicated by the $2F_o$-F_c electron density (grey, contoured at 1 σ). Fe is colored in orange, N atoms are in blue, and O atoms/water molecules are in red. The number schemes in **Dimer A** and **Dimer B** are the same as those in Figure 4.17A.

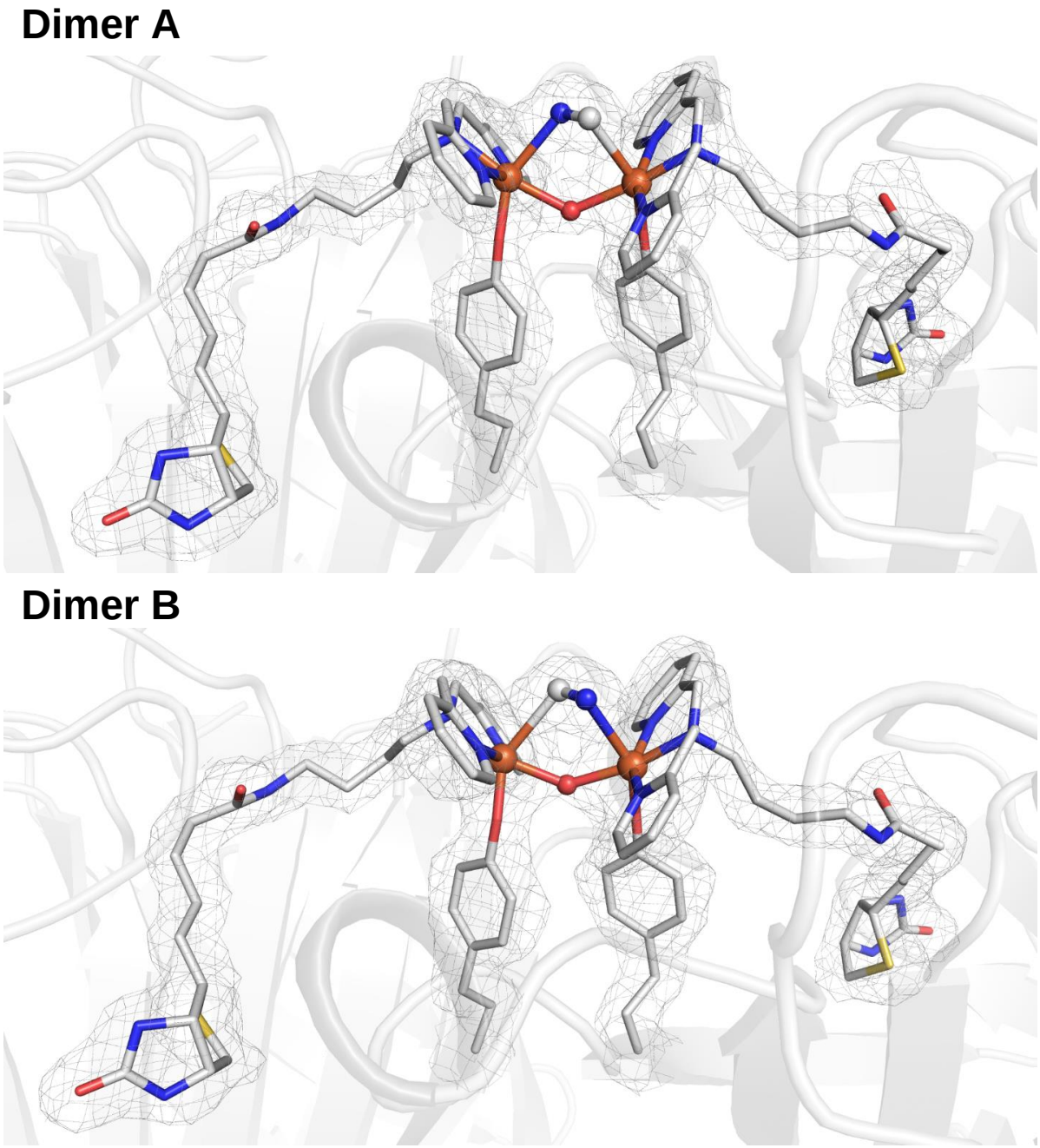

Figure 4.27 Close-up views of the Fe sites in the molecular structure of **Precious–CN** solved in C121 symmetry. **Dimers A** and **B** of the tetrameric Sav are shown for clarity. The protein is displayed in cartoon representation, and the Fe complex and residues 124 are displayed as sticks. The position of the ligand molecules is indicated by the $2F_o$-F_c electron density (grey, contoured at 1 σ). Fe is colored in orange, N atoms are in blue, and O atoms/water molecules are in red. The number schemes in **Dimer A** and **Dimer B** are the same as those in Figure 4.21A.

Table 4.1 Selected bond lengths and (Å) and angles (°) for **Precious**, **Precious–OAc**, **Precious–N_3**, **Precious–SCN**, and **Precious–CN**.

Bond lengths and angles	**Precious**	**Precious–OAc**	**Precious–N_3**	**Precious–SCN**	**Precious–CN**
Fe–O1	1.78	1.82	1.81	1.82	1.83
Fe–O2	2.10	2.12	2.14	2.16	2.04
Fe–O3	2.17	2.20	–	–	–
Fe'–O4	3.39	2.23	–	–	–
Fe–S/N	–	–	–	2.42	–
Fe–N1	2.03	2.06	2.10	2.06	2.08
Fe–N2	1.98	1.99	2.02	2.02	2.01
Fe–N3	1.91	1.92	1.97	1.93	1.94
Fe–N4	–	–	2.45	–	–
Fe'–N6	–	–	2.45	–	–
Fe–C/N	–	–	–	–	2.47
O1–Fe–N2	87	82	86	83	85
O1–Fe–N1	127	121	110	115	116
O1–Fe–N3	110	112	105	111	108
O2–Fe–N2	108	105	109	110	109
O3–Fe–O1	146	151	–	–	–
O3–Fe–O2	79	86	–	–	–
O3–Fe–N1	87	84	–	–	–
O3–Fe–N2	99	91	–	–	–
O3–Fe–N3	78	86	–	–	–
O1–Fe–N4	–	–	165	–	–
O1–Fe–O2	68	70	78	68	74
N1–Fe–N2	77	77	75	74	76
N1–Fe–N3	76	78	77	77	76
N1–Fe–N4	–	–	85	–	–
N1–Fe–O2	165	170	172	175	169
N2–Fe–N3	153	155	152	151	152
N2–Fe–N4	–	–	96	–	–
N3–Fe–N4	–	–	80	–	–
N3–Fe–O2	97	100	99	99	99
N4–Fe–O2	–	–	88	–	–
Fe–O2–Fe'	141	134	126	122	132
Fe···Fe'	3.96	3.91	3.82	3.77	3.73
Fe–N4–N5	–	–	96	–	–
Fe–S/N–C	–	–	–	90	–
N2–Fe–S/N	–	–	–	100	–
N1–Fe–S/N	–	–	–	82	–
N3–Fe–S/N	–	–	–	75	–
O2–Fe–S/N	–	–	–	94	–
O1–Fe–S/N	–	–	–	162	–
O1–Fe–C/N	–	–	–	–	149
O2–Fe–C/N	–	–	–	–	80
N1–Fe–C/N	–	–	–	–	91
N2–Fe–C/N	–	–	–	–	87
N3–Fe–C/N	–	–	–	–	93
Fe–C/N–C/N	–	–	–	–	109

Table 4.2 X-ray Crystallography Data Processing and Refinement Statistics for $I4_122$ symmetry solutions of **Precious**, **Precious–OAc**, and **Precious–N_3**.

Identification			
Sav Mutant	$K_{121}A$-$L_{124}Y$	$K_{121}A$-$L_{124}Y$	$K_{121}A$-$L_{124}Y$
Fe complex	$[Fe_2^{III}$(biot-bu-dpa)$_2$(OAc)(μ–O)$(O_{Y_{124}})_2]$ (**Precious**)	$[Fe_2^{III}$(biot-bu-dpa)$_2$(μ–1,3–OAc)(μ–O)$(O_{Y_{124}})_2]$ (**Precious–OAc**)	$[Fe_2^{III}$(biot-bu-dpa)$_2$(μ–1,3–N_3)(μ–O)$(O_{Y_{124}})_2]$ (**Precious–N_3**)
PDB Code	6VOZ	6VO9	6VOB
Fe complex PDB 3-letter code	KM3	KM3	KM3
Data Processing			
Unit Cell	a, b, c = 57.7 Å, 57.7 Å, 184.2 Å α, β, γ = 90°	a, b, c = 57.9 Å, 57.9 Å, 184.7 Å α, β, γ = 90°	a, b, c = 57.7 Å, 57.7 Å, 183.8 Å α, β, γ = 90°
Space Group	$I4_122$	$I4_122$	$I4_122$
Resolution (Å)	37.29 – 1.30	46.16 – 1.50	55.02 – 1.70
Highest resolution shell (Å)	1.32 – 1.30	1.53 – 1.50	1.73 – 1.70
R_{merge} (%)	7.1 (145)	8.2 (71)	17 (193)
No. of unique reflections	38785 (1888)	21730 (953)	17637 (897)
Multiplicity	13.3 (12.6)	6.4 (5.4)	25.4 (24.5)
I/Sig(I)	19.2 (1.5)	11.6 (1.9)	17.0 (2.6)
Completeness	99.9 (99.2)	84.5 (75.3)	100 (100)
CC(1/2)	0.999 (0.79)	0.993 (0.81)	0.998 (0.772)
Beamline	SSRL 12.2	SSRL 12.2	ALS 8.2.1
Structure Refinement			
R_{work}	0.18	0.18	0.17
R_{free}	0.20	0.21	0.20
Rmsd bond length (Å)	0.018	0.014	0.016
Rmsd bond angle (°)	2.840	2.865	2.712
Rmsd compared to biotin-Sav WT (PDB 1STP) (Å)	0.64	0.65	0.63
No. ligands			
Fe complex	1	1	1
Water	119	93	95
Acetate	1	1	1

Table 4.3 Summary of structural details for **Precious**, **Precious–OAc**, and **Precious–N_3**.

PDB Code	6VOZ	6VO9	6VOB
Complex	**Precious**	**Precious–OAc**	**Precious–N_3**
Electron density at Fe in F_o–F_c omit map (σ)	19	25	25
Anomalous dispersion density at Fe (σ)	10	5	9
Geometry of Fe complex	Distorted octahedral	Distorted octahedral	Distorted octahedral
Coordination number of Fe complex	6	6	6
Occupancy of Fe complex (%)	60	100	100
B-factor (Å^2)			
Overall protein	19	17	17
L124Y	20	20	22
K121A	15	14	14
Fe complex	29	22	22
DPA	28	22	21
Fe	28	30	30
Acetate	24	27	–
Azide	–	–	25
Distance Fe–Fe (Å)	3.96	3.91	3.82

Table 4.4 X-ray Crystallography Data Processing and Refinement Statistics for C121 symmetry solutions of **Precious**, **Precious–OAc**, and **Precious–N_3**.

Identification			
Sav Mutant	$K_{121}A$-$L_{124}Y$	$K_{121}A$-$L_{124}Y$	$K_{121}A$-$L_{124}Y$
Fe complex	$[Fe_2^{III}$(biot-bu-dpa)$_2$(OAc)(μ–O)$(O_{Y_{124}})_2]$ (**Precious**)	$[Fe_2^{III}$(biot-bu-dpa)$_2$(μ–1,3–OAc)(μ–O)$(O_{Y_{124}})_2]$ (**Precious–OAc**)	$[Fe_2^{III}$(biot-bu-dpa)$_2$(μ–1,3–N_3)(μ–O)$(O_{Y_{124}})_2]$ (**Precious–N_3**)
PDB Code	6VP1	6VP3	6VP2
Fe complex PDB 3-letter code	KM3	KM3	KM3
Data Processing			
Unit Cell	a, b, c = 193.0 Å, 57.7 Å, 57.7 Å α, β, γ = 90°, 107.4°, 90°	a, b, c = 193.5 Å, 57.9 Å, 57.9 Å α, β, γ = 90°, 107.4°, 90°	a, b, c = 192.8 Å, 57.6 Å, 57.7 Å α, β, γ = 90°, 107.4°, 90°
Space Group	C121	C121	C121
Resolution (Å)	37.29 – 1.45	46.16 – 1.65	55.00 – 1.80
Highest resolution shell (Å)	1.47 – 1.45	1.68 – 1.65	1.84 – 1.80
R_{merge} (%)	5.4 (66)	7.4 (28)	14 (92)
No. of unique reflections	104561 (5170)	47899 (2078)	55911 (3174)
Multiplicity	3.6 (3.3)	2.4 (2.3)	6.8 (6.4)
I/Sig(I)	13.0 (2.4)	7.7 (2.3)	10.2 (2.4)
Completeness	97.6 (97.2)	65.2 (57.7)	99.6 (98)
CC(1/2)	0.989 (0.795)	0.989 (0.905)	0.995 (0.765)
Beamline	SSRL 12.2	SSRL 12.2	ALS 8.2.1
Structure Refinement			
R_{work}	0.18	0.18	0.17
R_{free}	0.20	0.22	0.20
Rmsd bond length (Å)	0.016	0.013	0.013
Rmsd bond angle (°)	3.022	2.868	2.679
Rmsd compared to biotin-Sav WT (PDB 1STP) (Å)	0.63	0.64	0.63
No. ligands			
Fe complex	4	4	4
Water	214	498	424
Acetate	2	2	–
Azide	–	–	2

Table 4.5 Summary of structural details for **Precious**, **Precious–OAc**, and **Precious–N_3**.

PDB Code	6VP1	6VP3	6VP2
Complex	**Precious**	**Precious–OAc**	**Precious–N_3**
Electron density at Fe in F_o–F_c omit map (σ)	19	20	25
Anomalous dispersion density at Fe (σ)	–	–	–
Geometry of Fe complex	Distorted octahedral	Distorted octahedral	Distorted octahedral
Coordination number of Fe complex	6	6	6
Occupancy of Fe complex (%)	80	100	100
B-factor (Å²)			
Overall protein	18	16	17
L124Y	20	20	23
K121A	15	14	14
Fe complex	29	22	22
DPA	28	22	21
Fe	34	28	31
Acetate	27	28	–
Azide	–	–	23
Dimer A Distance Fe–Fe (Å)	4.01	3.95	3.75
Dimer B Distance Fe–Fe (Å)	3.99	4.02	3.71

*B-factors were averaged from the Sav tetramer

Table 4.6 X-ray Crystallography Data Processing and Refinement Statistics for $I4_122$ and C121 symmetry solutions of **Precious–SCN** and **Precious–CN**.

Identification			
Sav Mutant	$K_{121}A$-$L_{124}Y$	$K_{121}A$-$L_{124}Y$	$K_{121}A$-$L_{124}Y$
Fe complex	$[Fe_2^{III}$(biot-bu-dpa)$_2$(μ–1,3–SCN)(μ–O)$(O_{Y_{124}})_2]$ (**Precious–SCN**)	$[Fe_2^{III}$(biot-bu-dpa)$_2$(μ–1,2–CN)(μ–O)$(O_{Y_{124}})_2]$ (**Precious–CN**)	$[Fe_2^{III}$(biot-bu-dpa)$_2$(μ–1,3–CN)(μ–O)$(O_{Y_{124}})_2]$ (**Precious–CN**)
PDB Code	Unpublished	Unpublished	Unpublished
Fe complex PDB 3-letter code	KM3	KM3	KM3
Data Processing			
Unit Cell	a, b, c = 57.7 Å, 57.7 Å, 184.0 Å α, β, γ = 90°	a, b, c = 57.6 Å, 57.6 Å, 183.5 Å α, β, γ = 90°	a, b, c = 192.3 Å, 57.6 Å, 57.6 Å α, β, γ = 90°, 107.4°, 90°
Space Group	$I4_122$	$I4_122$	C121
Resolution (Å)	55.05 – 1.90	45.86 – 1.70	45.86 – 1.90
Highest resolution shell (Å)	1.94 – 1.90	1.73 – 1.70	1.94 – 1.90
R_{merge} (%)	134 (1239)	21 (184)	15 (82)
No. of unique reflections	12788 (804)	17537 (899)	45992 (2913)
Multiplicity	14.4 (14.4)	11.7 (11.7)	3.3 (3.0)
I/Sig(I)	5.0 (3.2)	9.1 (1.8)	6.3 (1.7)
Completeness	100 (100)	100 (100)	97.1 (96.3)
CC(1/2)	0.577 (0.323)	0.997 (0.380)	0.990 (0.467)
Beamline	ALS 8.2.1	ALS 5.0.2	ALS 5.0.2
Structure Refinement			
R_{work}	0.22	0.19	0.19
R_{free}	0.27	0.22	0.12
Rmsd bond length (Å)	0.011	0.013	0.016
Rmsd bond angle (°)	2.709	2.685	2.705
Rmsd compared to biotin-Sav WT (PDB 1STP) (Å)	0.63	0.64	0.62
No. ligands			
Fe complex	1	1	1
Water	122	71	275
SCN	1	–	–
CN	–	1	2

Table 4.7 Summary of structural details for **Precious–SCN** and **Precious–CN**.

PDB Code	Unpublished	Unpublished	Unpublished
Complex	**Precious–SCN**	**Precious–CN** ($I4_122$)	**Precious–CN** (C121)
Electron density at Fe in F_o–F_c omit map (σ)	19	21	17
Anomalous dispersion density at Fe (σ)	5	5	–
Geometry of Fe complex	Distorted octahedral	Distorted octahedral	Distorted octahedral
Coordination number of Fe complex	6	6	6
Occupancy of Fe complex (%)	100	100	100
B-factor (Å^2)			
Overall protein	11	21	22
L124Y	18	27	30
K121A	8	18	21
Fe complex	17	34	36
DPA	17	33	35
Fe	26	46	55
Isothiocyanate	20	–	–
Cyanide	–		24
Fe–Fe (Å)	3.77	3.73	
Dimer A Distance Fe–Fe (Å)	–	–	3.83
Dimer B Distance Fe–Fe (Å)	–	–	3.82

*B-factors were averaged from the Sav tetramer

Table 4.8 Precious bond lengths and distances from C121 symmetry solution.

Bond lengths (Å) and angles (°)	**Monomer 1**	**Monomer 2**	**Monomer 3**	**Monomer 4**
Fe–O1	1.88	1.90	1.86	1.89
Fe–O2	2.16	2.14	2.16	2.12
Fe–O3	2.22	–	2.15	–
Fe'–O3'		2.18	–	2.13
Fe'–O4	–	3.60	–	3.50
Fe–O4'	3.56	–	3.57	–
Fe–N1	2.03	2.03	2.03	2.03
Fe–N2	1.94	1.95	1.94	1.95
Fe–N3	1.97	1.97	1.97	1.98
Dimer A (1 & 2)			**Dimer B (3 & 4)**	
Fe–O2–Fe'	138		138	
Fe···Fe'	4.01		3.99	

Table 4.9 Precious–OAc bond lengths and distances from C121 symmetry solution.

Bond lengths (Å) and angles (°)	**Monomer 1**	**Monomer 2**	**Monomer 3**	**Monomer 4**
Fe–O1	1.78	1.69	1.76	1.81
Fe–O2	2.05	2.26	–	–
Fe–O3	2.22	–	2.18	–
Fe'–O4	–	2.35	–	2.40
Fe–N1	2.03	2.02	2.05	2.02
Fe–N2	1.98	1.95	1.99	1.97
Fe–N3	1.91	1.93	1.92	1.90
Dimer A (1 & 2)			**Dimer B (3 & 4)**	
Fe–O2–Fe'	132		–	
Fe···Fe'	3.95		4.02	

Table 4.10 Precious–N_3 bond lengths and distances from C121 symmetry solution.

Bond lengths (Å) and angles (°)	**Monomer 1**	**Monomer 2**	**Monomer 3**	**Monomer 4**
Fe–O1	1.81	1.81	1.77	1.82
Fe–O2	2.12	2.16	2.05	2.04
Fe–C/N	2.47	–	2.60	–
Fe'–C/N	–	2.48	–	2.53
Fe–N1	2.06	2.06	2.05	2.05
Fe–N2	2.01	2.00	2.00	2.00
Fe–N3	1.94	1.93	1.94	1.94
Dimer A (1 & 2)			**Dimer B (3 & 4)**	
Fe–O2–Fe'	127		139	
Fe···Fe'	3.83		3.82	

Table 4.11 Precious–CN bond lengths and distances from C121 symmetry solution.

Bond lengths (Å) and angles (°)	**Monomer 1**	**Monomer 2**	**Monomer 3**	**Monomer 4**
Fe–O1	1.77	1.77	1.79	1.78
Fe–O2	2.10	2.14	2.11	2.12
Fe–N4	2.34	–	2.29	–
Fe'–N6	–	2.33	–	2.30
Fe–N1	2.07	2.08	2.07	2.09
Fe–N2	2.01	2.00	2.02	2.01
Fe–N3	1.95	1.94	1.96	1.95
Dimer A (1 & 2)			**Dimer B (3 & 4)**	
Fe–O2–Fe'	124		122	
Fe···Fe'	3.75		3.71	

Table 4.12 EXAFS fit parameters for **Precious**. Fit 21 corresponds to the most reasonable fit of the data between k = 2 and 14 Å^{-1}.

	Fe–N/O			Fe–O/N			Fe---C			Fe---Fe			GOF		
Fit	**N**	**R(Å)**	**σ^2 (10^{-3})**	**N**	**R(Å)**	**σ^2 (10^{-3})**	**N**	**R(Å)**	**σ^2 (10^{-3})**	**N**	**R(Å)**	**σ^2 (10^{-3})**	**ΔE_0**	**F**	**F'**
1	1	2.13	1.87										8.95	307	782
2	2	2.12	5.71										8.04	236	686
3	3	2.11	9.46										7.03	204	637
4	4	2.09	13.27										5.86	192	617
5	1	2.14	0.89	1	2.01	5.56							4.67	232	680
6	1	2.12	1.88	2	2.02	9.11							5.54	194	621
7	2	2.09	4.21	1	1.94	3.31							6.33	190	615
8	3	2.07	7.84	1	1.90	3.11							5.09	177	594
9	4	2.10	8.03	1	1.89	4.79							3.54	159	562
10	5	2.09	10.43	1	1.87	4.70							3.03	163	569
11	2	2.17	4.25	2	2.02	3.57							4.23	164	571
				1	1.87	2.14									
12	2	2.16	4.45	1	2.04	1.49	3	3.05	3.69				5.79	104	454
				1	1.91	3.07									
13	3	2.12	5.96	1	1.92	5.74	3	3.05	3.44				5.38	109	466
14	3	2.12	5.92	1	1.92	5.61	3	3.05	3.44	1	4.12	13.22	5.14	102	451
15	4	2.11	8.29	1	1.89	5.29	3	3.05	3.53				4.73	107	461
16	4	2.11	8.29	1	1.89	5.32	3	3.05	3.52	1	4.11	12.94	4.75	100	446
17	3	2.12	6.01	1	1.92	5.84	3	3.05	3.55	1	4.07	7.83	5.30	90	422
							1	4.23	-3.20						
18	3	2.12	6.03	1	1.93	5.91	3	3.05	3.58				5.50	103	452
							1	4.23	-1.90						
19	3	2.12	6.02	1	1.92	5.90	3	3.05	3.48				5.48	105	457
							3	4.03	1.61						
							4	4.21	2.00						
20	3	2.12	6.06	1	1.93	5.94	3	3.05	3.47	1	4.03	3.90	5.49	87	417
							5	4.20	1.64						
21	**4**	**2.10**	**8.36**	**1**	**1.89**	**5.41**	**3**	**3.05**	**3.57**	**1**	**4.02**	**3.75**	**4.72**	**84**	**407**
							5	**4.20**	**1.61**						

APPENDIX A

Development of bis-biotinylated Cu^{II}–cyclam artificial proteins

Introduction

As described in previous chapters, our group and the Ward lab have utilized several biotinylated metal complexes to construct both biomimetic models of metalloproteins and artificial enzymes with enhanced functionality.[98,113,137,138,280,281] The library of synthesized biotinylated ligands is limited to mono-biotinylated ligands that have constructed both mononuclear and dinuclear active sites within streptavidin (Sav). To extend our approach, this appendix describes a collaborative project with the Ward lab to design a bis-biotinylated 1,8-Dimethyl-1,4,8,11-tetraazacyclotetradecane (Figure A.1: dimethyl-cyclam) ligand that could utilize the full Sav dimer for productive chemistry. Designing a bis-biotinylated ligand is desirable because there would likely be more space in the Sav vestibule for the construction of active sites and the active site would be more accessible to substrates for reactivity. Additionally, a cyclam ligand is an attractive choice because the chemistry of metallated cyclam complexes has been thoroughly investigated by synthetic chemists.[282–294,294–300,300–326] For example, Nam and Que have successfully generated and characterized a high valent Fe^{IV}–oxido species from $[Fe^{II}(TMC)(OTf)_2]$ (TMC: 1,4,8,11-

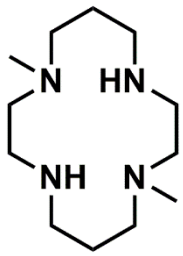

dimethyl-cyclam

Figure A.1 ChemDraw representation of dimethyl cyclam (dmc).

tetramethyl-1,4,8,11-tetraazacyclotetradecane) and dioxygen, which is known to be the competent oxidant in several nonheme Fe metalloproteins. [283,294,9]

This appendix was work done in collaboration with Dr. Ryan Peterson and Dr. Joan Serrano-Plana from the Ward lab at the University of Basel in Switzerland. This appendix details the construction and characterization by X-ray diffraction (XRD) of three new Cu^{II} artificial metalloproteins (ArMs) using the bis-biotinylated dimethyl-cyclam ligand (bis-biot-dmc).

Results and Discussion

Design Concepts. In order to take advantage of the full Sav dimer, constructing a ligand of appropriate length was critical. In the dinuclear Fe^{III} work (detailed in Chapter 4), it was determined that that a 4-carbon linker between the biotin moiety and the metal chelator was necessary to assemble a dinuclear center coupled through a bridging atom. Similarly, for a ligand to span the Sav dimer, there would need to be greater than a 4-atom linker so that the cyclam ligand would dock at the interface of the Sav vestibule. In addition, the choice of dimethyl-cyclam as the starting synthon was in order to ensure biotinylation of only two *trans* amino groups. Initial studies with the bis-biot-dmc ligand utilized Cu^{II} for metallation because from previous work in our group, obtaining molecular structures is less difficult with Cu complexes than the other first-row transition metals. Additionally, Cu^{II} has a spectroscopic handle by both electron paramagnetic resonance (EPR) and electronic absorbance spectroscopies.

Synthesis of bis-biot-dmc and Cu^{II} complex. Synthesis of bis-biot-dmc was accomplished by first Cbz-protecting the two free amine groups of dimethyl-cyclam in dichloroethane. Acid-base extraction afforded a pale pink solid that is the bis-Cbz-protected

Scheme A.1 First synthetic route of bis-biot-dmc.

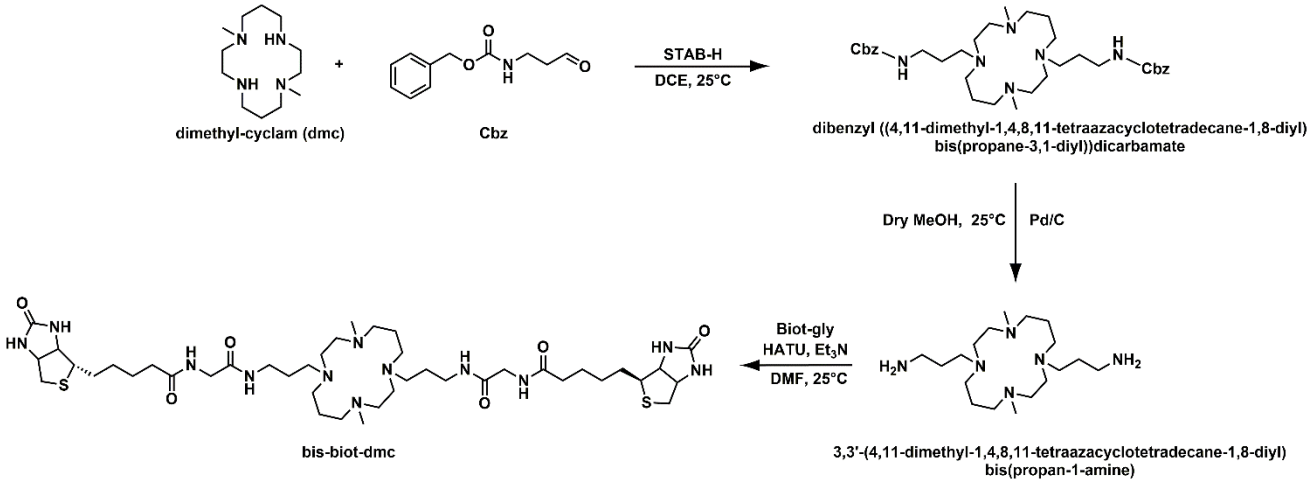

dimethyl-cyclam. Palladium on carbon deprotection in dry methanol yielded the free amine as a white solid. A glycine modified version of biotin (Biot-gly), was coupled to the free amine dimethyl-cyclam using an amide coupling agent HATU with triethylamine in DMF. Addition of acid and precipitation with diethyl ether afforded a mixture of mono-biotinylated and bis-biotinylated dimethyl-cyclam, which was then purified via reverse phase high performance liquid chromatography (HPLC) (Scheme A.1).

Another synthetic route was attempted to increase the yield of preparing the bis-biot-dmc ligand that was similar to the preparation of biot-n-dpa (n=2,3,4; Chapter 2 and 4). The free amine groups of dimethyl-cyclam were protected by *N*-(2-bromopropylphthalimide, with KI and K_2CO_3, in acetonitrile. Acid-base extraction, followed by column chromatography, afforded pure bis-phthalimide protected dimethyl-cyclam. The bis-phthalimide-protected dimethyl-cyclam was deprotected via hydrazine monohydrate in heated ethanol to yield the free amine as a yellow oil. Biotinylation with the free amine and a glycine modified pentafluorophenol ester of biotin (Biot-gly-PFP) was performed in DMF

Scheme A.2 Second proposed synthetic route for bis-biot-dmc.

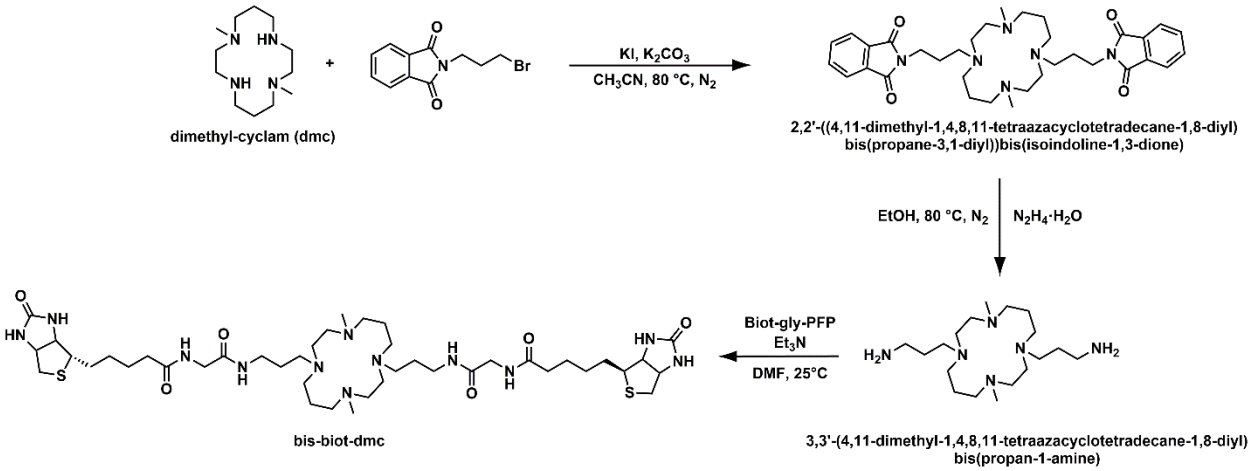

with triethylamine. Biotinylation yielded a mixture of mono-biotinylated and bis-biotinylated dimethyl-cyclam that was unable to be purified (Scheme A.2). Further experiments are necessary to improve the final purification step of bis-biot-dmc.

The Cu^{II} complex was prepared by treatment of bis-biot-dmc with 3 equivalents of $Cu^{II}(OTf)_2$ in a mixture of 1:1 acetonitrile/methanol, followed by diethyl ether precipitation to yield a light blue solid of $[Cu^{II}(bis\text{-}biot\text{-}dmc)]^{2+}$. Titration experiments were done with 2-(4'-hydroxyazo-benzene)benzoic acid (HABA) to determine the binding stoichiometry of

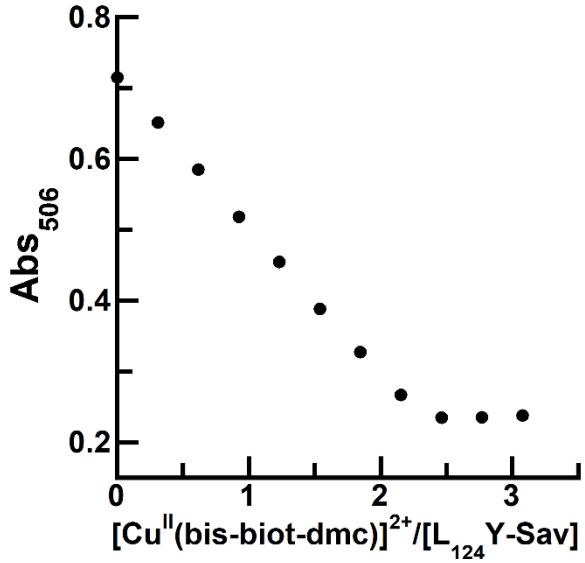

Figure A.2 HABA titration of $[Cu^{II}(bis\text{-}biot\text{-}dmc)]^{2+} \subset L_{124}Y\text{-}Sav$.

the Cu^{II} complex to Sav. The HABA studies indicated a 2:1 bis-bioinylated Cu^{II} complex to protein host ratio, confirming complete occupancy Sav (Figure A.2).

204*Structural Characterization of [Cu^{II}(bis-biot-dmc)]^2⊂WT Sav (**4**).* Single crystals of **4** were prepared by soaking wild-type (WT)-Sav crystals with [Cu^{II}(bis-biot-dmc)]$^{2+}$ overnight. Analysis of the molecular structure of **4**, resolved to 1.63 Å, revealed a mononuclear Cu complex immobilized within each Sav dimer (Figures A.3A, A.3C). The molecular structure showed the success of the ligand design because the bis-biot-dmc ligand was able to span the full dimer of Sav and have the metal chelating dmc ligand dock

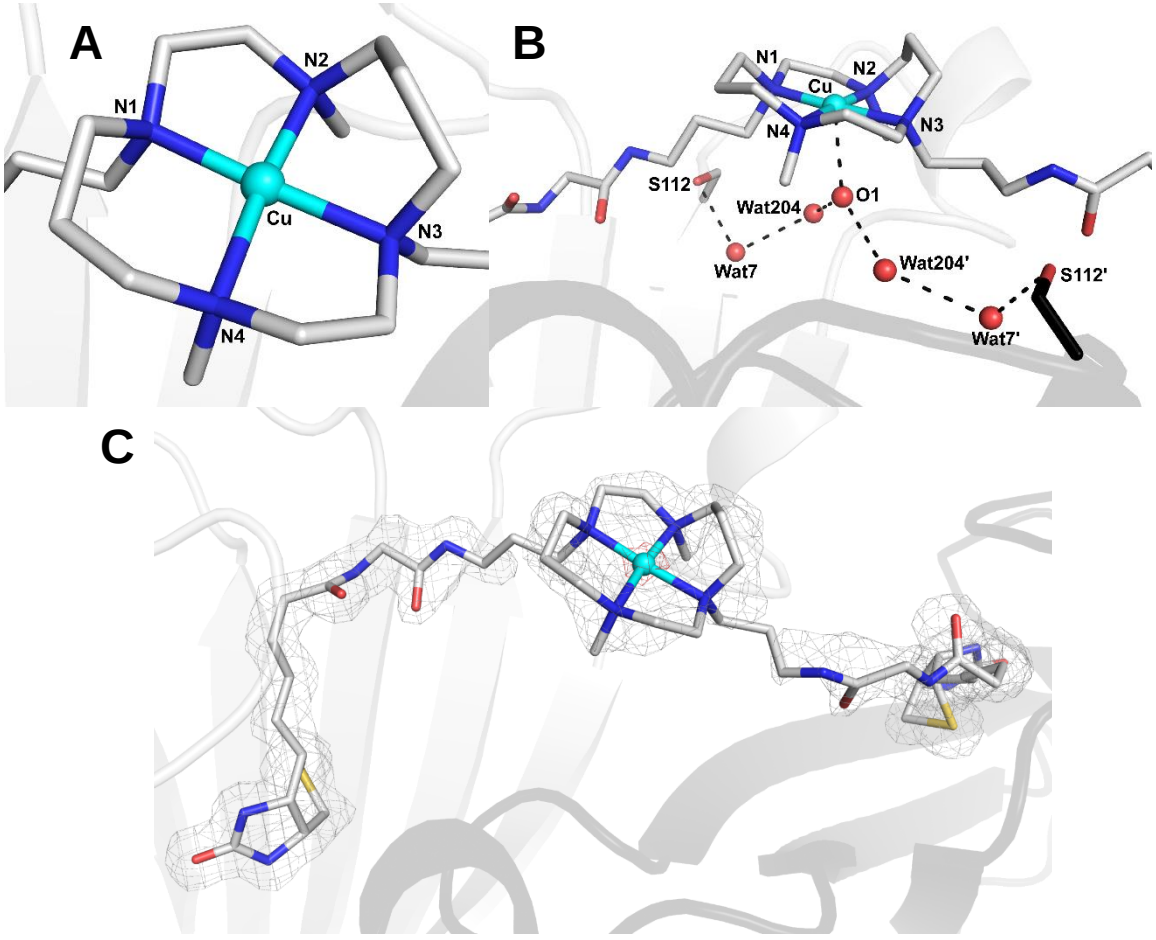

Figure A.3 Close up view of the Cu site in the molecular structure of **4** (**A**), H-bonding network (**B**), and the position of the ligand molecules is indicated by the $2F_o$-F_c electron density (grey, contoured at 1 σ) and anomalous difference density (red, contoured at 4 σ) (**C**). The protein is displayed in cartoon representation and the Cu complex as well as residues 112 as sticks. Cu is colored in cyan, N atoms in blue, and O atoms/water molecules are displayed as red spheres. H-bonds are shown as black dashed lines.

directly at the interface of the Sav dimer. Nitrogen donors N1-N4 from the dmc ligand are coordinated to the Cu center with an average bond distance of 2.13 Å. The 4-coordinate Cu complex has a τ_4 value of 0.07, indicating square planar geometry. There is an additional water molecule (Wat38) that is 2.56 Å away the Cu center, which is longer than a typical distance for a bond (Tables A.1, A.2, and A.3). However, Wat38 does participate in an extended hydrogen-bonding (H-bonding) network with nearby water molecules and the serine amino acid residue at position 112 (Figure A.3B). It is possible that Wat38 is bound to the Cu center, but the bond length is longer because the water molecule is participating in an extended H-bonding network.

*Structural Characterization of [Cu^{II}(bis-biot-dmc)]$^{2+}$⊂L$_{124}$Y-Sav (**5**).* To investigate the effect of the protein environment on Cu^{II} complex, the L$_{124}$Y-Sav variant, previously described in Chapter 4, was utilized. The L$_{124}$Y-Sav variant introduces a tyrosine mutation that could possibly act as a ligand to the Cu center or participate in H-bonding interactions near the Cu complex. Single crystals of **5** were prepared by soaking L$_{124}$Y-Sav crystals with

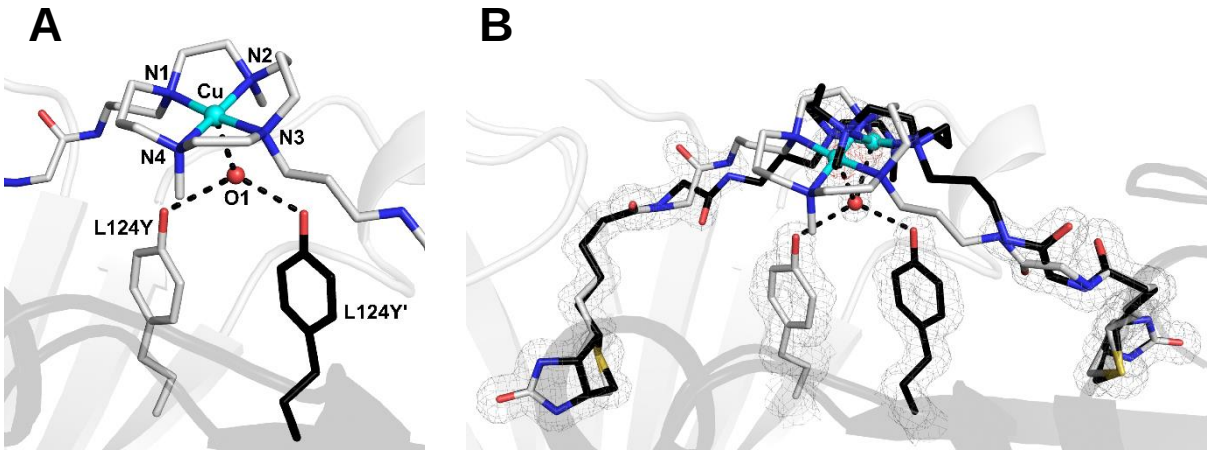

Figure A.4 Close up view of the Cu site in the molecular structure of **5** (**A**) and the position of the ligand molecules is indicated by the *2F$_o$-F$_c$* electron density (grey, contoured at 1 σ) and anomalous difference density (red, contoured at 3 σ) (**B**). The protein is displayed in cartoon representation and the Cu complex as well as residues 124 as sticks. Cu is colored in cyan, N atoms in blue, and O atoms/water molecules are displayed as red spheres. H-bonds are shown as black dashed lines.

[Cu^{II}(bis-biot-dmc)]$^{2+}$ overnight. The molecular structure was resolved to a 1.35 Å resolution and revealed a highly disordered Cu complex (Figure A.4A and A.4B). The Cu complex was disordered over two places at the interface of the Sav vestibule. In both conformations, the primary coordination sphere is similar to that of **4**, including a water molecule (Wat1) with a Cu–O bond distance of 2.48 Å (Tables A.1, A.2, and A.3). Wat1 is participating in a bifurcated H-bond with both tyrosine residues at the interface of the Sav vestibule with a distance of O1···Y124/Y124' of 2.71 Å. Tyrosine residues participating in H-bonding near an active site is important in several metalloproteins such as the oxygen evolving complex (OEC) or ribonucleotide reductase (detailed in Chapter 4) for their function.[260,327]

*Structural Characterization of [Cu^{II}(bis-biot-dmc)]^2⊂L_{124}E-S_{112}K-Sav (**6**).* Another protein investigated was a variant that placed a carboxylate-containing residue near the Cu^{II} complex. Single crystals of **6** were prepared by soaking L_{124}E-S_{112}K-Sav crystals with [Cu^{II}(bis-biot-dmc)]$^{2+}$ overnight. The molecular structure was resolved to a 1.32 Å

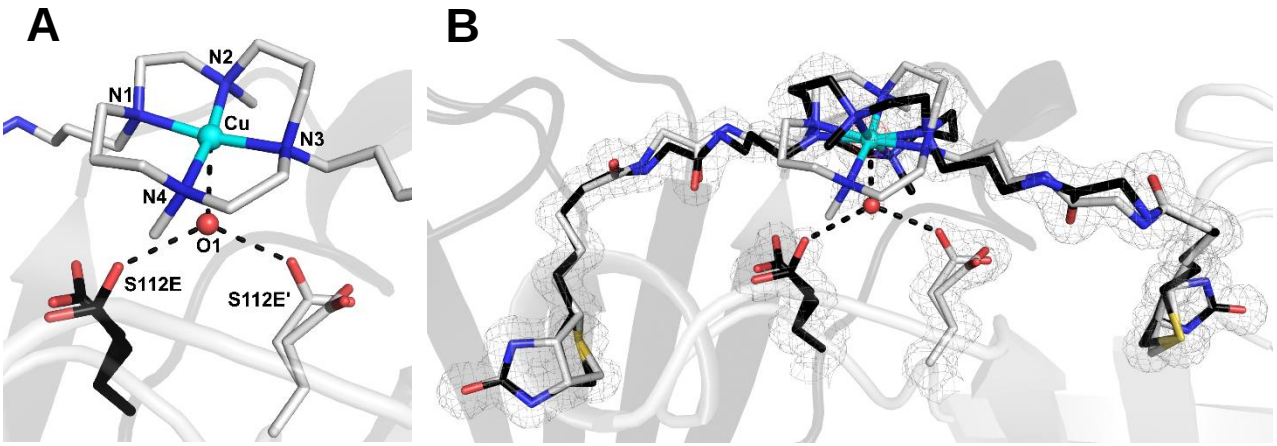

Figure A.5 Close up view of the Cu site in the molecular structure of **6** (**A**) and the position of the ligand molecules is indicated by the $2F_o$-F_c electron density (grey, contoured at 1 σ) and anomalous difference density (red, contoured at 7 σ) (**B**). The protein is displayed in cartoon representation and the Cu complex as well as residues 124 as sticks. Cu is colored in cyan, N atoms in blue, and O atoms/water molecules are displayed as red spheres.

resolution to reveal a disordered Cu complex (Figure A.5A and A.5B). There was only anomalous density for the Cu ion in one location but the ligand was disordered over two locations. The primary coordination sphere for both conformations of the ligand is similar to that of **4** and **5**, including the water molecule. The distance Wat1···Cu is 2.38 Å and compared to **4** and **5**, this is the closest water molecule distance to the Cu complex. Additionally, O1 is participating in a bifurcated H-bond, similarly to **5**, but with the disordered glutamate residues at position 124 (Tables A.1, A.2, and A.3). One conformation, modelled at 50%, is poised to H-bond with Wat1, with a Wat1···E124/E124' distance of 2.67 Å. While this system does not allow for the carboxylate residue to coordinate to the Cu-cyclam active site, participating in a H-bonding interaction near the active site has been known in native systems to be important for function.

Summary and Conclusions

In this Appendix, a new bis-biotinylated ligand was developed and three new Cu^{II} ArMs were constructed. The bis-biotinylated ligand was designed to take advantage of the full Sav dimer for productive chemistry. A modified cyclam was chosen as the ligand because several biomimetic models of protein active sites have been successfully characterized and used for structure and function studies. In these studies, Cu was chosen as the first attempt to make metal complexes with the bis-biot-dmc ligand because we have been successful in designing and obtaining molecular structures of Cu complexes in Sav (Chapter 2). Constructing the mononuclear Cu complex in WT-Sav demonstrated that the design of the bis-biot-dmc ligand was successfully able to span the full Sav dimer. Further structural work showed that placing a tyrosine or a glutamate residue near the Cu complex using different Sav variants, both residues were able to participate in H-bonding

interactions with the Cu complex. These foundational studies highlight the utility of a bis-biotinylated ligand and provide opportunities for future studies investigating the effects of noncovalent interactions with the Cu^{II} complex. Importantly, the synthesis of the bis-biot-dmc ligand is difficult and in need of further development to increase the yield and purity of the final product. In order to purify the ligand, reverse-phase HPLC could be utilized. Moreover, in the Ward lab, initial studies of $[Fe^{II}$(bis-biot-dmc)$]^{2+}\subset$Sav and $[Mn^{II}$(bis-biot-dmc)$]^{2+}\subset$Sav and their reactivity with olefins have been investigated, but no reactivity or structural data has been successfully collected. The successful development of a bis-biotinylated ligand highlights the versatility of biot-Sav technology and the promise of studying how noncovalent interactions can affect structure and function of metalloproteins.

Experimental Details

General Methods. All commercially available reagents were obtained of the highest purity and used as received. Acetonitrile (CH_3CN), diethyl ether, dichloroethane (DCE), dichloromethane (DCM), dimethylformamide (DMF), chloroform ($CHCl_3$), and methanol (CH_3OH) were degassed with argon and dried by vacuum filtration through activated alumina according to the procedure by Grubbs. Triethylamine was distilled from KOH. Thin-layer chromatography (TLC) was performed on Merck 60 F254 aluminum-backed silica plates or Merck 60 F254 glass-backed basic aluminum oxide plates. Eluted plates were visualized using UV light. Silica or basic alumina gel chromatography was performed with the indicated solvent system using Fisher reagent silica gel 60 (230-400 mesh) or Sigma reagent Brockmann 1 basic aluminum oxide 58 (150 mesh). Biotin pentafluorophenol ester (biot-PFP) was prepared according to literature procedure.[184]

Physical Methods

Instrumentation. ^{1}H and ^{19}F NMR spectra were recorded at 500 MHz and 400 MHz, respectively. ^{1}H NMR spectra were reported in ppm on the δ scale and referenced to tetramethylsilane or solvent residual. The data are presented as follows: chemical shift, multiplicity (s = singlet, d = doublet, t = triplet, q = quartet, quin = quintet, m = multiplet, br = broad), and integration. Mass spectra were measured on a MicroMass AutoSpec E, a MicroMass Analytical 7070E, or a MicroMass LCT Electrospray instrument. Electronic absorbance spectra were recorded with a Cary 50 or 8453 Agilent UV-vis spectrophotometer.

Preparative Methods

First synthetic route.

Dibenzyl((4,11-dimethyl-1,4,8,11-tetraazacyclotetradecane-1,8-diyl)bis(propane-3,1-diyl))dicarbamate. A solution (5 mL) of dimethylcyclam (228 mg) and 2.1 equivalents of 3-[(Benzyloxycarbonyl)amino]propionaldehyde (Cbz) (450 mg) was prepared in DCE. Sodium triacetoxyborohydride (STAB-H) (500 mg) was added and allowed to react overnight at room temperature. The resulting solution was added to ~ 50 ml of water and the pH was adjusted to 1. The resulting aqueous solution was extracted 4 x 25 mL with DCM and the organic phase discarded. The pH of the aqueous layer was adjusted to pH ~12 with NaOH and extracted with 3 x 25 mL DCM. The organic phase was collected, dried with Na_2SO_4, and solvent removed to yield a pale pink solid (550 mg). Note: the product has limited solubility in CH_3OH and could possibly be used for purification by crystallization. ^{1}H (500 MHz, $CDCl_3$) δ 8.2 (t, 2H), 7.3 (m, 12H), 5.1 (s, 4H) 3.3 (t, 4H), 2.2 (m, 14H), 2.1 (s, 4H).

3,3'-(4,11-dimethyl-1,4,8,11-tetraazacyclotetradecane-1,8-diyl)bis(propan-1-amine). Dibenzyl((4,11-dimethyl-1,4,8,11-tetraazacyclotetradecane-1,8-diyl)bis(propane-3,1-diyl))dicarbamate (50 mg) was deprotected using 10% Pd/C in 17 mL of dry methanol (starting material was not fully soluble but product was). The solution was filtered through a celite plug and reduced to dryness to yield a white solid (330 mg). ^{1}H (500 MHz, MeOD) δ 3.33 (t, 5H), 2.96 (t, 1H), 2.65 (m, 1H) 2.48 (t, 3H), 2.33 (s, 1H), 1.74 (m, 2H).

Bis-biot-dmc-cyclam. 3,3'-(4,11-dimethyl-1,4,8,11-tetraazacyclotetradecane-1,8-diyl)bis(propan-1-amine), 2.1 equivalents of Biotin-gly, 2 equivalents of amide coupling agent 1-[Bis(dimethylamino)methylene]-1*H*-1,2,3-triazolo[4,5-*b*]pyridinium 3-oxid hexafluorophosphate (HATU), and 4.75 equivalents of triethylamine were stirred in DMF at room temperature for 2.5 hours. 10 equivalents concentrated HCl was added to the solution, followed by precipitation with diethyl ether. The resulting solution was centrifuged and suspended/precipitated with heated 2- propanol/diethyl ether. The sample was suspended in water, adjusted to pH 3, and filtered through a 0.45 μM filter. The solution was purified by column chromatography via reverse phase C-18 HLPC (A: Water + 0.1% formic acid; B: CH_3CN +0.1 % formic acid). The sample was loaded with 100% A and then slow gradient 1-2% per min. The product typically eluted with ~13% B. The solution was reduced to dryness and was a white solid (the bis-formate salt). It should be noted that this reaction could be optimized and may be cleaner by using the biot-gly-PFP for the biotin coupling and CH_3CN as solvent. Additionally, ligand binding to the C18-column is very sensitive to pH. Use caution when purifying this ligand, sometimes for unknown reasons the sample does not stick to the column well. Do not discard any solution until the product

is obtained. The wavelengths 216 and 220 nm are used for UV-detection. ^{1}H (500 MHz, DMSO) δ 8.29 (s, 2H), 8.05 (t, 2H), 7.87 (t, 2H) 6.43 (s, 2H), 4.30 (t, 2H), 4.15 (t, 2H), 3.64 (s, 6H), 3.10 (m, 6H), 2.82 (m, 2H), 2.64 (32H), 2.38 (t, 4H), 1.53 (18H).

Second Synthetic Route.

2,2'-(4,11-dimethyl-1,4,8,11-tetraazacyclotetradecane-1,8-diyl)bis(propane-3,1-diyl))bis(isoindoline-1,3-dione).[137] Dimethyl-cyclam (2.61 g, 11.4 mmol), *N*-(2-Bromoethyl)phthalimide (6.43 g, 24.0 mmol), KI (0.38 g, 2.28 mmol) and K_2CO_3 (12.6 g, 91.4 mmol) were dissolved in 210 mL CH_3CN and refluxed for 24 h. The solution was cooled to room temperature, filtered, and reduced to dryness. The maroon-brown residue was dissolved in 50 mL DCM and washed with 3 x 30 mL aqueous $NaHCO_3$ (with a small addition of brine) and 2 x 50 mL water. The maroon-brown organic layer was acidified with 20 mL 12 mM HCl dissolved in 40 mL water and washed with 5 x 50 mL DCM. The aqueous layer was carefully neutralized with solid $NaHCO_3$ and extracted with 4 x 50 mL DCM. The solution was dried with $MgSO_4$, filtered and reduced to dryness to yield a pale yellow foamy solid. The crude product was purified via column chromatography with basic alumina and CH_3OH:$CHCl_3$ (10:90) as the eluent to yield pure product as a pale yellow solid (1.11 g, 16%). ^{1}H (500 MHz, $CDCl_3$) δ 7.82 (d, 4H), 7.69 (d, 2H), 3.70 (t, 4H), 2.51 (m, 12H), 2.42 (m, 8H), 2.19 (s, 6H), 1.81 (quintet, 4H), 1.58 (quintet, 4H).

3,3'-(4,11-dimethyl-1,4,8,11-tetraazacyclotetradecane-1,8-diyl)bis(propan-1-amine).[137] Hydrazine monohydrate (0.89 mL, 0.02 mol) and **2,2'-(4,11-dimethyl-1,4,8,11-tetraazacyclotetradecane-1,8-diyl)bis(propane-3,1-diyl))bis(isoindoline-1,3-dione)** (1.11 g, 1.84 mmol) were dissolved in 25 mL EtOH and refluxed under N_2 for 3 h. The phthalhydrazide byproduct precipitated as a white solid after 10 min of reflux. The

solution was filtered to remove the phthalhydrazide and washed with 3 x 20 mL $CHCl_3$. The solution was reduced to dryness, and the yellow, oily residue was dissolved in 20 mL $CHCl_3$ and 20 mL of 1 M NaOH. The aqueous layer was extracted with 3 x 20 mL $CHCl_3$, dried over $MgSO_4$, filtered, and reduced to dryness. The product was recovered as a yellow oil (0.19 g, 30%). ^{1}H (500 MHz, $CDCl_3$) δ 2.46 (m, H), 2.33 (m, 20H), 2.22 (s, 6H), 1.64 (m, 8H).

Biot-glycine (Biot-gly). Glycine (0.73 g, 9.68 mmol) was dissolved in 5 mL nanopure water and triethylamine (1.47 mL, 10.6 mmol) was added. Biot-PFP (3.61 g, 8.80 mmol) was dissolved in 80 mL DMF and added to the glycine solution with an additional 5 mL nanopure water. The solution was allowed to stir under N_2 overnight. The solution was reduced to dryness and then triturated with diethyl ether until a free flowing solid formed (1 day). The white solid was filtered, washed with diethyl ether, and dried under vacuum (2.86 g, 82%). ^{1}H (400 MHz, DMSO) δ 8.05 (s, 1H), 6.39 (s, 1H), 6.33 (s, 1H), 4.30 (t, 1H), 4.13 (t, 1H), 3.71 (d, 2H), 3.08 (quintet, 1H), 2.84 (dd, 1H), 2.56 (d, 1H), 2.15 (t, 2H), 1.49 (m, 6H).

Biot-gly-PFP. Biot-glycine (0.79 g, 2.78 mmol) was dissolved in 40 mL DMF in a 70 °C oil bath. After 30 min, the solution was cooled to room temperature and pentafluorophenyl trifluoroacetate (0.68 mL, 3.96 mmol) and triethylamine (0.68 mL, 4.84 mmol) were added slowly. The resulting dark red-orange solution stirred under N_2 for one hour. An orange solid precipitated and was dried under vacuum. The orange solid was washed with diethyl ether until a white solid remained (3-7 days), which was dried under vacuum. ^{1}H (400 MHz, DMSO) δ 8.05 (s, 1H), 6.39 (s, 1H), 6.33 (s, 1H), 4.30 (t, 1H), 4.13 (t, 1H), 3.72 (d, 2H), 3.08 (quintet, 1H), 2.83 (dd, 1H), 2.56 (d, 1H), 2.13 (t, 2H), 1.47 (m, 6H). ^{19}F (400 MHz,

DMSO) δ -153.1, -157.8, -162.5. Note: sometimes a peak at -165.8 is present but the origin is unknown.

Bis-biot-dmc-cyclam. A solution of biot-gly-PFP (1.05 g, 2.24 mmol), **3,3'-(4,11-dimethyl-1,4,8,11-tetraazacyclotetradecane-1,8-diyl)bis(propan-1-amine)**, (0.19 g, 0.56 mmol), and triethylamine (0.13 g, 1.24 mmol) in 6 mL 1:1 DMF:nanopure water (note: if not dissolving – add more water or heat until everything is soluble) was allowed to stir overnight. The DMF:nanopure water was removed under vacuum to yield a sticky tan residue. The residue was triturated with diethyl ether until a free-flowing solid formed (3-7 days). The light tan solid was filtered, washed with diethyl ether, and dried under vacuum. A mixture of mono-biotinylated and bis-biotinylated dmc ligand was present, and further purification is needed. The solid was stored under an inert atmosphere. MS (ESI, CH_3OH) *m/z* calcd $C_{42}H_{76}N_{12}O_6S_2$ [M + (H^+)] 909.55, found 909.0.

Note: One suggestion is to dissolve the biot-gly-PFP in DMF:nanopure water first (and heat if necessary), then add the triethylamine and **3,3'-(4,11-dimethyl-1,4,8,11-tetraazacyclotetradecane-1,8-diyl)bis(propan-1-amine)** and stir overnight.

Preparation of Metal Complexes

[Cu^{II}(bis-biot-dmc)$(OTf)_2$]. Ligand dissolved in methanol with 4 equivalents of triethylamine. 3 equivalents of $Cu(OTf)_2$ dissolved in acetonitrile and added to ligand to make 1:1 CH_3CN: MeOH. Stir at RT for 1 h. Precipitate and wash solid with diethyl ether.

Spectroscopic methods

HABA Titrations. To 2.4 mL of 8 μM Sav in 200 mM sodium phosphate buffer at pH 7 was added 300 μL of a 10 mM 2-(4′-hydroxyazobenzene)benzoic acid (HABA) in 200 mM phosphate buffer pH 7. After 5 min equilibration, the absorbance at 506 nm was recorded.

A solution of 1 mM Cu complex in nanopure water was added in 4-20 μL portions until approximately 2 equivalents had been added. The absorbance at 506 nm was recorded until no further changes in intensity were observed.

Protein Preparation and Crystallography

Protein Expression and Purification

Preparation of Sav variants. The construction of L_{124}Y-Sav and L_{124}E-Sav and other variants was achieved by site-directed mutagenesis (SDM) using the pET11b-Sav plasmid, the appropriate primers and, and Q5 polymerase. These Sav variants were prepared in the Ward lab.[114,328]

Amplification of pET24a-Sav mutant plasmids was accomplished by the transformation of SDM reaction mixtures into DH5α ultracompetent cells. Plasmids were isolated using a Miniprep kit from Qiagen, eluting the final plasmid with distilled deionized-water (ddH_2O, 18 MΩ cm^{-1}). DNA sequencing was performed by Genewiz.

Sav Expression. Transformation of 4 μL amplified plasmids into 50 μL Rosetta cells or bl21 cells was followed by rescue with 450 μL LB media. Of this solution, 200 μL was spread aseptically onto LB/Kanamycin agar plates and incubated overnight at 37 °C. Inoculation of a starter culture containing 500 mL LB media and the same antibiotic from a single colony was followed by incubation overnight at 37 °C and shaking at 225 rpm. From this starter culture, 25 mL was used to inoculate each 2L flask containing 500 mL LB media, 25 mL each of 20x sugar (12% glycerol, 1% glucose, 10% lactose) and salt (1 M Na_2HPO_4, 1 M KH_2PO_4, 0.5 M $(NH_4)_2SO_4$) stocks, 1 mL of 1 M $MgSO_4$, 100 μL 5000x trace metal mix (containing 1 M $CaCl_2$, 100 mM $FeCl_3$, 10 mM $MnCl_2$, 10 mM $ZnSO_4$, 2 mM $CoCl_2$, 2 mM $CuCl_2$, 2 mM $NiCl_2$, 2 mM Na_2MoO_4, and 2 mM H_3BO_3 all in 60 mM HCl), and 250 μL of 100 mg/mL Kanamycin.

Incubation at 37 °C and 225 rpm was continued until cells reached OD_{600} = 0.6–0.8, at which point the temperature was dropped to 25 °C and cultures incubated another 24 h.

Sav purification. Cultures were centrifuged at 4000 x *g* for 20 min at 4 °C. The resulting cell pellet was resuspended in lysis buffer (50 mL per 1 L expressed) containing 20 mM Tris buffer pH 7.4, 1 mg/mL lysozyme, and a spatula tip of DNase I. The suspension was then allowed to shake at 25 °C and 225 rpm for 6-8 h followed by one overnight freeze-thaw cycle. Dialysis against 6 M guanidinium hydrochloride pH 1.5 for 24 h was followed by neutralization via dialysis against 20 mM Tris buffer pH 7.4 for 24 h, and against nanopure H_2O for another 24 h. Dialysis overnight against iminobiotin (IB) buffer containing 500 mM NaCl and 50 mM $NaHCO_3$ at pH 10.5 afforded the crude, biotin-free lysate. This material was centrifuged at 10,000 x *g* for 1 h at 4 °C and the soluble portion loaded onto an iminobiotin-agarose column pre-equilibrated with IB buffer. The column was washed with 6 column volumes (CVs) of IB buffer or until the absorbance at 280 nm (A_{280}) dropped to zero. Elution with 1% acetic acid in nanopure H_2O, and pooling fractions by A_{280}, provided highly pure (>95%) Sav as assessed by 18% SDS-PAGE. Pooled fractions were dialyzed against 10 mM Tris pH 7.4 for 24 h followed by dialysis in ddH_2O for an additional 72 h and were then lyophilized. Yields of lyophilized protein were typically 100 mg per L expressed, and the solid protein was stored at 4 °C.

Protein Crystallization

*Crystallization of [Cu^{II}(bis-biot-dmc)$^{2+}$⊂WT-Sav] (**4**).* Apo-Sav protein was crystallized by sitting drop vapor diffusion method. Diffraction quality crystals were grown at room temperature by mixing 4 µL of protein solution (26 mg/mL lyophilized protein in water) and 1 µL of crystallization buffer (2.0 ammonium sulfate, 0.1 M sodium acetate, pH 4). The

droplet was equilibrated against a reservoir solution of 100 µL crystallization buffer. Single crystals of Sav were prepared by soaking apo-crystals in soaking buffer (2.6 ammonium sulfate, 0.1 M sodium acetate pH 6) with a 10 mM stock solution of $[Cu^{II}(bis\text{-}biot\text{-}dmc)]^{2+}$ in nanopure water (9 µL crystallization buffer, 1 µL $[Cu^{II}(bis\text{-}biot\text{-}dmc)]^{2+}$) overnight. After the soaking, crystals were transferred to cryo-protectant for 1 min (30% glycerol in crystallization buffer) and shock-frozen in liquid nitrogen.

*Crystallization of $[Cu^{II}(bis\text{-}biot\text{-}dmc)^{2+}\subset L_{124}Y\text{-}Sav]$ (**5**).* Apo-Sav protein was crystallized by sitting drop vapor diffusion method. Diffraction quality crystals were grown at room temperature by mixing 4 µL of protein solution (26 mg/mL lyophilized protein in water) and 1 µL of crystallization buffer (2.0 ammonium sulfate, 0.1 M sodium acetate, pH 4). The droplet was equilibrated against a reservoir solution of 100 µL crystallization buffer. Single crystals of Sav were prepared by soaking apo-crystals in soaking buffer (2.6 ammonium sulfate, 0.1 M sodium acetate pH 6) with a 10 mM stock solution of µL $[Cu^{II}(bis\text{-}biot\text{-}dmc)]^{2+}$ in nanopure water (9 µL crystallization buffer, 1 µL $[Cu^{II}(bis\text{-}biot\text{-}dmc)]^{2+}$) overnight. After the soaking, crystals were transferred to cryo-protectant for 1 min (30% glycerol in crystallization buffer) and shock-frozen in liquid nitrogen.

*Crystallization of $[Cu^{II}(bis\text{-}biot\text{-}dmc)^{2+}\subset L_{124}E\text{-}S_{112}K\text{-}Sav]$ (**6**).* Apo-Sav protein was crystallized by sitting drop vapor diffusion method. Diffraction quality crystals were grown at room temperature by mixing 4 µL of protein solution (26 mg/mL lyophilized protein in water) and 1 µL of crystallization buffer (2.0 ammonium sulfate, 0.1 M sodium acetate, pH 4). The droplet was equilibrated against a reservoir solution of 100 µL crystallization buffer. Single crystals of Sav were prepared by soaking apo-crystals in soaking buffer (2.6 ammonium sulfate, 0.1 M sodium acetate pH 6) with a 10 mM stock solution of $[Cu^{II}(bis\text{-}$

biot-dmc)]$^{2+}$) in nanopure water (9 µL crystallization buffer, 1 µL [Cu^{II}(bis-biot-dmc)]$^{2+}$) overnight. After the soaking, crystals were transferred to cryo-protectant for 1 min (30% glycerol in crystallization buffer) and shock-frozen in liquid nitrogen.

X-ray diffraction data collection processing. X-ray diffraction data were collected at the Swiss Light Source at a wavelength of 1 Å. X-ray diffraction data was processed with XDS[192] and scaled with AIMLESS (CCP4 Suite). The structures were solved by molecular replacement using program PHASER (CCP4 Suite) and the structure 2QCB from the PDB as input model ligand with water molecules removed. For structure refinement REFMAC5 (CCP4 Suite) and PHENIX.REFINE were used. Ligand manipulation was carried out with program REEL. For water picking, electron density, and structure visualization, the software COOT[197] was used. Figures were drawn with PyMOL (the PyMOL Molecular Graphics System, Version 1.8.2.3, Schrödinger, LLC). Crystallographic details, processing and refinement statistics are given in Tables A.2-A.5.

Structural Results.

Crystal Color. All crystals of Sav soaked with complexes [Cu^{II}(bis-biot-dmc)]$^{2+}$ changed from colorless to light blue.

Structural Refinement. Apo-crystals of proteins WT-Sav, L124Y-Sav, and L124E-S112K-Sav soaked with [Cu^{II}(bis-biot-dmc)]$^{2+}$ constituted space group $I4_122$ with unit cell parameters reported in Tables A.2 and A.3. A single Sav monomer was obtained per asymmetric unit after molecular replacement. Protein residues 2-10 and 135-159 of the N- and C-terminus, respectively, were not resolved in the electron density, presumably due to disorder. Starting from the Sav monomer the biological homotetramer is generated by application of crystallographic C_2-symmetry axes along the x-, y- and z-axes of the unit cell. The overall

protein structures are virtually identical to structure biotin ⊂ WT Sav (PDB 1STP, see Tables A.2, A.4).

Because the crystallographic C_2-symmetry axis lies directly at the interface where the two monomers of Sav connect, the apo-crystals of proteins WT-Sav, L_{124}Y-Sav, and L_{124}E-S_{112}K-Sav soaked with $[Cu^{II}(bis\text{-}biot\text{-}dmc)]^{2+}$ were also solved in reduced C121 symmetry to ensure that the dimethyl-cyclam ligand and water molecule density were not an artifact of symmetry. The unit cell parameters are reported in Table A.4 and A.5. A single Sav tetramer was obtained per asymmetric unit after molecular replacement.

General Complex Modeling. For all structures of apo-protein crystals soaked with the corresponding Cu-complexes the following general observations were made: i) residual electron density in the F_o-F_c map was observed in the biotin binding pocket, ii) in the biotin vestibule which is flanked by protein residues of loop-3,4^A (the superscript number indicates Sav monomer within tetramer) loop-4,5^C, loop-5,6^A loop-7,8^A and loop-7,8^B, and iii) an anomalous dispersion density map indicated a significant peak in the biotin vestibule superimposed with the electron density peak. The residual electron density was fit with the corresponding Cu-complexes, which projected Cu to the position of the strong anomalous density peak.

Structural Refinement of **4**. In both $I4_122$ and C121 symmetry solutions, the Cu^{II} complex and the water molecule were modelled at 100% occupancy. In the I4122 symmetry solution, the Cu^{II} complex was modelled at 50% occupancy because it spans the full Sav dimer. There were no significant changes between the two solutions of the ArM (Figure A.7, Tables A.4, 4.5, and A.6).

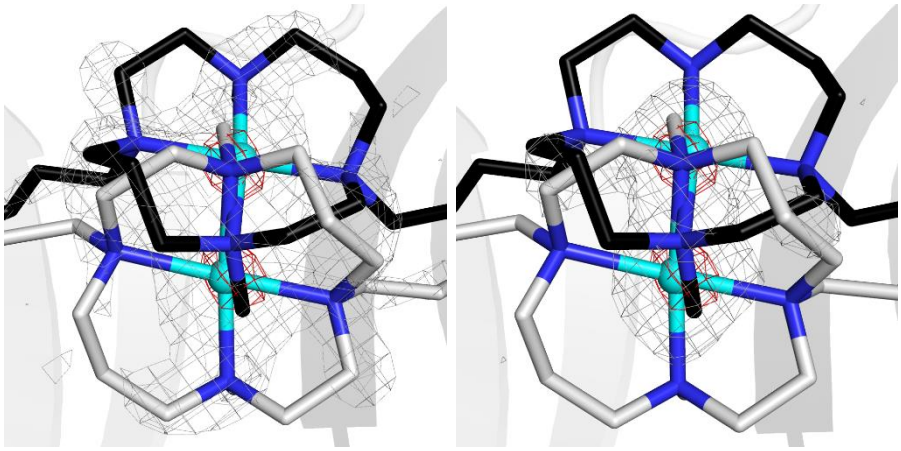

Figure A.6 Close up view of the Cu site in the molecular structure of **5** and the position of the ligand molecules is indicated by the $2F_o$-F_c electron density (grey) and contoured at 0.6 σ (**A**) and 1.0 σ (**B**). The protein is displayed in cartoon representation and the Cu complex as sticks. Cu is colored in cyan and N atoms are in blue. The number scheme in **A** and **B** are the same as in Figure A.4A

Structural Refinement of **5**. In the $I4_122$ symmetry solution, there was significant disorder associated with the dimethyl-cyclam ligand that made identifying the location of the ligand difficult. Because of the disorder, the density of the dimethyl-cyclam was modelled using the density of the Cu centers as the anchor point. As is, this structure is not of publishable quality because the ligand is modelled by mostly chemical intuition based on reasonable bond lengths and angles of a Cu^{II}–cyclam compound. Below, there is a comparison with different levels of sigma (σ) levels for the $2F_o$-F_c electron density displayed for clarification of how the ligand was modelled into the density. Using σ = 0.6 (Figure A.6A), the ligand density is clearer for modelling, but it is not publishable quality (σ = 1.0: Figure A.6B). Additionally, there is some unmodelled density near the active site, which is another possible location of the ligand but was more difficult to model because that model would not allow for the metal center to be fit in the proper location. The ligand was modelled with 50% occupancy because the ligand spans the Sav dimer.

In the C121 symmetry solution, the Cu^{II} complex density was similarly disordered as in the higher symmetry solution (Figure A.8, Tables A.4, A.5, and A.7). The ligand was modelled similarly to the $I4_122$ symmetry solution, with 50% for each conformation of the Cu^{II} complex in both Sav dimers. The lower symmetry solution was important for the determining that the density of the water molecule involved in the bifurcated H-bond with the tyrosine amino acid residues was not an artifact of symmetry. The water density was found in the same location as in the higher symmetry solution, indicating that it is not an artifact. Each conformation was modelled with 50% occupancy in each of the Sav dimers.

Structural Refinement of **6**. In the $I4_122$ symmetry solution, the Cu^{II}-complex was disordered and revealed two conformations of the ligand. The Cu^{II} center was modelled at 80% occupancy due to some negative density surrounding the metal center. The decrease of the metal center occupancy could be because the metal is located directed at the interface of the Sav dimer, which in $I4_122$ symmetry is the center of symmetry for the solution of the molecular structure. Moreover, there is significant disorder in the dimethyl-cyclam ligand which could cause there to be extra negative density surrounding the metal center. The ligand was modelled at 50% occupancy because it spans the Sav dimer. The water molecule was modelled with 100% occupancy. Additionally, there is some unmodelled density above the complex because it was unclear whether that extra density was due to the complex being located at the center of symmetry, disorder of the complex, or if an additional water molecule could be fit.

In the C121 symmetry solution, the bis-biot-dmc ligand was modelled with 100% occupancy (Figure A.9, Tables A.4, A.5, and A.8). The Cu center was again modelled to 80% occupancy, which could be a product of the disorder associated with the complex. There is

a discrepancy in location of the water molecule between the symmetry solutions. In the C121 symmetry solution, in Dimer A, it is clear that there is a water molecule axial to the Cu complex. However, the distances of the H-bonding interactions have changed from O1⋯E124/E124' distance of 2.67 Å to an elongation of one of the H-bonding interactions to 3.16 Å. The same effect is seen in Dimer B, except that the elongation is longer to 3.80 Å. However, in Dimer B, it is more difficult to assign the location of the water molecule because there the density is more disordered in Dimer B than in Dimer A. The change between symmetry solutions can be related to two reasons: 1) the water molecule is disordered and decreasing the resolution of the structure when lowering the symmetry causes the location of the water molecule to be more difficult to determine, or 2) the water molecule is only present in Dimer A in this structure and in the high symmetry solution, the occupancy is being affected because the water molecule is at the center of symmetry. With this discrepancy, this structure would need to be reproduced for better quality data for publication.

Dimer A

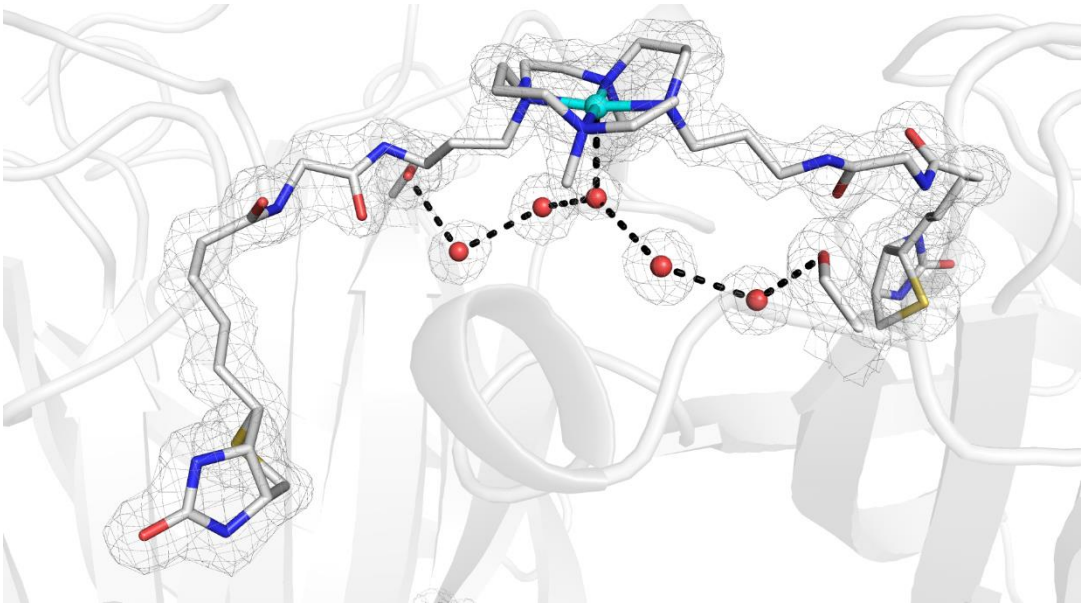

Dimer B

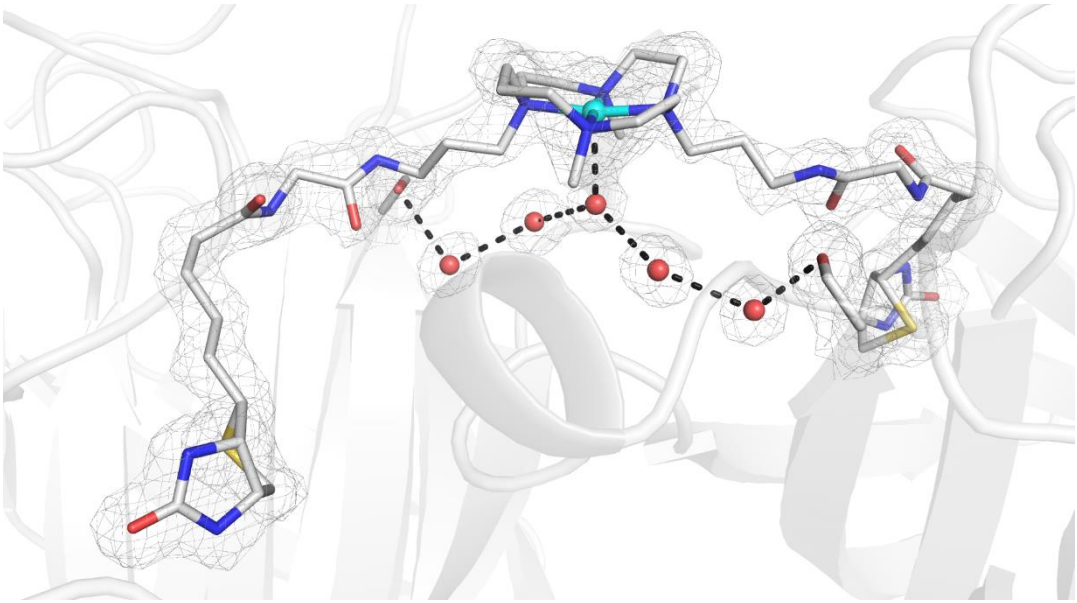

Figure A.7 Close up views of the Cu sites in the molecular structure of **4** solved in C121 symmetry. **Dimer A** and **B** of the tetrameric Sav are shown for clarity. The protein is displayed in cartoon representation and the Cu complex. The position of the ligand molecules is indicated by the $2F_o$-F_c electron density (grey, contoured at 1 σ). Cu is colored in cyan, N atoms are in blue, and O atoms/water molecules are in red. The number schemes in **Dimer A** and **Dimer B** are the same as those in Figure A.3A. H-bonds are shown as black dashed lines.

Dimer A

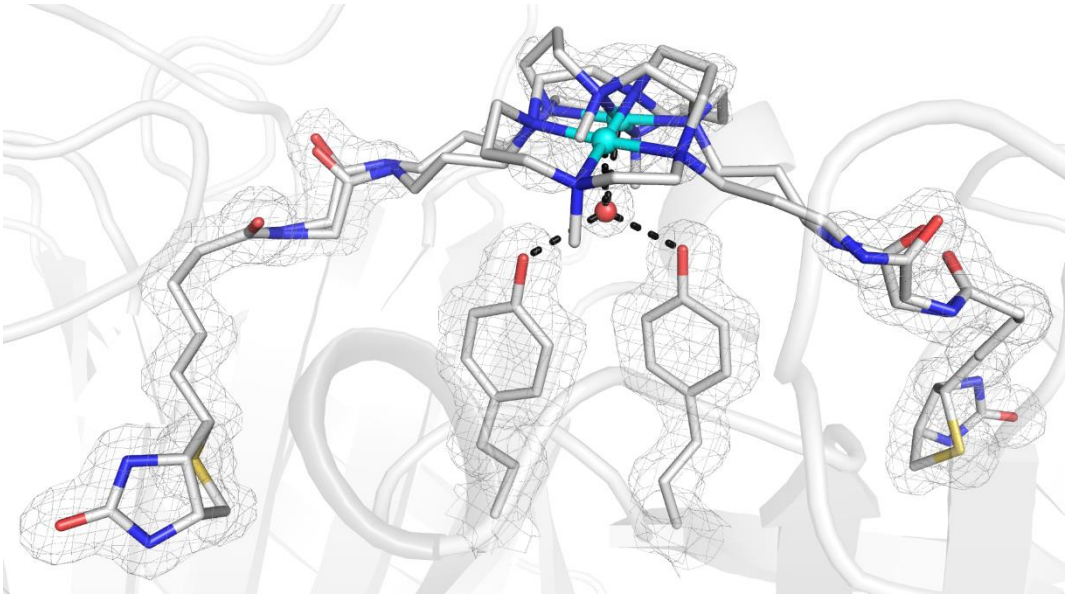

Dimer B

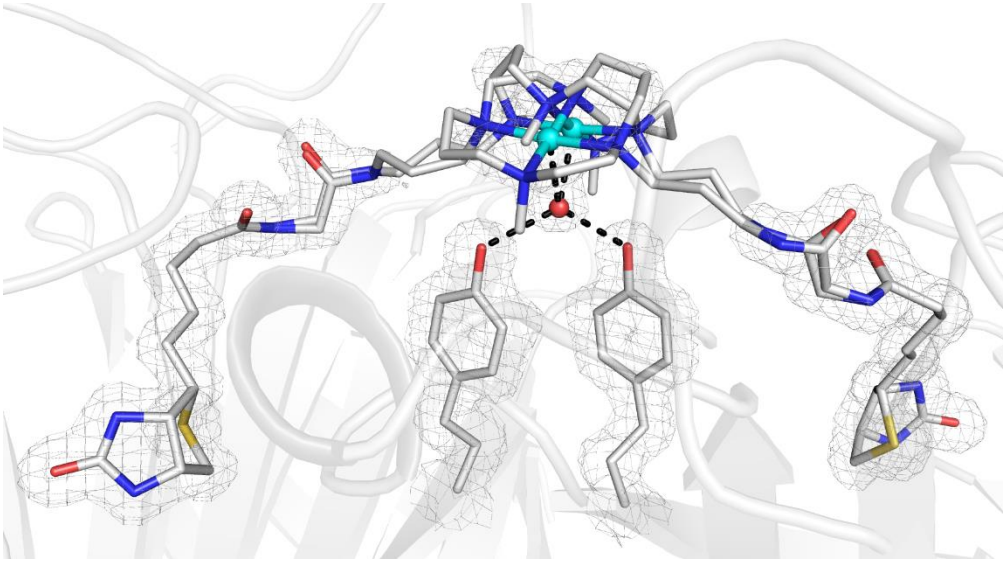

Figure A.8 Close up views of the Cu sites in the molecular structure of **5** solved in C121 symmetry. **Dimer A** and **B** of the tetrameric Sav are shown for clarity. The protein is displayed in cartoon representation and the Cu complex. The position of the ligand molecules is indicated by the $2F_o$-F_c electron density (grey, contoured at 1 σ). Cu is colored in cyan, N atoms are in blue, and O atoms/water molecules are in red. The number schemes in **Dimer A** and **Dimer B** are the same as those in Figure A.4A. H-bonds are shown as black dashed lines.

Dimer A

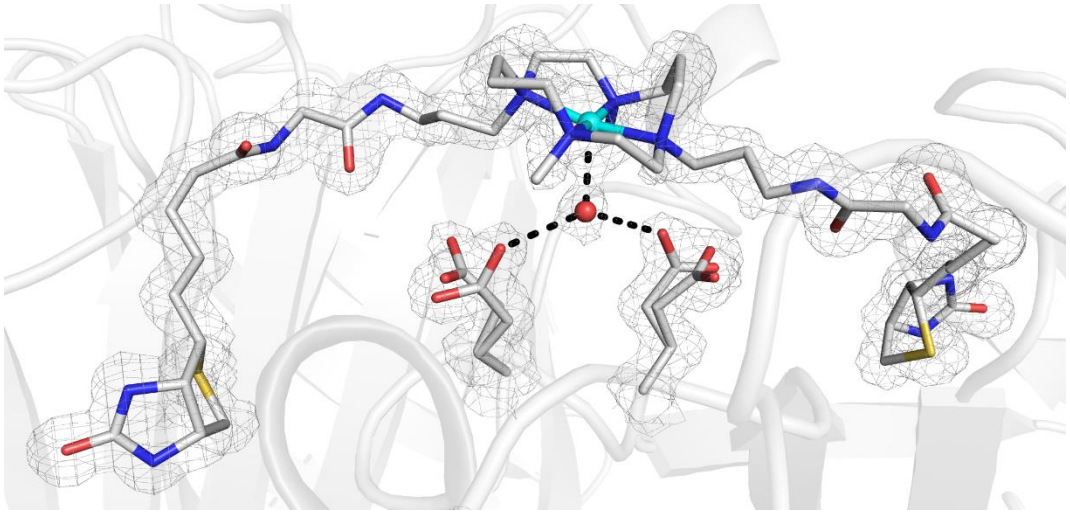

Dimer B

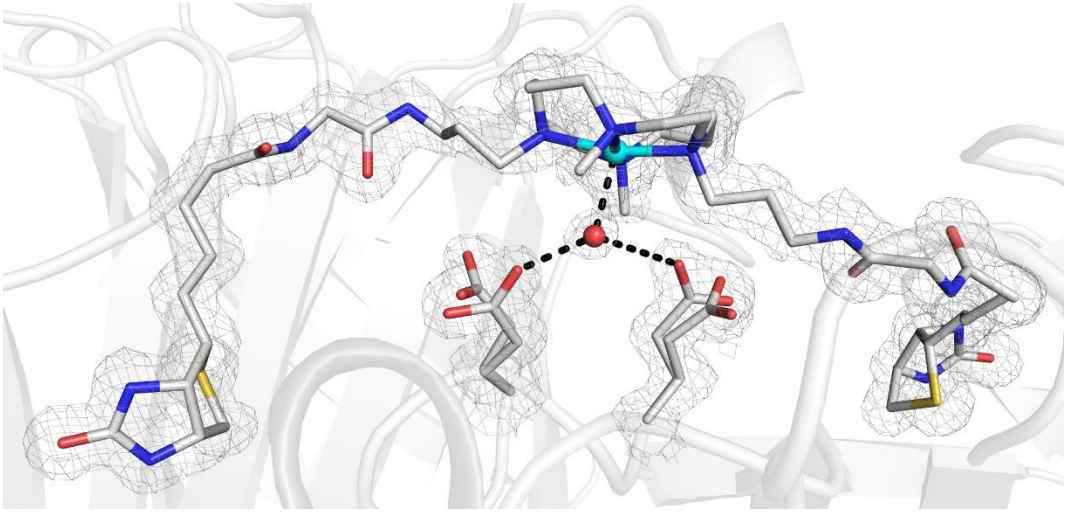

Figure A.9 Close up views of the Cu sites in the molecular structure of **6** solved in C121 symmetry. **Dimer A** and **B** of the tetrameric Sav are shown for clarity. The protein is displayed in cartoon representation and the Cu complex. The position of the ligand molecules is indicated by the $2F_o$-F_c electron density (grey, contoured at 1 σ). Cu is colored in cyan, N atoms are in blue, and O atoms/water molecules are in red. The number schemes in **Dimer A** and **Dimer B** are the same as those in Figure A.5A. H-bonds are shown as black dashed lines.

Table A.1 Selected Bond lengths and (Å) and Angles (°) for **4**, **5**, and **6**.

Bond lengths (Å) and angles (°)	**4**	**5A**	**5B**	**6A**	**6B**
Cu–N1	2.00	2.18	2.15	2.09	2.11
Cu–N2	2.09	2.10	2.08	2.02	2.12
Cu–N3	2.12	2.15	2.18	2.10	2.08
Cu–N4	2.29	2.08	2.10	2.09	1.99
Cu–O1	2.56	2.48	2.48	2.38	2.38
O1···Y124/Y124’	–	2.71	2.71	–	–
O1···E124/E124’	–	–	–	2.67	2.67
N1–Cu–N2	87	79	77	79	97
N2–Cu–N3	92	99	105	99	93
N3–Cu–N4	82	77	79	86	80
N1–Cu–N4	99	105	94	94	100
N1–Cu–N3	177	175	175	170	168
N2–Cu–N4	174	173	173	172	171
O1···Wat204/Wat204’	3.13	–	–	–	–
Wat204/Wat204’···Wat7/Wat7’	2.96	–	–	–	–
Wat7/Wat7’···S112/S112’	2.91	–	–	–	–

Table A.2 X-ray Crystallography Data Processing and Refinement Statistics for $I4_122$ symmetry solutions of **4**, **5**, and **6**.

Identification			
Sav Mutant	WT	$L_{124}Y$	$L_{124}E$-$S_{112}K$
Cu complex	$[Cu^{II}$(bis-biot-dmc)$]^{2+}$ (**4**)	$[Cu^{II}$(bis-biot-dmc)$]^{2+}$ (**5**)	$[Cu^{II}$(bis-biot-dmc)$]^{2+}$ (**6**)
PDB Code Cu complex	Unpublished	Unpublished	Unpublished
PDB 3-letter code	Unpublished	Unpublished	Unpublished
Data Processing			
Unit Cell	a, b, c = 57.7 Å, 57.7 Å, 183.8 Å α, β, γ = 90°	a, b, c = 57.6 Å, 57.6 Å, 183.5 Å α, β, γ = 90°	a, b, c = 57.6 Å, 57.6 Å, 183.8 Å α, β, γ = 90°
Space Group	$I4_122$	$I4_122$	$I4_122$
Resolution (Å)	45.95 – 1.63	45.87 –1.35	45.95 –1.32
Highest resolution shell (Å)	1.66 – 1.63	1.37 –1.35	1.35 –1.32
R_{merge} (%)	10 (61)	5 (140)	5 (87)
No. of unique reflections	19736 (821)	34527 (1699)	36995 (1856)
Multiplicity	11.0 (5.8)	12.6 (12.6)	12.0 (9.2)
I/Sig(I)	17.5 (2.4)	27.6 (2.0)	29.5 (2.4)
Completeness	99.9 (86.0)	100 (100)	100 (100)
CC(1/2)	0.997 (0.786)	1.000 (0.661)	1.000 (0.787)
Beamline	SLS	SLS	SLS
Structure Refinement			
R_{work}	0.22	0.18	0.20
R_{free}	0.26	0.20	0.21
Rmsd bond length (Å)	0.013	0.018	0.017
Rmsd bond angle (°)	2.944	3.541	3.486
Rmsd compared to biotin-Sav WT (PDB 1STP) (Å)	0.69	0.64	0.62
No. ligands			
Cu complex	1	1	1
Water	83	93	77

Table A.3 Summary of structural details for **4**, **5**, and **6**.

PDB Code	Unpublished	Unpublished	Unpublished
Complex	**4**	**5**	**6**
Electron density at Cu in F_o–F_c omit map (σ)	19	8	36
Anomalous dispersion density at Cu (σ)	6	7	20
Geometry of Cu complex	Square planar	Square planar	Square planar
Coordination number of Cu complex	4	4	4
Occupancy of Cu complex (%)	100	100	80
B-factor (Å²)			
Overall protein	16	19	16
Cu complex	21	26	18
DPA	21	26	18
Cu	36	43	23

Table A.4 X-ray Crystallography Data Processing and Refinement Statistics for C121 symmetry solutions of **4**, **5**, and **6**.

Identification			
Sav Mutant	WT	$L_{124}Y$	$L_{124}E$-$S_{112}K$
Cu complex	$[Cu^{II}$(bis-biot-dmc)$]^{2+}$ (**4**)	$[Cu^{II}$(bis-biot-dmc)$]^{2+}$ (**5**)	$[Cu^{II}$(bis-biot-dmc)$]^{2+}$ (**6**)
PDB Code	Unpublished	Unpublished	Unpublished
Cu complex PDB 3-letter code	Unpublished	Unpublished	Unpublished
Data Processing			
Unit Cell	a, b, c = 192.6 Å, 57.7 Å, 57.7 Å α, β, γ = 90°, 107.4°, 90°	a, b, c = 192.3 Å, 57.6 Å, 57.6 Å α, β, γ = 90°, 107.4°, 90°	a, b, c = 192.6 Å, 57.6 Å, 57.6 Å α, β, γ = 90°, 107.4°, 90°
Space Group	C121	C121	C121
Resolution (Å)	45.95 – 1.70	45.87 – 1.52	45.95 – 1.40
Highest resolution shell (Å)	1.73 – 1.70	1.55 – 1.52	1.42 – 1.40
R_{merge} (%)	7.9 (44)	3.4 (41)	4.0 (55)
No. of unique reflections	65933 (3405)	92167 (4522)	118114 (5803)
Multiplicity	3.1 (2.4)	3.4 (3.3)	3.3 (3.2)
I/Sig(I)	10.0 (2.2)	13.1 (2.2)	16.9 (2.0)
Completeness	99.1 (98.5)	99.7 (99.6)	99.6 (99.9)
CC(1/2)	0.994 (0.788)	0.999 (0.830)	0.999 (0.712)
Beamline	SLS	SLS	SLS
Structure Refinement			
R_{work}	0.22	0.17	0.19
R_{free}	0.25	0.19	0.20
Rmsd bond length (Å)	0.012	0.015	0.015
Rmsd bond angle (°)	2.730	3.414	3.047
Rmsd compared to biotin-Sav WT (PDB 1STP) (Å)	0.63	0.63	0.61
No. ligands			
Cu complex	2	2	2
Water	366	353	298

Table A.5 Summary of structural details for **4**, **5**, and **6**.

PDB Code	Unpublished	Unpublished	Unpublished
Complex	**4**	**5**	**6**
Electron density at Cu in F_o–F_c omit map (σ)	19	8	31
Geometry of Fe complex	Square planar	Square planar	Square planar
Coordination number of Cu complex	4	4	4
Occupancy of Cu complex (%)	100	100	80
B-factor (Å²)			
Overall protein	17	20	16
Cu complex	25	30	23
DPA	25	29	23
Cu	38	51	25

*B-factors were averaged from the Sav tetramer

Table A.6 4 bond lengths and distances from C121 symmetry solution.

Bond lengths (Å)	**Dimer A**	**Dimer B**
Fe–N1	2.04	2.00
Fe–N2	2.35	2.38
Fe–N3	2.06	2.04
Fe–N4	2.38	2.35
Fe–O1	2.74	2.67
O1···Wat81	3.06	–
Wat81···Wat29	2.92	–
Wat29···S112	2.95	–
O1···Wat104	3.30	–
Wat104···Wat48	2.91	–
Wat48···S112’	2.92	–
O1···Wat58	–	3.30
Wat58···Wat46	–	2.91
Wat46···S112	–	2.98
O1···Wat68	–	3.14
Wat68···Wat33	–	2.97
Wat33···S112’	–	2.95

Table A.7 5 bond lengths and distances from C121 symmetry solution.

Bond lengths (Å)	**Dimer A1**	**Dimer A2**	**Dimer B1**	**Dimer B2**
Fe–N1	2.13	2.17	2.15	2.16
Fe–N2	2.09	2.03	2.10	2.09
Fe–N3	2.17	2.13	2.17	2.13
Fe–N4	2.09	2.11	2.09	2.10
Fe–O1	2.64	2.60	2.61	2.52
O1···Y124	2.62	–	2.63	–
O1···Y124’	2.62	–	2.55	–

Table A.8 6 bond lengths and distances from C121 symmetry solution.

Bond lengths (Å)	**Dimer A**	**Dimer B**
Fe–N1	2.10	2.12
Fe–N2	2.06	2.10
Fe–N3	2.10	2.08
Fe–N4	2.08	2.02
Fe–O1	2.39	2.42
O1···E124	2.66	2.64
O1···E124’	3.16	3.80

APPENDIX B

Seeing Red: Part II

Introduction

As described in Chapter 3, dioxygen activation is an important process that occurs in several metalloproteins. Nonheme Fe oxygenases utilize mononuclear Fe active sites to bind and activate dioxygen, while concomitantly oxidizing a variety of substrates.[143] To study this, bioinorganic chemists have designed several synthetic and biological systems (described in Chapter 3) that activate dioxygen and oxidize substrates.[51,165] This appendix details the continued work on binding dioxygen to a mononuclear Fe^{II}–ArM (**3**) as described in Chapter 3. Electronic absorbance, electron paramagnetic resonance (EPR), and Mössbauer spectroscopies and X-ray diffraction (XRD) were used to study three new mononuclear Fe ArMs.

Results and Discussion

Design concepts. In Chapter 3, the work detailed our studies on treating **3** with dioxygen in the presence of substrate phenylpyruvate. This appendix describes the work done on treating **3** with dioxygen with no substrate present and with substrate phenylglyoxylic acid present (PGA: Figure B.1A). PGA was chosen as a substrate because several synthetic systems have used PGA as an analog for α-ketoglutarate as observed in the α-ketoglutarate-dependent monooxygenases. Additionally, PGA does not have the

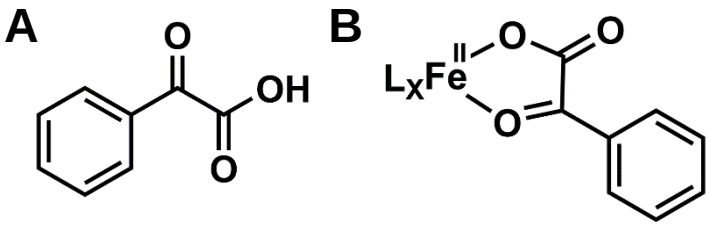

Figure B.1 ChemDraw representation of PGA (**A**) and common bidentate coordination of PGA to an $Fe^{II}L_X$ complex (L_X = ligand) (**B**).

benzylic carbon site that would be able to undergo C–H bond activation, which would allow it to serve again as a spectroscopic handle for binding (λ_{max} ~ 400-650 nm: Figure B.1B) to an Fe^{II} center and a control analog for the sodium phenylpyruvate studies for determination of the origin of reactivity.[143]

Solution studies of dioxygen binding to Fe^{II}–ArM. The ArM containing the Fe^{II} complex, [Fe^{II}(biot-et-dpa)(OH_2)$_2$(κ^1-O_{E112})⊂K_{121}A -S_{112}E-Sav] (**3**), was prepared and characterized as described in Chapter 3. Initial studies with **3** showed that it reacts with dioxygen (**3–O$_2$**) in 50 mM phosphate buffer pH 8 at 4 °C, causing the initial λ_{max} = 375 nm band to decrease and subsequent growth of an intense absorbance in the UV region of the spectrum that is masked by the absorbance bands of the protein (Figure B.2A). EPR and Mössbauer spectroscopy were utilized to further interrogate the species formed after addition of dioxygen. In the parallel-mode (‖-mode) EPR spectrum, **3** exhibits a broad signal with a *g* value at 8.8, which is consistent with a high spin Fe^{II} species with an S = 2 spin ground state. The Mössbauer spectrum revealed an isomer shift (δ) of 1.32 mm/s and a quadrupole splitting (ΔE_Q) of 3.20 mm/s, which is also indicative of a high spin Fe^{II}

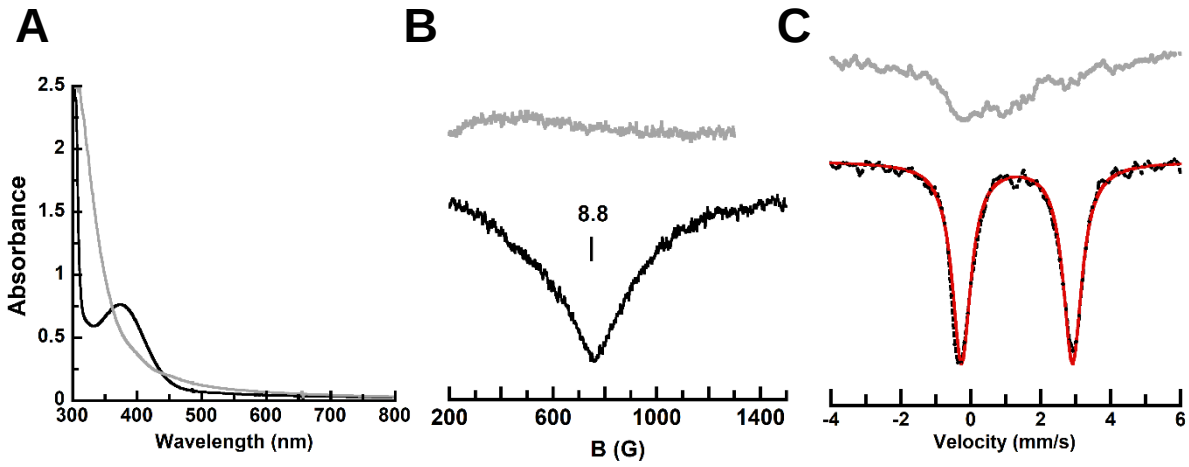

Figure B.2 Electronic absorbance (**A**), EPR (**B**), and Mössbauer (**C**) spectra for **3–O$_2$**. Recorded in 50 mM phosphate buffer pH 8 at 4 °C, 10 K, and 4 K, respectively. The initial spectrum is shown as a black line and the final spectrum is shown as a grey line. Simulation is shown as a red line.

species. After exposure to excess dioxygen, the signal is silent in both the perpendicular-mode (⊥-mode) and ∥-mode EPR spectrum (Figure B.2B: ⊥-mode shown – grey line). To investigate this further, Mössbauer spectroscopy was utilized to gain a better understanding of the oxidation state of the Fe center and determine if **3–O$_2$** was a coupled system. The Mössbauer spectrum revealed a broad paramagnetic spectrum that has not provided any conclusive information on the identity of **3–O$_2$** (Figure B.2C: grey line). The reaction was also monitored by stopped-flow spectroscopy at room temperature. The stopped-flow experiment showed the appearance of an absorbance feature at λ_{max} = 320 nm that grows in on the millisecond time scale and remains constant (Figure B.3). An absorbance feature at λ_{max} = 320 nm is suggestive of a synthetic Fe^{III}–superoxido species based on literature precedence.[216,218,220,223,329–333] However, it is reported that high spin Fe^{III}–superoxido species are ∥-mode EPR active with a *g* value ~ 8.[218] With an absorbance feature at λ_{max} = 320 nm, a silent EPR spectrum, and a broad paramagnetic Mössbauer spectrum, more work is needed to elucidate the identity of **3–O$_2$** in solution.

*Structural characterization of **3–O$_2$**.* In order to help determine what species is formed upon adding dioxygen to **3**, single crystals of **3–O$_2$** were prepared by soaking

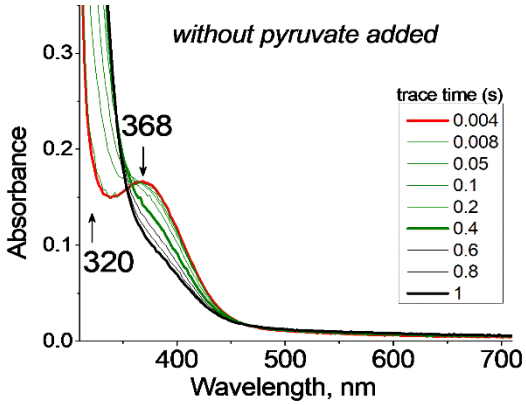

Figure B.3 Stopped flow electronic absorption spectra of reaction of **3** with **O$_2$** recorded in 50 mM phosphate buffer pH 8 at room temperature (RT).

crystals of apo-$K_{121}A$-$S_{112}E$-Sav with $[Fe^{II}(biot\text{-}et\text{-}dpa)(OH_2)_2]Br_2$ in an anaerobic chamber overnight and then subsequently exposing them to O_2–saturated buffer. The molecular structures obtained from two different crystals showed different conformations of the O_2 binding to the Fe center (Figure B.4). Both molecular structures had a similar primary coordination sphere to the fully bound pyridine conformation of the Fe^{II}–ArM (**3b**: Figure 3.8). The first molecular structure (**3–O_2–1**: Figure B.4 and B.9) was resolved to 1.70 Å and revealed an elongated density in the equatorial plane that has been modelled to an O_2 unit. The O_2 unit is slightly asymmetrically coordinated to the Fe center with bond distances of Fe–O3 and Fe–O4 at 2.27 Å and 2.46 Å and O3–O4 bond distance of 1.45 Å. The O_2 unit is angling towards a water molecule (O5) that is bound the Fe center and possible participating in a H-bonding interaction with an O4···O5 distance of 2.55 Å. O5 is also participating in a H-bonding network with Wat2 and the residue N_{49}. The second molecular structure (**3–O_2–2**: Figure B.4 and B.9) has a similar asymmetric O_2 coordination as seen in **Structure 3E** (detailed in Chapter 3), with Fe–O3 and Fe–O4 bond distances of 2.09 and 2.38 Å. While structure **3–O_2–2** looks similar to **Structure 3E**, **3–O_2–1** is different than other Fe–O_2 structures described in Chapter 3. The difference is observed in that O4 is

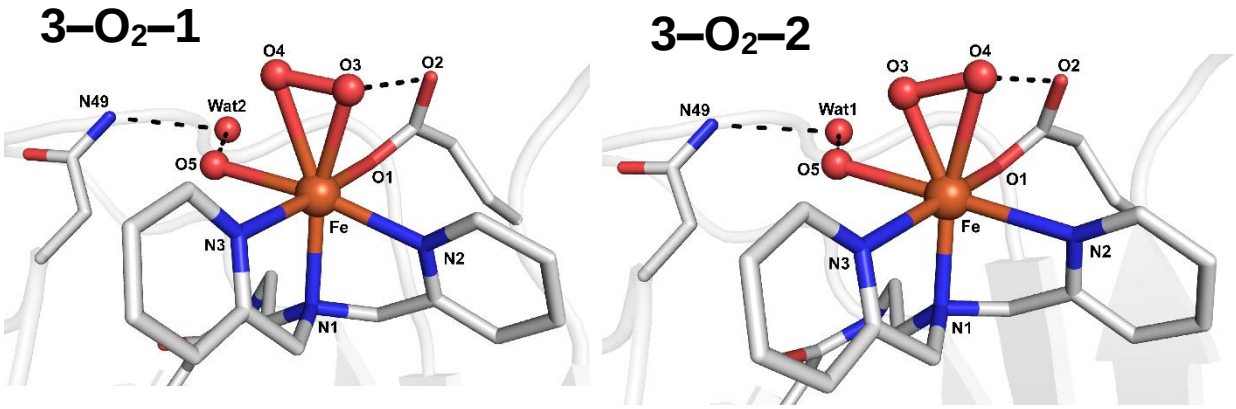

Figure B.4 Molecular structures of **3–O_2** showing two conformations of O_2 binding (**3–O_2–1**) and (**3–O_2–2**). Fe ions are shown in orange, N atoms are in blue, and O atoms/water molecules are colored in red. H-bonds are shown as black dashed lines.

either participating in a H-bond with O2 from the glutamate residue (**3–O_2–2**) or with O5 (**3–O_2–1**). Additionally, the distance between the O atom (O3: **3–O_2–2**; and O2: **3–O_2–1**) and O2 of the glutamate residue decreases from 3.12 Å to 2.93 Å as the O_2 unit moves towards the proposed final structure detailed in Chapter 3 (Tables B.1, B.2, and B.3).

*Solution studies of PGA binding to **3** (**3–PGA**).* As described in Chapter 1, the cofactor α-ketoglutarate coordinates in a bidentate fashion to the Fe center to prime the Fe active site for dioxygen activation in α-ketoglutarate-dependent oxygenases. Similar to studies done in Chapter 3 with phenylpyruvate, initial studies began by adding 20 equivalents of PGA in a nanopure water solution to **3** in 50 mM phosphate buffer pH 8. Monitoring the reaction by UV-vis spectroscopy, there was an absorbance band that grows in around λ_{max} ~ 350 nm, which was similar to what was observed using phenylpyruvate in Chapter 3, can be attributed to the absorbance associated with PGA alone (Figure B.5A). There were no absorbance features that could be attributed to the coordination of the PGA to the Fe^{II} center.[140,231,236,334] With similar optical features to what was seen with phenylpyruvate, Mössbauer and EPR spectroscopies were used to determine if the **3–PGA** had similar

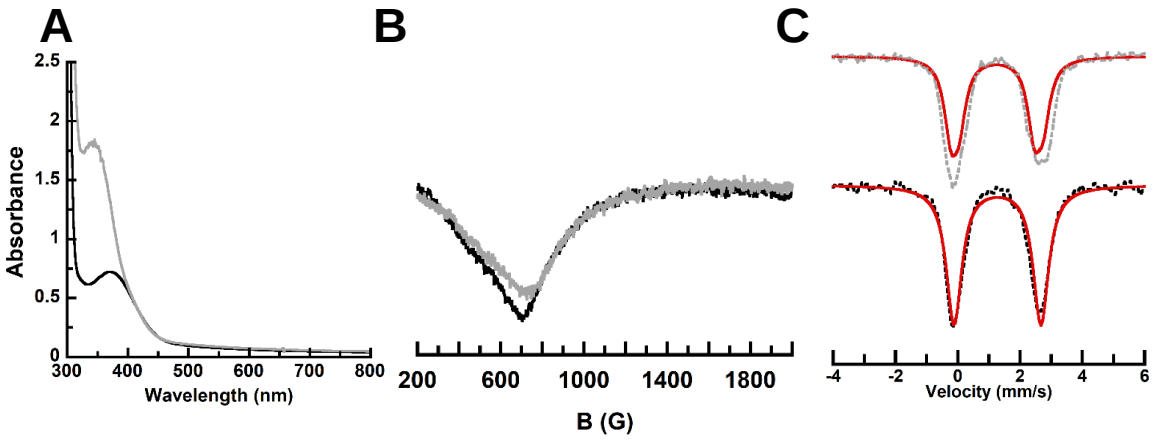

Figure B.5 Electronic absorbance (**A**), EPR (**B**), and Mössbauer (**C**) spectra for **3–PGA**. Recorded in 50 mM phosphate buffer pH 8 at 4 °C, 10 K, and 4 K, respectively. The initial spectrum is shown as a black line and final spectrum is shown as a grey line. Simulation is shown as a red line.

spectroscopic features. In the ‖-mode EPR spectrum, there was no significant shift upon addition of PGA, which was different than the small shift that was seen from the phenylpyruvate studies (Figure B.5B). The Mössbauer spectrum indicated that there were two species present. The first species was still 50% of **3** with an δ = 1.29 mm/s and a ΔE_Q = 3.15 mm/s and the second species was 50% with a similar δ = 1.25 mm/s to **3** but a slight shift in the ΔE_Q from 3.20 mm/s to 2.36 mm/s, similar to the shift seen with phenylpyruvate (Figure B.5C). Using PGA, the Mössbauer results showed there was not full incorporation of the PGA into **3**. The solution studies did show that some of the spectroscopic features were similar to what was seen in the phenylpyruvate studies, indicating that there was a change upon adding PGA but the location of the PGA was unknown.

*Structural characterization of **3–PGA**.* In order to determine if PGA was interacting with the biotinylated Fe complex in Sav in the same way as the phenylpyruvate, X-ray

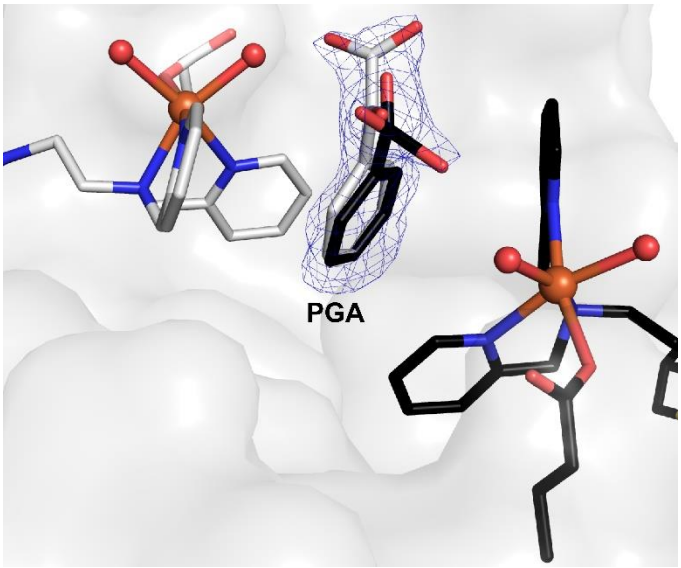

Figure B.6 Molecular structure of **3–PGA**. Fe ions are shown in orange, N atoms are in blue and O atoms/water molecules are colored in red. The position of the PGA is indicated by the $2F_o$-F_c electron density map (blue, contoured at 1 σ).

crystallography was utilized. Single crystals of Sav were prepared by an additional soaking of crystals of **3** with a 100 mM solution of PGA. Analysis of the crystals that diffracted to a 1.70 Å resolution revealed a similar molecular structure to **3–phenylpyruvate** (from Chapter 3) and PGA was modelled in the same location as phenylpyruvate (Figure B.6 and B.10). PGA was participating in a π-stacking interaction with the pyridine rings of the dpa ligand with an average $centroid_{py}$–$centroid_{ph}$ distance of 4.78 Å (Tables B.1, B.4, and B.5). While the Mössbauer spectrum indicated that there was not full occupancy of PGA within **3**, PGA was modelled with 100% occupancy in the molecular structure. The discrepancy could be attributed to the difference in conditions for obtaining a molecular structure versus solution studies – a more concentrated stock solution of PGA is utilized to obtain the molecular structure than can be used for the solution studies. The docking of PGA near the Fe complex agrees with the subtle changes in the solution spectroscopy because PGA does not alter the primary coordination sphere, but rather the secondary coordination sphere of the **3**.

*Solution studies of dioxygen binding to **3–PGA** (**3–PGA–O_2**).* In order to determine whether PGA could perform similar chemistry to what was seen in the phenylpyruvate studies or what is seen in native metalloproteins, initial solution studies were performed to add excess dioxygen to **3–PGA** and monitor the changes by UV-vis, EPR, and Mössbauer spectroscopies. Addition of excess dioxygen to **3–PGA** at 4 °C produces a new spectrum with a new absorbance around $\lambda_{max} \sim$ 300-350 nm (sh) (Figure B.7A). However, this absorbance feature is broad, with high intensity, and therefore, difficult to determine the exact absorbance band. After exposure to dioxygen for 90 min, the signal was silent in both the ⊥-mode and ∥-mode EPR spectrum (Figure B.7B: ⊥-mode shown – grey line).

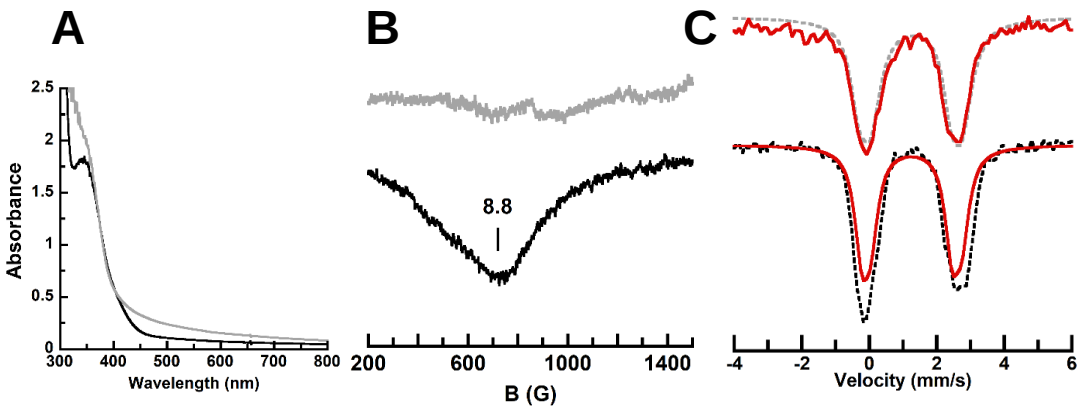

Figure B.7 Electronic absorbance (**A**), EPR (**B**), and Mössbauer (**C**) spectra for **3–PGA–O2**. Recorded in 50 mM phosphate buffer pH 8 at 4 °C, 10 K, and 4 K, respectively. The initial spectrum is shown as a black line and the final spectrum is shown as a grey line. Simulation is shown as a red line.

Additionally, the Mössbauer spectrum revealed that there is no change to the Fe^{II} center after addition of O_2 with PGA present (Figure B.7C). More studies will have to be done to determine why there are differences between the EPR and Mössbauer studies and if O_2 is coordinating to the Fe^{II} center in **3–PGA–O2** in solution.

*Structural characterization of **3–PGA–O2**.* To help determine if dioxygen is coordinating to the Fe center in **3–PGA–O2**, single crystals of **3–PGA** were prepared as described above and then subsequently exposed to O_2–saturated buffer. The structure of **3–PGA–O2** was resolved to 1.44 Å and revealed a mononuclear Fe complex immobilized within each Sav subunit. There were two conformations of the dpa ligand. The major confirmation of the dpa ligand (**3–PGA–O2 –1**) was modelled with 70% occupancy and found to coordinate to the Fe center; whereas, the minor confirmation of the dpa ligand (**3–PGA–O2 –2**) was modelled with 30% occupancy and it was not coordinated to the Fe center. In comparison to **3**, **3–PGA–O2** has a majority of the pyridine coordinated to the Fe center. One water ligand was replaced by an elongated density that has been modelled to an O_2 unit with 90% occupancy (Figure B.8). Interestingly, the O_2 coordination site is the

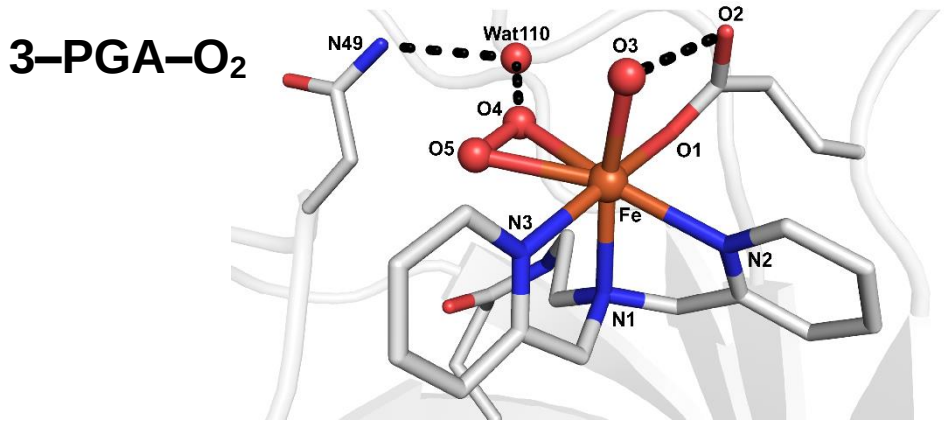

Figure B.8 Molecular structure of **3–PGA–O_2** Fe ions are in orange, N atoms are in blue, and O atoms/water molecules are colored in red.

same as where the azido ligand coordinated to the Fe^{III} center in **2–N_3** (Figure 2.11). The O_2 is asymmetrically coordinated to the Fe center with bond distances of Fe–O4 and Fe–O5 at 2.17 and 2.31 Å, and the O4–O5 bond distance is 1.37 Å (Tables B.1, B.4, and B.5). There are additional H-bonding interactions with O3 and a nearby structural water molecule (Wat110) that is also H-bonded to the residue of N_{49}. Additionally, density for PGA was observed in the location as seen in **3–PGA**; however, the density was only discernible at 0.5 σ and was therefore omitted from the structure solution. Further solution spectroscopy experiments are necessary to elucidate the identity of the O_2 unit in this structure and more structural work is needed to determine if PGA is present.

Summary and Conclusions

In this Appendix, the mononuclear Fe ArM **3** was shown crystallographically to bind dioxygen without substrate and with the substrate PGA. **3–PGA** was also shown to dock PGA in a π-stacking interaction with the pyridine rings of the dpa ligand in the Sav vestibule. Molecular structures revealed without substrate, dioxygen coordinates to the Fe center asymmetrically in the equatorial plane of the Fe complex. Whereas, with substrate PGA present, the dioxygen coordinates asymmetrically in the axial position to the Fe center.

The structures described in this appendix and in Chapter 3 support that there are several locations and modes that dioxygen can coordinate to the Fe center. In native metalloproteins, there is regulation by the coordination environment around an active site that can aid in dioxygen coordination to a metal center. However, in Sav, there is no imposed regulation on dioxygen binding to the metal center. Future studies should include mutating key amino acid residues near the Fe active site within **3** to help stabilize the Fe–O_2 species. Additionally, while crystallographic data shows dioxygen coordination to the Fe centers of these ArMs, more work is necessary to determine if dioxygen coordinates to the Fe^{II} ArMs in solution.

Experimental Details.

General Methods. All commercially available reagents were obtained of the highest purity and used as received. Acetonitrile (CH_3CN), Ethanol (EtOH) and diethyl ether were degassed with argon and dried by vacuum filtration through activated alumina according to the procedure by Grubbs.[183] Triethylamine was distilled from KOH. Thin-layer chromatography (TLC) was performed on Merck 60 F254 aluminum-backed silica plates or Merck 60 F254 glass-backed basic aluminum oxide plates. Eluted plates were visualized using UV light. Silica or basic alumina gel chromatography was performed with the indicated solvent system using Fisher reagent silica gel 60 (230-400 mesh) or Sigma reagent Brockmann 1 basic aluminum oxide 58 (150 mesh). Biotin pentafluorophenol ester (biot-PFP)[184] and di-(2-picolyl)amine[185] were prepared according to literature procedures.

Physical Methods

Instrumentation. Electronic absorbance spectra were recorded with a Cary 50 or 8453 Agilent UV-vis spectrophotometer. X-band (9.64 GHz and 9.32 GHz) EPR spectra were

recorded on a Bruker spectrometer equipped with Oxford liquid helium cryostats. The quantification of all signals is relative to a CuEDTA spin standard. The concentration of the standard was derived from an atomic absorption standard (Aldrich). For all instruments, the microwave frequency was calibrated with a frequency counter and the magnetic field with an NMR gaussmeter. A modulation frequency of 100 kHz was used for all EPR spectra. The EPR simulation software (SpinCount) was written by our collaborating author Michael P. Hendrich. Mössbauer spectra were recorded with a Janis Research Super-Varitemp dewar. Isomer shifts are reported relative to Fe metal at 298 K. Stopped-flow experiments were performed with an SX20 apparatus (Applied Photophysics) with a 1-cm path length cell at room temperature inside an anaerobic glovebox. Stock solutions of the Fe^{II} protein were prepared to obtain a final concentration of 0.5 mM in 50 mM phosphate buffer, pH 8. Oxygenated solutions at 50 mM in the same buffer were prepared in 1.2 mL glass vials capped with septa and were used immediately. After each experiment, remaining premixed solutions were recovered from the stopped-flow apparatus to confirm the concentration of the reactants.

Preparative methods

Biot-et-dpa and $[Fe^{II}(\text{biot-ethyl-dpa})(OH_2)_2]Br_2$ were prepared as described in Chapter 2.

Spectroscopic Methods

HABA Titrations. To 2.4 mL of 8 μM Sav in 200 mM sodium phosphate buffer at pH 7 was added 300 μL of a 10 mM 2-(4′-hydroxyazobenzene)benzoic acid (HABA) in 200 mM phosphate buffer pH 7. After 5 min equilibration, the absorbance at 506 nm was recorded. A solution of 1 mM Fe complex in nanopure water was added in 4-20 μL portions until

approximately 4 equivalents had been added. The absorbance at 506 nm was recorded until no further changes in intensity were observed.

Electronic Absorption Studies. A solution of lyophilized protein (250 μM) was prepared in nanopure water. Four equivalents of Fe complex (1 mM) in nanopure water were added to the protein solution. Samples were prepared in a final volume of 500 μL containing 50 mM potassium phosphate buffer at the indicated pH. For PGA samples, 20 equivalents of PGA (20 mM) in nanopure water was added after **3** is prepared. For O_2 samples, 5 mL of O_2 was added by gas-tight syringe after the sample was prepared.

EPR Studies. A solution of protein (500 μM) was prepared in nanopure water. Four equivalents of Fe complex (2 mM) in nanopure water were added to the protein solution. Samples were prepared a final volume of 200 μL containing 50 mM potassium phosphate buffer at the indicated pH. For PGA samples, 20 equivalents of PGA (40 mM) in nanopure water was added to the sample after **3** is prepared. For O_2 samples, 5 mL of O_2 was added by gas-tight syringe after the sample was prepared. The sample was frozen at 77 K in liquid nitrogen and measured at 10 K.

Mössbauer studies. A solution of protein (500 μM) was prepared in nanopure water. Four equivalents of Fe complex (2 mM) in nanopure water were added to the protein solution. Samples were prepared in a final volume of 300 μL containing 50 mM potassium phosphate buffer at the indicated pH. For PGA samples, 20 equivalents of PGA (40 mM) in nanopure water was added to the sample after **3** is prepared. For O_2 samples, 5 mL of O_2 was added by gas-tight syringe after the sample was prepared. The sample was solution Mössbauer cup, frozen at 77 K in liquid nitrogen and measured at 4 K.

Stopped-Flow Spectroscopy. A solution of protein (250 μM) was prepared in nanopure water. Four equivalents of Fe complex (1 mM) in nanopure water were added to the protein solution. Samples were prepared in a final volume of 600 μL containing 50 mM potassium phosphate buffer at the indicated pH. Samples were run on the stopped-flow UV-vis spectrophotometer by rapidly mixing the prepared ArM sample and O_2-saturated buffer, collecting at 1 ms (500 points) for 1 s. For **3–O_2**, the kinetics are biphasic; the global analysis uses an [a>b>c] model but in the absence of a large number of absorption features a simpler [A>B] with heterogeneous kinetics are also acceptable.

Protein Preparation and Crystallography

Protein Expression and Purification

Preparation of Sav variants. The construction of K_{121}A-S_{112}E-Sav and other variants was achieved by site-directed mutagenesis (SDM) using the codon optimized K_{121}A-pET24a-Sav plasmid,[191] the following primers and, and Q5 polymerase.

S_{112}E_fwd: 5'-GACCTACGGCACCACCGAAGCAAATGC-3'

S_{112}E_rev: 5'-GTGCCGTAGGTCAGCAGCCACTGG-3'

Amplification of pET24a-Sav mutant plasmids was accomplished by the transformation of SDM reaction mixtures into DH5α ultracompetent cells. Plasmids were isolated using a Miniprep kit from Qiagen, eluting the final plasmid with distilled deionized-water (ddH_2O, 18 MΩ cm^{-1}). DNA sequencing was performed by Genewiz.

Sav Expression. Transformation of 4 μL amplified plasmids into 50 μL Rosetta cells or bl21 cells was followed by rescue with 450 μL LB media. Of this solution, 200 μL was spread aseptically onto LB/Kanamycin agar plates and incubated overnight at 37 °C. Inoculation of a starter culture containing 500 mL LB media and the same antibiotic from a single colony

was followed by incubation overnight at 37 °C and shaking at 225 rpm. From this starter culture, 25 mL was used to inoculate each 2L flask containing 500 mL LB media, 25 mL each of 20x sugar (12% glycerol, 1% glucose, 10% lactose) and salt (1 M Na_2HPO_4, 1 M KH_2PO_4, 0.5 M $(NH_4)_2SO_4$) stocks, 1 mL of 1 M $MgSO_4$, 100 µL 5000x trace metal mix (containing 1 M $CaCl_2$, 100 mM $FeCl_3$, 10 mM $MnCl_2$, 10 mM $ZnSO_4$, 2 mM $CoCl_2$, 2 mM $CuCl_2$, 2 mM $NiCl_2$, 2 mM Na_2MoO_4, and 2 mM H_3BO_3 all in 60 mM HCl), and 250 µL of 100 mg/mL Kanamycin. Incubation at 37 °C and 225 rpm was continued until cells reached OD_{600} = 0.6–0.8, at which point the temperature was dropped to 25 °C and cultures incubated another 24 h.

Sav purification. Cultures were centrifuged at 4000 x *g* for 20 min at 4 °C. The resulting cell pellet was resuspended in lysis buffer (50 mL per 1 L expressed) containing 20 mM Tris buffer pH 7.4, 1 mg/mL lysozyme, and a spatula tip of DNase I. The suspension was then allowed to shake at 25 °C and 225 rpm for 6-8 h followed by one overnight freeze-thaw cycle. Dialysis against 6 M guanidinium hydrochloride pH 1.5 for 24 h was followed by neutralization via dialysis against 20 mM Tris buffer pH 7.4 for 24 h, and against nanopure H_2O for another 24 h. Dialysis overnight against iminobiotin (IB) buffer containing 500 mM NaCl and 50 mM $NaHCO_3$ at pH 10.5 afforded the crude, biotin-free lysate. This material was centrifuged at 10,000 x *g* for 1 h at 4 °C and the soluble portion loaded onto an iminobiotin-agarose column pre-equilibrated with IB buffer. The column was washed with 6 column volumes (CVs) of IB buffer or until the absorbance at 280 nm (A_{280}) dropped to zero. Elution with 1% acetic acid in nanopure H_2O, and pooling fractions by A_{280}, provided highly pure (>95%) Sav as assessed by 18% SDS-PAGE. Pooled fractions were dialyzed against 10 mM Tris pH 7.4 for 24 h followed by dialysis in ddH_2O for an additional 72 h and were then

lyophilized. Yields of lyophilized protein were typically 100 mg per L expressed, and the solid protein was stored at 4 °C.

Protein Crystallization

*Crystallization of [Fe^{II}(biot-et-dpa(OH_2)$_2$(κ^1-O_{E112})⊂K_{121}A-S_{112}E-Sav] (**3**).* Apo-Sav protein was crystallized by sitting drop vapor diffusion method under an inert atmosphere. Diffraction quality crystals were grown at room temperature by mixing 3.5 μL of protein solution (26 mg/mL lyophilized protein in water) and 1.5 μL of crystallization buffer (2.0 ammonium sulfate, 0.1 M sodium acetate, pH 4). The droplet was equilibrated against a reservoir solution of 100 μL crystallization buffer. Single crystals of Sav were prepared by soaking apo-crystals in a soaking buffer (2.6 ammonium sulfate, 0.1 M sodium acetate, pH 8) with a 10 mM stock solution of [Fe^{II}(biot-et-dpa)(OH_2)$_2$]Br_2 in nanopure water (9 μL crystallization buffer, 1 μL [Fe^{II}(biot-et-dpa)(OH_2)$_2$]Br_2) overnight. After the soaking, crystals were transferred to cryo-protectant for 1 min (30% glycerol in soaking buffer) and shock-frozen in liquid nitrogen.

*Crystallization of [Fe^{II}(biot-et-dpa(OH_2)$_2$(κ^1-O_{E112})(O_2)⊂K_{121}A-S_{112}E-Sav] (**3–O_2**).* Apo-Sav protein was crystallized by sitting drop vapor diffusion method under an inert atmosphere. Diffraction quality crystals were grown at room temperature by mixing 3.5 μL of protein solution (26 mg/mL lyophilized protein in water) and 1.5 μL of crystallization buffer (2.0 ammonium sulfate, 0.1 M sodium acetate, pH 4). The droplet was equilibrated against a reservoir solution of 100 μL crystallization buffer. Single crystals of Sav were prepared by soaking apo-crystals in a soaking buffer (2.6 ammonium sulfate, 0.1 M sodium acetate, pH 8 or 3.0 M ammonium sulfate) with a 10 mM stock solution of [Fe^{II}(biot-et-dpa)(OH_2)$_2$]Br_2 in nanopure water (9 μL crystallization buffer, 1 μL [Fe^{II}(biot-et-dpa)(OH_2)$_2$]Br_2) overnight.

After the second soaking, the crystals were transferred to O_2-saturated soaking buffer (10 uL) for 30 min. Then, the crystals were transferred to cryo-protectant for 1 min (30% glycerol in soaking buffer) and shock-frozen in liquid nitrogen.

*Crystallization of [Fe^{II}(biot-et-dpa$(OH_2)_2$(κ^1-O_{E112})⊂K_{121}A-S_{112}E-Sav] + PGA (**3–PGA**).* Apo-Sav protein was crystallized by sitting drop vapor diffusion method under an inert atmosphere. Diffraction quality crystals were grown at room temperature by mixing 3.5 μL of protein solution (26 mg/mL lyophilized protein in water) and 1.5 μL of crystallization buffer (2.0 ammonium sulfate, 0.1 M sodium acetate, pH 4). The droplet was equilibrated against a reservoir solution of 100 μL crystallization buffer. Single crystals of Sav were prepared by soaking apo-crystals in a soaking buffer (2.6 ammonium sulfate, 0.1 M sodium acetate, pH 8 or 3.0 M ammonium sulfate) with a 10 mM stock solution of [Fe^{II}(biot-et-dpa)$(OH_2)_2$]Br_2 in nanopure water (9 μL crystallization buffer, 1 μL [Fe^{II}(biot-et-dpa)$(OH_2)_2$]Br_2) overnight. After this initial soaking, crystals were again soaked in a soaking buffer (2.6 ammonium sulfate, 0.1 M sodium acetate, pH 6) with a 200 mM stock solution of PGA in nanopure water for 5-10 min (9 μL soaking buffer, 1 μL PGA). After the second soaking, the crystals were transferred to cryo-protectant for 1 min (30% glycerol in soaking buffer) and shock-frozen in liquid nitrogen.

*Crystallization of [Fe^{II}(biot-et-dpa$(OH_2)_2$(κ^1-O_{E112})(O_2)⊂K_{121}A-S_{112}E-Sav] + PGA (**3–PGA–O_2**).* Apo-Sav protein was crystallized by sitting drop vapor diffusion method under an inert atmosphere. Diffraction quality crystals were grown at room temperature by mixing 3.5 μL of protein solution (26 mg/mL lyophilized protein in water) and 1.5 μL of crystallization buffer (2.0 ammonium sulfate, 0.1 M sodium acetate, pH 4). The droplet was equilibrated against a reservoir solution of 100 μL crystallization buffer. Single crystals of Sav were

prepared by soaking apo-crystals in a soaking buffer (2.6 ammonium sulfate, 0.1 M sodium acetate, pH 8 or 3.0 ammonium sulfate) with a 10 mM stock solution of [Fe^{II}(biot-et-dpa)$(OH_2)_2$]Br_2 in nanopure water (9 µL crystallization buffer, 1 µL [Fe^{II}(biot-et-dpa)$(OH_2)_2$]Br_2) overnight. After this initial soaking, crystals were again soaked in a soaking buffer (2.6 ammonium sulfate, 0.1 M sodium acetate, pH 6) with a 200 mM stock solution of PGA in nanopure water for 5-10 min (9 µL soaking buffer, 1 µL sodium phenylpyruvate). After the second soaking, the crystals were transferred to O_2-saturated soaking buffer (10 µL) for 1 min-3 h. Then, the crystals were transferred to cryo-protectant for 1 min (30% glycerol in soaking buffer) and shock-frozen in liquid nitrogen.

X-ray diffraction data collection processing. X-ray diffraction data were collected at the Advanced Light Source (BL 5.0.2) at a wavelength of 1 Å. Data was collected with vector (ALS) data collection using exposure time/frame 1/0.5 s/deg. X-ray diffraction data was processed with XDS[192] or iMosflm[193] and scaled with AIMLESS (CCP4 Suite).[193] The structures were solved by molecular replacement using program PHASER (CCP4 Suite)[193] and the structure 2QCB from the PDB as input model ligand with water molecules removed. For structure refinement REFMAC5 (CCP4 Suite)[194] and PHENIX.REFINE[195] were used. Ligand manipulation was carried out with program REEL using the small molecule crystal structure RAGQEV01 from the Cambridge Structural Database as an input model.[248] For water picking, electron density, and structure visualization, the software COOT[197] was used. Figures were drawn with PyMOL (the PyMOL Molecular Graphics System, Version 1.8.2.3, Schrödinger, LLC). Crystallographic details, processing and refinement statistics are given in Supplementary Table B.2-B.5.

Structural Results.

Crystal Color. All crystals of Sav soaked with $[Fe^{II}(biot\text{-}et\text{-}dpa)(OH_2)_2]Br_2$ changed from colorless to pale yellow. Crystals soaked with PGA remained yellow. Crystals soaked with O_2 with and without PGA remained yellow.

Structural Refinement. Apo-crystals of proteins $K_{121}A\text{-}S_{112}E$-Sav soaked with $[Fe^{II}(biot\text{-}et\text{-}dpa)(OH_2)_2]Br_2$ constituted space group $I4_122$ with unit cell parameters reported in Tables B.2-B.5. A single Sav monomer was obtained per asymmetric unit after molecular replacement. Protein residues 2-10 and 135-159 of the N- and C-terminus, respectively, were not resolved in the electron density, presumably due to disorder. Starting from the Sav monomer, the biological homotetramer is generated by application of crystallographic C_2-symmetry axes along the x-, y- and z-axes of the unit cell. The overall protein structures are virtually identical to structure biotin ⊂ WT-Sav (PDB 1STP, see Tables B.2, B.4, and B.6).

Because PGA is located at the crystallographic C_2-symmetry axis, the structures with PGA were also solved in reduced C121 symmetry to ensure that the PGA density was not an artifact of symmetry. The unit cell parameters are reported in Table B.6 and B.7. A single Sav tetramer was obtained per asymmetric unit after molecular replacement.

General Complex and O_2 Modeling. For all structures of apo-protein crystals soaked with the corresponding Fe-complexes the following general observations were made: i) residual electron density in the F_o-F_c map was observed in the biotin binding pocket, ii) in the biotin vestibule which is flanked by protein residues of loop-$3,4^A$ (the superscript number indicates Sav monomer within tetramer) loop-$4,5^C$, loop-$5,6^A$ loop-$7,8^A$ and loop-$7,8^B$, and iii) an anomalous dispersion density map indicated a significant peak in the biotin vestibule superimposed with the electron density peak. The residual electron density was fit with the

corresponding Fe-complexes, which projected Fe to the position of the strong anomalous density peak.

The O_2 ligand was modelled using the PDB PEO for hydrogen peroxide. Each density that was modelled for an O_2 ligand was only done so after attempting to model with one or two water molecules and determining through B-factors, negative density in the F_o-F_c map, or distances between atoms that were not chemically reasonable that water was not a reasonable fit for the density. Additionally, the PDB OXY for dioxygen was also used to determine if the O_2 unit was more similar to a superoxido rather than a peroxido ligand. However, often, the O–O bond distance was contracted to ~1.2 Å, which is shortened from known Fe–O_2 complexes. Additionally, the O_2 unit would not fit the full span of unmodelled density, and there would be some additional density in the F_o-F_c map, indicating that OXY was not a reasonable fit. Designing a ligand to incorporate an O_2 ligand with restraints on the O_2 ligand was done and the solutions were similar with similar O–O bond distances. However, the final solution was not determined using a model with O_2 restraints because the Fe complex was synthesized, placed into Sav, phenylpyruvate was added, and then dioxygen was added; it was not a pre-synthesized complex that would have provided knowledge of where the O_2 ligand was coordinating or the bond distances. In this way, PEO was added after fitting the Fe complex to ensure the most accurate fit of the O_2 ligand that would match how the experiment was conducted. Lastly, using PEO and not a restraints file, allowed for the refinement to indicate what the O–O bond distance was, rather than a bias being placed by designing a restraints file.

Structural refinement of ***3–O₂–1****.* For the $I4_122$ symmetry solution, the Fe complex was modelled with 100% occupancy in the dpa bound confirmation. The glutamate residue was

modelled with 80% coordinated to the Fe center and 20% not coordinated to the Fe center. The Fe atom and O_2 unit were modelled with 100% occupancy. The anomalous map was too weak to show a signal at the Fe center; however, the Fe omit map showed density until 18 σ, which is indicative of a heavy scattering atom.

*Structural refinement of **3–O₂–2**.* For the $I4_122$ symmetry solution, the Fe complex was modelled with 100% occupancy in the dpa bound confirmation. The glutamate residue was modelled with 100% occupancy bound to the Fe center. The Fe atom and O_2 unit were modelled with 100% occupancy. This structure was added to show that this asymmetric binding is observed without a substrate present; however, the $2F_o$-F_c density around the O_2 unit at 1 σ connects to the O4 density. It is possible that the O_2 unit is disordered and that causes the diffuse density. Further work is necessary to determine that this structure is reproducible.

*Structural refinement of **3–PGA**.* For the solution of **3–PGA**, the Fe complex and the glutamate residue were modelled with 100% occupancy. In the higher symmetry solution, the PGA molecule was modelled with 50% occupancy because it is located at the center of symmetry for the Sav dimer. The density for PGA shows some disorder in the α-keto carboxylate group – modelling in two locations. Important to note is the high B-factor for PGA in both the high and low symmetry solutions. In the high symmetry solution, the high B-factor is most likely because: 1) PGA sits at the center of symmetry for the Sav dimer, 2) there is some disorder associated with the carboxylate group of PGA, and 3) PGA is docked in between the two Fe complexes by π-stacking interactions but it is also solvent exposed to the surface of the protein and the surface of the protein always exhibits higher B-factors because of disorder. In the higher symmetry solution, there was a small amount of extra

unmodelled density in the F_o-F_c between the two cis water molecules bound to the Fe center. This extra unmodelled density was not seen in the lower symmetry solution, possibly because the it was significantly lower resolution. In other structures solved with PGA or phenylpyruvate, that extra density is often fit to an O_2 molecule. In this case, O_2 was not fit because the extra unmodelled density was not seen in the lower symmetry solution, but it is worth noting the extra density is present in the higher symmetry solution (Figure B.10, Tables B.6, B.7, and B.8).

*Structure Refinement of **3–PGA–O$_2$.*** The $I4_122$ symmetry solution showed disorder in both the dpa ligand and the glutamate residue (80% bound to Fe, 20% not bound to Fe). The unbound and bound conformation of the dpa ligand was modelled with 30% (**3–PGA–O$_2$–2**) and 70% (**3–PGA–O$_2$–1**), respectively. The Fe occupancy was modelled at 80%, which could be due to the disorder associated with the full Fe complex. Additionally, the O_2 unit was modelled with 90% occupancy, which could be because of 1) the disorder in the Fe complex or 2) this structure represents an intermediate O_2 species for this ArM. It is likely that PGA is present because at low σ values (less than 1 σ), the density is similar to the density for PGA in the structure **3–PGA**. However, upon refinement, there was not enough density to assign the PGA molecule.

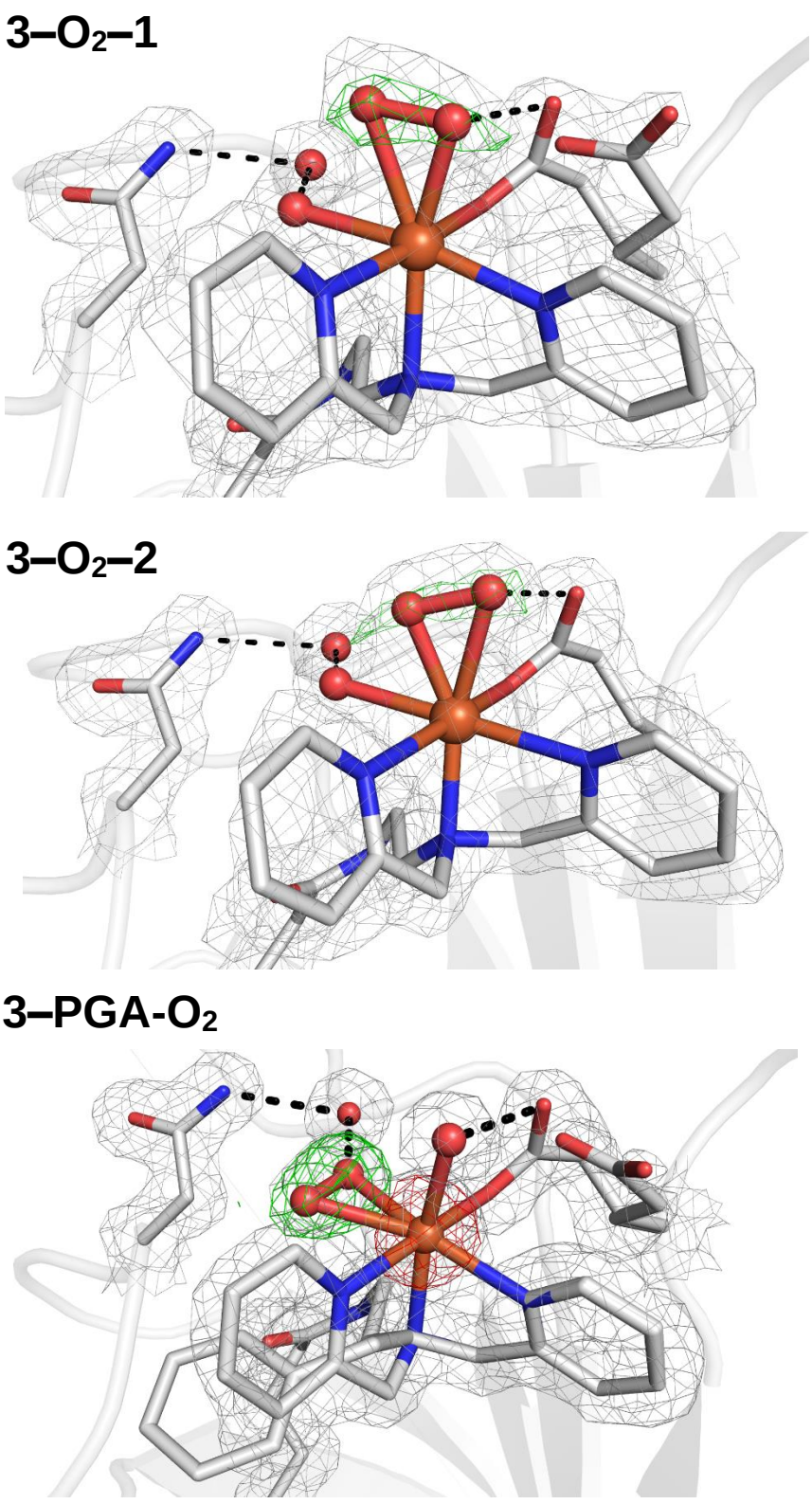

Figure B.9 Molecular structures of **3–O₂** and **3–PGA–O₂**. The position of the cofactor indicated by the $2F_o$-F_c electron density map (grey, contoured at 1 σ), the omit map of O_2 (green, contoured at 3 σ) and the anomalous map (red, contoured at 3 σ). The number schemes in **3–O₂** and **3–PGA–O₂** are the same as those in Figure B.4 and B.8. H-bonds are shown as black dashed lines.

Dimer A

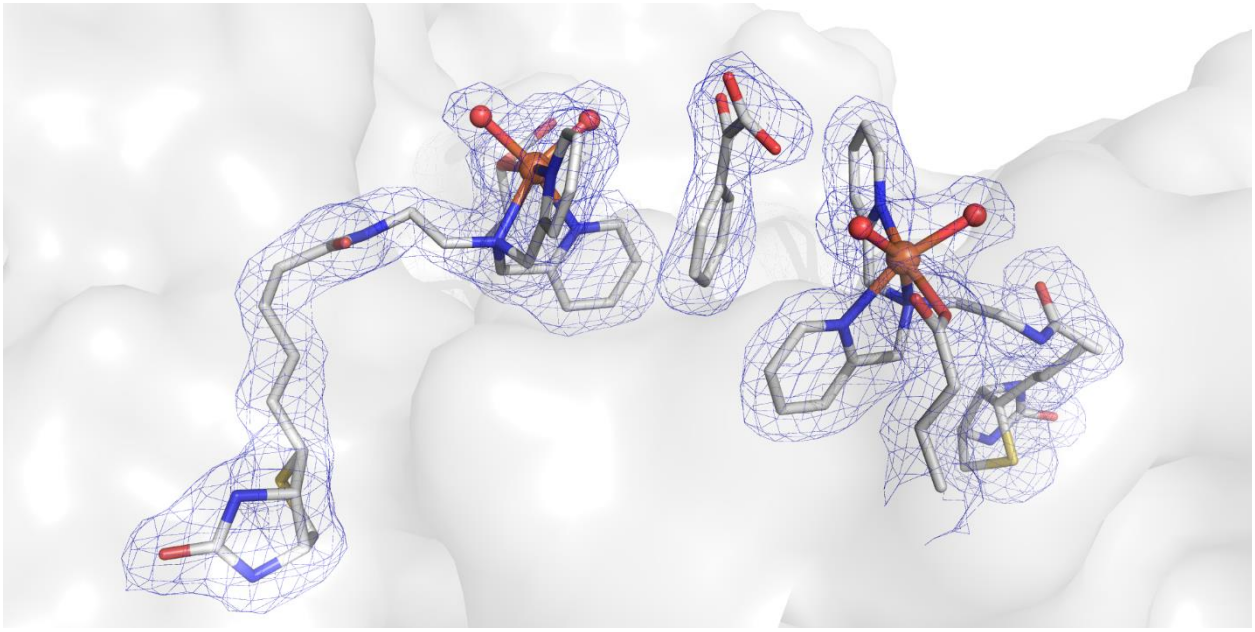

Dimer B

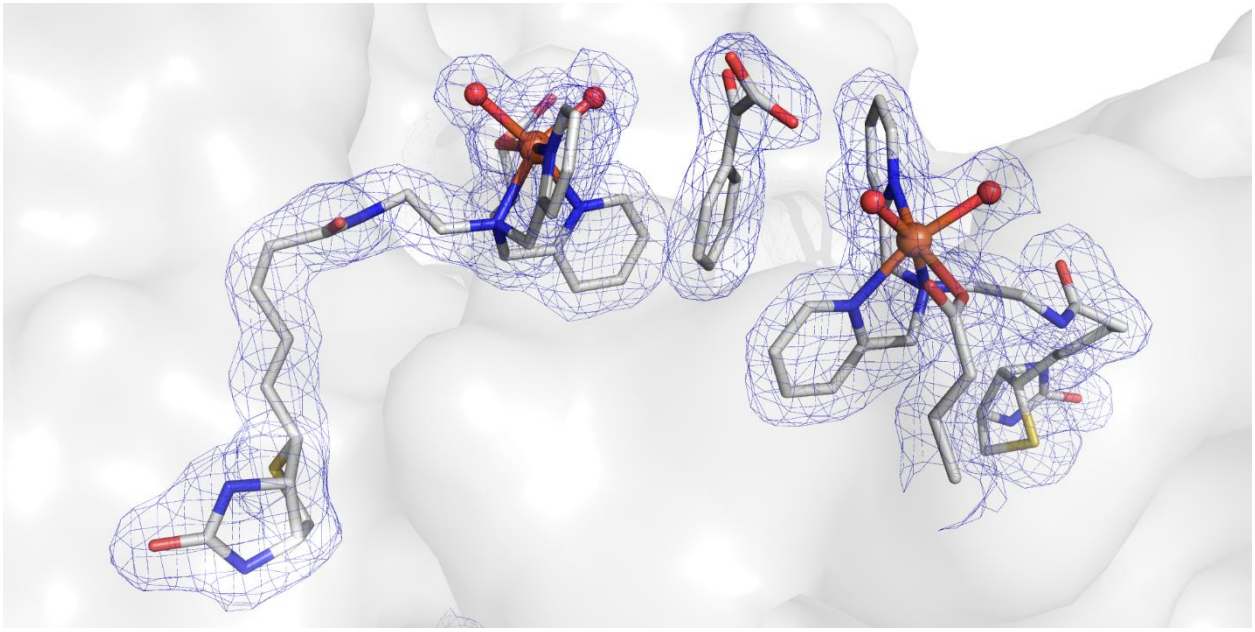

Figure B. 10 Close up views of the Fe sites in the molecular structure of **3–PGA** solved in C121 symmetry. Dimer A and B of the tetrameric Sav are shown for clarity. The protein is displayed in cartoon representation and the Fe complex as well as residues 112 as sticks. The position of the ligand molecules is indicated by the $2F_o$-F_c electron density (blue, contoured at 1 σ). Fe is colored in orange, N atoms are in blue, and O atoms/water molecules are in red. The number schemes in **3–PGA** are the same as those in Figure B.6.

Table B.1 Selected bond lengths and (Å) and angles (°) for **3–O_2**, **3–PGA**, **3–PGA–O_2**.

Bond lengths and angles	**3–O_2–1**	**3–O_2–2**	**3–PGA**	**3–PGA–O_2–1**	**3–PGA–O_2–2**
Fe–O1	2.41	2.38	2.19	2.14	2.14
Fe–O3	2.27	2.09	2.15	2.17	2.17
Fe–O4	2.46	2.38	2.24	2.17	2.17
Fe–O5	2.32	2.33	–	2.31	2.31
Fe–N1	2.32	2.15	2.31	2.23	2.13
Fe–N2	2.31	2.49	2.28	2.30	2.29
Fe–N3	2.32	2.51	2.25	2.18	–
N1–Fe–O3	160	154	158	165	161
N1–Fe–N2	72	79	69	71	72
N2–Fe–O4	–	–	165	160	159
O3–Fe–O4	–	–	98	91	91
O1–Fe–N1	97	99	96	95	101
O1–Fe–N2	84	86	84	80	80
O1–Fe–N3	170	167	164	168	–
O1–Fe–O3	92	98	52	93	93
O1–Fe–O4	–	–	86	81	81
N1–Fe–O4	–	–	103	103	103
N2–Fe–O3	92	122	–	98	97
O1–Fe–O5	94	95	–	–	–
O3–Fe–O5	100	58	–	–	–
N2–Fe–O5	169	179	–	–	–
N1–Fe–O5	98	100	–	–	–
N3–Fe–O5	77	76	–	–	–
N1–Fe–N3	80	73	77	76	–
N2–Fe–N3	104	103	107	103	–
N3–Fe–O3	94	86	98	97	–
N3–Fe–O4	–	–	81	94	–
O2–O3	1.45	1.45	–	–	–
Fe–O3–O4	79	83	–	–	–
Fe–O4–O5	–	–	–	78	78
O3–O4	–	–	–	1.37	1.37
Average $centroid_{py}\cdots centroid_{ph}$	–	–	4.78	–	–
O3···O2	3.12	–	2.74	–	–
O4···O3	–	2.93	–	–	–
O5···Wat2	2.66	–	–	–	–
Wat2···N49	3.02	–	–	–	–
O5···Wat1	–	2.69	–	–	–
Wat1···N49	–	3.03	–	–	–
O4···Wat3	–	–	2.62	–	–
Wat3···N49	–	–	3.30	–	–
O4···Wat110	–	–	–	2.28	2.28
Wat110···N49	–	–	–	3.02	3.02

Table B.2 X-ray Crystallography Data Processing and Refinement Statistics for $I4_122$ symmetry solutions of **3–O₂–1** and **3–O₂–1**.

Identification		
Sav Mutant	$K_{121}A$-$S_{112}E$	$K_{121}A$-$S_{112}E$
Fe complex	$[Fe^{II}$(biot-et-dpa$(OH_2)_2$ $(\kappa^1$-$O_{E_{112}})]^+ + O_2$ (**3–O₂–1**)	$[Fe^{II}$(biot-et-dpa$(OH_2)_2$ $(\kappa^1$-$O_{E_{112}})]^+ + O_2$ (**3–O₂–2**)
PDB Code	Unpublished	Unpublished
Fe complex PDB 3-letter code	QGI	QGI
Data Processing		
Unit Cell	a, b, c = 57.5 Å, 57.5 Å, 183.3 Å α, β, γ = 90°	a, b, c = 57.6 Å, 57.6 Å, 183.5 Å α, β, γ = 90°
Space Group	$I4_122$	$I4_122$
Resolution (Å)	45.81 – 1.70	45.87 – 1.60
Highest resolution shell (Å)	1.73– 1.70	1.63– 1.60
R_{merge} (%)	26 (140)	20 (171)
No. of unique reflections	17501 (913)	20987 (999)
Multiplicity	12.8 (13.9)	13.0 (14.1)
I/Sig(I)	7.6 (2.6)	9.1 (2.2)
Completeness	100.0 (100.0)	100.0 (100.0)
CC(1/2)	0.986 (0.914)	0.994 (0.793)
Beamline	ALS 5.0.2	ALS 5.0.2
Structure Refinement		
R_{work}	0.26	0.29
R_{free}	0.29	0.27
Rmsd bond length (Å)	0.013	0.013
Rmsd bond angle (°)	2.299	2.340
Rmsd compared to biotin-Sav WT (PDB 1STP) (Å)	0.68	0.67
No. ligands		
Fe complex	1	1
Water	43	52
PGA	–	–
O_2	1	1

Table B.3 Summary of structural details for **3–O_2–1** and **3–O_2–1**.

PDB Code	Unpublished	Unpublished
Complex	**3–O_2–1**	**3–O_2–2**
Electron density at Fe in F_o–F_c omit map (σ)	18	17
Anomalous dispersion density at Fe (σ)	–	–
Geometry of Fe complex	Distorted octahedral	Distorted octahedral
Coordination number of Fe complex	7-coordinate	7-coordinate
Occupancy of Fe complex (%)	100	100
B-factor (Å^2)		
Overall protein	19	19
S112E	80/20: 22/14	22
K121A	17	16
Fe complex	23	24
DPA	22	24
Fe	36	32
PGA	–	–
O_2	42	35
Distance Fe–Fe (Å)	10	10

Table B.4 X-ray Crystallography Data Processing and Refinement Statistics for $I4_122$ symmetry solutions of **3–PGA** and **3–PGA–O_2**.

Identification		
Sav Mutant	$K_{121}A$-$S_{112}E$	$K_{121}A$-$S_{112}E$
Fe complex	$[Fe^{II}$(biot-et-dpa$(OH_2)_2(\kappa^1$-$O_{E_{112}})]^+$ + PGA (**3–PGA**)	$[Fe^{II}$(biot-et-dpa$(OH_2)_2(\kappa^1$-$O_{E_{112}})]^+$ + PGA + O_2 (**3–PGA–O_2**)
PDB Code	Unpublished	Unpublished
Fe complex PDB 3-letter code	QGI	QGI
Data Processing		
Unit Cell	a, b, c = 57.5 Å, 57.5 Å, 182.9 Å α, β, γ = 90°	a, b, c = 57.8 Å, 57.8 Å, 184.1 Å α, β, γ = 90°
Space Group	$I4_122$	$I4_122$
Resolution (Å)	45.72 – 1.70	46.03 – 1.44
Highest resolution shell (Å)	1.73– 1.70	1.47– 1.44
R_{merge} (%)	16 (242)	9.4 (149)
No. of unique reflections	17441 (890)	28847 (1430)
Multiplicity	25.2 (24.7)	25.1 (25.7)
I/Sig(I)	15.9 (2.0)	27.6 (2.7)
Completeness	100.0 (100)	100.0 (100.0)
CC(1/2)	0.999 (0.810)	1.000 (0.844)
Beamline	ALS 5.0.2	ALS 5.0.2
Structural Refinement		
R_{work}	0.21	0.17
R_{free}	0.24	0.19
Rmsd bond length (Å)	0.012	0.017
Rmsd bond angle (°)	2.214	2.541
Rmsd compared to biotin-Sav WT (PDB 1STP) (Å)	0.85	0.68
No. ligands		
Fe complex	1	1
Water	51	103
PGA	1	Disordered
O_2	–	1

Table B.5 Summary of structural details for **3–PGA** and **3–PGA–O_2**.

PDB Code	Unpublished	Unpublished
Complex	**3–PGA**	**3–PGA–O_2**
Electron density at Fe in F_o–F_c omit map (σ)	10	45
Anomalous dispersion density at Fe (σ)	13	23
Geometry of Fe complex	Distorted octahedral	Distorted octahedral
Coordination number of Fe complex	6	6
Occupancy of Fe complex (%)	100	80
B-factor (Å²)		
Overall protein	27	16
S112E	24	80/20: 15/9
K121A	23	12
Fe complex	27	16
DPA	27	16
Fe	30	18
PGA	51	–
O_2		29
Distance Fe–Fe (Å)	10	10

Table B.6 X-ray Crystallography Data Processing and Refinement Statistics for C121 symmetry solution of **3–PGA**.

Identification	
Sav Mutant	$K_{121}A\text{-}S_{112}E$
Fe complex	$[Fe^{II}(biot\text{-}et\text{-}dpa(OH_2)_2(\kappa^1\text{-}O_{E_{112}})]^+$ + PGA (**3–PGA**)
PDB Code	Unpublished
Fe complex PDB 3-letter code	QGI
Data Processing	
Unit Cell	a, b, c = 191.6 Å, 57.4 Å, 57.4 Å α, β, γ = 90°, 107.4°, 90°
Space Group	C121
Resolution (Å)	41.80 – 1.99
Highest resolution shell (Å)	2.04 – 1.99
R_{merge} (%)	12 (66)
No. of unique reflections	41038 (3078)
Multiplicity	3.6 (3.8)
I/Sig(I)	7.5 (2.2)
Completeness	99.8 (100.0)
CC(1/2)	0.993 (0.736)
Beamline	ALS 5.0.2
Structure Refinement	
R_{work}	0.21
R_{free}	0.24
Rmsd bond length (Å)	0.010
Rmsd bond angle (°)	2.098
Rmsd compared to biotin-Sav WT (PDB 1STP) (Å)	0.70
No. ligands	
Fe complex	4
Water	183
PGA	2

Table B.7 Summary of structural details for **3–PGA**.

PDB Code	Unpublished
Complex	**3–PGA**
Electron density at Fe in F_o–F_c omit map (σ)	8
Geometry of Fe complex	Distorted octahedral
Coordination number of Fe complex	6
Occupancy of Fe complex (%)	100
B-factor (Å^2)	
Overall protein	28
S112E	27
K121A	24
Fe complex	28
DPA	27
Fe	32
PGA	58
Distance Fe–Fe (Å)	10

*B-factors were averaged from the Sav tetramer

Table B.8 3–PGA bond lengths and distances from C121 symmetry solution.

Bond lengths (Å)	**Monomer A**	**Monomer B**	**Monomer C**	**Monomer D**
Fe–O1	2.15	2.11	2.07	2.17
Fe–O3	2.12	2.10	2.10	2.16
Fe–O4	2.13	2.14	2.20	2.18
Fe–N1	2.32	2.35	2.31	2.33
Fe–N2	2.34	2.34	2.29	2.26
Fe–N3	2.21	2.16	2.21	2.17
O3···O2	2.59	2.63	2.74	2.83
O4···Wat3	2.62	–	–	–
Wat3···N49	3.43	–	–	–
O4···Wat6	–	2.51	–	–
Wat6···N49	–	3.55	–	–
O4···Wat9	–	–	–	2.67
Wat9···N49	–	–	–	3.38
O4···Wat12	–	–	2.74	–
Wat12···N49	–	–	3.20	–
	Dimer A		**Dimer B**	
Average $centroid_{py}$··· $centroid_{ph}$	4.80		4.84	

APPENDIX C

An Anteater and a Jawhawk walk into a lab…

Introduction

As described in Chapter 1, mononuclear Fe enzymes are responsible for several important reactions involving dioxygen activation. There are also many examples of Mn-dependent metalloproteins that are important for dioxygen activation, such as scavenging reactive oxygen species (ROS) in Mn superoxide dismutase (Mn-SOD: Figure C.1A) and water splitting in the oxygen evolving complex (OEC: Figure C.1B) of Photosystem II.[251,335–339] Mn enzymes often feature histidine and carboxylate residues and utilize a common set of Mn–oxygen reactive intermediates to catalyze several chemical transformations. Proposed reactive intermediates include Mn–superoxido, peroxido, hydroperoxido, or oxido species. Several bioinorganic chemists have designed synthetic systems and artificial metalloproteins (ArMs) to elucidate the important coordination sphere effects that

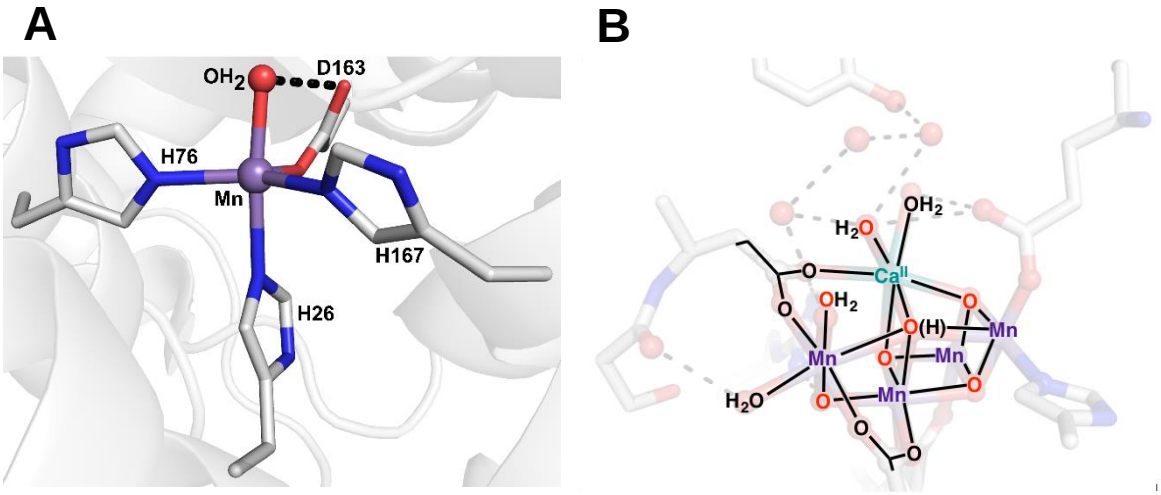

Figure C.1 Active sites of Mn-SOD (**A**: PDB 5A9G) and the OEC of Photosystem II (**B**: 3WU2). H-bonding interaction shown in dashed black lines. OEC Pymol image is from the dissertation of Dr. Victoria F. Oswald.

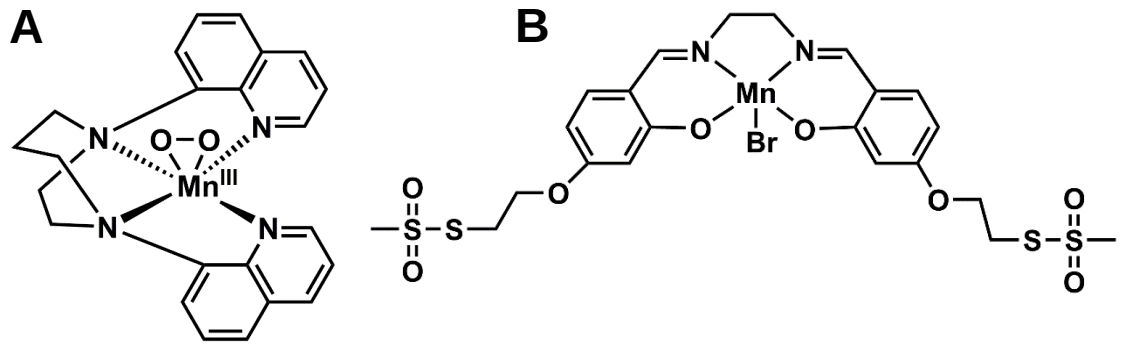

Figure C.2 ChemDraw representations of the Mn^{III}–peroxo species from Jackson (**A**) and the Mn–salen complex immobilized in apo-myoglobin from Lu (**B**).

contribute to the overall function of Mn metalloproteins.[49,73,75,76,340–373] For example, Jackson and coworkers have successfully developed synthetic systems that have trapped several reactive oxygen intermediates, including a Mn^{III}–peroxido and a Mn^{IV}–oxo species, and explored their C–H bond activation and oxygen atom transfer ability. Utilizing the L_7BQ (1,4-di(quinoline-8-yl)-1,4-diazepane) ligand, Denler successfully formed and characterized a Mn^{III}–peroxido species that was able to perform aldehyde deformylation with cyclohexanecarboxyaldehyde and 2-phenylpropionaldehyde (with acid impurities) (Figure C.2A).[371] In addition to synthetic systems, Lu and coworkers have designed an artificial metalloprotein by incorporating an achiral Mn-salen complex into apo sperm whale myoglobin via a dual anchoring approach (Figure C.2B). Immobilizing the Mn-salen complex into myoglobin significantly enhanced the rate and enantiomeric excess of the Mn-salen complex towards the catalytic sulfoxidation of thioanisole.[370]

This appendix was work done in collaboration with Dr. Melissa Denler from the Jackson lab at the University of Kansas. The details of the design and characterization of two new Mn artificial metalloproteins (ArMs) with carboxylate coordination using electron paramagnetic resonance (EPR) spectroscopy and X-ray diffraction (XRD) are discussed.

Results and Discussion

Design concepts. To design Mn ArMs, the ligands described in Chapter 2 and Chapter 4 (biot-et-dpa, biot-pr-dpa) were utilized. With the success of coordinating an endogenous glutamate residue to an Fe center within Streptavidin (Sav) (details in Chapter 2), two Mn ArMs were designed to support the coordination of a glutamate residue to the Mn center.

Synthesis and Characterization of Biotinylated Mn^{II} compounds. The ligands biot-et-dpa and biot-pr-dpa were prepared as described in Chapter 2 and 4. The Mn^{II} complexes were prepared by treatment of biot-n-dpa (n=et, pr) with $Mn^{II}Br_2$ in acetonitrile, which immediately precipitated as a white solid. The Mn^{II} compounds were stored under an inert atmosphere. The Mn^{II} compounds were analyzed by ESI-MS giving molecular ion peaks corresponding to $[Mn^{II}(\text{biot-n-dpa})Br]^+$. The perpendicular ($\perp$-mode) mode EPR spectra showed signals centered around g = 5 and 2, which are consistent with a low spin S = 1/2 mononuclear Mn^{II} species (Figure C.3). Additionally, there is well-resolved 6-line hyperfine splitting associated with g = 2 signal, which is consistent with a Mn center having a nuclear

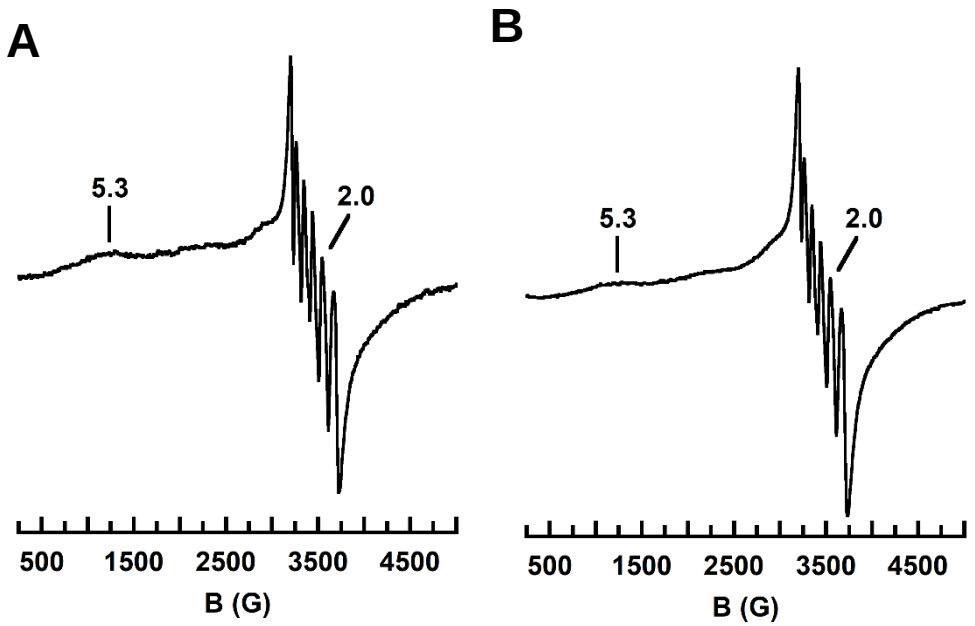

Figure C.3 EPR spectra of $[Mn^{II}(\text{biot-et-dpa})Br_2]$ (**A**) and $[Mn^{II}(\text{biot-pr-dpa})Br_2]$ (**B**) recorded in 50 mM Mes buffer pH 6 at 77 K.

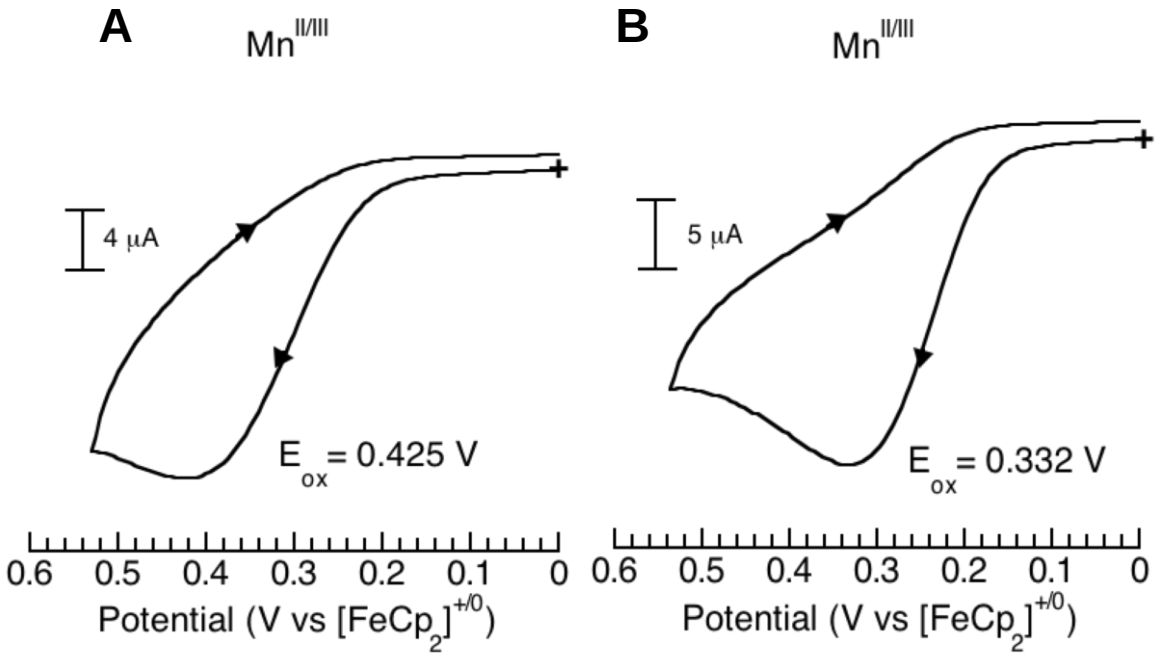

Figure C.4 Cylic voltammagrams of [Mn^{II}(biot-et-dpa)Br_2] (**A**) [Mn^{II}(biot-pr-dpa)Br_2] (**B**) recorded in DMF: $Mn^{II/III}$ couple. Measurements were done at room temperature with a scan rate of 100 mV/s.

spin of $I = 5/2$ (Figure C.3). Comparable studies were done in DMF/THF (Figure C.11). The hyperfine splitting in both the buffer and DMF/THF studies possibly indicates either multiple conformations of species or more than one species present in solution. There were no visible absorbance bands in the UV-vis spectra for the Mn^{II} complexes, which is common for spin forbidden Mn^{II} compounds. Electrochemical data revealed an irreversible one electron redox couple at 0.425 V vs $[FeCp_2]^{+/0}$ for [Mn^{II}(biot-et-dpa)Br_2] and 0.332 V vs $[FeCp_2]^{+/0}$ for [Mn^{II}(biot-pr-dpa)Br_2] (Figure C.4: isolated). The one electron event is thought to be the $Mn^{II/III}$ redox couple and is possibly irreversible because the Mn^{II} complexes undergo a conformational change at the Mn^{III} oxidation state. There was an unassignable redox event that was also observed. It is possible that the redox event could be attributed to the buffer, or an oxidation of the ligand (Figure C.10: full). Titration experiments were done with 2-(4'-hydroxyazo-benzene)benzoic acid (HABA) to determine the binding stoichiometry of the [Mn^{II}(biot-n-dpa)Br_2] complexes to Sav. The HABA studies

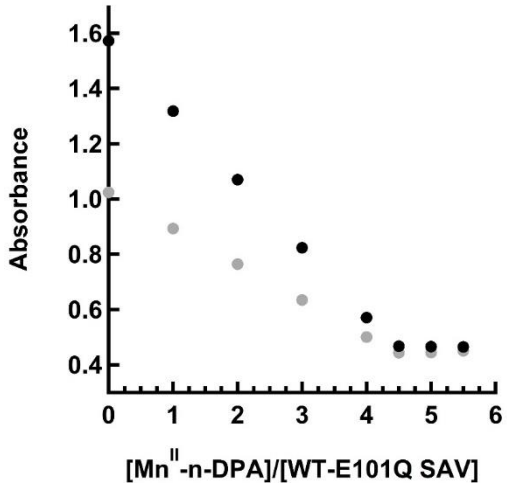

Figure C.5 HABA Titrations of **C1** (black) and **C2** (grey).

indicated a 4:1 biotinylated Mn^{II} complex to protein host ratio, confirming complete occupancy within Sav (Figure C.5).

Spectroscopic Characterization of Mn^{II}-n-dpa⊂2xMS$_{112}$E (n=2, 3). The ArMs containing the [Mn^{II}(biot-et-dpa)Br_2] (**C1**) and [Mn^{II}(biot-pr-dpa)Br_2] (**C2**) were prepared by incubating a water solution of the complexes with 2xM-S$_{112}$E-Sav at pH 6 in MES buffer

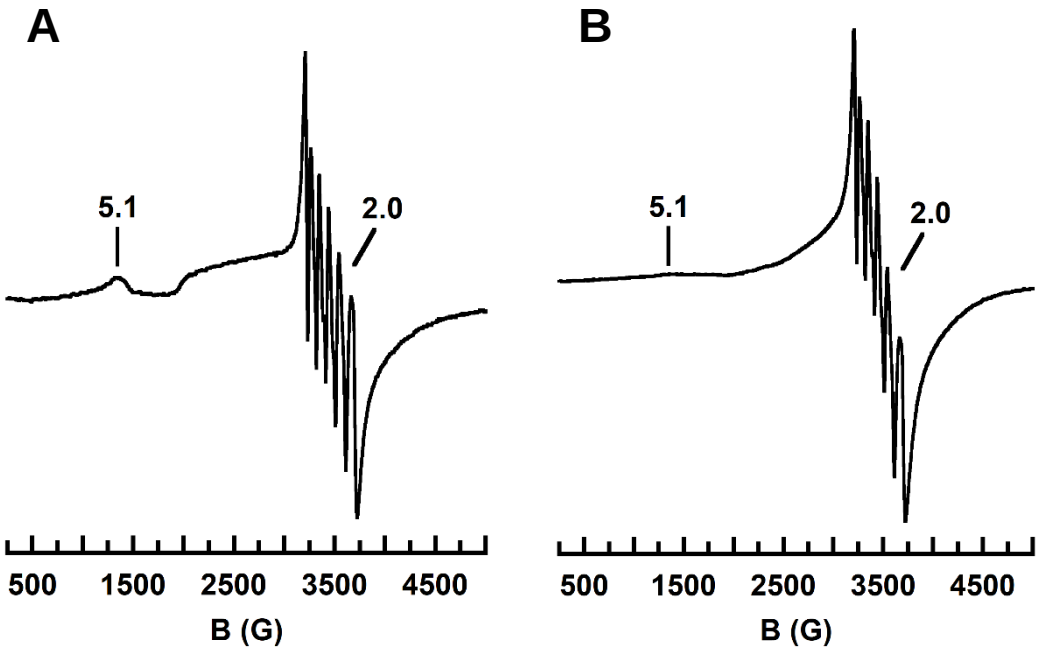

Figure C.6 EPR spectra of **C1** (**A**) and **C2** (**B**) recorded in 50 mM Mes buffer pH 6 at 77 K.

(50 mM). The EPR spectra for both **C1** and **C2** still revealed a signal centered at g = 5 and 2, with similar hyperfine splitting as seen in the Mn complexes outside the protein host (Figure C.6). The hyperfine splitting indicated the possibility of different conformations of the complex within Sav. Further work determining the species present in solution is necessary.

*Structural Characterization of **C1**.* Single crystals of **C1** were prepared by soaking crystals of apo-2xM-S_{112}E-Sav with [Mn^{II}(biot-et-dpa)Br_2]. Its structure was solved to a resolution of 1.49 Å to reveal a mononuclear Mn immobilized within each subunit of Sav. The structure of **C1** was similar to the structure of **1a** (detailed in Chapter 2), with the pyridine off conformation modelled to 100% occupancy (Figure C.7A and C.7B). Instead of a mixture of unbound and bound pyridine group to the Fe center, in **C1**, the pyridine is completely unbound to the Mn center. While the dpa ligand and water molecules adopts a similar conformation to **1a**, the carboxylate amino acid residue is rotated ~90° away from the Mn center and modelled to 70% occpuancy (Figure C.7C). There are two conformations of the gluatamate residue and the second conformation overlays with the second gluatamate conformation from **1a**, but is modelled with 30% occpuancy (Figure C.7C). As modelled, the carboxylate residue is near the Mn center with a Mn–O1 bond distance of 2.65 Å, which is typically considered too long to be a bond. However, upon reviewing the other bond distances to the Mn center, the Mn–N2, Mn–O3, and Mn–O2 bond distances are 2.50, 2.34, and 2.48 Å, respectively, which are also longer than the comparable **1a**

structure. At this time, the density has been modelled to reflect a possible coordination of the glutamate residue, but more work is necessary to ensure that this is the correct orientation of the Mn complex and the glutamate residue. In addition to the primary coordination sphere similarities, there are several noncovalent interactions that are similar

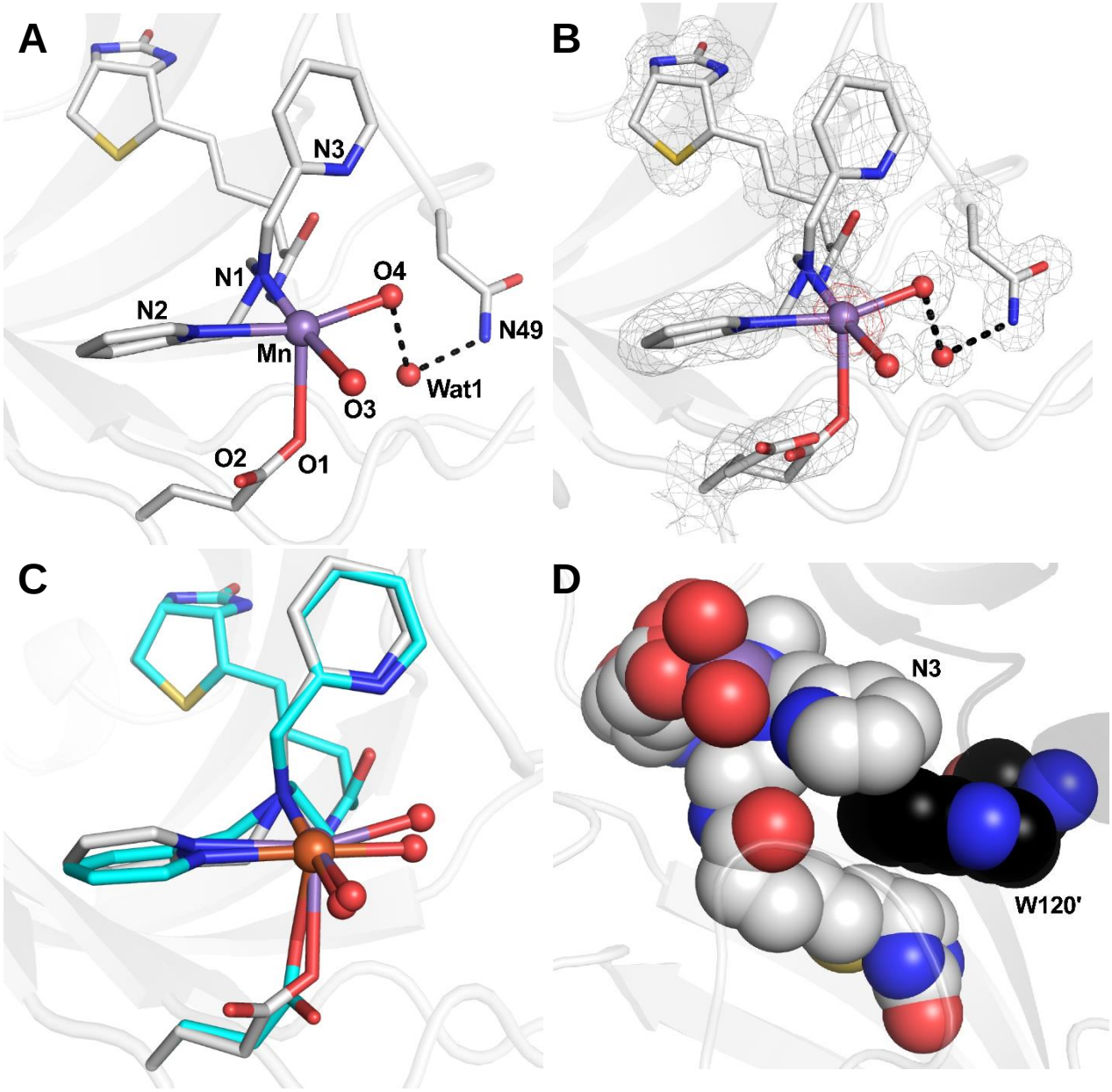

Figure C.7 Molecular structure of **C1** (**A**). The position of the complex is indicated by the $2F_o$-F_c electron density map (grey, contoured at 1 σ) and anomalous map (red, contoured at 4 σ) (**B**). Overlay of the molecular structures of **C1** (grey) and **1a** (cyan) (**C**). A partial space-filling representation of **C1** highlighting the π-stacking interaction of the biotinylated Mn^{II} complex that includes one of its pyridine rings with $W_{120'}$ from the neighboring subunit (**D**, black). Mn ions are colored in purple, N atoms are in blue, O atoms/water molecules are in red. H-bonds are shown as black dashed lines.

to **1a**. For example, O3 is participating in the same H-bonding interaction with a nearby water molecule (Wat1) and the residue group of N_{49}. Also, the unbound pyridine group is participating in the same π-stacking interaction with the residue W_{120} from the adjacent subunit with a $centroid_{py}\cdots centroid_{Trp}$ distance of 4.74 Å (Figure C.7D, Tables C.1, C.2, and C.3).

*Structural Characterization of **C2**.* Single crystals of **C2** were prepared as described above, but instead using [Mn^{II}(biot-pr-dpa)Br_2]. Analysis of the structure resolved to 1.46 Å

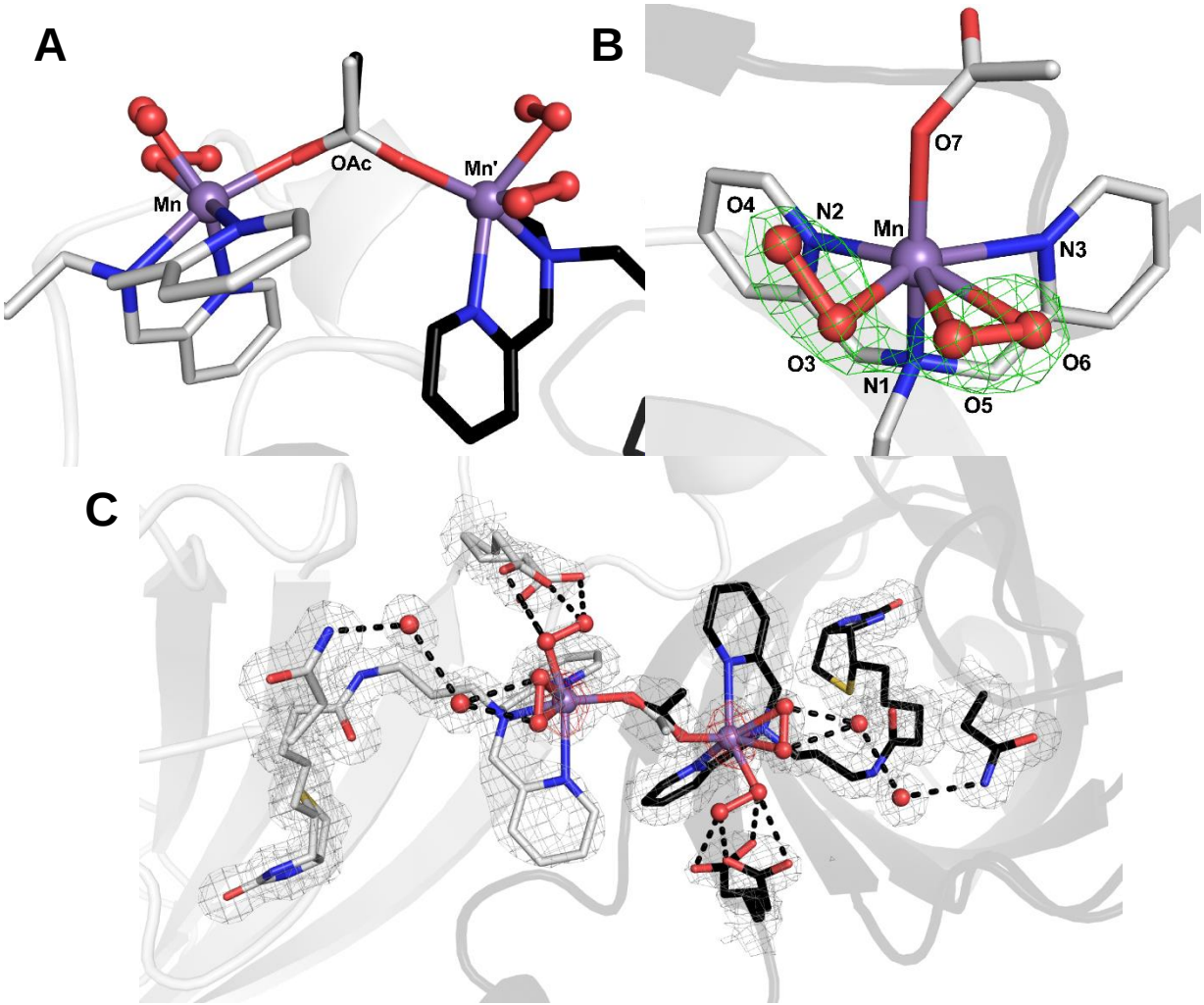

Figure C.8 Molecular structure of **C2** with closeup view of the Mn dimer (**A**), the two conformations of O_2 binding with omit map displayed, only half of the dimer is shown for clarity (**B**: green, contoured at 3 σ) and the cofactor indicated by the $2F_o$-F_c electron density map (**C**: grey, contoured at 1 σ). Mn ions are colored in purple, N atoms are in blue, O atoms/water molecules are in red. H-bonds are shown as black dashed lines.

resolution revealed a primary coordination sphere similar to bound confirmation of the Fe^{II} complex, **1b** (detailed in Chapter 2). Using the longer linker length of propyl, an unexpected piece of density was found between the two immobilized Mn complexes within the Sav dimer. This density was modelled to an acetato ligand that was bridging the two Mn centers with Mn–O7/O7' bond distances of 2.24 and 2.05 Å (Figure C.8A). EPR studies conflict with the molecular structure because an EPR signal is observed for **C2** that indicates the species is a mononuclear Mn^{II} complex. However, the conditions for crystallography and solution studies are different and the presence of acetate in the crystallization buffer is likely the source of the difference between the crystallographic and solution studies. In addition to forming a dinuclear Mn complex within Sav, there was also elongated and disordered density in place of the *cis* water ligands that were present in **1b**. This density was modelled to an O_2 unit that is disordered over two locations (Figure C.8B

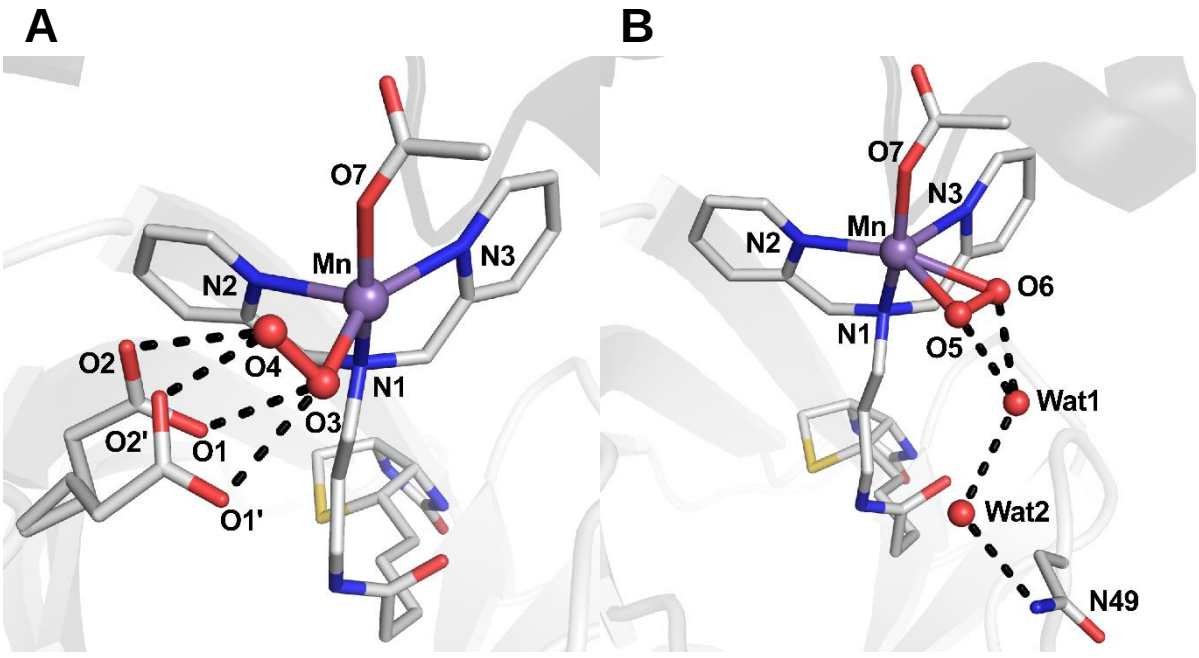

Figure C.9 Molecular structure of **C2** with closeup view of the two conformations of O_2 binding (**A**: end on; **B**: side on), only half of the dimer is shown for clarity. Mn ions are colored in purple, N atoms are in blue, O atoms/water molecules are in red.

and C.8C). In one coordination site, the O_2 unit is modelled to 50% occupancy and is coordinated in an asymmetric side-on fashion to the Mn center with Mn–O5 and Mn–O6 bond distance of 2.24 Å and 2.40 Å and a Mn–O5–O6 bond angle of 78° (Figure C.9B). In this location, the distal oxygen, O6, is participating in a H-bonding network with O6 H-bonded to Wat1, Wat1 H-bonded to Wat2, and Wat2 H-bonded to the residue group of N_{49}. In the second coordination site, the O_2 unit is again modelled to 50% occupancy and is coordinated in an end-on fashion with a Mn–O3 bond distance of 2.10 Å with a Mn–O5–O6 bond angle of 97° (Figure C.9A). It is possible that this O_2 unit is participating in H-bonding interactions because both the proximal and distal oxygen, O3 and O4 respectively, are within H-bonding distance to the carboxylate group of the glutamate residue. The glutamate residue is modelled with two conformations at 70% and 30% occupancy. O3 and O4 are within H-bonding distance of either conformation of the glutamate carboxylate group, with distances ranging from 2.54–3.32 Å (Figure C.9A). More studies would need to be done to determine if the O_2 unit is a hydroperoxido ligand that could participate in H-bonding interactions with the carboxylate group.

Summary and Conclusions

In this Appendix, two new Mn ArMs (**C1** and **C2**) were designed and characterized via EPR spectroscopy and XRD. The work between **C1** and **C2** highlight the synthetic advantage of biot-Sav technology because the two Mn complexes [Mn^{II}(biot-et-dpa)Br_2] and [Mn^{II}(biot-pr-dpa)Br_2] only differ by one carbon atom in the linker between the biotin moiety and the dpa chelator. This subtle change led to major changes in the molecular structures of **C1** and **C2**, specifically, that with the ethyl linker length, a mononuclear Mn complex was constructed, whereas, with the propyl linker length, a dinuclear Mn complex

was constructed. While the role of the carboxylate group from the glutamate residue is unclear based on the structural data so far, it is possible that in **C1**, it is coordinated to the Mn center and in **C2**, it is H-bonding to an O_2 unit bonded to the Mn center, providing a stabilization effect for the reactive species. Initial studies with H_2O_2 were attempted but more work will need to be conducted to determine the reactivity of **C1** and **C2**. Additionally, more extensive EPR studies with and without acetate present need to be conducted to determine if a dinuclear Mn center can be formed in Sav in solution. More structural data is needed to determine if the glutamate is coordinated to the Mn center in **C1** and if O_2 can be reproducibly bound to the Mn centers in **C2**. Lastly, if O_2 is coordinated to the Mn center, resonance Raman would be necessary determine the identity of the O_2 ligand.

Experimental Details.

General Methods. All commercially available reagents were obtained of the highest purity and used as received. Acetonitrile (CH_3CN) and diethyl ether were degassed with argon and dried by vacuum filtration through activated alumina according to the procedure by Grubbs.[183] Triethylamine was distilled from KOH. Thin-layer chromatography (TLC) was performed on Merck 60 F254 aluminum-backed silica plates or Merck 60 F254 glass-backed basic aluminum oxide plates. Eluted plates were visualized using UV light. Silica or basic alumina gel chromatography was performed with the indicated solvent system using Fisher reagent silica gel 60 (230-400 mesh) or Sigma reagent Brockmann 1 basic aluminum oxide 58 (150 mesh). Biotin pentafluorophenol ester (biot-PFP)[184] and di-(2-picolyl)amine[185] were prepared according to literature procedures.

Physical Methods

Instrumentation. Mass spectra were measured on a MicroMass AutoSpec E, a MicroMass Analytical 7070E, or a MicroMass LCT Electrospray instrument. Electronic absorbance spectra were recorded with a Cary 50 or 8453 Agilent UV-vis spectrophotometer. X-band (9.64 GHz) EPR spectra were recorded on a Bruker spectrometer equipped with Oxford liquid helium cryostats. The quantification of all signals was relative to a CuEDTA spin standard. The concentration of the standard was derived from an atomic absorption standard (Aldrich). For all instruments, the microwave frequency was calibrated with a frequency counter and the magnetic field with an NMR gaussmeter. A modulation frequency of 100 kHz was used for all EPR spectra. The EPR simulation software (SpinCount) was written by our collaborating author Michael P. Hendrich.[186] Cyclic voltammetry experiments were conducted using a CH1600C electrochemical analyzer.

Preparative methods

Biot-et-dpa was prepared as described in Chapter 2 and biot-pr-dpa was prepared as described in Chapter 4.

Preparation of metal complexes

[Mn^{II}(biot-et-dpa)Br_2].[187] [Mn^{II}(biot-et-dpa)Br_2] was prepared by addition of biot-et-dpa (40.2 mg, 0.08 mmol) in 10 mL CH_3CN to $MnBr_2$ (20.3 mg, 0.09 mmol). A white solid immediately precipitated from the solution. The suspension was allowed to stir under N_2 for 30 min, after which the white solid was collected via filtration, washed with CH_3CN:diethyl ether (1:1), and dried under vacuum (47.3 mg, 87%). The solid was stored under an inert atmosphere. HR-MS (ESI, 1% DMF:MeCN) m/z calcd for $C_{24}H_{32}MnN_6O_2SBr$ [M – (Br^-)] 602.09, found 604.0.

[Mn^{II}(biot-pr-dpa)Br_2].[187] [Mn^{II}(biot-pr-dpa)Br_2] was prepared by addition of biot-pr-dpa (40.7 mg, 0.19 mmol) in 10 mL CH_3CN to $MnBr_2$ (83.1 mg, 0.17 mmol). A white solid immediately precipitated from the solution. The suspension was allowed to stir under N_2 for 30 min, after which the white solid was collected via filtration, washed with CH_3CN:diethyl ether (1:1), and dried under vacuum (86.1 mg, 72%). The solid was stored under an inert atmosphere. MS (ESI, 1% DMF:MeCN) m/z calcd for $C_{25}H_{34}MnN_6O_2SBr$ [M – (Br^-)] 616.10, found 618.0.

Spectroscopic methods

HABA Titrations. To 2.4 mL of 8 μM Sav in 200 mM sodium phosphate buffer at pH 7 was added 300 μL of a 10 mM 2-(4′-hydroxyazobenzene)benzoic acid (HABA) in 200 mM phosphate buffer pH 7. After 5 min equilibration, the absorbance at 506 nm was recorded. A solution of 1 mM Mn complex in nanopure water was added in 4-20 μL portions until approximately 4 equivalents had been added. The absorbance at 506 nm was recorded until no further changes in intensity were observed.

EPR Studies. A solution of protein (750 μM) was prepared in nanopure water. Four equivalents of Mn^{II} complex (3 mM) in nanopure water were added to the protein solution. Samples were prepared in a final volume of 200 μL containing 50 mM MES buffer at the indicated pH. The sample was frozen at 77 K in liquid nitrogen and run at 77 K. Samples were also prepared with 10 mM Mn^{II} complex in a total volume of 200 μL DMF/THF (Figure C.9). It is important to note it is possible that DMF disrupts the Mn^{II} complexes. This same effect was seen for the Fe^{III} complexes described in Chapter 4.

Electrochemical Measurements. Experiments were conducted using a CH1600C electrochemical analyzer with 0.1 M tetrabutylammonium perchlorate (TBAP) as the

supporting electrolyte. A glassy carbon electrode was used for the working electrode with a $AgNO_3$ reference electrode and a platinum wire counter electrode. A ferrocenium/ferrocene couple ($[FeCp_2]^{+/0}$) was used as an internal standard. A solution of 100 mM Mn^{II} complex was prepared in a final volume of 4 mL of electrolyte:DMF solution (0.1 M TBAP in DMF).

Protein Preparation and Crystallography

Protein Expression and Purification

Preparation of Sav variants. The construction of $E_{101}Q$-$K_{121}A$-$S_{112}E$-Sav and other variants was achieved by site-directed mutagenesis (SDM) using the codon optimized $K_{121}A$-pET24a-Sav plasmid,[191] the following primers and, and Q5 polymerase.

$E_{101}Q$_fwd: 5'-GGTGCACAAGCACGCATTAATACCC-3'

$E_{101}Q$ _rev: 5'-GTGCTTGTGCACCACCAACATACTG-3'

$S_{112}E$_fwd: 5'-GACCTACGGCACCACCGAAGCAAATGC-3'

$S_{112}E$_rev: 5'-GTGCCGTAGGTCAGCAGCCACTGG-3'

Amplification of pET24a-Sav mutant plasmids was accomplished by the transformation of SDM reaction mixtures into DH5α ultracompetent cells. Plasmids were isolated using a Miniprep kit from Qiagen, eluting the final plasmid with distilled deionized-water (ddH_2O, 18 MΩ cm^{-1}). DNA sequencing was performed by Genewiz.

Sav Expression. Transformation of 4 μL amplified plasmids into 50 μL Rosetta cells or bl21 cells was followed by rescue with 450 μL LB media. Of this solution, 200 μL was spread aseptically onto LB/Kanamycin agar plates and incubated overnight at 37 °C. Inoculation of a starter culture containing 500 mL LB media and the same antibiotic from a single colony was followed by incubation overnight at 37 °C and shaking at 225 rpm. From this starter

culture, 25 mL was used to inoculate each 2L flask containing 500 mL LB media, 25 mL each of 20x sugar (12% glycerol, 1% glucose, 10% lactose) and salt (1 M Na_2HPO_4, 1 M KH_2PO_4, 0.5 M $(NH_4)_2SO_4$) stocks, 1 mL of 1 M $MgSO_4$, 100 µL 5000x trace metal mix (containing 1 M $CaCl_2$, 100 mM $FeCl_3$, 10 mM $MnCl_2$, 10 mM $ZnSO_4$, 2 mM $CoCl_2$, 2 mM $CuCl_2$, 2 mM $NiCl_2$, 2 mM Na_2MoO_4, and 2 mM H_3BO_3 all in 60 mM HCl), and 250 µL of 100 mg/mL Kanamycin. Incubation at 37 °C and 225 rpm was continued until cells reached OD_{600} = 0.6–0.8, at which point the temperature was dropped to 25 °C and cultures incubated another 24 h.

Sav purification. Cultures were centrifuged at 4000 x *g* for 20 min at 4 °C. The resulting cell pellet was resuspended in lysis buffer (50 mL per 1 L expressed) containing 20 mM Tris buffer pH 7.4, 1 mg/mL lysozyme, and a spatula tip of DNase I. The suspension was then allowed to shake at 25 °C and 225 rpm for 6-8 h followed by one overnight freeze-thaw cycle. Dialysis against 6 M guanidinium hydrochloride pH 1.5 for 24 h was followed by neutralization via dialysis against 20 mM Tris buffer pH 7.4 for 24 h, and against nanopure H_2O for another 24 h. Dialysis overnight against iminobiotin (IB) buffer containing 500 mM NaCl and 50 mM $NaHCO_3$ at pH 10.5 afforded the crude, biotin-free lysate. This material was centrifuged at 10,000 x *g* for 1 h at 4 °C and the soluble portion loaded onto an iminobiotin-agarose column pre-equilibrated with IB buffer. The column was washed with 6 column volumes (CVs) of IB buffer or until the absorbance at 280 nm (A_{280}) dropped to zero. Elution with 1% acetic acid in nanopure H_2O, and pooling fractions by A_{280}, provided highly pure (>95%) Sav as assessed by 18% SDS-PAGE. Pooled fractions were dialyzed against 10 mM Tris pH 7.4 for 24 h followed by dialysis in ddH_2O for an additional 72 h and were then lyophilized. Yields of lyophilized protein were typically 100 mg per L expressed, and the solid protein was stored at 4 °C.

Protein Crystallization

*Crystallization of [Mn^{II}(biot-et-dpa)(OH_2)$_2$(κ^1-O_{E112})⊂2xM-S_{112}E-Sav] (**C1**).* Apo-Sav protein was crystallized by sitting drop vapor diffusion method. Diffraction quality crystals were grown at room temperature by mixing 3.5 µL of protein solution (26 mg/mL lyophilized protein in water) and 1.5 µL of crystallization buffer (2.0 ammonium sulfate, 0.1 M sodium acetate, pH 4). The droplet was equilibrated against a reservoir solution of 100 µL crystallization buffer. Single crystals of Sav were prepared by soaking apo-crystals in a soaking buffer (2.6 ammonium sulfate, 0.1 M sodium acetate, pH 6) with a 10 mM stock solution of [Mn^{II}(biot-et-dpa)Br_2] in nanopure water (9 µL crystallization buffer, 1 µL [Mn^{II}(biot-et-dpa)Br_2]) for 3 h. After the soaking, crystals were transferred to cryo-protectant for 1 min (30% glycerol in soaking buffer) and shock-frozen in liquid nitrogen. It was difficult to obtain this molecular structure; the one reported here was the only successful crystal after many attempts.

*Crystallization of [Mn^{II}(biot-pr-dpa)(O_2)(OAc)⊂2xM-S_{112}E-Sav] (**C2**).* Apo-Sav protein was crystallized by sitting drop vapor diffusion method. Diffraction quality crystals were grown at room temperature by mixing 3.5 µL of protein solution (26 mg/mL lyophilized protein in water) and 1.5 µL of crystallization buffer (2.0 ammonium sulfate, 0.1 M sodium acetate, pH 4). The droplet was equilibrated against a reservoir solution of 100 µL crystallization buffer. Single crystals of Sav were prepared by soaking apo-crystals in a soaking buffer (2.6 ammonium sulfate, 0.1 M sodium acetate, pH 6) with a 10 mM stock solution of [Mn^{II}(biot-pr-dpa)Br_2] in nanopure water (9 µL crystallization buffer, 1 µL [Mn^{II}(biot-pr-dpa)Br_2]) overnight. After the soaking, crystals were transferred to cryo-protectant for 1 min (30% glycerol in soaking buffer) and shock-frozen in liquid nitrogen. It is important to note that

this was all performed in air and not in an inert atmosphere. It is necessary to perform these same experiments by purposefully the soaking the Mn^{II} crystals in an O_2-saturated buffer and obtain the molecular structure.

X-ray diffraction data collection processing. X-ray diffraction data were collected at the the Advanced Light Source (BL 8.2.1 and 8.2.2) at a wavelength of 1 Å. X-ray diffraction data was processed with XDS[192] or iMosflm[193] and scaled with AIMLESS (CCP4 Suite).[193] The structures were solved by molecular replacement using program PHASER (CCP4 Suite)[193] and the structure 2QCB from the PDB as input model ligand with water molecules removed. For structure refinement REFMAC5 (CCP4 Suite)[194] and PHENIX.REFINE[195] were used. Ligand manipulation was carried out with program REEL using the small molecule crystal structure RAGQEV01 from the Cambridge Structural Database as an input model.[248] For water picking, electron density, and structure visualization, the software COOT[197] was used. Figures were drawn with PyMOL (the PyMOL Molecular Graphics System, Version 1.8.2.3, Schrödinger, LLC). Crystallographic details, processing and refinement statistics are given in Supplementary Table C.2-C.5.

Structural Results.

Crystal Color. All crystals of Sav soaked with [Mn^{II}(biot-n-dpa)Br_2] were colorless.

Structural Refinement. Apo-crystals of proteins 2xM-Sav soaked with [Mn^{II}(biot-n-dpa)Br_2] constituted space group $I4_122$ with unit cell parameters reported in Tables C.2 and C.3. A single Sav monomer was obtained per asymmetric unit after molecular replacement. Protein residues 2-10 and 135-159 of the N- and C-terminus, respectively, were not resolved in the electron density, presumably due to disorder. Starting from the Sav monomer, the biological homotetramer is generated by application of crystallographic C_2-

symmetry axes along the x-, y- and z-axes of the unit cell. The overall protein structures are virtually identical to structure biotin ⊂ WT-Sav (PDB 1STP, see Tables C.2 and C.4).

Because **C2** had a bridging acetato ligand located at the crystallographic C_2-symmetry axis, **C2** was also solved in reduced C121 symmetry to ensure that the acetate density was not an artifact of symmetry. The unit cell parameters are reported in Table C.4 and C.5. A single Sav tetramer was obtained per asymmetric unit after molecular replacement.

General Complex Modeling. For all structures of apo-protein crystals soaked with the corresponding Mn-complexes the following general observations were made: i) residual electron density in the F_o-F_c map was observed in the biotin binding pocket, ii) in the biotin vestibule which is flanked by protein residues of loop-3,4^A (the superscript number indicates Sav monomer within tetramer) loop-4,5^C, loop-5,6^A loop-7,8^A and loop-7,8^B, and iii) an anomalous dispersion density map indicated a significant peak in the biotin vestibule superimposed with the electron density peak. The residual electron density was fit with the corresponding Mn-complexes, which projected Mn to the position of the strong anomalous density peak.

*Structural refinement of **C1.*** In $I4_122$ symmetry, the refinement statistics show that the detector could have been moved closer to the crystal in order to get a higher resolution structure. The high I/Sig(I) and $CC_{1/2}$ are indicators that the resolution is lower than the structure could have been. This also may have an effect on the bond distances that are seen in the structure. Most of the primary coordination sphere bond distances to the Mn center are much longer than normally seen in Sav structures with the dpa ligand. This can also be because there is disorder in the ligand, making it more challenging to fit the complex. With

this structure because of the significantly longer bond lengths, it is modelled with the glutamate amino acid residue coordinating to the Mn center but this must be reproduced to ensure this is the correct modelling.

Structural refinement of ***C2.*** In the $I4_122$ symmetry solution, the F_o-F_c density showed disordered density spread over both of the open coordination sites to the Mn center. Because of the diffuse nature of the density, O_2 was fit to both locations with 50% occupancy. Acetate was modelled to 50% because it is at the center of C_2 symmetry. The acetate density seemed to also indicate that the acetate ligand was disordered. The larger B-factor is likely because of this disorder and because it is at the surface of the protein and solvent exposed.

In the C121 symmetry solution, there was still density in the F_o-F_c map to be able to model the acetato ligand in the same location as was seen in the $I4_122$ symmetry solution, indicating that the acetate is not an artifact of symmetry (Figure C.12, Tables C.4, C.5, and C.6). O_2 was modelled in the same manner as in the $I4_122$ symmetry solution. The O5–O6 O_2 ligand has strong density at 1σ; however, the O3–O4 O_2 ligand had weak density that could be seen at 1 σ, but was more observable at 0.8 σ. It is possible because of the disorder associated with the O_2 ligand that at lower symmetry, it is not a significant enough resolution to be able to see both O_2 confirmations. The disorder of the O_2 ligand can be responsible for the higher B-factors observed. Additionally, the disorder of the complex can explain the decreased occupancy for the Mn center. Lastly, the glutamate was modelled with two confirmations at 50% each, which is different than the 70/30 ratio seen in the $I4_122$ symmetry solution. At lower symmetry, the disorder of the glutamate side chain made determining the dominant confirmation difficult and thus, was left at 50%.

Additionally, it is possible that in both the high and low symmetry solutions, there could be a water ligand disordered at 50% occupancy; meaning that when the O_2 ligand is in one coordination site, the other could be occupied by water and vice versa. This was modelled but ultimately not left in the final solution because it was difficult to make a reasonable assignment with the density. Poulder maps supported that O_2 was reasonable fit for the density and the B-factors for the O_2 unit lowered without water molecules fit.

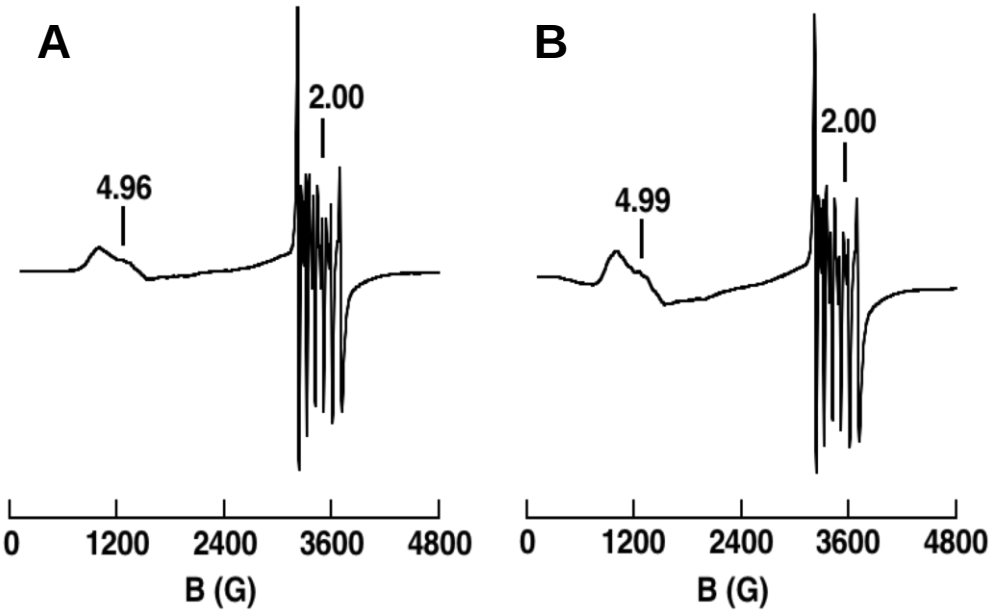

Figure C.10 EPR spectra of [Mn^{II}(biot-et-dpa)Br_2] (**A**) [Mn^{II}(biot-pr-dpa)Br_2] (**B**) recorded in DMF/THF at 77 K.

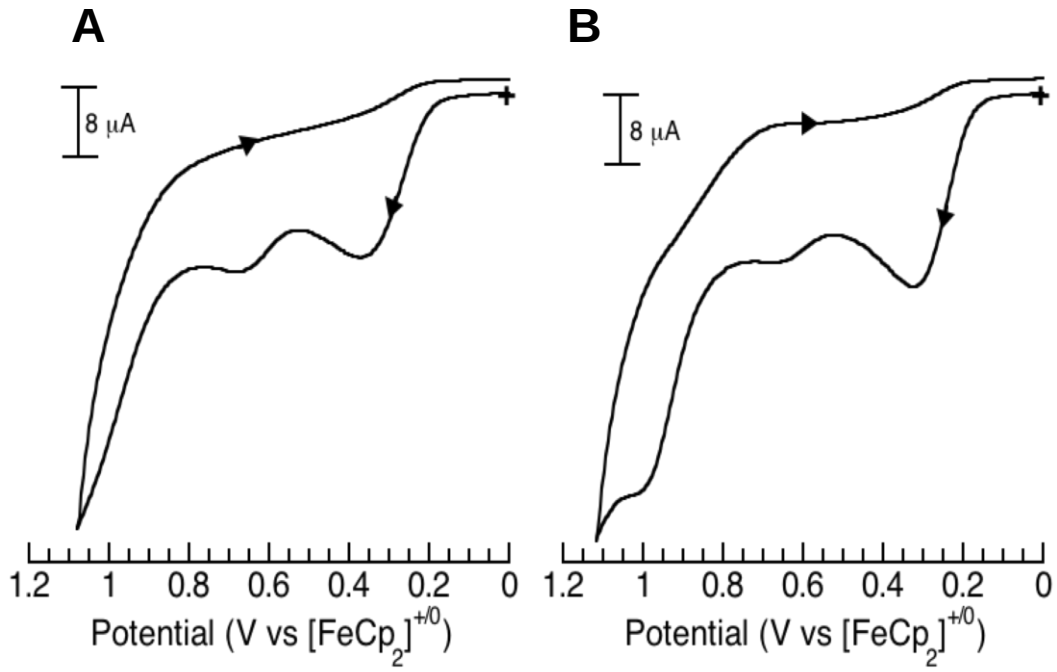

Figure C.11 Cyclic voltammagrams of [Mn^{II}(biot-et-dpa)Br_2] (**A**) [Mn^{II}(biot-pr-dpa)Br_2] (**B**) recorded in DMF. Measurements were collected at RT with a scan rate of 100 mV/s.

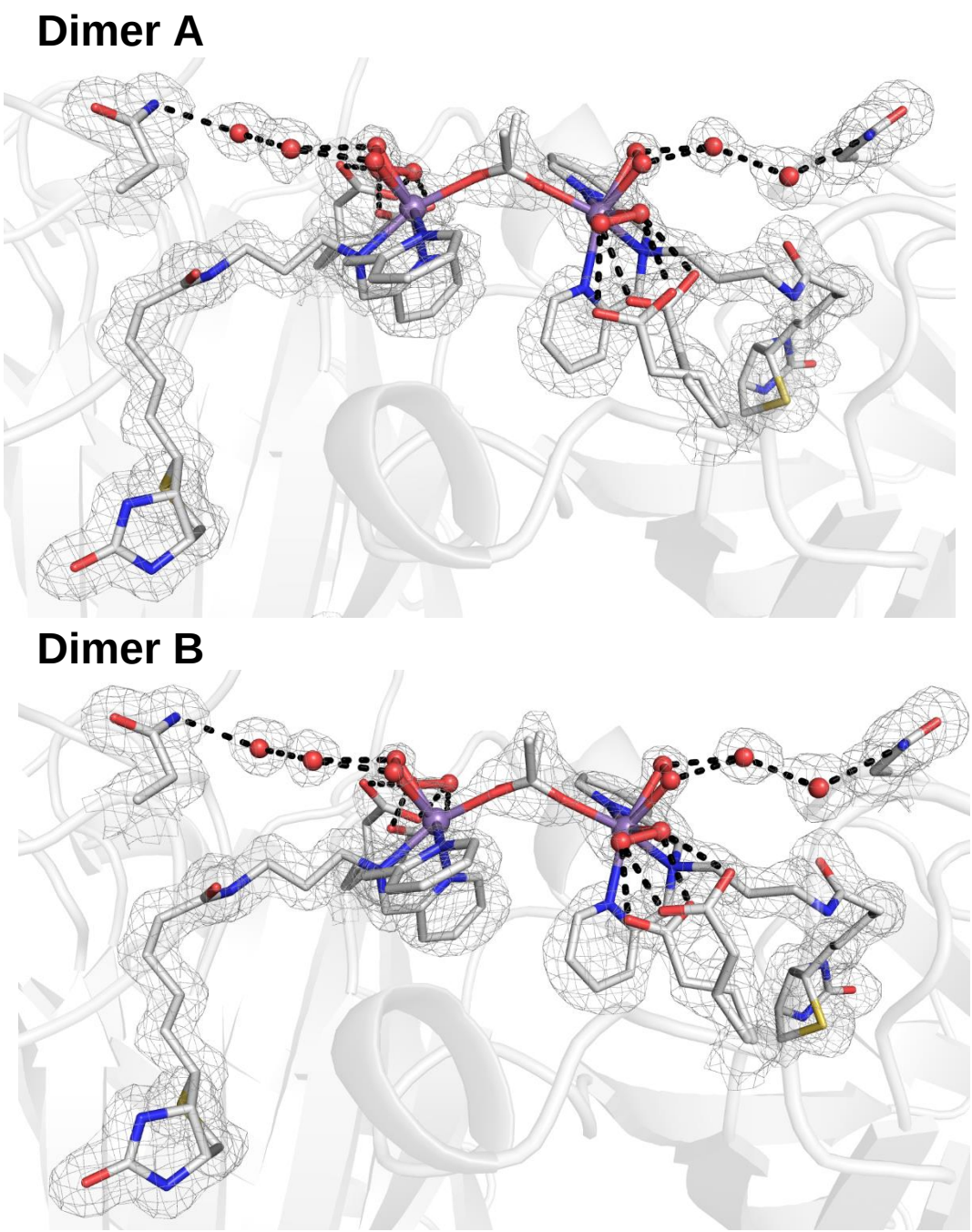

Figure C.12 Close up views of the Mn sites in the molecular structure of **C2** solved in C121 symmetry. **Dimer A** and **B** of the tetrameric Sav are shown for clarity. The protein is displayed in cartoon representation and the Mn complex as well as residues 112 as sticks. The position of the ligand molecules is indicated by the $2F_o$-F_c electron density (grey, contoured at 1 σ). Mn is colored in purple, N-atoms are in blue, and O atoms/water molecules are in red. The number scheme for **Dimer A** and **Dimer B** is the same as in Figure C.9. H-bonds are shown in black dashed lines.

Table C.1 Selected bond lengths and (Å) and angles (°) for **C1** and **C2**.

Bond lengths and angles	**C1**	**C2**
Mn–O1	2.65	–
Mn–O3	2.48	2.10
Mn–O4	2.34	2.62
Mn–O5	–	2.24
Mn–O6	–	2.40
Mn–O7/O7’	–	2.24/2.05
Mn–N1	1.79	2.28
Mn–N2	2.58	2.34
Mn–N3	–	2.56
O3–O4	–	1.47
O5–O6	–	1.42
N1–Mn–O3	158	95
N1–Mn–N2	72	74
N2–Mn–O4	163	–
O3–Mn–O4	88	–
O1–Mn–N1	129	–
O1–Mn–N2	90	–
O1–Mn–O3	69	–
O1–Mn–O4	107	–
N1–Mn–O4	95	–
N3–Mn–O4	–	–
N3–Mn–O3	–	152
N3–Mn–N1	–	79
N3–Mn–N2	–	112
N2–Mn–O3	100	92
O5–Mn–N1	–	97
O5–Mn–N2	–	140
O5–Mn–N3	–	104
O7–Mn–O3	–	99
O7–Mn–O5	–	98
O7–Mn–N1	–	164
O7–Mn–N2	–	97
O7–Mn–N3	–	93
Mn–O3–O4	–	97
Mn–O5–O6	–	78
N3···O4	3.20	–
O3···O2	3.43	–
O3···O1/O1’	–	2.56/2.79
O4···O2/O2’	–	2.60/2.51
O4···Wat1	2.72	–
Wat1···N49	2.96	–
$centroid_{W120}$···$centroid_{py}$	4.74	–
O5···Wat1	–	2.75
O6···Wat1	–	2.58
Wat1···Wat2	–	2.89
Wat2···N49	–	2.80

Table C.2 X-ray Crystallography Data Processing and Refinement Statistics for $I4_122$ symmetry solutions of **C1** and **C2**.

Identification		
Sav Mutant	2xM-$S_{112}E$	2xM-$S_{112}E$
Fe complex	$[Mn^{II}$(biot-et-dpa)$(OH_2)_2(\kappa^1\text{-}O_{E112})]^+$ (**C1**)	$[Mn^{II}$(biot-pr-dpa)$(O_2)(OAc)]^+$ (**C2**)
PDB Code	Unpublished	Unpublished
Mn complex PDB 3-letter code	Unpublished	Unpublished
Data Processing		
Unit Cell	a, b, c = 57.7 Å, 57.7 Å, 183.8 Å α, β, γ = 90°	a, b, c = 57.4 Å, 57.4 Å, 182.6 Å α, β, γ = 90°
Space Group	$I4_122$	$I4_122$
Resolution (Å)	55.03 – 1.49	54.78 – 1.46
Highest resolution shell (Å)	1.51– 1.49	1.49 – 1.46
R_{merge} (%)	5.0 (29)	6.5 (51)
No. of unique reflections	26138 (1230)	26954 (1283)
Multiplicity	26.5 (19.9)	9.9 (7.0)
I/Sig(I)	45.3 (10.1)	18.1 (2.7)
Completeness	99.9 (98.6)	99.7 (98.6)
CC(1/2)	1.000 (0.978)	0.999 (0.886)
Beamline	ALS 8.2.2	ALS 8.2.1
Structure Refinement		
R_{work}	0.16	0.17
R_{free}	0.18	0.19
Rmsd bond length (Å)	0.020	0.019
Rmsd bond angle (°)	3.713	2.410
Rmsd compared to biotin-Sav WT (PDB 1STP) (Å)	0.66	0.66
No. ligands		
Mn complex	1	1
Water	93	96
Acetate	–	1
O_2	–	1

Table C.3 Summary of structural details for **C1** and **C2**.

PDB Code	Unpublished	Unpublished
Complex	**C1**	**C2**
Electron density at Mn in F_o–F_c omit map (σ)	16	32
Anomalous dispersion density at Mn (σ)	17	14
Geometry of Mn complex	Square pyramidal	Square pyramidal or Distorted octahedral
Coordination number of Mn complex	5	5- or 6-coordinate
Occupancy of Mn complex (%)	70	100
B-factor (Å^2)		
Overall protein	15	16
S112E (70/30)	20/9	18/13
K121A	11	12
E101Q	42	35
Mn complex	18	24
DPA	17	28
Mn	34	23
Acetate	–	31
O_2	–	27
Distance Mn···Mn (Å)	10	6

Table C.4 X-ray Crystallography Data Processing and Refinement Statistics for C121 symmetry solution of **C2**.

Identification	
Sav Mutant	2xM-S_{112}E
Mn complex	$[Mn^{II}(biot\text{-}pr\text{-}dpa)(O_2)(OAc)]^+$ (**C2**)
PDB Code	Unpublished
Mn complex PDB 3-letter code	Unpublished
Data Processing	
Unit Cell	a, b, c = 191.4 Å, 57.4 Å, 57.4 Å α, β, γ = 90°, 107.5°, 90°
Space Group	C121
Resolution (Å)	54.78 – 1.54
Highest resolution shell (Å)	1.57 – 1.54
R_{merge} (%)	5.2 (26)
No. of unique reflections	84588 (3818)
Multiplicity	2.8 (2.5)
I/Sig(I)	10.7 (2.3)
Completeness	96.1 (88.1)
CC(1/2)	0.994 (0.888)
Beamline	ALS 8.2.1
Structure Refinement	
R_{work}	0.17
R_{free}	0.19
Rmsd bond length (Å)	0.017
Rmsd bond angle (°)	2.239
Rmsd compared to biotin-Sav WT (PDB 1STP) (Å)	0.65
No. ligands	
Mn complex	4
Water	379
Acetate	2
O_2	4

Table C.5 Summary of structural details for **C2**.

PDB Code	Unpublished
Complex	**C2**
Electron density at Mn in F_o–F_c omit map (σ)	32
Anomalous dispersion density at Mn (σ)	–
Geometry of Mn complex	Square pyramidal or distorted octahedral
Coordination number of Mn complex	5- or 6-coordinate
Occupancy of Mn complex (%)	100
B-factor (Å²)	
Overall protein	16
E101Q	45
S112E	15
K121A	12
Mn complex	23
DPA	23
Mn	28
Acetate	31
O_2	25
Distance Mn–Mn (Å)	6

*B-factors were averaged from the Sav tetramer

Table C.6 C2 bond lengths and distances from C121 symmetry solution.

Bond lengths (Å)	**Monomer 1**	**Monomer 2**	**Monomer 3**	**Monomer 4**
Mn–O1	–	–	–	–
Mn–O2	–	–	–	–
Mn–O3	2.05	2.11	2.06	2.05
Mn–O4	2.51	2.55	2.59	2.62
Mn–O5	2.23	2.19	2.25	2.22
Mn–O6	2.43	2.36	2.41	2.30
Mn–O7/O7’	2.06/2.20	2.03/2.19	2.00/2.18	2.05/2.23
Mn–N1	2.30	2.33	2.31	2.25
Mn–N2	2.30	2.32	2.36	2.34
Mn–N3	2.59	2.43	2.51	2.53
O3···O1/O1’	2.83/2.96	2.51/3.29	2.57/2.86	2.48/2.94
O4···O2/O2’	3.10/2.52	2.51/2.96	2.68/2.55	2.59/2.60
O5···Wat3	2.86	–	–	–
O6···Wat3	2.55	–	–	–
Wat3···Wat4	2.82	–	–	–
Wat4···N49	2.81	–	–	–
O5···Wat1	–	2.75	–	–
O6···Wat1	–	2.42	–	–
Wat1···Wat2	–	3.00	–	–
Wat2···N49	–	2.82	–	–
O5···Wat7	–	–	2.79	–
O6···Wat7	–	–	2.44	–
Wat7···Wat8	–	–	2.98	–
Wat8···N49	–	–	2.78	–
O5···Wat5	–	–	–	2.81
O6···Wat5	–	–	–	2.49
Wat5···Wat6	–	–	–	2.94
Wat6···N49	–	–	–	2.89
Dimer A (1 & 2)		**Dimer B (3 & 4)**		
Mn···Mn’	5.85		5.84	

References

(1) Holm, R. H.; Kennepohl, P.; Solomon, E. I. Structural and Functional Aspects of Metal Sites in Biology. *Chem. Rev.* **1996**, *96*, 2239–2314.

(2) Hegg, E. L.; Que, L. The 2-His-1-Carboxylate Facial Triad - An Emerging Structural Motif in Mononuclear Non-Heme Iron(II) Enzymes. *Eur. J. Biochem.* **1997**, *250*, 625–629.

(3) Kal, S.; Que, L. Dioxygen Activation by Nonheme Iron Enzymes with the 2-His-1-Carboxylate Facial Triad That Generate High-Valent Oxoiron Oxidants. *J. Biol. Inorg. Chem.* **2017**, *22*, 339–365.

(4) Koehntop, K. D.; Emerson, J. P.; Que, L. The 2-His-1-Carboxylate Facial Triad: A Versatile Platform for Dioxygen Activation by Mononuclear Non-Heme Iron(II) Enzymes. *J. Biol. Inorg. Chem.* **2005**, *10*, 87–93.

(5) Hausinger, R. P. Fe(II)/α-Ketoglutarate-Dependent Hydroxylases and Related Enzymes. *Crit. Rev. Biochem. Mol. Biol.* **2004**, *39*, 21–68.

(6) Bugg, T. D.; Ramaswamy, S. Non-Heme Iron-Dependent Dioxygenases: Unravelling Catalytic Mechanisms for Complex Enzymatic Oxidations. *Curr. Opin. Chem. Biol.* **2008**, *12*, 134–140.

(7) Schofield, C. J.; Zhang, Z. 2-Oxoglutarate-Dependent Oxygenases and Related Enzymes. *Curr. Opin. Struct. Biol.* **1999**, *9*, 722–731.

(8) Kovaleva, E. G.; Lipscomb, J. D. Versatility of Biological Non-Heme Fe(II) Centers in Oxygen Activation Reactions. *Nat. Chem. Biol.* **2008**, *4*, 186–193.

(9) Price, J. C.; Barr, E. W.; Tirupati, B.; Bollinger, J. M.; Krebs, C. The First Direct Characterization of a High-Valent Iron Intermediate in the Reaction of an α-Ketoglutarate-Dependent Dioxygenase: A High-Spin Fe(IV) Complex in Taurine/α-Ketoglutarate Dioxygenase (TauD) from Escherichia Coli. *Biochemistry* **2003**, *42*, 7497–7508.

(10) Elkins, J. M.; Ryle, M. J.; Clifton, I. J.; Dunning Hotopp, J. C.; Lloyd, J. S.; Burzlaff, N. I.; Baldwin, J. E.; Hausinger, R. P.; Roach, P. L. X-Ray Crystal Structure of Escherichia Coli Taurine/α-Ketoglutarate Dioxygenase Complexed to Ferrous Iron and Substrates. *Biochemistry* **2002**, *41*, 5185–5192.

(11) Ryle, M. J.; Padmakumar, R.; Hausinger, R. P. Stopped-Flow Kinetic Analysis of Escherichia Coli Taurine/α- Ketoglutarate Dioxygenase: Interactions with α Ketoglutarate, Taurine, and Oxygen. *Biochemistry* **1999**, *38*, 15278–15286.

(12) Martinez, S.; Hausinger, R. P. Catalytic Mechanisms of Fe(II)- and 2-Oxoglutarate-Dependent Oxygenases. *J. Biol. Chem.* **2015**, *290*, 20702–20711.

(13) Ryle, M. J.; Koehntop, K. D.; Liu, A.; Que, L.; Hausinger, R. P. Interconversion of Two Oxidized Forms of Taurine/α-Ketoglutarate Dioxygenase, a Non-Heme Iron Hydroxylase: Evidence for Bicarbonate Binding. *Proc. Natl. Acad. Sci. U. S. A.* **2003**, *100*, 3790–3795.

(14) McCusker, K. P.; Klinman, J. P. An Active-Site Phenylalanine Directs Substrate Binding and C-H Cleavage in the α-Ketoglutarate-Dependent Dioxygenase TauD. *J. Am. Chem. Soc.* **2010**, *132*, 5114–5120.

(15) McCusker, K. P.; Klinman, J. P. Modular Behavior of TauD Provides Insight into the Origin of Specificity in α-Ketoglutarate-Dependent Nonheme Iron Oxygenases. *Proc.*

Natl. Acad. Sci. U. S. A. **2009**, *106*, 19791–19795.
(16) Holmes, M. A.; Trong, I. Le; Turley, S.; Sieker, L. C.; Stenkamp, R. E. Structures of Deoxy and Oxy Hemerythrin at 2.0 Å Resolution. *J. Mol. Biol.* **1991**, *218*, 583–593.
(17) Shiemke, A. K.; Loehr, T. M.; Sanders-Loehr, J. Resonance Raman Study of Oxyhemerythrin and Hydroxomethemerythrin. Evidence for Hydrogen Bonding of Ligands to the Fe-O-Fe Center. *J. Am. Chem. Soc.* **1986**, *108*, 2437–2443.
(18) Shiemke, A. K.; Loehr, T. M.; Sanders-Loehr, J. Resonance Raman Study of the μ-Oxo-Bridged Binuclear Iron Center in Oxyhemerythrin. *J. Am. Chem. Soc.* **1984**, *106*, 4951–4956.
(19) Okamura, M. Y.; Klotz, I. M.; Johnson, C. E.; Winter, M. R. C.; Williams, R. J. P. The State of Iron in Hemerythrin. A Mössbauer Study. *Biochemistry* **1969**, *8*, 1951–1958.
(20) Armstrong, G. D.; Geoffrey Sykes, A. Reactions of O2 with Hemerythrin, Myoglobin, and Hemocyanin: Effects of D2O on Equilibration Rate Constants and Evidence for H-Bonding. *Inorg. Chem.* **1986**, *25*, 3135–3139.
(21) Dunn, J. B. R.; Shriver, D. F.; Klotz, I. M. Resonance Raman Studies of the Electronic State of Oxygen in Hemerythrin. *Proc. Natl. Acad. Sci. U. S. A.* **1973**, *70*, 2582–2584.
(22) Brunold, T. C.; Solomon, E. I. Reversible Dioxygen Binding to Hemerythrin. 2. Mechanism of the Proton- Coupled Two-Electron Transfer to O2 at a Single Iron Center. *J. Am. Chem. Soc.* **1999**, *121*, 8288–8295.
(23) Que, L.; Ho, R. Y. N. Dioxygen Activation by Enzymes with Mononuclear Non-Heme Iron Active Sites. *Chem. Rev.* **1996**, *96*, 2607–2624.
(24) Wada, A.; Honda, Y.; Yamaguchi, S.; Nagatomo, S.; Kitagawa, T.; Jitsukawa, K.; Masuda, H. Steric and Hydrogen-Bonding Effects on the Stability of Copper Complexes with Small Molecules. *Inorg. Chem.* **2004**, *43*, 5725–5735.
(25) Sallmann, M.; Limberg, C. Utilizing the Trispyrazolyl Borate Ligand for the Mimicking of O2-Activating Mononuclear Nonheme Iron Enzymes. *Acc. Chem. Res.* **2015**, *48*, 2734–2743.
(26) Chatterjee, S.; Sengupta, K.; Mondal, B.; Dey, S.; Dey, A. Factors Determining the Rate and Selectivity of 4e-/4H+ Electrocatalytic Reduction of Dioxygen by Iron Porphyrin Complexes. *Acc. Chem. Res.* **2017**, *50*, 1744–1753.
(27) Hematian, S.; Garcia-Bosch, I.; Karlin, K. D. Synthetic Heme/Copper Assemblies: Toward an Understanding of Cytochrome c Oxidase Interactions with Dioxygen and Nitrogen Oxides. *Acc. Chem. Res.* **2015**, *48*, 2462–2474.
(28) Nam, W.; Lee, Y. M.; Fukuzumi, S. Hydrogen Atom Transfer Reactions of Mononuclear Nonheme Metal-Oxygen Intermediates. *Acc. Chem. Res.* **2018**, *51*, 2014–2022.
(29) Nam, W.; Lee, Y. M.; Fukuzumi, S. Tuning Reactivity and Mechanism in Oxidation Reactions by Mononuclear Nonheme Iron(IV)-Oxo Complexes. *Acc. Chem. Res.* **2014**, *47*, 1146–1154.
(30) Siegbahn, P. E. M.; Borowski, T. Modeling Enzymatic Reactions Involving Transition Metals. *Acc. Chem. Res.* **2006**, *39*, 729–738.
(31) Chufán, E. E.; Puiu, S. C.; Karlin, K. D. Heme-Copper/Dioxygen Adduct Formation, Properties, and Reactivity. *Acc. Chem. Res.* **2007**, *40*, 563–572.
(32) Nam, W. Synthetic Mononuclear Nonheme Iron-Oxygen Intermediates. *Acc. Chem. Res.* **2015**, *48*, 2415–2423.
(33) Nam, W. High-Valent Iron(IV)-Oxo Complexes of Heme and Non-Heme Ligands in Oxygenation Reactions. *Acc. Chem. Res.* **2007**, *40*, 522–531.

(34) Suzuki, M. Ligand Effects on Dioxygen Activation by Copper and Nickel Complexes: Reactivity and Intermediates. *Acc. Chem. Res.* **2007**, *40*, 609–617.
(35) Natale, D.; Mareque-Rivas, J. C. The Combination of Transition Metal Ions and Hydrogen-Bonding Interactions. *Chem. Commun.* **2002**, *8*, 425–437.
(36) Korendovych, I. V.; Kryatov, S. V.; Rybak-Akimova, E. V. Dioxygen Activation at Non-Heme Iron: Insights from Rapid Kinetic Studies. *Acc. Chem. Res.* **2007**, *40*, 510–521.
(37) Nam, W. Dioxygen Activation by Metalloenzymes and Models. *Acc. Chem. Res.* **2007**, *40*, 465.
(38) Solomon, E. I.; Stahl, S. S. Introduction: Oxygen Reduction and Activation in Catalysis. *Chem. Rev.* **2018**, *118*, 2299–2301.
(39) Adam, S. M.; Wijeratne, G. B.; Rogler, P. J.; Diaz, D. E.; Quist, D. A.; Liu, J. J.; Karlin, K. D. Synthetic Fe/Cu Complexes: Toward Understanding Heme-Copper Oxidase Structure and Function. *Chem. Rev.* **2018**, *118*, 10840–11022.
(40) Valentine, J. S. The Dioxygen Ligand in Mononuclear Group VIII Transition Metal Complexes. *Chem. Rev.* **1973**, *73*, 235–245.
(41) Kovacs, J. A. Synthetic Analogues of Cysteinate-Ligated Non-Heme Iron and Non-Corrinoid Cobalt Enzymes. *Chem. Rev.* **2004**, *104*, 825–848.
(42) Tshuva, E. Y.; Lippard, S. J. Synthetic Models for Non-Heme Carboxylate-Bridged Diiron Metalloproteins: Strategies and Tactics. *Chem. Rev.* **2004**, *104*, 987–1012.
(43) Cook, S. A.; Borovik, A. S. Molecular Designs for Controlling the Local Environments around Metal Ions. *Acc. Chem. Res.* **2015**, *48*, 2407–2414.
(44) Borovik, A. S. Bioinspired Hydrogen Bond Motifs in Ligand Design: The Role of Noncovalent Interactions in Metal Ion Mediated Activation of Dioxygen. *Acc. Chem. Res.* **2005**, *38*, 54–61.
(45) Yamaguchi, S.; Nagatomo, S.; Kitagawa, T.; Funahashi, Y.; Ozawa, T.; Jitsukawa, K.; Masuda, H. Copper Hydroperoxo Species Activated by Hydrogen-Bonding Interaction with Its Distal Oxygen. *Inorg. Chem.* **2003**, *42*, 6968–6970.
(46) Costas, M.; Mehn, M. P.; Jensen, M. P.; Que Jr., L. Dioxygen Activation at Mononuclear Nonheme Iron Active Sites: Enzymes, Models, and Intermediates. *Chem. Rev.* **2004**, *104*, 939–986.
(47) Nam, W. Dioxygen Activation by Metalloenzymes and Models. *Acc. Chem. Res.* **2007**, *40*, 465.
(48) Que, L. The Road to Non-Heme Oxoferryls and Beyond. *Acc. Chem. Res.* **2007**, *40*, 493–500.
(49) Rice, D. B.; Massie, A. A.; Jackson, T. A. Manganese-Oxygen Intermediates in O-O Bond Activation and Hydrogen-Atom Transfer Reactions. *Acc. Chem. Res.* **2017**, *50*, 2706–2717.
(50) Nam, W. High-Valent Iron(IV)-Oxo Complexes of Heme and Non-Heme Ligands in Oxygenation Reactions. *Acc. Chem. Res.* **2007**, *40*, 522–531.
(51) Gordon, J. B.; Vilbert, A. C.; Dimucci, I. M.; MacMillan, S. N.; Lancaster, K. M.; Moënne-Loccoz, P.; Goldberg, D. P. Activation of Dioxygen by a Mononuclear Nonheme Iron Complex: Sequential Peroxo, Oxo, and Hydroxo Intermediates. *J. Am. Chem. Soc.* **2019**, *141*, 17533–17547.
(52) Nivorozhkin, A. L.; Girerd, J. Oxygen Activation by Mononuclear Non-Heme Iron Proteins. *Angew. Chem., Int. Ed.* **2013**, *53*, 1689–1699.
(53) Decker, A.; Solomon, E. I. Dioxygen Activation by Copper, Heme and Non-Heme Iron

Enzymes: Comparison of Electronic Structures and Reactivities. *Curr. Opin. Chem. Biol.* **2005**, *9*, 152–163.
(54) Gunay, A.; Theopold, K. H. C-H Bond Activations by Metal Oxo Compounds. *Chem. Rev.* **2010**, *110*, 1060–1081.
(55) Que, L.; Ho, R. Y. N. Dioxygen Activation by Enzymes with Mononuclear Non-Heme Iron Active Sites. *Chem. Rev.* **1996**, *96*, 2607–2624.
(56) Holm, R. H. Synthetic Approaches to the Active Sites of Iron-Sulfur Proteins. *Acc. Chem. Res.* **1977**, *10*, 427–434.
(57) Solomon, E. I.; Zhang, Y. The Electronic Structures of Active Sites in Non-Heme Iron Enzymes. *Acc. Chem. Res.* **1992**, *25*, 343–352.
(58) Krebs, C.; Fujimori, D. G.; Walsh, C. T.; Bollinger, J. M. Non-Heme Fe(IV)-Oxo Intermediates. *Acc. Chem. Res.* **2007**, *40*, 484–492.
(59) Puri, M.; Que, L. Toward the Synthesis of More Reactive S = 2 Non-Heme Oxoiron(IV) Complexes. *Acc. Chem. Res.* **2015**, *48*, 2443–2452.
(60) Sun, W.; Sun, Q. Bioinspired Manganese and Iron Complexes for Enantioselective Oxidation Reactions: Ligand Design, Catalytic Activity, and Beyond. *Acc. Chem. Res.* **2019**, *52*, 2370–2381.
(61) Solomon, E. I.; Light, K. M.; Liu, L. V.; Srnec, M.; Wong, S. D. Geometric and Electronic Structure Contributions to Function in Non-Heme Iron Enzymes. *Acc. Chem. Res.* **2013**, *46*, 2725–2739.
(62) Collman, J. P.; Gagne, R. R.; Reed, C. A.; Robinson, W. T.; Rodley, G. A. Structure of an Iron (II) Dioxygen Complex; a Model for Oxygen Carrying Hemeproteins. *Proc. Natl. Acad. Sci. U. S. A.* **1974**, *71*, 1326–1329.
(63) Collman, J. P.; Gagné, R. R.; Reed, C. A. A Paramagnetic Dioxygen Complex of Iron(II) Derived from a "Picket Fence" Porphyrin. Further Models for Hemoproteins. *J. Am. Chem. Soc.* **1974**, *96*, 2629–2631.
(64) Wuenschell, G. E.; Tetreau, C.; Lavalette, D.; Reed, C. A. H-Bonded Oxyhemoglobin Models with Substituted Picket-Fence Porphyrins: The Model Compound Equivalent of Site-Directed Mutagenesis. *J. Am. Chem. Soc.* **1992**, *114*, 3346–3355.
(65) Shook, R. L.; Borovik, A. S. The Effects of Hydrogen Bonds on Metal-Mediated O2 Activation and Related Processes. *Chem. Commun.* **2008**, 6095–6107.
(66) Shook, R. L.; Borovik, A. S. The Role of the Secondary Coordination Sphere in Metal-Mediated Dioxygen Activation. *Inorg. Chem.* **2010**, *49*, 3646–3660.
(67) Cook, S. A.; Hill, E. A.; Borovik, A. S. Lessons from Nature: A Bio-Inspired Approach to Molecular Design. *Biochemistry* **2015**, *54*, 4167–4180.
(68) Shirin, Z.; Hammes, B. S.; Young, V. G.; Borovik, A. S. Hydrogen Bonding in Metal Oxo Complexes : Synthesis and Structure of a Monomeric Manganese (III)-Oxo Complex and Its Hydroxo Analogue. *J. Am. Chem. Soc.* **2000**, *122*, 1836–1837.
(69) Gupta, R.; MacBeth, C. E.; Young, V. G.; Borovik, A. S. Isolation of Monomeric MnIII/II-OH and MnIII-O Complexes from Water: Evaluation of O-H Bond Dissociation Energies. *J. Am. Chem. Soc.* **2002**, *124*, 1136–1137.
(70) Macbeth, C. E.; Golombek, A. P.; Jr, V. G. Y.; Borovik, A. S. O2 Activation by Nonheme Iron Complexes : A Monomeric Fe(III)–Oxo Complex Derived From O2. *Science* **2000**, *289*, 938–941.
(71) Lacy, D. C.; Gupta, R.; Stone, K. L.; Greaves, J.; Ziller, J. W.; Hendrich, M. P.; Borovik, A. S. Formation, Structure, and EPR Detection of a High Spin Fe(IV)-Oxo Species Derived

from Either an Fe(III)-Oxo or Fe(III)-OH Complex. *J. Am. Chem. Soc.* **2010**, *132*, 12188–12190.
(72) Hill, E. A.; Weitz, A. C.; Onderko, E.; Romero-Rivera, A.; Guo, Y.; Swart, M.; Bominaar, E. L.; Green, M. T.; Hendrich, M. P.; Lacy, D. C.; Borovik, A. S. Reactivity of an Fe^{IV}-Oxo Complex with Protons and Oxidants. *J. Am. Chem. Soc.* **2016**, *138*, 13143–13146.
(73) Taguchi, T.; Gupta, R.; Lassalle-Kaiser, B.; Boyce, D. W.; Yachandra, V. K.; Tolman, W. B.; Yano, J.; Hendrich, M. P.; Borovik, A. S. Preparation and Properties of a Monomeric High-Spin Mn(V)-Oxo Complex. *J. Am. Chem. Soc.* **2012**, *134*, 1996–1999.
(74) Gupta, R.; Taguchi, T.; Lassalle-Kaiser, B.; Bominaar, E. L.; Yano, J.; Hendrich, M. P.; Borovik, A. S. High-Spin Mn–oxo Complexes and Their Relevance to the Oxygen-Evolving Complex within Photosystem II. *Proc. Natl. Acad. Sci. U. S. A.* **2015**, *112*, 5319–5324.
(75) Shook, R. L.; Gunderson, W. A.; Greaves, J.; Ziller, J. W.; Hendrich, M. P.; Borovik, A. S. A Monomeric Mn(III)-Peroxo Complex Derived Directly from Dioxygen. *J. Am. Chem. Soc.* **2008**, *130*, 8888–8889.
(76) Shook, R. L.; Peterson, S. M.; Greaves, J.; Moore, C.; Rheingold, A. L.; Borovik, A. S. Catalytic Reduction of Dioxygen to Water with a Monomeric Manganese Complex at Room Temperature. *J. Am. Chem. Soc.* **2011**, *133*, 5810–5817.
(77) Park, Y. J.; Ziller, J. W.; Borovik, A. S. The Effects of Redox-Inactive Metal Ions on the Activation of Dioxygen: Isolation and Characterization of a Heterobimetallic Complex Containing a Mn^{III}-(μ-OH)-Ca^{II} Core. *J. Am. Chem. Soc.* **2011**, *133*, 9258–9261.
(78) Park, Y. J.; Cook, S. A.; Sickerman, N. S.; Sano, Y.; Ziller, J. W.; Borovik, A. S. Heterobimetallic Complexes with M^{III} -(μ-OH)-M^{II} Cores (M^{III} = Fe, Mn, Ga; M^{II} = Ca, Sr, and Ba): Structural, Kinetic, and Redox Properties. *Chem. Sci.* **2013**, *4*, 717–726.
(79) Sano, Y.; Weitz, A. C.; Ziller, J. W.; Hendrich, M. P.; Borovik, A. S. Unsymmetrical Bimetallic Complexes with M^{II}–(μ-OH)–M^{III} Cores ($M^{II}M^{III}$ = $Fe^{II}Fe^{III}$, $Mn^{II}Fe^{III}$, $Mn^{II}Mn^{III}$): Structural, Magnetic, and Redox Proper. *Inorg. Chem.* **2013**, *52*, 10229–10231.
(80) Sano, Y.; Lau, N.; Weitz, A. C.; Ziller, J. W.; Hendrich, M. P.; Borovik, A. S. Models for Unsymmetrical Active Sites in Metalloproteins: Structural, Redox, and Magnetic Properties of Bimetallic Complexes with M^{II}-(μ-OH)-Fe^{III} Cores. *Inorg. Chem.* **2017**, *56*, 14118–14128.
(81) Lau, N.; Sano, Y.; Ziller, J. W.; Borovik, A. S. Modular Bimetallic Complexes with a Sulfonamido-Based Ligand. *Dalton Trans.* **2018**, *47*, 12362–12372.
(82) Akabori, S.; Izumi, Y.; Fujii, Y.; Sakurai, S. An Asymmetric Catalyst. *Nature* **1956**, *77*, 1374–1378.
(83) Rosati, F.; Roelfes, G. Artificial Metalloenzymes. *ChemCatChem* **2010**, *2*, 916–927.
(84) Yu, F.; Cangelosi, V. M.; Zastrow, M. L.; Tegoni, M.; Plegaria, J. S.; Tebo, a. G.; Mocny, C. S.; Ruckthong, L.; Qayyum, H.; Pecoraro, V. L. Protein Design: Toward Functional Metalloenzymes. *Chem. Rev.* **2014**, *114*, 3495–3578.
(85) Churchfield, L. A.; Tezcan, F. A. Design and Construction of Functional Supramolecular Metalloprotein Assemblies. *Acc. Chem. Res.* **2019**, *52*, 345–355.
(86) Dong, Y.; Ménage, S.; Brennan, B. A.; Elgren, T. E.; Jang, H. G.; Pearce, L. L.; Que, L. Dioxygen Binding to Diferrous Centers . Models for Diiron-Oxo Proteins. *J. Am. Chem. Soc.* **1993**, *115*, 1851–1859.
(87) Marchi-Delapierre, C.; Rondot, L.; Cavazza, C.; Ménage, S. Oxidation Catalysis by

Rationally Designed Artificial Metalloenzymes. *Isr. J. Chem.* **2015**, *55*, 61–75.
(88) Oohora, K.; Onoda, A.; Hayashi, T. Hemoproteins Reconstituted with Artificial Metal Complexes as Biohybrid Catalysts. *Acc. Chem. Res.* **2019**, *52*, 945–954.
(89) Zastrow, M. L.; Pecoraro, V. L. Designing Hydrolytic Zinc Metalloenzymes. *Biochemistry* **2014**, *53*, 957–978.
(90) Cangelosi, V. M.; Deb, A.; Penner-Hahn, J. E.; Pecoraro, V. L. A de Novo Designed Metalloenzyme for the Hydration of CO2. *Angew. Chem., Int. Ed.* **2014**, *53*, 7900–7903.
(91) Plegaria, J. S.; Duca, M.; Tard, C.; Friedlander, T. J.; Deb, A.; Penner-Hahn, J. E.; Pecoraro, V. L. De Novo Design and Characterization of Copper Metallopeptides Inspired by Native Cupredoxins. *Inorg. Chem.* **2015**, *54*, 9470–9482.
(92) Tebo, A. G.; Pecoraro, V. L. Artificial Metalloenzymes Derived from Three-Helix Bundles. *Curr. Opin. Chem. Biol.* **2015**, *25*, 65–70.
(93) Mathieu, E.; Tolbert, A. E.; Koebke, K. J.; Tard, C.; Iranzo, O.; Penner-Hahn, J. E.; Policar, C.; Pecoraro, V. Rational De Novo Design of a Cu Metalloenzyme for Superoxide Dismutation. *Chem. Eur. J.* **2020**, *26*, 249–258.
(94) Chakraborty, S.; Yudenfreundkravitz, J.; Thulstrup, P. W.; Hemmingsen, L.; Degrado, W. F.; Pecoraro, V. L. Design of a Three-Helix Bundle Capable of Binding Heavy Metals in a Triscysteine Environment. *Angew. Chem., Int. Ed.* **2011**, *50*, 2049–2053.
(95) Lu, Y.; Yeung, N.; Sieracki, N.; Marshall, N. M. Design of Functional Metalloproteins. *Nature* **2009**, *460*, 855–862.
(96) Ueno, T.; Abe, S.; Yokoi, N.; Watanabe, Y. Coordination Design of Artificial Metalloproteins Utilizing Protein Vacant Space. *Coord. Chem. Rev.* **2007**, *251*, 2717–2731.
(97) Lu, Y.; Berry, S. M.; Pfister, T. D. Engineering Novel Metalloproteins: Design of Metal-Binding Sites into Native Protein Scaffolds. *Chem. Rev.* **2001**, *101*, 3047–3080.
(98) Heinisch, T.; Ward, T. R. Artificial Metalloenzymes Based on the Biotin-Streptavidin Technology: Challenges and Opportunities. *Acc. Chem. Res.* **2016**, *49*, 1711–1721.
(99) Hartwig, J. F.; Ward, T. R. New "Cats" in the House: Chemistry Meets Biology in Artificial Metalloenzymes and Repurposed Metalloenzymes. *Acc. Chem. Res.* **2019**, *52*, 1145.
(100) Nastri, F.; Chino, M.; Maglio, O.; Bhagi-Damodaran, A.; Lu, Y.; Lombardi, A. Design and Engineering of Artificial Oxygen-Activating Metalloenzymes. *Chem. Soc. Rev.* **2016**, *45*, 5020–5054.
(101) Fontecave, M.; Menage, S. Functional Models of Non-Heme Diiron Enzymes. *Coord. Chem. Rev.* **1998**, *178–180*, 1555–1572.
(102) Simmons, T. R.; Berggren, G.; Bacchi, M.; Fontecave, M.; Artero, V. Mimicking Hydrogenases : From Biomimetics to Artificial Enzymes. *Coord. Chem. Rev.* **2014**, *270–271*, 127–150.
(103) Reetz, M. T. Directed Evolution of Artificial Metalloenzymes: A Universal Means to Tune the Selectivity of Transition Metal Catalysts? *Acc. Chem. Res.* **2019**, *52*, 336–344.
(104) Lombardi, A.; Pirro, F.; Maglio, O.; Chino, M.; DeGrado, W. F. De Novo Design of Four-Helix Bundle Metalloproteins: One Scaffold, Diverse Reactivities. *Acc. Chem. Res.* **2019**, *52*, 1148–1159.
(105) Calhoun, J. R.; Nastri, F.; Maglio, O.; Pavone, V.; Lombardi, A.; Degrado, W. F. Artificial Diiron Proteins : From Structure to Function †. *Biopolymers* **2005**, *80*, 264–278.

(106) Maglio, O.; Nastri, F.; Torres, R.; Rosales, M. De; Faiella, M.; Pavone, V.; Degrado, W. F.; Lombardi, A. Diiron-Containing Metalloproteins : Developing Functional Models. *C. R. Chim.* **2007**, *10*, 703–720.
(107) Wade, H.; Stayrook, S. E.; Degrado, W. F. The Structure of a Designed Diiron(III) Protein: Implications for Cofactor Stabilization and Catalysis**. *Angew. Chem., Int. Ed.* **2006**, *45*, 4951–4954.
(108) Wilson, M. E.; Whitesides, G. M. Conversion of a Protein to a Homogeneous Asymmetric Hydrogenation Catalyst by Site-Specific Modification with a Diphosphinerhodium(I) Moiety. *J. Am. Chem. Soc.* **1978**, *100*, 306–307.
(109) Ward, T. R. Artificial Metalloenzymes Based on the Biotin - Avidin Technology : Enantioselective Catalysis and Beyond. *Acc. Chem. Res.* **2011**, *44*, 47–57.
(110) Liang, A. D.; Serrano-Plana, J.; Peterson, R. L.; Ward, T. R. Artificial Metalloenzymes Based on the Biotin-Streptavidin Technology: Enzymatic Cascades and Directed Evolution. *Acc. Chem. Res.* **2019**, *52*, 585–595.
(111) Skander, M.; Humbert, N.; Gradinaru, J.; Loosli, A.; Zocchi, A.; Ward, T. R.; Neucha, C. Artificial Metalloenzymes: (Strept)Avidin as Host for Enantioselective Hydrogenation by Achiral Biotinylated Rhodium - Diphosphine Complexes. *J. Am. Chem. Soc.* **2008**, *126*, 14411–14418.
(112) Schwizer, F.; Okamoto, Y.; Heinisch, T.; Gu, Y.; Pellizzoni, M. M.; Lebrun, V.; Reuter, R.; Köhler, V.; Lewis, J. C.; Ward, T. R. Artificial Metalloenzymes: Reaction Scope and Optimization Strategies. *Chem. Rev.* **2017**, *118*, 142–231.
(113) Liang, A. D.; Serrano-plana, J.; Peterson, R. L.; Ward, T. R. Arti Fi Cial Metalloenzymes Based on the Biotin − Streptavidin Technology : Enzymatic Cascades and Directed Evolution. **2018**, No. i.
(114) Jeschek, M.; Reuter, R.; Heinisch, T.; Trindler, C.; Klehr, J.; Panke, S.; Ward, T. R. Directed Evolution of Artificial Metalloenzymes for in Vivo Metathesis. *Nature* **2016**, *537*, 661–665.
(115) Pordea, A.; Mathis, D.; Ward, T. R. Incorporation of Biotinylated Manganese-Salen Complexes into Streptavidin: New Artificial Metalloenzymes for Enantioselective Sulfoxidation. *J. Organomet. Chem.* **2009**, *694*, 930–936.
(116) Pordea, A.; Creusa, M.; Panek, J.; Duboc, C.; Mathis, D.; Novic, M.; Ward, T. R. Artificial Metalloenzyme for Enantioselective Sulfoxidation Based on Vanadyl-Loaded Streptavidin. *J. Am. Chem. Soc.* **2008**, *130*, 8085–8088.
(117) Köhler, V.; Mao, J.; Heinisch, T.; Pordea, A.; Sardo, A.; Wilson, Y. M.; Knörr, L.; Creus, M.; Prost, J. C.; Schirmer, T.; Ward, T. R. OsO4•streptavidin: A Tunable Hybrid Catalyst for the Enantioselective Cis-Dihydroxylation of Olefins. *Angew. Chem., Int. Ed.* **2011**, *50*, 10863–10866.
(118) Hyster, T. K.; Knörr, L.; Ward, T. R.; Rovis, T. Biotinylated Rh(III) Complexes in Engineered Streptavidin for Accelerated Asymmetric C-H Activation. *Science* **2012**, *338*, 500–503.
(119) Dürrenberger, M.; Heinisch, T.; Wilson, Y. M.; Rossel, T.; Nogueira, E.; Knörr, L.; Mutschler, A.; Kersten, K.; Zimbron, M. J.; Pierron, J.; Schirmer, T.; Ward, T. R. Artificial Transfer Hydrogenases for the Enantioselective Reduction of Cyclic Imines. *Angew. Chem., Int. Ed.* **2011**, *50*, 3026–3029.
(120) Lu, Y.; Yeung, N.; Sieracki, N.; Marshall, N. M. Design of Functional Metalloproteins. *Nature* **2009**, *460*, 855–862.

(121) Ueno, T.; Ohashi, M.; Kono, M.; Kondo, K.; Suzuki, A.; Yamane, T.; Watanabe, Y. Crystal Structures of Artificial Metalloproteins: Tight Binding of Fe^{III}(Schiff-Base) by Mutation of Ala71 to Gly in Apo-Myoglobin. *Inorg. Chem.* **2004**, *43*, 2852–2858.
(122) Ozaki, S.; Matsui, T.; Watanabe, Y. Conversion of Myoglobin into a Peroxygenease: A Catalytic Intermediate of Sulfoxidation and Epoxidation by the F43H/H64L Mutant. *J. Am. Chem. Soc.* **1997**, *119*, 6666–6667.
(123) Lu, Y. Biosynthetic Inorganic Chemistry. *Angew. Chem., Int. Ed.* **2006**, *45*, 5588–5601.
(124) Lu, Y. Metalloprotein and Metallo-DNA/RNAzyme Design: Current Approaches, Success Measures, and Future Challenges. *Inorg. Chem.* **2006**, *45*, 9930–9940.
(125) Berggren, G.; Adamska, A.; Lambertz, C.; Simmons, T. R.; Esselborn, J.; Atta, M.; Gambarelli, S.; Mouesca, J. M.; Reijerse, E.; Lubitz, W.; Happe, T.; Artero, V.; Fontecave, M. Biomimetic Assembly and Activation of [FeFe]-Hydrogenases. *Nature* **2013**, *499*, 66–69.
(126) Esmieu, C.; Cherrier, M. V.; Amara, P.; Girgenti, E.; Marchi-Delapierre, C.; Oddon, F.; Iannello, M.; Jorge-Robin, A.; Cavazza, C.; Ménage, S. An Artificial Oxygenase Built from Scratch: Substrate Binding Site Identified Using a Docking Approach. *Angew. Chem. Int. Ed.* **2013**, *52*, 3922–3925.
(127) Cavazza, C.; Bochot, C.; Rousselot-Pailley, P.; Carpentier, P.; Cherrier, M. V.; Martin, L.; Marchi-Delapierre, C.; Fontecilla-Camps, J. C.; Ménage, S. Crystallographic Snapshots of the Reaction of Aromatic C-H with O2 Catalysed by a Protein-Bound Iron Complex. *Nat. Chem.* **2010**, *2*, 1069–1076.
(128) Roelfes, G. LmrR: A Privileged Scaffold for Artificial Metalloenzymes. *Acc. Chem. Res.* **2019**, *52*, 545–556.
(129) Lewis, J. C. Beyond the Second Coordination Sphere: Engineering Dirhodium Artificial Metalloenzymes to Enable Protein Control of Transition Metal Catalysis. *Acc. Chem. Res.* **2019**, *52*, 576–584.
(130) Song, W. J.; Tezcan, F. A. A Designed Supramolecular Protein Assembly with in Vivo Enzymatic Activity. *Science* **2014**, *346*, 1525–1528.
(131) DeChancie, J.; Houk, K. N. The Origins of Femtomolar Protein-Ligand Binding: Hydrogen-Bond Cooperativity and Desolvation Energetics in the Biotin-(Strept)Avidin Binding Site. *J. Am. Chem. Soc.* **2007**, *129*, 5419–5429.
(132) Hendrickson, W. A.; Pähler, A.; Smith, J. L.; Satow, Y.; Merritt, E. A.; Phizackerley, R. P. Crystal Structure of Core Streptavidin Determined from Multiwavelength Anomalous Diffraction of Synchrotron Radiation. *Proc. Natl. Acad. Sci. U. S. A.* **1989**, *86*, 2190–2194.
(133) Oohora, K.; Burazerovic, S.; Onoda, A.; Wilson, Y. M.; Ward, T. R.; Hayashi, T. Chemically Programmed Supramolecular Assembly of Hemoprotein and Streptavidin with Alternating Alignment. *Angew. Chem. Int. Ed.* **2012**, *51*, 3818–3821.
(134) Hyre, D. E.; Trong, I. L. E.; Merritt, E. A.; Eccleston, J. F.; Green, N. M.; Stenkamp, R. E. Cooperative Hydrogen Bond Interactions in the Streptavidin – Biotin System. *Protein Sci.* **2006**, *15*, 459–467.
(135) Freitag, S.; Trong, I. L. E.; Klumb, L.; Stayton, P. S.; Stenkamp, R. E. Structural Studies of the Streptavidin Binding Loop. *Protein Sci.* **1997**, *6*, 1157–1166.
(136) Weber, P. C.; Ohlendorf, D. H.; Wendoloski, J. J.; Salemme, F. R. Structural Origins of High-Affinity Biotin Binding to Streptavidin. *Science* **1989**, *243*, 85–88.
(137) Mann, S. I.; Heinisch, T.; Weitz, A. C.; Hendrich, M. P.; Ward, T. R.; Borovik, A. S.

Modular Artificial Cupredoxins. *J. Am. Chem. Soc.* **2016**, *138*, 9073–9076.
(138) Mann, S. I.; Heinisch, T.; Ward, T. R.; Borovik, A. S. Peroxide Activation Regulated by Hydrogen Bonds within Artificial Cu Proteins. *J. Am. Chem. Soc.* **2017**, *139*.
(139) Solomon, E. I.; Brunold, T. C.; Davis, M. I.; Kemsley, J. N.; Lee, S.-K.; Lehnert, N.; Neese, F.; Skulan, A. J.; Yang, Y.-S.; Zhou, J. Geometric and Electronic Structure/Function Correlations in Non-Heme Iron Enzymes. *Chem. Rev.* **2000**, *100*, 235–350.
(140) Bruijnincx, P. C. A.; van Koten, G.; Klein Gebbink, R. J. M. Mononuclear Non-Heme Iron Enzymes with the 2-His-1-Carboxylate Facial Triad: Recent Developments in Enzymology and Modeling Studies. *Chem. Soc. Rev.* **2008**, *37*, 2716–2744.
(141) Davis, K. M.; Altmyer, M.; Martinie, R. J.; Schaperdoth, I.; Krebs, C.; Bollinger, J. M.; Boal, A. K. Structure of a Ferryl Mimic in the Archetypal Iron(II)- and 2-(Oxo)-Glutarate-Dependent Dioxygenase, TauD. *Biochemistry* **2019**, *58*, 4218–4223.
(142) Bollinger, J. M.; Price, J. C.; Hoffart, L. M.; Barr, E. W.; Krebs, C. Mechanism of Taurine: α-Ketoglutarate Dioxygenase (TauD) from Escherichia Coli. *Eur. J. Inorg. Chem.* **2005**, *2005*, 4245–4254.
(143) Costas, M.; Mehn, M. P.; Jensen, M. P.; Que Jr., L. Dioxygen Activation at Mononuclear Nonheme Iron Active Sites: Enzymes, Models, and Intermediates. *Chem. Rev.* **2004**, *104*, 939–986.
(144) Valegard, K.; Terwisscha van Scheltinga, A. C.; Lloyd, M. D.; Hara, T.; Ramaswamy, S.; Perrakis, A.; Thompson, A.; Lee, H.-J.; Baldwin, J. E.; Schofield, C. J.; Andersson, J. H.; Anderrson, I. Structure of a Cephalosporin Synthase. *Nature* **1998**, *394*, 805–809.
(145) Minor, W.; Steczko, J.; Stec, B.; Otwinowski, Z.; Bolin, J. T.; Walter, R.; Axelrod, B. Crystal Structure of Soybean Lipoxygenase L-1 at 1.4 Å Resolution. *Biochemistry* **1996**, *35*, 10687–10701.
(146) Ha, E. H.; Ho, R. Y. N.; Krisiel, J. F.; Valentine, J. S. Modeling the Reactivity of α-Ketoglutarate-Dependent Non-Heme Iron(II)-Containing Enzymes. *Angew. Chem., Int. Ed.* **1995**, *34*, 2265–2266.
(147) Oldenburg, P. D.; Ke, C. Y.; Tipton, A. A.; Shteinman, A. A.; Que, L. A Structural and Functional Model for Dioxygenases with a 2-His-1-Carboxylate Triad. *Angew. Chem., Int. Ed.* **2006**, *45*, 7975–7978.
(148) Chiou, Y.-M.; Que, L. Models for α-Keto Acid-Dependent Non-Heme Iron Enzymes: Structures and Reactivity of $[Fe^{II}(L)(O_2CCOPh)](ClO_4)$ Complexes. *J. Am. Chem. Soc* **1995**, *117*, 3999–4013.
(149) Chiou, Y. M.; Que, L. Model Complexes for α-Keto Acid-Dependent Enzymes. Structure and Reactivity of {Fe^{II}[Tris[(6-Methyl-2-Pyridyl)Methyl]Amine](Benzoylformate)}(ClO_4). *J. Am. Chem. Soc.* **1992**, *114*, 7567–7568.
(150) Chiou, Y. -M; Que, L. A Model for α-Keto Acid Dependent Nonheme Iron Enzymes: Structure and Reactivity of $[Fe_2^{II}(Me_2Hdp)_2(Bf)](ClO_4)$. *Angew. Chem., Int. Ed.* **1994**, *33*, 1886–1888.
(151) Hagadorn, J. R.; Que, J.; Tolman, W. B. N-Donor Effects on Carboxylate Binding in Mononuclear Iron(II) Complexes of a Sterically Hindered Benzoate Ligand. *Inorg. Chem.* **2000**, *39*, 6086–6090.
(152) Kitajima, N.; Moro-oka, Y.; Tamura, N.; Amagai, H.; Fukui, H.; Mizutani, Y.; Mathur, R.; Heerwegh, K.; Reed, C. A.; Randall, C. R.; Tatsumi, K. Monomelic Carboxylate Ferrous Complexes as Models for the Dioxygen Binding Sites in Non-Heme Iron Proteins. The

Reversible Formation and Characterization of μ-Peroxo Diferric Complexes. *J. Am. Chem. Soc.* **1994**, *116*, 9071–9085.
(153) Bruijnincx, P. C. A.; Lutz, M.; Spek, A. L.; Hagen, W. R.; Weckhuysen, B. M.; Van Koten, G.; Gebbink, R. J. M. K. Modeling the 2-His-1-Carboxylate Facial Triad: Iron-Catecholato Complexes as Structural and Functional Models of the Extradiol Cleaving Dioxygenases. *J. Am. Chem. Soc.* **2007**, *129*, 2275–2286.
(154) Moelands, M. A. H.; Nijsse, S.; Folkertsma, E.; De Bruin, B.; Lutz, M.; Spek, A. L.; Gebbink, R. J. M. K. Bioinspired Nonheme Iron Complexes Derived from an Extended Series of N,N,O-Ligated BAIP Ligands. *Inorg. Chem.* **2013**, *52*, 7394–7410.
(155) Folkertsma, E.; De Waard, E. F.; Korpershoek, G.; Van Schaik, A. J.; Solozabal Mirón, N.; Borrmann, M.; Nijsse, S.; Moelands, M. A. H.; Lutz, M.; Otte, M.; Moret, M. E.; Gebbink, R. J. M. K. Mimicry of the 2-His-1-Carboxylate Facial Triad Using Bulky N,N,O-Ligands: Non-Heme Iron Complexes Featuring a Single Facial Ligand and Easily Exchangeable Co-Ligands. *Eur. J. Inorg. Chem.* **2016**, 1319–1332.
(156) Burzlaff, N. Biomimetic Trispyrazolylborato Iron Complexes. *Angew. Chem., Int. Ed.* **2009**, *48*, 5580–5582.
(157) Beck, A.; Weibert, B.; Burzlaff, N. Monoanionic N,N,O-Scorpionate Ligands and Their Iron(II) and Zinc(II) Complexes: Models for Mononuclear Active Sites of Non-Heme Iron Oxidases and Zinc Enzymes. *Eur. J. Inorg. Chem.* **2001**, 521–527.
(158) Beck, A.; Barth, A.; Hubner, E.; Burzlaff, N. Bis(Pyrazol-1-Yl)Acetates as Tripodal Heteroscorpionate Ligands in Iron Chemistry: Syntheses and Structures of Iron(II) and Iron(III) Complexes with Bpza, Bdmpza, and Bdtbpza Ligands. *Inorg. Chem.* **2003**, *42*, 7182–7188.
(159) Cappillino, P. J.; Miecznikowski, J. R.; Tyler, L. A.; Tarves, P. C.; McNally, J. S.; Lo, W.; Kasibhatla, B. S. T.; Krzyaniak, M. D.; McCracken, J.; Wang, F.; Armstrong, W. H.; Caradonna, J. P. Studies of Iron(II) and Iron(III) Complexes with Fac-N2O, Cis-N2O2 and N2O3 Donor Ligands: Models for the 2-His 1-Carboxylate Motif of Non-Heme Iron Monooxygenases. *Dalton Trans.* **2012**, *41*, 5662–5677.
(160) Rocks, S. S.; Brennessel, W. W.; Machonkin, T. E.; Holland, P. L. Solid-State and Proton NMR Characterization of an Iron(II) Complex of a Tridentate, Facially Coordinating N,N,O Donor Ligand. *Inorg. Chim. Acta.* **2009**, *362*, 1387–1390.
(161) Dhanalakshmi, T.; Bhuvaneshwari, M.; Palaniandavar, M. Iron(III) Complexes of Certain Meridionally Coordinating Tridentate Ligands as Models for Non-Heme Iron Enzymes: The Role of Carboxylate Coordination. *J. Inorg. Biochem.* **2006**, *100*, 1527–1534.
(162) Rittle, J.; Field, M. J.; Green, M. T.; Tezcan, F. A. An Efficient, Step-Economical Strategy for the Design of Functional Metalloproteins. *Nat. Chem.* **2019**, *11*, 434–441.
(163) Liu, J.; Chakraborty, S.; Hosseinzadeh, P.; Yu, Y.; Tian, S.; Petrik, I.; Bhagi, A.; Lu, Y. Metalloproteins Containing Cytochrome, Iron–Sulfur, or Copper Redox Centers. *Chem. Rev.* **2014**, *114*, 4366–4469.
(164) McLaughlin, M. P.; Retegan, M.; Bill, E.; Payne, T. M.; Shafaat, H. S.; Peña, S.; Sudhamsu, J.; Ensign, A. A.; Crane, B. R.; Neese, F.; Holland, P. L. Azurin as a Protein Scaffold for a Low-Coordinate Nonheme Iron Site with a Small-Molecule Binding Pocket. *J. Am. Chem. Soc.* **2012**, *134*, 19746–19757.
(165) Cavazza, C.; Bochot, C.; Rousselot-Pailley, P.; Carpentier, P.; Cherrier, M. V; Martin, L.; Marchi-Delapierre, C.; Fontecilla-Camps, J. C.; Ménage, S. Crystallographic Snapshots

of the Reaction of Aromatic C-H with O_2 Catalysed by a Protein-Bound Iron Complex. *Nat. Chem.* **2010**, *2*, 1069–1076.
(166) Snyder, R. A.; Betzu, J.; Butch, S. E.; Reig, A. J.; DeGrado, W. F.; Solomon, E. I. Systematic Perturbations of Binuclear Non-Heme Iron Sites: Structure and Dioxygen Reactivity of de Novo Due Ferri Proteins. *Biochemistry* **2015**, *54*, 4637–4651.
(167) Faiella, M.; Andreozzi, C.; Torres, R.; Rosales, M. De; Pavone, V.; Maglio, O.; Nastri, F.; Degrado, W. F.; Lombardi, A. An Artificial Di-Iron Oxo-Protein with Phenol Oxidase Activity. *Nat. Chem. Biol.* **2009**, *5*, 882–884.
(168) Wilson, M. E.; Whitesides, G. M. Conversion of a Protein to a Homogeneous Asymmetric Hydrogenation Catalyst by Site-Specific Modification with a Diphosphinerhodium(I) Moiety. *J. Am. Chem. Soc.* **1978**, *100*, 306–307.
(169) Ward, T. R. Artificial Metalloenzymes Based on the Biotin-Avidin Technology: Enantioselective Catalysis and Beyond. *Acc. Chem. Res.* **2011**, *44*, 47–57.
(170) Olshansky, L.; Huerta-Lavorie, R.; Nguyen, A. I.; Vallapurackal, J.; Furst, A.; Tilley, T. D.; Borovik, A. S. Artificial Metalloproteins Containing Co_4O_4 Cubane Active Sites. *J. Am. Chem. Soc.* **2018**, *140*, 2739–2742.
(171) Skander, M.; Humbert, N.; Collot, J.; Gradinaru, J.; Klein, G.; Loosli, A.; Sauser, J.; Zocchi, A.; Gilardoni, F.; Ward, T. R. Artificial Metalloenzymes: (Strept)Avidin as Host for Enantioselective Hydrogenation by Achiral Biotinylated Rhodium-Diphosphine Complexes. *J. Am. Chem. Soc.* **2004**, *126*, 14411–14418.
(172) Andersen, O. A.; Flatmark, T.; Hough, E. High Resolution Crystal Structures of the Catalytic Domain of Human Phenylalanine Hydroxylase in Its Catalytically Active Fe(II) Form and Binary Complex with Tetrahydrobiopterin. *J. Mol. Biol.* **2001**, *314*, 279–291.
(173) Groom, C. R.; Bruno, I. J.; Lightfoot, M. P.; Ward, S. C. The Cambridge Structural Database. *Acta Cryst* **2016**, *72*, 171–179.
(174) Hirata, K.; Shinzawa-Itoh, K.; Yano, N.; Takemura, S.; Kato, K.; Hatanaka, M.; Muramoto, K.; Kawahara, T.; Tsukihara, T.; Yamashita, E.; Tono, K.; Ueno, G.; Hikima, T.; Murakami, H.; Inubushi, Y.; Yabashi, M.; Ishikawa, T.; … Ago, H. Determination of Damage-Free Crystal Structure of an X-Ray-Sensitive Protein Using an XFEL. *Nat. Methods* **2014**, *11*, 734–736.
(175) Suga, M.; Akita, F.; Hirata, K.; Ueno, G.; Murakami, H.; Nakajima, Y.; Shimizu, T.; Yamashita, K.; Yamamoto, M.; Ago, H.; Shen, J.-R. Native Structure of Photosystem II at 1.95 Å Resolution Viewed by Femtosecond X-Ray Pulses. *Nature* **2014**, *517*, 1–17.
(176) Kern, J.; Yachandra, V. K.; Yano, J. Metalloprotein Structures at Ambient Conditions and in Real-Time: Biological Crystallography and Spectroscopy Using X-Ray Free Electron Lasers. *Curr. Opin. Struct. Biol.* **2015**, *34*, 87–98.
(177) Kern, J.; Tran, R.; Alonso-Mori, R.; Koroidov, S.; Echols, N.; Hattne, J.; Ibrahim, M.; Gul, S.; Laksmono, H.; Sierra, R. G.; Gildea, R. J.; Han, G.; Hellmich, J.; Lassalle-Kaiser, B.; Chatterjee, R.; Brewster, A. S.; Stan, C. A.; … Yachandra, V. K. Taking Snapshots of Photosynthetic Water Oxidation Using Femtosecond X-Ray Diffraction and Spectroscopy. *Nat. Commun.* **2014**, *5*, 4371.
(178) Mcdonald, A. R.; Bukowski, M. R.; Farquhar, E. R.; Jackson, T. A.; Koehntop, K. D.; Seo, M. S.; Hont, R. F. De; Stubna, A.; Halfen, J. A.; Mu, E. Sulfur versus Iron Oxidation in an Iron - Thiolate Model Complex. *J. Am. Chem. Soc.* **2010**, *132*, 17118–17129.
(179) England, J.; Farquhar, E. R.; Guo, Y.; Cranswick, M. A.; Ray, K.; Eckard, M.; Que, L.

Characterization of a Tricationic Trigonal Bipyramidal Iron (IV) Cyanide Complex , with a Very High Reduction Potential , and Its Iron (II) and Iron (III) Congeners. *Inorg. Chem.* **2011**, *50*, 2885–2896.
(180) Rohde, J.; Shan, X.; Lim, M. H.; Klinker, E. J.; Chen, K.; Nam, W.; Que, L. Structural Insights into Nonheme Alkylperoxoiron (III) and Oxoiron (IV) Intermediates by X-Ray Absorption Spectroscopy. *J. Am. Chem. Soc.* **2004**, *126*, 16750–16761.
(181) Berry, J. F.; Bill, E.; Bothe, E.; Weyhermüller, T.; Wieghardt, K. Octahedral Non-Heme Non-Oxo Fe(IV) Species Stabilized by a Redox-Innocent N-Methylated Cyclam-Acetate Ligand. *J. Am. Chem. Soc.* **2005**, *127*, 11550–11551.
(182) Grapperhaus, C. A.; Mienert, B.; Bill, E.; Weyhermüller, T.; Wieghardt, K. Mononuclear (Nitrido)Iron(V) and (Oxo)Iron(IV) Complexes via Photolysis of [(Cyclam-Acetato)$Fe^{III}(N_3)]^+$ and Ozonolysis of [(Cyclam-Acetato)$Fe^{III}O_3SCF_3)]^+$ Water/Acetone Mixtures. *Inorg. Chem.* **2000**, *39*, 5306–5317.
(183) Pangborn, A. B.; Giardello, M. A.; Grubbs, R. H.; Rosen, R. K.; Timmers, F. J. Safe and Convenient Procedure for Solvent Purification. *Organometallics* **1996**, *15*, 1518–1520.
(184) Chambers, J. M.; Lindqvist, L. M.; Webb, A.; Huang, D. C. S.; Savage, G. P.; Rizzacasa, M. A. Synthesis of Biotinylated Episilvestrol: Highly Selective Targeting of the Translation Factors EIF4AI/II. *Org. Lett.* **2013**, *15*, 1406–1409.
(185) Incarvito, C.; Lam, M.; Rhatigan, B.; Rheingold, A. L.; Qin, C. J.; Gavrilova, A. L.; Bosnich, B. Bimetallic Reactivity. Preparations, Properties and Structures of Complexes Formed by Unsymmetrical Binucleating Ligands Bearing 4- and 6-Coordinate Sites Supported by Alkoxide Bridges. *Dalton Trans.* **2001**, *23*, 3478–3488.
(186) Petasis, D. T.; Hendrich, M. P. Quantitative Interpretation of Multifrequency Multimode EPR Spectra of Metal Containing Proteins, Enzymes, and Biomimetic Complexes. *Methods Enzym.* **2015**, *563*, 171–208.
(187) Baffert, C.; Romero, I.; Jacques, P.; Deronzier, A. Synthesis and Structural Characterization of Five- , Six- , and Seven-Coordinate Mononuclear Manganese (II) Complexes with N -Tridentate Ligands. *Inorg. Chim. Acta.* **2004**, *357*, 3430–3436.
(188) Mukherjee, J.; Balamurugan, V.; Gupta, R.; Mukherjee, R. Synthesis and Properties of Fe III and Co III Complexes : Structures Methyl [2- (2-Pyridyl) Ethyl] (2-Pyridylmethyl) Amine] †. *Dalton Trans.* **2003**, 3686–3692.
(189) George, G. N. In EXAFSPAK: A Suite of Computer Programs for Analysis of X-Ray Absorption Spectra. **1990**.
(190) Ankudinov, A.; Ravel, B. Real-Space Multiple-Scattering Calculation and Interpretation of x-Ray-Absorption near-Edge Structure. *Phys. Rev. B - Condens. Matter Mater. Phys.* **1998**, *58*, 7565–7576.
(191) Mallin, H.; Hestericová, M.; Reuter, R.; Ward, T. R. Library Design and Screening Protocol for Artificial Metalloenzymes Based on the Biotin-Streptavidin Technology. *Nat. Protoc.* **2016**, *11*, 835–852.
(192) Kabsch, W. XDS. *Acta Crystallogr. Sect. D Biol. Crystallogr.* **2010**, *66*, 125–132.
(193) Evans, P. R. An Introduction to Data Reduction: Space-Group Determination, Scaling and Intensity Statistics. *Acta Crystallogr. Sect. D Biol. Crystallogr.* **2011**, *67*, 282–292.
(194) Murshudov, G. N.; Vagin, A. A.; Dodson, E. J. Refinement of Macromolecular Structures by the Maximum-Likelihood Method. *Acta Crystallogr. Sect. D Biol. Crystallogr.* **1997**, *53*, 240–255.

(195) Adams, P. D.; Afonine, P. V.; Bunkóczi, G.; Chen, V. B.; Davis, I. W.; Echols, N.; Headd, J. J.; Hung, L. W.; Kapral, G. J.; Grosse-Kunstleve, R. W.; McCoy, A. J.; Moriarty, N. W.; Oeffner, R.; Read, R. J.; Richardson, D. C.; Richardson, J. S.; Terwilliger, T. C.; Zwart, P. H. PHENIX: A Comprehensive Python-Based System for Macromolecular Structure Solution. *Acta Crystallogr. Sect. D Biol. Crystallogr.* **2010**, *66*, 213–221.
(196) Visvaganesan, K.; Mayilmurugan, R.; Suresh, E.; Palaniandavar, M. Iron(III) Complexes of Tridentate 3N Ligands as Functional Models for Catechol Dioxygenases: The Role of Ligand N-Alkyl Substitution and Solvent on Reaction Rate and Product Selectivity. *Inorg. Chem.* **2007**, *46*, 10294–10306.
(197) Emsley, P.; Cowtan, K. Coot: Model-Building Tools for Molecular Graphics. *Acta Crystallogr. Sect. D Biol. Crystallogr.* **2004**, *60*, 2126–2132.
(198) Fuller, F. D.; Gul, S.; Chatterjee, R.; Burgie, E. S.; Young, I. D.; Lebrette, H.; Srinivas, V.; Brewster, A. S.; Michels-clark, T.; Clinger, J. A.; Andi, B.; Ibrahim, M.; Pastor, E.; Lichtenberg, C. De; Hussein, R.; Pollock, C. J.; Zhang, M.; … Yano, J. Drop-on-Demand Sample Delivery for Studying Biocatalysts in Action at X-Ray Free-Electron Lasers. *Nat. Publ. Gr.* **2017**, *14*, 443–449.
(199) Brewster, A. S.; Waterman, D. G.; Parkhurst, J. M.; Gildea, R. J.; Michels-clark, T. M.; Young, I. D.; Bernstein, H. J.; Winter, G.; Evans, G.; Sauter, N. K. Processing XFEL Data with Cctbx.Xfel and DIALS. *Comput. Crystallgraphy Newsl.* **2016**, *7*, 32–53.
(200) Brewster, A. S.; Waterman, D. G.; Parkhurst, J. M.; Gildea, R. J.; Young, I. D.; Riordan, L. J. O.; Yano, J.; Winter, G.; Evans, G.; Sauter, N. K. Improving Signal Strength in Serial Crystallography with DIALS Geometry Refinement Research Papers. *Acta Crystallogr* **2018**, 877–894.
(201) Sauter, N. K. XFEL Diffraction : Developing Processing Methods to Optimize Data Quality. *J. Synchrotron Rad.* **2015**, *22*, 239–248.
(202) Solomon, E. I.; Wong, S. D.; Liu, L. V.; Decker, A.; Chow, M. S. Peroxo and Oxo Intermediates in Mononuclear Nonheme Iron Enzymes and Related Active Sites. *Curr. Opin. Chem. Biol.* **2009**, *13*, 99–113.
(203) Que, L. The Oxo/Peroxo Debate: A Nonheme Iron Perspective. *J. Biol. Inorg. Chem.* **2004**, *9*, 684–690.
(204) Karlsson, A.; Parales, J. V.; Parales, R. E.; Gibson, D. T.; Eklund, H.; Ramaswamy, S. Crystal Structure of Naphthalene Dioxygenase: Side-on Binding of Dioxygen to Iron. *Science* **2003**, *299*, 1039–1042.
(205) Kovaleva, E. G.; Lipscomb, J. D. Crystal Structures of Fe2+ Dioxygenase Superoxo, Alkylperoxo, and Bound Product Intermediates. *Science* **2007**, *316*, 453–458.
(206) Zang, Y.; Kim, J.; Dong, Y.; Wilkinson, E. C.; Appelman, E. H.; Que, L. Models for Nonheme Iron Intermediates : Structural Basis for Tuning the Spin States of Fe (TPA) Complexes. *J. Am. Chem. Soc* **1997**, *119*, 4197–4205.
(207) Widger, L. R.; Jiang, Y.; McQuilken, A. C.; Yang, T.; Siegler, M. A.; Matsumura, H.; Moënne-Loccoz, P.; Kumar, D.; De Visser, S. P.; Goldberg, D. P. Thioether-Ligated Iron(II) and Iron(III)-Hydroperoxo/Alkylperoxo Complexes with an H-Bond Donor in the Second Coordination Sphere. *Dalton Trans.* **2014**, *43*, 7522–7532.
(208) Hong, S.; Lee, Y. M.; Cho, K. Bin; Seo, M. S.; Song, D.; Yoon, J.; Garcia-Serres, R.; Clémancey, M.; Ogura, T.; Shin, W.; Latour, J. M.; Nam, W. Conversion of High-Spin Iron(III)-Alkylperoxo to Iron(IV)-Oxo Species via O-O Bond Homolysis in Nonheme Iron Models. *Chem. Sci.* **2014**, *5*, 156–162.

(209) Namuswe, F.; Hayashi, T.; Jiang, Y.; Kasper, G. D.; Narducci Sarjeant, A. A.; Moënne-Loccoz, P.; Goldberg, D. P. Influence of the Nitrogen Donors on Nonheme Iron Models of Superoxide Reductase: High-Spin FeIII-OOR Complexes. *J. Am. Chem. Soc.* **2010**, *132*, 157–167.
(210) Namuswe, F.; Kasper, G. D.; Narducci Sarjeant, A. A.; Hayashi, T.; Krest, C. M.; Green, M. T.; Moënne-Loccoz, P.; Goldberg, D. P. Rational Tuning of the Thiolate Donor in Model Complexes of Superoxide Reductase: Direct Evidence for a Trans Influence in FeIII-OOR Complexes. *J. Am. Chem. Soc.* **2008**, *130*, 14189–14200.
(211) Krishnamurthy, D.; Kasper, G. D.; Namuswe, F.; Kerber, W. D.; Sarjeant, A. A. N.; Moënne-Loccoz, P.; Goldberg, D. P. A Low-Spin Alkylperoxo-Iron(III) Complex with Weak Fe-O and O-O Bonds: Implications for the Mechanism of Superoxide Reductase. *J. Am. Chem. Soc.* **2006**, *128*, 14222–14223.
(212) Kim, J.; Zang, Y.; Costas, M.; Harrison, R. G.; Wilkinson, E. C.; Que, L. A Nonheme Iron(II) Complex That Models the Redox Cycle of Lipoxygenase. *J. Biol. Inorg. Chem.* **2001**, *6*, 275–284.
(213) Lehnert, N.; Ho, R. Y. N.; Que, L.; Solomon, E. I. Spectroscopic Properties and Electronic Structure of Low-Spin Fe(III)-Alkylperoxo Complexes: Homolytic Cleavage of the O-O Bond. *J. Am. Chem. Soc.* **2001**, *123*, 8271–8290.
(214) Hazell, A.; McKenzie, C. J.; Nielsen, L. P.; Schindler, S.; Weitzer, M. Mononuclear Non-Heme Iron(III) Peroxide Complexes: Syntheses, Characterisation, Mass Spectrometric and Kinetic Studies. *J. Chem. Soc., Dalt. Trans.* **2002**, 310–317.
(215) Wada, A.; Ogo, S.; Watanabe, Y.; Mukai, M.; Kitagawa, T.; Jitsukawa, K.; Masuda, H.; Einaga, H. Synthesis and Characterization of Novel Alkylperoxo Mononuclear Iron(III) Complexes with a Tripodal Pyridylamine Ligand: A Model for Peroxo Intermediates in Reactions Catalyzed by Non-Heme Iron Enzymes. *Inorg. Chem.* **1999**, *38*, 3592–3593.
(216) Blakely, M. N.; Dedushko, M. A.; Yan Poon, P. C.; Villar-Acevedo, G.; Kovacs, J. A. Formation of a Reactive, Alkyl Thiolate-Ligated Fe(III)-Superoxo Intermediate Derived from Dioxygen. *J. Am. Chem. Soc.* **2019**, *141*, 1867–1870.
(217) Hong, S.; Sutherlin, K. D.; Park, J.; Kwon, E.; Siegler, M. A.; Solomon, E. I.; Nam, W. Crystallographic and Spectroscopic Characterization and Reactivities of a Mononuclear Non-Haem Iron(III)-Superoxo Complex. *Nat. Commun.* **2014**, *5*, 1–7.
(218) Mbughuni, M. M.; Chakrabarti, M.; Hayden, J. A.; Bominaar, E. L.; Hendrich, M. P.; Münck, E.; Lipscomb, J. D. Trapping and Spectroscopic Characterization of an FeIII-Superoxo Intermediate from a Nonheme Mononuclear Iron-Containing Enzyme. *Proc. Natl. Acad. Sci. U. S. A.* **2010**, *107*, 16788–16793.
(219) Simaan, A. J.; Döpner, S.; Banse, F.; Bourcier, S.; Bouchoux, G.; Boussac, A.; Hildebrandt, P.; Girerd, J. J. Fe(III)-Hydroperoxo and Peroxo Complexes with Aminopyridyl Ligands and the Resonance Raman Spectroscopic Identification of the Fe-O and O-O Stretching Modes. *Eur. J. Inorg. Chem.* **2000**, *2000*, 1627–1633.
(220) Chiang, C.; Kleespies, S. T.; Stout, H. D.; Meier, K. K.; Li, P.; Bominaar, E. L.; Que, L.; Mu, E.; Lee, W. Characterization of a Paramagnetic Mononuclear Nonheme Iron-Superoxo Complex. *J. Am. Chem. Soc* **2014**, *136*, 10846–10849.
(221) Roelfes, G.; Vrajmasu, V.; Chen, K.; Ho, R. Y. N.; Rohde, J. U.; Zondervan, C.; La Crois, R. M.; Schudde, E. P.; Lutz, M.; Spek, A. L.; Hage, R.; Feringa, B. L.; Munck, E.; Que, L. End-on and Side-on Peroxo Derivatives of Non-Heme Iron Complexes with Pentadentate

Ligands: Models for Putative Intermediates in Biological Iron/Dioxygen Chemistry. *Inorg. Chem.* **2003**, *42*, 2639–2653.
(222) Bang, S.; Lee, Y. M.; Hong, S.; Cho, K. Bin; Nishida, Y.; Seo, M. S.; Sarangi, R.; Fukuzumi, S.; Nam, W. Redox-Inactive Metal Ions Modulate the Reactivity and Oxygen Release of Mononuclear Non-Haem Iron(III)-Peroxo Complexes. *Nat. Chem.* **2014**, *6*, 934–940.
(223) Mukherjee, A.; Cranswick, M. A.; Chakrabarti, M.; Paine, T. K.; Fujisawa, K.; Münck, E.; Que, L. Oxygen Activation at Mononuclear Nonheme Iron Centers: A Superoxo Perspective. *Inorg. Chem.* **2010**, *49*, 3618–3628.
(224) Horner, O.; Jeandey, C.; Oddou, J. L.; Bonville, P.; Latour, J. M. A Mössbauer Study of $[Fe(Edta)(O_2)]^{3-}$ Agrees with a High-Spin Fe^{III} Peroxo Complex. *Eur. J. Inorg. Chem.* **2002**, *2002*, 1186–1189.
(225) Simaan, A. J.; Banse, F.; Girerd, J. J.; Wieghardt, K.; Bill, E. The Electronic Structure of Non-Heme Iron(III)-Hydroperoxo and Iron(III)-Peroxo Model Complexes Studied by Mössbauer and Electron Paramagnetic Resonance Spectroscopies. *Inorg. Chem.* **2001**, *40*, 6538–6540.
(226) Kishima, T.; Matsumoto, T.; Nakai, H.; Hayami, S.; Ohta, T.; Ogo, S. A High-Valent Iron(IV) Peroxo Core Derived from O2. *Angew. Chem., Int. Ed.* **2016**, *55*, 724–727.
(227) Rohde, J. U.; Bukowski, M. R.; Que, L. Functional Models for Mononuclear Nonheme Iron Enzymes. *Curr. Opin. Chem. Biol.* **2003**, *7*, 674–682.
(228) Cho, J.; Jeon, S.; Wilson, S. A.; Liu, L. V; Kang, E. A.; Braymer, J. J.; Lim, M. H.; Hedman, B.; Hodgson, K. O.; Valentine, J. S.; Solomon, E. I.; Nam, W. Structure and Reactivity of a Mononuclear Non-Haem Iron(III)-Peroxo Complex. *Nature* **2011**, *478*, 502–505.
(229) Jana, R. D.; Sheet, D.; Chatterjee, S.; Paine, T. K. Aliphatic C-H Bond Halogenation by Iron(II)-α-Keto Acid Complexes and O2: Functional Mimicking of Nonheme Iron Halogenases. *Inorg. Chem.* **2018**, *57*, 8769–8777.
(230) Sheet, D.; Bhattacharya, S.; Paine, T. K. Dioxygen Activation and Two Consecutive Oxidative Decarboxylations of Phenylpyruvate by Nonheme Iron(II) Complexes: Functional Models of Hydroxymandelate Synthase (HMS) and CloR. *Chem. Commun.* **2015**, *51*, 7681–7684.
(231) Chatterjee, S.; Paine, T. K. Olefin Cis-Dihydroxylation and Aliphatic C-H Bond Oxygenation by a Dioxygen-Derived Electrophilic Iron-Oxygen Oxidant. *Angew. Chem., Int. Ed.* **2015**, *54*, 9338–9342.
(232) Ha, E. H.; Ho, R. Y. N.; Kisiel, J. F.; Valentine, J. S. Modeling the Reactivity of α-Ketoglutarate-Dependent Non-Heme Iron(II)-Containing Enzymes. *Inorg. Chem.* **1995**, *34*, 2265–2266.
(233) Pratter, S. M.; Konstantinovics, C.; Di Giuro, C. M. L.; Leitner, E.; Kumar, D.; De Visser, S. P.; Grogan, G.; Straganz, G. D. Inversion of Enantioselectivity of a Mononuclear Non-Heme Iron(II)-Dependent Hydroxylase by Tuning the Interplay of Metal-Center Geometry and Protein Structure. *Angew. Chem., Int. Ed.* **2013**, *52*, 9677–9681.
(234) Paria, S.; Halder, P.; Paine, T. K. Oxidative Carbon-Carbon Bond Cleavage of a α-Hydroxy Ketone by a Functional Model of 2,4'-Dihydroxyacetophenone Dioxygenase. *Angew. Chem., Int. Ed.* **2012**, *51*, 6195–6199.
(235) Paria, S.; Chatterjee, S.; Paine, T. K. Reactivity of an Iron-Oxygen Oxidant Generated upon Oxidative Decarboxylation of Biomimetic Iron(II) α-Hydroxy Acid Complexes. *Inorg. Chem.* **2014**, *53*, 2810–2821.
(236) Paine, T. K.; England, J.; Que, L. Iron-Catalyzed C2-C3 Bond Cleavage of

Phenylpyruvate with O2: Insight into Aliphatic C-C Bond-Cleaving Dioxygenases. *Chem. Eur. J.* **2007**, *13*, 6073–6081.
(237) Mehn, M. P.; Fujisawa, K.; Hegg, E. L.; Que, L. Oxygen Activation by Nonheme Iron(II) Complexes: α-Keto Carboxylate versus Carboxylate. *J. Am. Chem. Soc.* **2003**, *125*, 7828–7842.
(238) Paine, T. K.; Zheng, H.; Que, L. Iron Coordination Chemistry of Phenylpyruvate: An Unexpected K3-Bridging Mode That Leads to Oxidative Cleavage of the C2-C3 Bond. *Inorg. Chem.* **2005**, *44*, 474–476.
(239) Paine, T. K.; Paria, S.; Que, L. Oxidative Decarboxylation of α-Hydroxy Acids by a Functional Model of the Nonheme Iron Oxygenase, CloR. *Chem. Commun.* **2010**, *46*, 1830–1832.
(240) Chiou, Y. M.; Que, L. Models for α-Keto Acid-Dependent Non-Heme Iron Enzymes: Structures and Reactivity of $[Fe^{II}(L)(O_2CCOPh)](ClO_4)$ Complexes. *J. Am. Chem. Soc.* **1995**, *117*, 3999–4013.
(241) Ho, R. Y. N.; Mehn, M. P.; Hegg, E. L.; Liu, A.; Ryle, M. J.; Hausinger, R. P.; Que, L. Resonance Raman Studies of the Iron(II)-α-Keto Acid Chromophore in Model and Enzyme Complexes. *J. Am. Chem. Soc.* **2001**, *123*, 5022–5029.
(242) Hegg, E. L.; Ho, R. Y. N.; Que, L. Oxygen Activation and Arene Hydroxylation by Functional Mimics of α-Keto Acid-Dependent Iron(II) Dioxygenases. *J. Am. Chem. Soc.* **1999**, *121*, 1972–1973.
(243) Das, O.; Chatterjee, S.; Paine, T. K. Functional Models of α-Keto Acid Dependent Nonheme Iron Oxygenases: Synthesis and Reactivity of Biomimetic Iron(II) Benzoylformate Complexes Supported by a 2,9-Dimethyl-1,10-Phenanthroline Ligand. *J. Biol. Inorg. Chem.* **2013**, *18*, 401–410.
(244) Roelfes, G.; Vrajmasu, V.; Chen, K.; Ho, R. Y. N.; Rohde, J. U.; Zondervan, C.; La Crois, R. M.; Schudde, E. P.; Lutz, M.; Spek, A. L.; Hage, R.; Feringa, B. L.; Munck, E.; Que, L. End-on and Side-on Peroxo Derivatives of Non-Heme Iron Complexes with Pentadentate Ligands: Models for Putative Intermediates in Biological Iron/Dioxygen Chemistry. *Inorg. Chem.* **2003**, *42*, 2639–2653.
(245) Simaan, A. J.; Girerd, J.; Wieghardt, K.; Bill, E. The Electronic Structure of Non-Heme Iron(III)-Hydroperoxo and Iron(III)-Peroxo Model Complexes Studied by Mössbauer and Electron Paramagnetic Resonance Spectroscopies. *Inorg. Chem.* **2001**, *40*, 6538–6540.
(246) Ho, R. Y. N.; Roelfes, G.; Feringa, B. L.; Que, L. Raman Evidence for a Weakened O - O Bond in Mononuclear Low-Spin Iron(III)-Hydroperoxides. *J. Am. Chem. Soc.* **1999**, *121*, 264–265.
(247) Katona, G.; Carpentier, P.; Nivière, V.; Amara, P.; Adam, V.; Ohana, J.; Tsanov, N.; Bourgeois, D. Raman-Assisted Crystallography. *Science* **2007**, *316*, 449–453.
(248) Visvaganesan, K.; Mayilmurugan, R.; Suresh, E.; Palaniandavar, M. Iron(III) Complexes of Tridentate 3N Ligands as Functional Models for Catechol Dioxygenases: The Role of Ligand N-Alkyl Substitution and Solvent on Reaction Rate and Product Selectivity. *Inorg. Chem.* **2007**, *46*, 10294–10306.
(249) Jasniewski, A. J.; Que, L. Dioxygen Activation by Nonheme Diiron Enzymes: Diverse Dioxygen Adducts, High-Valent Intermediates, and Related Model Complexes. *Chem. Rev.* **2018**, *118*, 2554–2592.
(250) Klotz, I. M.; Kurtz, D. M. Binuclear Oxygen Carriers: Hemerythrin. *Acc. Chem. Res.*

1984, *17*, 16–22.
(251) Boal, A. K.; Stubbe, J.; Rosenzweig, A. C.; Fe, W. Class Ib Ribonucleotide Reductase. *Science* **2010**, *329*, 1526–1530.
(252) Wallar, B. J.; Lipscomb, J. D. Dioxygen Activation by Enzymes Containing Binuclear Non-Heme Iron Clusters. *Chem. Rev.* **1996**, *96*, 2625–2657.
(253) Tinberg, C. E.; Lippard, S. J. Dioxygen Activation in Soluble Methane Monooxygenase. *Acc. Chem. Res.* **2011**, *44*, 280–288.
(254) Uppenberg, J.; Lindqvist, F.; Svensson, C.; Ek-Rylander, B.; Andersson, G. Crystal Structure of a Mammalian Purple Acid Phosphatase. *J. Mol. Biol.* **1999**, *290*, 201–211.
(255) Guddat, L. W.; Mcalpine, A. S.; Hume, D.; Hamilton, S.; Martin, J. L. Crystal Structure of Mammalian Purple Acid Phosphatase. *Structure* **1999**, *7*, 757–767.
(256) Davis, J. C.; Lin, S. S.; Bruce, A. Kinetics and Optical Spectroscopic Studies on the Purple Acid Phosphatase from Beef Spleen. *Biochemistry* **1981**, *20*, 4062–4067.
(257) Que, L. Metalloproteins With Phenolate Coordination. *Coord. Chem. Rev.* **1983**, *50*, 73–108.
(258) Bollinger, J. M.; Stubbe, J. A.; Huynh, B. H.; Edmondson, D. E. Novel Diferric Radical Intermediate Responsible for Tyrosyl Radical Formation in Assembly of the Cofactor of Ribonucleotide Reductase. *J. Am. Chem. Soc.* **1991**, *113*, 6289–6291.
(259) Sturgeon, B. E.; Burdi, D.; Chen, S.; Huynh, B. H.; Edmondson, D. E.; Stubbe, J. A.; Hoffman, B. M. Reconsideration of X, the Diiron Intermediate Formed during Cofactor Assembly in E. Coli Ribonucleotide Reductase. *J. Am. Chem. Soc.* **1996**, *118*, 7551–7557.
(260) Minnihan, E. C.; Nocera, D. G.; Stubbe, J. Reversible, Long-Range Radical Transfer in E. Coli Class Ia Ribonucleotide Reductase. *Acc. Chem. Res.* **2013**, *46*, 2524–2535.
(261) Solomon, E. I.; Brunold, T. C.; Davis, M. I.; Kemsley, J. N.; Lee, S. K.; Lehnert, N.; Neese, F.; Skulan, A. J.; Yang, Y. S.; Zhou, J. Geometric and Electronic Structure/Function Correlations in Non-Heme Iron Enzymes. *Chem. Rev.* **2000**, *100*, 235–350.
(262) Que, L.; Dong, Y. Modeling the Oxygen Activation Chemistry of Methane Monooxygenase and Ribonucleotide Reductase. *Acc. Chem. Res.* **1996**, *29*, 190–196.
(263) Kurtz, D. M. Oxo- and Hydroxo-Bridged Diiron Complexes: A Chemical Perspective on a Biological Unit. *Chem. Rev.* **1990**, *90*, 585–606.
(264) Que, Jr., L.; Tolman, W. B. Bis(μ-Oxo)Dimetal "Diamond" Cores in Copper and Iron Complexes Relevant to Biocatalysis. *Angew. Chem., Int. Ed.* **2002**, *41*, 1821.
(265) Tshuva, E. Y.; Lippard, S. J. Synthetic Models for Non-Heme Carboxylate-Bridged Diiron Metalloproteins : Strategies and Tactics. *Chem. Rev.* **2004**, *104*, 987–1012.
(266) Do, L. H.; Lippard, S. J. Evolution of Strategies to Prepare Synthetic Mimics of Carboxylate-Bridged Diiron Protein Active Sites. *J. Inorg. Biochem.* **2011**, *105*, 1774–1785.
(267) Friedle, S.; Lippard, S. J. Current Challenges of Modeling Diiron Enzyme Active Sites for Dioxygen Activation by Biomimetic Synthetic Complexes. *Chem. Soc. Rev* **2010**, *39*, 2768–2779.
(268) Arii, H.; Nagatomo, S.; Kitagawa, T.; Miwa, T.; Jitsukawa, K.; Einaga, H.; Masuda, H. A Novel Diiron Complex as a Functional Model for Hemerythrin. *J. Inorg. Biochem.* **2000**, *82*, 153–162.
(269) Kodera, M.; Itoh, M.; Kano, K. A Diiron Center Stabilized by a Bis-TPA Ligand as a Model of Soluble Methane Monooxygenase: Predominant Alkene Epoxidation with

H2O2. *Angew. Chem., Int. Ed.* **2005**, *44*, 7104–7106.
(270) Kodera, M.; Kawahara, Y.; Hitomi, Y.; Nomura, T.; Ogura, T.; Kobayashi, Y. Reversible O − O Bond Scission of Peroxodiiron(III) to High-Spin Oxodiiron(IV) in Dioxygen Activation of a Diiron Center with a Bis-Tpa Dinucleating Ligand as a Soluble Methane Monooxygenase Model. *J. Am. Chem. Soc* **2012**, *134*, 13236–13239.
(271) Paretsky, J. D. Streptavidin as a Host for Copper(II) Complexes. Ph.D. Dissertation, University of California, Irvine, CA. **2015**.
(272) Averill, B. A.; Burman, S.; Zirino, T.; Sanders-loehr, J.; Loehr, T. M.; Sage, J. T.; Debrunner, P. G. Spectroscopic and Magnetic Studies of the Purple Acid Phosphatase from Bovine Spleen. *J. Am. Chem. Soc.* **1987**, *109*, 3760–3767.
(273) Hotzelmann, R.; Wieghardt, K.; Flörke, U.; Haupt, H. jürgen; Weatherburn, D. C.; Bonvoisin, J.; Blondin, G.; Girerd, J. J. Spin Exchange Coupling in Asymmetric Heterodinuclear Complexes Containing the μ-Oxo-Bis(μ-Acetato)Dimetal Core. *J. Am. Chem. Soc.* **1992**, *114*, 1681–1696.
(274) Solomon, E. I.; Park, K. Structure/Function Correlations over Binuclear Non-Heme Iron Active Sites. *J. Biol. Inorg. Chem.* **2016**, *21*, 575–588.
(275) Meyer, K.; Bill, E.; Mienert, B.; Weyhermüller, T.; Wieghardt, K. Photolysis of Cis- and Trans-$[Fe^{III}(Cyclam)(N_3)_2]^+$ Complexes: Spectroscopic Characterization of a Nitridoiron(V) Species. *J. Am. Chem. Soc.* **1999**, *121*, 4859–4876.
(276) Wojdyr, M. A General-Purpose Peak Fitting Program. *J. Appl. Crystallogr* **2010**, *43*, 1126–1128.
(277) Matsumura, H.; Hayashi, T.; Chakraborty, S.; Lu, Y.; Moënne-Loccoz, P. The Production of Nitrous Oxide by the Heme/Nonheme Diiron Center of Engineered Myoglobins (FeBMbs) Proceeds through a Trans -Iron-Nitrosyl Dimer. *J. Am. Chem. Soc.* **2014**, *136*, 2420–2431.
(278) Hayashi, T.; Caranto, J. D.; Matsumura, H.; Kurtz, D. M.; Moënne-Loccoz, P. Vibrational Analysis of Mononitrosyl Complexes in Hemerythrin and Flavodiiron Proteins: Relevance to Detoxifying No Reductase. *J. Am. Chem. Soc.* **2012**, *134*, 6878–6884.
(279) Lu, S.; Sazinsky, M. H.; Whittaker, J. W.; Lippard, S. J.; Moënne-Loccoz, P. Fourier Transform Infrared Characterization of the Azido Complex of Methane Monooxygenase Hydroxylase from Methylococcus Capsulatus (Bath). *J. Am. Chem. Soc.* **2005**, *127*, 4148–4149.
(280) Mann, S. I.; Heinisch, T.; Ward, T. R.; Borovik, A. S. Coordination Chemistry within a Protein Host : Regulation of the Secondary Coordination Sphere †. **2018**, 4413–4416.
(281) Olshansky, L.; Huerta-Lavorie, R.; Nguyen, A. I.; Vallapurackal, J.; Furst, A.; Tilley, T. D.; Borovik, A. S. Artificial Metalloproteins Containing Co_4O_4 Cubane Active Sites. *J. Am. Chem. Soc.* **2018**, jacs.7b13052.
(282) Kent Barefield, E. Coordination Chemistry of N-Tetraalkylated Cyclam Ligands-A Status Report. *Coord. Chem. Rev.* **2010**, *254*, 1607–1627.
(283) Kim, S. O.; Sastri, C. V.; Seo, M. S.; Kim, J.; Nam, W. Dioxygen Activation and Catalytic Aerobic Oxidation by a Mononuclear Nonheme Iron(II) Complex. *J. Am. Chem. Soc.* **2005**, *127*, 4178–4179.
(284) Sreedaran, S.; Shanmuga Bharathi, K.; Kalilur Rahiman, A.; Rajesh, K.; Nirmala, G.; Narayanan, V. Synthesis, Spectral, Magnetic, Electrochemical and Catalytic Studies of Cyclam-Based Copper(II) and Nickel(II) Complexes - Effect of N-Substitution. *J. Coord. Chem.* **2008**, *61*, 3594–3609.

(285) Tfouni, E.; Ferreira, K. Q.; Doro, F. G.; Silva, R. S. Da; Rocha, Z. N. Da. Ru(II) and Ru(III) Complexes with Cyclam and Related Species. *Coord. Chem. Rev.* **2005**, *249*, 405–418.
(286) Froehlich, J. D.; Kubiak, C. P. Homogeneous CO_2 Reduction by Ni(Cyclam) at a Glassy Carbon Electrode. *Inorg. Chem.* **2012**, *51*, 3932–3934.
(287) Elias, H. Kinetics and Mechanism of Metal Complex Formation with N4-Donor Macrocycles of the Cyclam Type. *Coord. Chem. Rev.* **1999**, *187*, 37–73.
(288) Tamanini, E.; Katewa, A.; Sedger, L. M.; Todd, M. H.; Watkinson, M. A Synthetically Simple, Click-Generated Cyclam-Based Zinc(Ll) Sensor. *Inorg. Chem.* **2009**, *48*, 319–324.
(289) Aliaga-Alcalde, N.; DeBeer George, S.; Mienert, B.; Bill, E.; Wieghardt, K.; Neese, F. The Geometric and Electronic Structure of [(Cyclam-Acetato)Fe(N)] +: A Genuine Iron(v) Species with a Ground-State Spin S = 1/2. *Angew. Chemie - Int. Ed.* **2005**, *44*, 2908–2912.
(290) Kim, S.-Y.; Jung, I.-S.; Lee, E.; Kim, J.; Sakamoto, S.; Yamaguchi, K.; Kim, K. Macrocycles within Macrocycles: Cyclen, Cyclam, and Their Transition Metal Complexes Encapsulated in Cucurbit[8]Uril. *Angew. Chem., Int. Ed.* **2001**, *40*, 2119–2121.
(291) Yin, G.; Danby, A. M.; Kitko, D.; Carter, J. D.; Scheper, W. M.; Busch, D. H. Olefin Epoxidation by Alkyl Hydroperoxide with a Novel Cross-Bridged Cyclam Manganese Complex: Demonstration of Oxygenation by Two Distinct Reactive Intermediates. *Inorg. Chem.* **2007**, *46*, 2173–2180.
(292) Yu, M.; Price, J. R.; Jensen, P.; Lovitt, C. J.; Shelper, T.; Duffy, S.; Windus, L. C.; Avery, V. M.; Rutledge, P. J.; Todd, M. H. Copper, Nickel, and Zinc Cyclam-Amino Acid and Cyclam-Peptide Complexes May Be Synthesized with "Click" Chemistry and Are Noncytotoxic. *Inorg. Chem.* **2011**, *50*, 12823–12835.
(293) Froehlich, J. D.; Kubiak, C. P. The Homogeneous Reduction of CO_2 by $[Ni(Cyclam)]^+$: Increased Catalytic Rates with the Addition of a CO Scavenger. *J. Am. Chem. Soc.* **2015**, *137*, 3565–3573.
(294) Thibon, A.; England, J.; Martinho, M.; Young, V. G.; Frisch, J. R.; Guillot, R.; Girerd, J. J.; Münck, E.; Que, L.; Banse, F. Proton- and Reductant-Assisted Dioxygen Activation by a Nonheme Iron(II) Complex to Form an Oxoiron(IV) Intermediate. *Angew. Chem., Int. Ed.* **2008**, *47*, 7064–7067.
(295) Addison, A. W.; Sinn, E. A Stable Bis(Thiolate) of Copper(II) with Long Axial Copper-Sulfur Linkages: Crystal and Molecular Structure of Trans-$[Cu(Cyclam)(SC_6F_5)_2]$. *Inorg. Chem.* **1983**, *22*, 1225–1228.
(296) Hubin, T. J.; Alcock, N. W.; Busch, D. H. Copper(I) and Copper(II) Complexes of an Ethylene Cross-Bridged Cyclam. *Acta Crystallogr. Sect. C Cryst. Struct. Commun.* **2000**, *56*, 37–39.
(297) Hubin, T. J.; Alcock, N. W.; Morton, M. D.; Busch, D. H. Synthesis, Structure, and Stability in Acid of Copper(II) and Zinc(II) Complexes of Cross-Bridged Tetraazamacrocycles. *Inorg. Chim. Acta.* **2003**, *348*, 33–40.
(298) Shircliff, A. D.; Wilson, K. R.; Cannon-Smith, D. J.; Jones, D. G.; Zhang, Z.; Chen, Z.; Yin, G.; Prior, T. J.; Hubin, T. J. Synthesis, Structural Studies, and Oxidation Catalysis of the Manganese(II), Iron(II), and Copper(II) Complexes of a 2-Pyridylmethyl Pendant Armed Side-Bridged Cyclam. *Inorg. Chem. Commun.* **2015**, *59*, 71–75.
(299) Lima, L. M. P.; Esteban-Gómez, D.; Delgado, R.; Platas-Iglesias, C.; Tripier, R. Monopicolinate Cyclen and Cyclam Derivatives for Stable Copper(II) Complexation.

Inorg. Chem. **2012**, *51*, 6916–6927.
(300) Hoppe, T.; Schaub, S.; Becker, J.; Würtele, C.; Schindler, S. Characterization of a Macrocyclic End-on Peroxido Copper Complex. *Angew. Chem., Int. Ed.* **2013**, *52*, 870–873.
(301) Crabtree, R. H.; Hlatky, G. G.; Holt, E. M. Crystal and Molecular Structure of Di(Perchlorato)(1,4,8,11-Tetraazacyclotetradecane)Copper(II). Cu(Cyclam)(ClO_4)$_2$. *Inorg. Chim. Acta* **1987**, *130*, 5–7.
(302) McAuley, A.; Subramanian, S. Formation of Multinuclear Complexes: New Developments from Cyclam Derivatives. *Coord. Chem. Rev.* **2000**, *200–202*, 75–103.
(303) Liang, X.; Sadler, P. J. Cyclam Complexes and Their Applications in Medicine. *Chem. Soc. Rev.* **2004**, *33*, 246–266.
(304) Cho, J.; Sarangi, R.; Nam, W. Mononuclear Metal-O2 Complexes Bearing Macrocyclic N-Tetramethylated Cyclam Ligands. *Acc. Chem. Res.* **2012**, *45*, 1321–1330.
(305) Zhou, A.; Prakash, J.; Rohde, G. T.; Klein, J. E. M. N.; Kleespies, S. T.; Draksharapu, A.; Fan, R.; Guo, Y.; Cramer, C. J.; Que, L. The Two Faces of Tetramethylcyclam in Iron Chemistry: Distinct Fe-O-M Complexes Derived from [$Fe^{IV}(O_{Anti/Syn})$(TMC)]$^{2+}$ Isomers. *Inorg. Chem.* **2017**, *56*, 518–527.
(306) Barefield, E. K.; Wagner, F. Metal Complexes of 1, 4, 8, 11-Tetramethy 1-1, 4, 8, 11-Tetraazacyclotetradecane, N-Tetramethylcyclam. *Inorg. Chem.* **1973**, *12*, 2435–2439.
(307) Jones, D. G.; Wilson, K. R.; Cannon-Smith, D. J.; Shircliff, A. D.; Zhang, Z.; Chen, Z.; Prior, T. J.; Yin, G.; Hubin, T. J. Synthesis, Structural Studies, and Oxidation Catalysis of the Late-First-Row-Transition-Metal Complexes of a 2-Pyridylmethyl Pendant-Armed Ethylene Cross-Bridged Cyclam. *Inorg. Chem.* **2015**, *54*, 2221–2234.
(308) Klein, J. E. M. N.; Draksharapu, A.; Shokri, A.; Cramer, C. J.; Que, L. On the Lewis Acidity of the Oxoiron(IV) Unit in a Tetramethylcyclam Complex. *Chem. Eur. J.* **2018**, *24*, 5373–5378.
(309) England, J.; Prakash, J.; Cranswick, M. A.; Mandal, D.; Guo, Y.; Münck, E.; Shaik, S.; Que, L. Oxoiron(IV) Complex of the Ethylene-Bridged Dialkylcyclam Ligand Me2EBC. *Inorg. Chem.* **2015**, *54*, 7828–7839.
(310) Feng, Y.; England, J.; Que, L. Iron-Catalyzed Olefin Epoxidation and Cis-Dihydroxylation by Tetraalkylcyclam Complexes: The Importance of Cis-Labile Sites. *ACS Catal.* **2011**, *1*, 1035–1042.
(311) Hubin, T. J.; McCormick, J. M.; Alcock, N. W.; Clase, H. J.; Busch, D. H. Crystallographic Characterization of Stepwise Changes in Ligand Conformations as Their Internal Topology Changes and Two Novel Cross-Bridged Tetraazamacrocyclic Copper(II) Complexes. *Inorg. Chem.* **1999**, *38*, 4435–4446.
(312) Ouyang, Y.; Yu, L. H.; Liao, D. Z.; Jiang, Z. H.; Yan, S. P. Synthesis, Crystal Structure and Magnetic Properties of a New Binuclear Copper(II)-Copper(II) Complex of a Macrocyclic Oxamide. *J. Coord. Chem.* **2005**, *58*, 1361–1367.
(313) Garcia-Bosch, I.; Cowley, R. E.; Díaz, D. E.; Siegler, M. A.; Nam, W.; Solomon, E. I.; Karlin, K. D. Dioxygen Activation by a Macrocyclic Copper Complex Leads to a Cu_2O_2 Core with Unexpected Structure and Reactivity. *Chem. Eur. J.* **2016**, *22*, 5133–5137.
(314) Andrioletti, B.; Ricard, D.; Boitrel, B. Cyclam-Strapped Porphyrins and Their Iron(III)-Copper(II) Complexes as Models for the Resting State of Cytochrome c Oxidase. *New J. Chem.* **1999**, *23*, 1143–1150.
(315) Khin, C.; Lim, M. D.; Tsuge, K.; Iretskii, A.; Wu, G.; Ford, P. C. Amine Nitrosation via NO

Reduction of the Polyamine Copper(II) Complex Cu(DAC)2+. *Inorg. Chem.* **2007**, *46*, 9323–9331.
(316) Kim, S.; Minier, M. A.; Loas, A.; Becker, S.; Wang, F.; Lippard, S. J. Achieving Reversible Sensing of Nitroxyl by Tuning the Ligand Environment of Azamacrocyclic Copper(II) Complexes. *J. Am. Chem. Soc.* **2016**, *138*, 1804–1807.
(317) Reveal, F. H.; Bonds, H.; Emsley, J.; Arif, M.; Bates, P. A.; Hursthouseb, M. X-Ray Structures of [Cu(Cyclam)(H_2O)$_2$]$F_2$4$H_2$0 (Cyclam = 1,4,8,11-Tetra-Azacyclotetradecane) and [Cu(En)$_2$(H_2O)$_2$]F_2H_2O (En = Ethylenediamine) Reveal [F(H<sub>2. *J. Chem. Soc., Chem. Commun.* **1988**, 1387–1388.
(318) Hunter, T. M.; McNae, I. W.; Liang, X.; Bella, J.; Parsons, S.; Walkinshaw, M. D.; Sadler, P. J. Protein Recognition of Macrocycles: Binding of Anti-HIV Metallocyclams to Lysozyme. *Proc. Natl. Acad. Sci. U. S. A.* **2005**, *102*, 2288–2292.
(319) Woodard, B.; Willett, R. D.; Haddad, S.; Twamley, B.; Gomez-Garcia, C. J.; Coronado, E. Structure of Two Azide Salts of a Copper(II) Macrocycle and Magnetic Properties of Cu(14ane)Cu(N3)4. *Inorg. Chem.* **2004**, *43*, 1822–1824.
(320) Yu, F.; Li, F.; Hu, J.; Bai, L.; Zhu, Y.; Sun, L. Electrocatalytic Water Oxidation by a Macrocyclic Cu(II) Complex in Neutral Phosphate Buffer. *Chem. Commun.* **2016**, *52*, 10377–10380.
(321) Abdullah, N.; Arifin, Z.; Tiekink, E. R. T.; Sharmin, N.; Ahmad Tajidi, N. S.; Mat Hussin, S. A. Covalent and Ionic Cu(II) Complexes with Cyclam and Substituted Benzoato Ligands: Structural, Thermal, Redox and Mesomorphic Properties. *J. Coord. Chem.* **2016**, *69*, 862–878.
(322) Meyer, M.; Frémond, L.; Espinosa, E.; Guilard, R.; Ou, Z.; Kadish, K. M. Synthesis, Characterization, and X-Ray Crystal Structures of Cyclam Derivatives. 5. Copper(II) Binding Studies of a Pyridine-Strapped 5,12-Dioxocyclam-Based Macrobicycle. *Inorg. Chem.* **2004**, *43*, 5572–5587.
(323) Fortier, D. G.; Mcauley, A. Synthesis of a Novel Macrobicyclic Ligand, 15-Thia-1,5,8,12-Tetraazabicyclo[10. 5.2]Nonadecane, and Its Nickel(II) and Copper(II) Complexes. X-Ray Crystal Structures of[Cu(L1)](C104)2and [Ni(Ll)(C104)]C104. *Inorg. Chem.* **1989**, *28*, 655–662.
(324) Oshio, H. Structures and Magnetic Properties of [M(Cyclam)(CH_3CN)$_2$][Ni(Dmit)$_2$]$_2$ (M = Cu, Ni) and [Cu(Cyclam)]$_2$[2,5-DM-DCNQI]$_5$. *Inorg. Chem.* **1993**, *32*, 4123–4130.
(325) Dong, Y.; Lawrance, G. A.; Lindoy, L. F.; Turner, P. Macrocyclic Ligand Design. Interaction of a Series of Successively N-Benzylated Derivatives of 1,4,8,11-Tetraazacyclotetradecane (Cyclam) with Copper(II) and Nickel(II). *Dalton Trans.* **2003**, 1567–1576.
(326) Kurosaki, H.; Bucher, C.; Espinosa, E.; Barbe, J. M.; Guilard, R. Synthesis and Characterization of a 1,8-Difunctionalized Dissymmetrical Cyclam Copper(II) Complex Bearing Pyridylmethyl and N,N-Dimethylcarbamoylmethyl Groups. *Inorg. Chim. Acta* **2001**, *322*, 145–149.
(327) Tommos, C.; Babcock, G. T. Oxygen Production in Nature: A Light-Driven Metalloradical Enzyme Process. *Acc. Chem. Res.* **1998**, *31*, 18–25.
(328) Gallizia, A.; De Lalla, C.; Nardone, E.; Santambrogio, P.; Brandazza, A.; Sidoli, A.; Arosio, P. Production of a Soluble and Functional Recombinant Streptavidin in Escherichia Coil. *Protein Expr. Purif.* **1998**, *14*, 192–196.
(329) Lee, Y. M.; Hong, S.; Morimoto, Y.; Shin, W.; Fukuzumi, S.; Nam, W. Dioxygen

Activation by a Non-Heme Iron(II) Complex: Formation of an Iron(IV)-Oxo Complex via C-H Activation by a Putative Iron(III)-Superoxo Species. *J. Am. Chem. Soc.* **2010**, *132*, 10668–10670.
(330) van der Donk, W. A.; Krebs, C.; Bollinger, J. M. Substrate Activation by Iron Superoxo Intermediates. *Curr. Opin. Struct. Biol.* **2010**, *20*, 673–683.
(331) Stout, H. D.; Kleespies, S. T.; Chiang, C. W.; Lee, W. Z.; Que, L.; Münck, E.; Bominaar, E. L. Spectroscopic and Theoretical Study of Spin-Dependent Electron Transfer in an Iron(III) Superoxo Complex. *Inorg. Chem.* **2016**, *55*, 5215–5226.
(332) Chiang, C. W.; Kleespies, S. T.; Stout, H. D.; Meier, K. K.; Li, P. Y.; Bominaar, E. L.; Que, L.; Münck, E.; Lee, W. Z. Characterization of a Paramagnetic Mononuclear Nonheme Iron-Superoxo Complex. *J. Am. Chem. Soc.* **2014**, *136*, 10846–10849.
(333) Miller, A. F. Superoxide Dismutases: Active Sites That Save, but a Protein That Kills. *Curr. Opin. Chem. Biol.* **2004**, *8*, 162–168.
(334) Ha, E. H.; Ho, R. Y. N.; Kisiel, J. F.; Valentine, J. S. Modeling the Reactivity of. Alpha.-Ketoglutarate-Dependent Non-Heme Iron (II)-Containing Enzymes. *Inorg. Chem.* **1995**, *34*, 2265–2266.
(335) Miller, A. F. Superoxide Dismutases: Active Sites That Save, but a Protein That Kills. *Curr. Opin. Chem. Biol.* **2004**, *8*, 162–168.
(336) Sheng, Y.; Abreu, I. A.; Cabelli, D. E.; Maroney, M. J.; Miller, A. F.; Teixeira, M.; Valentine, J. S. Superoxide Dismutases and Superoxide Reductases. *Chem. Rev.* **2014**, *114*, 3854–3918.
(337) Umena, Y.; Kawakami, K.; Shen, J. R.; Kamiya, N. Crystal Structure of Oxygen-Evolving Photosystem II at a Resolution of 1.9Å. *Nature* **2011**, *473*, 55–60.
(338) Yano, J.; Yachandra, V. K. Where Water Is Oxidized to Dioxygen: Structure of the Photosynthetic Mn4Ca Cluster from X-Ray Spectroscopy. *Inorg. Chem.* **2008**, *47*, 1711–1726.
(339) McEvoy, J. P.; Brudvig, G. W. Water-Splitting Chemistry of Photosystem II. *Chem. Rev.* **2006**, *106*, 4455–4483.
(340) Leto, D. F.; Ingram, R.; Day, V. W.; Jackson, T. A. Spectroscopic Properties and Reactivity of a Mononuclear Oxomanganese(IV) Complex. *Chem. Commun.* **2013**, *49*, 5378–5380.
(341) Leto, D. F.; Chattopadhyay, S.; Day, V. W.; Jackson, T. A. Reaction Landscape of a Pentadentate N5-Ligated MnII Complex with $O_2^{\cdot-}$ and H_2O_2 Includes Conversion of a Peroxomanganese(III) Adduct to a Bis(μ-Oxo)-Dimanganese(III, IV) Species. *Dalton Trans.* **2013**, *42*, 13014–13025.
(342) Roukoss, C.; Fiddy, S.; De Mallmann, A.; Rendón, N.; Basset, J. M.; Kuntz, E.; Copéret, C. Access to Well-Defined Isolated Fe(II) Centers on Silica and Their Use in Oxidation. *Dalton Trans.* **2007**, *47*, 5546–5548.
(343) Guo, M.; Corona, T.; Ray, K.; Nam, W. Heme and Nonheme High-Valent Iron and Manganese Oxo Cores in Biological and Abiological Oxidation Reactions. *ACS Cent. Sci.* **2019**, *5*, 13–28.
(344) Miao, C.; Wang, B.; Wang, Y.; Xia, C.; Lee, Y. M.; Nam, W.; Sun, W. Proton-Promoted and Anion-Enhanced Epoxidation of Olefins by Hydrogen Peroxide in the Presence of Nonheme Manganese Catalysts. *J. Am. Chem. Soc.* **2016**, *138*, 936–943.
(345) Miao, C.; Li, X. X.; Lee, Y. M.; Xia, C.; Wang, Y.; Nam, W.; Sun, W. Manganese Complex-Catalyzed Oxidation and Oxidative Kinetic Resolution of Secondary Alcohols by

Hydrogen Peroxide. *Chem. Sci.* **2017**, *8*, 7476–7482.
(346) Groni, S.; Blain, G.; Guillot, R.; Policar, C.; Anxolabéhère-Mallart, E. Reactivity of MnII with Superoxide. Evidence for a $[Mn^{III}OO]^{+}$ Unit by Low-Temperature Spectroscopies. *Inorg. Chem.* **2007**, *46*, 1951–1953.
(347) Geiger, R. A.; Chattopadhyay, S.; Day, V. W.; Jackson, T. A. A Series of Peroxomanganese(III) Complexes Supported by Tetradentate Aminopyridyl Ligands: Detailed Spectroscopic and Computational Studies. *J. Am. Chem. Soc.* **2010**, *132*, 2821–2831.
(348) Geiger, R. A.; Leto, D. F.; Chattopadhyay, S.; Dorlet, P.; Anxolabéhère-Mallart, E.; Jackson, T. A. Geometric and Electronic Structures of Peroxomanganese(III) Complexes Supported by Pentadentate Amino-Pyridine and -Imidazole Ligands. *Inorg. Chem.* **2011**, *50*, 10190–10203.
(349) Du, J.; Xu, D.; Zhang, C.; Xia, C.; Wang, Y.; Sun, W. Synthesis, Characterization, and Reactivity of a Side-on Manganese(III)-Peroxo Complex Bearing a Pentadentate Aminopyridine Ligand. *Dalton Trans.* **2016**, *45*, 10131–10135.
(350) So, H.; Park, Y. J.; Cho, K. Bin; Lee, Y. M.; Seo, M. S.; Cho, J.; Sarangi, R.; Nam, W. Spectroscopic Characterization and Reactivity Studies of a Mononuclear Nonheme Mn(III)-Hydroperoxo Complex. *J. Am. Chem. Soc.* **2014**, *136*, 12229–12232.
(351) Colmer, H. E.; Howcroft, A. W.; Jackson, T. A. Formation, Characterization, and O-O Bond Activation of a Peroxomanganese(III) Complex Supported by a Cross-Clamped Cyclam Ligand. *Inorg. Chem.* **2016**, *55*, 2055–2069.
(352) Seo, M. S.; Kim, J. Y.; Annaraj, J.; Kim, Y.; Lee, Y. M.; Kim, S. J.; Kim, J.; Nam, W. $[Mn(Tmc)(O_2)]^{+}$: A Side-on Peroxido Manganese(III) Complex Bearing a Non-Heme Ligand. *Angew. Chemie - Int. Ed.* **2007**, *46*, 377–380.
(353) Barman, P.; Upadhyay, P.; Faponle, A. S.; Kumar, J.; Nag, S. S.; Kumar, D.; Sastri, C. V.; de Visser, S. P. Deformylation Reaction by a Nonheme Manganese(III)–Peroxo Complex via Initial Hydrogen-Atom Abstraction. *Angew. Chem., Int. Ed.* **2016**, *55*, 11091–11095.
(354) Chen, J.; Lee, Y. M.; Davis, K. M.; Wu, X.; Seo, M. S.; Cho, K. Bin; Yoon, H.; Park, Y. J.; Fukuzumi, S.; Pushkar, Y. N.; Nam, W. A Mononuclear Non-Heme Manganese(IV)-Oxo Complex Binding Redox-Inactive Metal Ions. *J. Am. Chem. Soc.* **2013**, *135*, 6388–6391.
(355) Sankaralingam, M.; Lee, Y. M.; Jeon, S. H.; Seo, M. S.; Cho, K. Bin; Nam, W. A Mononuclear Manganese(III)-Hydroperoxo Complex: Synthesis by Activating Dioxygen and Reactivity in Electrophilic and Nucleophilic Reactions. *Chem. Commun.* **2018**, *54*, 1209–1212.
(356) Barman, P.; Vardhaman, A. K.; Martin, B.; Wörner, S. J.; Sastri, C. V.; Comba, P. Influence of Ligand Architecture on Oxidation Reactions by High-Valent Nonheme Manganese Oxo Complexes Using Water as a Source of Oxygen. *Angew. Chem., Int. Ed.* **2015**, *54*, 2095–2099.
(357) Garcia-Bosch, I.; Company, A.; Cady, C. W.; Styring, S.; Browne, W. R.; Ribas, X.; Costas, M. Evidence for a Precursor Complex in C-H Hydrogen Atom Transfer Reactions Mediated by a Manganese(IV) Oxo Complex. *Angew. Chem., Int. Ed.* **2011**, *50*, 5648–5653.
(358) Yin, G.; McCormick, J. M.; Buchalova, M.; Danby, A. M.; Rodgers, K.; Day, V. W.; Smith, K.; Perkins, C. M.; Kitko, D.; Carter, J. D.; Scheper, W. M.; Busch, D. H. Synthesis, Characterization, and Solution Properties of a Novel Cross-Bridged Cyclam

Manganese(IV) Complex Having Two Terminal Hydroxo Ligands. *Inorg. Chem.* **2006**, *45*, 8052–8061.
(359) Parsell, T. H.; Behan, R. K.; Green, M. T.; Hendrich, M. P.; Borovik, A. S. Preparation and Properties of a Monomeric MnIV-Oxo Complex. *J. Am. Chem. Soc.* **2006**, *128*, 8728–8729.
(360) Gupta, R.; Taguchi, T.; Borovik, A. S.; Hendrich, M. P. Characterization of Monomeric MnII/III/IV-Hydroxo Complexes from X- and Q-Band Dual Mode Electron Paramagnetic Resonance (EPR) Spectroscopy. *Inorg. Chem.* **2013**, *52*, 12568–12575.
(361) Taguchi, T.; Stone, K. L.; Gupta, R.; Kaiser-Lassalle, B.; Yano, J.; Hendrich, M. P.; Borovik, A. S. Preparation and Properties of an MnIV–hydroxide Complex: Proton and Electron Transfer at a Mononuclear Manganese Site and Its Relationship to the Oxygen Evolving Complex within Photosystem II. *Chem. Sci.* **2014**, *5*, 3064.
(362) Mullins, C. S.; Pecoraro, V. L. Reflections on Small Molecule Manganese Models That Seek to Mimic Photosynthetic Water Oxidation Chemistry. *Coord. Chem. Rev.* **2008**, *252*, 416–443.
(363) Goldsmith, C. R.; Cole, A. P.; Stack, T. D. P. C-H Activation by a Mononuclear Manganese(III) Hydroxide Complex: Synthesis and Characterization of a Manganese-Lipoxygenase Mimic? *J. Am. Chem. Soc.* **2005**, *127*, 9904–9912.
(364) Kovacs, J. A. Tuning the Relative Stability and Reactivity of Manganese Dioxygen and Peroxo Intermediates via Systematic Ligand Modification. *Acc. Chem. Res.* **2015**, *48*, 2744–2753.
(365) Neu, H. M.; Baglia, R. A.; Goldberg, D. P. A Balancing Act: Stability versus Reactivity of Mn(O) Complexes. *Acc. Chem. Res.* **2015**, *48*, 2754–2764.
(366) Charles Dismukes, G.; Brimblecombe, R.; Felton, G. A. N.; Pryadun, R. S.; Sheats, J. E.; Spiccia, L.; Swiegers, G. F. Development of Bioinspired Mn4O4-Cubane Water Oxidation Catalysts: Lessons from Photosynthesis. *Acc. Chem. Res.* **2009**, *42*, 1935–1943.
(367) Tsui, E. Y.; Tran, R.; Yano, J.; Agapie, T. Redox-Inactive Metals Modulate the Reduction Potential in Heterometallic Manganese-Oxido Clusters. *Nat. Chem.* **2013**, *5*, 293–299.
(368) Cady, C. W.; Crabtree, R. H.; Brudvig, G. W. Functional Models for the Oxygen-Evolving Complex of Photosystem II. *Coord. Chem. Rev.* **2008**, *252*, 444–455.
(369) Zhang, J. L.; Garner, D. K.; Liang, L.; Barrios, D. A.; Lu, Y. Noncovalent Modulation of PH-Dependent Reactivity of a Mn-Salen Cofactor in Myoglobin with Hydrogen Peroxide. *Chem. Eur. J.* **2009**, *15*, 7481–7489.
(370) Carey, J. R.; Ma, S. K.; Pfister, T. D.; Garne, D. K.; Kim, H. K.; Abramite, J. A.; Wang, Z.; Guo, Z.; Lu, Y. A Site-Selective Dual Anchoring Strategy for Artificial Metalloprotein Design. *J. Am. Chem. Soc.* **2004**, *126*, 10812–10813.
(371) Denler, M. C.; Wijeratne, G. B.; Rice, D. B.; Colmer, H. E.; Day, V. W.; Jackson, T. A. Mn(III)-Peroxo Adduct Supported by a New Tetradentate Ligand Shows Acid-Sensitive Aldehyde Deformylation Reactivity. *Dalton Trans.* **2018**, *47*, 13442–13458.
(372) Denler, M. C.; Massie, A. A.; Singh, R.; Stewart-Jones, E.; Sinha, A.; Day, V. W.; Nordlander, E.; Jackson, T. A. Mn(IV)-Oxo Complex of a Bis(Benzimidazolyl)-Containing N5 Ligand Reveals Different Reactivity Trends for Mn(IV)-Oxo than Fe(IV)-Oxo Species. *Dalton Trans.* **2019**, *48*, 5007–5021.
(373) Massie, A. A.; Denler, M. C.; Cardoso, L. T.; Walker, A. N.; Hossain, M. K.; Day, V. W.; Nordlander, E.; Jackson, T. A. Equatorial Ligand Perturbations Influence the

Reactivity of Manganese(IV)-Oxo Complexes. *Angew. Chem., Int. Ed.* **2017**, *56*, 4178–4182.